Oxidative damage to lung surfactant and lipid membranes

Oxidative Damage to Lung Surfactant and Lipid Membranes

Joanna Hemming

Institute of Structural and Molecular Biology

Birkbeck College, University of London

Submitted to the University of London in accordance with the requirements of the degree of Doctor of Philosophy

September 2014

Supervisor: Dr. Katherine Thompson

I, Joanna Hemming, confirm that the work presented in this thesis is my own. Where information has been derived from other sources, I confirm that this has been indicated in the thesis.

……..

Abstract

Lung surfactant is a mixed monolayer of lipids and proteins that reduce the surface tension at the air-lung interface to prevent alveolar collapse. Exposure of lung surfactant to ozone pollution has been linked to an increased risk of death due to respiratory diseases. This work aimed to determine the ozone damage caused to lung surfactant at the air-water interface. A range of analytical techniques showed that peptide mimics of surfactant protein B were rapidly oxidised by ozone but no cleavage of the peptides occurred. Neutron reflectivity revealed that the peptides remained at the air-water interface after oxidation but that their interaction with anionic phospholipids, thought to be crucial to their function, was significantly reduced. Neutron and X-ray reflectivity experiments showed that exposure of different lipid monolayers to ozone led to a loss of unsaturated phospholipid material from the interface, whereas oxidised cholesterol remained but the molecules were considerably reorganised. The ozonolysis of whole animal lung surfactant was then investigated and it was shown that material was lost from the interface during reaction and that the monolayer was much less capable of reducing surface tension. Additionally, molecular dynamics simulations were performed, determining that surfactant protein C can significantly influence the ordering of surrounding phospholipids in a monolayer and that palmitoylation of the protein leads to an increase in this ordering effect. Finally, the uses of neutron scattering to explore the oxidation of lipid membranes were investigated. It was shown that neutron reflectivity of supported phospholipid bilayers at the solid-liquid interface is a useful tool for determining their reactivity with different reactive oxygen species. Small angle neutron scattering and off-specular neutron reflectivity were also shown to be valuable methods for exploring the changes in lipid raft formation upon oxidation of phospholipids.

Acknowledgements

I could not have completed this thesis without the help and support of some amazing people. These include both scientific colleagues who provided interesting and useful discussions, as well as friends and family who have been there to support me through my PhD journey in London.

First and foremost I'd like to thank my fantastic supervisor Katherine, who has been a constant source of encouragement, support and expert knowledge during these three years. Thank you for guiding me and teaching me so much. Thanks also to Salvador and Bonnie for helpful discussions in our thesis committee meetings. I'd also like to sincerely thank Adrian Rennie and Jayne Lawrence for their expertise and company on neutron experiments, as well as help with data analysis and interpretation. The laser, neutron and X-ray experiments would not have been so successful without the help of the great instrument scientists including Max Skoda, Tom Arnold, Richard Campbell, Arwel Hughes, Nina Steinke, Ann Terry and Stan Botchway.

I would also like to thank past and current students in the group who worked on these projects, particularly Justyna for help with lung samples and X-ray data collection. Thanks also to Lili Cui from Jayne's group at King's for vesicle sample preparation and help with SANS.

I would like to thank my incredible friends and family for maintaining my positive outlook during my PhD and for all the happy and emotional times we've had. I cannot thank my parents and grandparents enough for the life they have given me and for always believing that I can do this, even if they don't understand what I'm doing. Thanks to my sister Charlie, brother Alex and Amy for being there for me, and for the love, laughter and countless hours of music. Thanks to my friends in London, we've supported and accompanied each other through this journey. Thanks to Gemma for getting me through so much, as well as my other beautiful friends from home, including my extended family, especially Tom. Finally, I thank Matt for the love, laughs, support and motivation while writing this thesis.

Table of Contents

List of Figures

List of Tables

List of Abbreviations

2-D	2-dimensional
2D-NMR	2-dimensional Nuclear Magnetic Resonance
3-D	3-dimensional
AFM	Atomic force microscopy
BAM	Brewster Angle Microscopy
CD	Circular Dichroism
Chol	Cholesterol
CID	Collision induced dissociation
COPD	Chronic Obstructive Pulmonary Disease
d_{31}POPC	Palmitoyl deuterated 1-palmitoyl–2-oleoyl phosphatidylcholine
d_{31}POPG	Palmitoyl tail deuterated 1-palmitoyl-2-oleoyl-*sn*-glycero-3-phospho-(1'-rac-glycerol)
d_{62} DPPC	Tail deuterated dipalmitoyl phosphatidylcholine
d_{62} DPPG	Tail deuterated 1,2-dipalmitoyl-*sn*-glycero-3-phosphoglycerol
DG	Diacylglycerol
DNA	Deoxyribonucleic Acid
DOPC	1,2-dioleoyl-*sn*-glycero-3-phosphocholine
DOPG	1,2-dioleoyl-*sn*-glycero-3-phospho-(1'-rac-glycerol)
DPPC	Dipalmitoyl Phosphatidylcholine
DPPG	1,2-dipalmitoyl-*sn*-glycero-3-phosphoglycerol
dpSP-C	dipalmitoylated surfactant protein C
DSSP	Define secondary structure of proteins

DTT	Dithiothreitol
E. Coli	*Escherichia coli*
EDTA	Ethylenediaminetetraacetic acid
FIDI-MS	Field-Induced Droplet Ionisation Mass Spectrometry
FTIR	Fourier Transform Infrared
GC	Gas Chromatography
GPI	Glycophosphatidylinositol
GROMACS	GROningen MAchine for Chemical Simulations
GROMOS	GROningen Molecular Simulation
HPLC	High Performance Liquid Chromatography
IRAAS	Infrared reflection-absorption spectroscopy
IRDS	Infant Respiratory Distress Syndrome
LC	Liquid-condensed
LC-MS	Liquid Chromatography Mass Spectrometry
LCAO	Linear Combination of Atomic Orbitals
L_d	Liquid Disordered Phase
LE	liquid-expanded
LINCS	LINear Constraint Solver
L_o	Liquid Ordered Phase
Lyso-*bis*-PA	Lyso-bis-phosphatidic acid
MD	Molecular Dynamics
NMR	Nuclear Magnetic Resonance
NO_x	Nitrogen Oxides

NPT	Isothermal-isobaric ensemble
NR	Neutron reflectivity
NRW	Null-reflecting Water
nSP-C	Non-palmitoylated surfactant protein C
NVT	Canonical ensemble
OPLS	Optimised potentials for liquid simulations
PAP	Pulmonary Alveolar Proteinosis
PAzPC	1-palmitoyl-2-azelaoyl-*sn*-glycero-3-phosphocholine
PBC	Periodic boundary conditions
PC	Phosphatidylcholine
$Pd_{17}OPC$	Oleoyl deuterated 1-palmitoyl–2-oleoyl phosphatidylcholine
PDB	Protein Data Bank
PE	Phosphatidylethanolamine
PG	Phosphatidylglycerol
PI	Phosphatidylinositol
PM-IRRAS	Polarisation modulation infrared reflectance absorption spectroscopy
POnPC	1-palmitoyl-2-(9'-oxo-nonanoyl)-*sn*-glycero-3-phosphocholine
POPC	1-palmitoyl–2-oleoyl phosphatidylcholine
POPE	1-palmitoyl-2-oleoyl-*sn*-glycero-3-phosphoethanolamine
POPG	1-palmitoyl-2-oleoyl-*sn*-glycero-3-phospho-(1'-rac-glycerol)
POPI	1-palmitoyl-2-oleoyl-*sn*-glycero-3-phosphoinositol
Ppm	Part per million
PTFE	Polytetrafluoroethylene

QCM	Quartz contrast matched
RMSD	Root-mean-square deviation
ROS	Reactive Oxygen Species
SANS	Small-angle Neutron Scattering
SDS	Sodium dodecyl sulphate
SDS-PAGE	Sodium dodecyl sulphate polyacrylamide gel electrophoresis
SLD	Scattering length density
SMB	Super-mini B
SP-A	Surfactant Protein A
SP-B	Surfactant Protein B
$SP\text{-}B_{1\text{-}25}$	Surfactant Protein B residues 1-25
SP-C	Surfactant Protein C
SP-D	Surfactant Protein D
SPC	Simple point charge water model
SPM	Sphingomyelin
SUVs	Small unilamellar vesicles
SWSE	Sum of weighted squared errors
TEMED	Tetramethylethylenediamine
TFE	Tetrafluoroethylene
T_m	Melting temperature: Transition from gel to liquid phase
UCSF	University of California, San Francisco
UK	United Kingdom
USA	United States of America

UV	Ultra Violet
VOC	Volatile Organic Carbons
WHO	World Health Organisation
wt %	Weight Percent

Chapter 1 Introduction

Oxidative damage to the body can be caused by exposure to an excess of endogenous oxidation sources, such as reactive oxygen species formed from normal cellular metabolism, as well as exogenous sources, such as air pollutants. An excess of oxidation damage can lead to a range of disorders such as Alzheimer's disease, Parkinson's disease, cancer and respiratory conditions. The effects of overexposure to oxidative species leading to these disorders are fairly well established, however the chemical, structural and mechanistic changes as a result of the oxidative damage are largely unknown. This thesis explores the chemical and structural damage to individual components of lung surfactant during exposure to the oxidative air pollutant ozone, and also the structural damage to lipid membranes by various reactive oxygen species.

1.1 Gas Exchange in the Lungs

In the lungs, gas exchange is mediated through an air-liquid interface (Figure 1.1). There is a discontinuity in energy across the interface as the energy of the surface layer is higher than that of the two bordering phases. The fundamental challenge to alveolar stability is during exhalation as the alveolar radius decreases, potentially increasing the surface tension. If surface tension does not decrease as the surface area is reduced, the pressure from surface tension will cause collapse of the alveoli. [1,2]

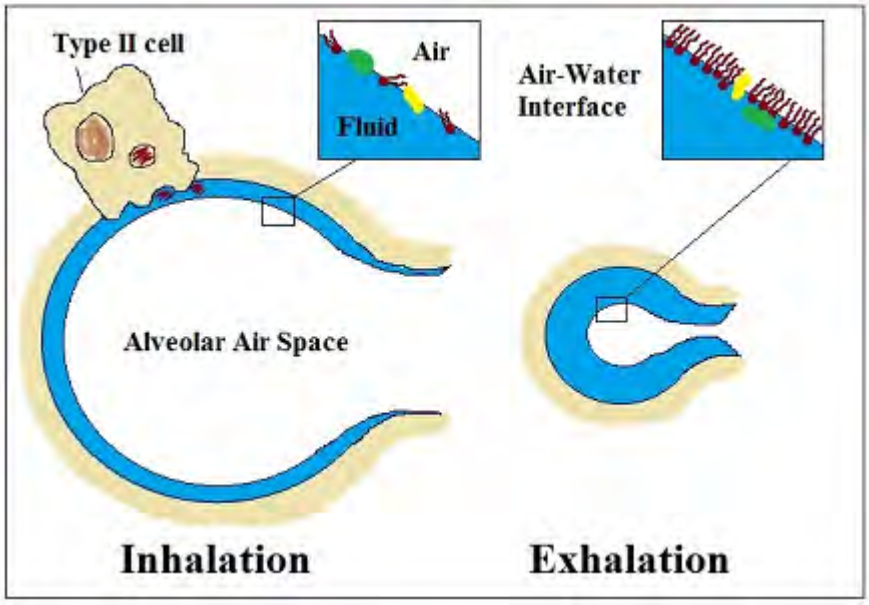

Figure 1.1. The air-liquid interface of the lung.

The epithelial cells in the lining of the alveoli have a layer of aqueous fluid to dissolve gaseous air molecules and aid exchange with the gas interface. The surface layer of the fluid has a monolayer of molecules at the air-liquid interface, an important feature of the lung surfactant.[1]

1.2 The Lung Surfactant

Lung surfactant is produced in the lung to decrease surface tension of the fluid lining from 70 mN m^{-1} at a pure water-air interface to approximately 0-1 mN m^{-1} during expiratory compression. There is approximately a constant amount of surfactant per alveolus. Thus, it can prevent collapse during exhalation as the surfactant becomes more concentrated on the surface due to the decrease in alveolar surface area (Figure 1.1).[3,4]

By reducing the surface tension within the lungs, the lung surfactant significantly contributes to maintaining normal mechanics of respiration. It reduces the energy required to inflate the lungs, therefore enabling maintenance of a large gas transfer area and increasing the lung compliance on inspiration. The lung surfactant also decreases elastic recoil, reducing the likelihood of alveolar collapse during expiration. [6, 7, 8]

Lung surfactant also exists in bronchioles and small airway passages to prevent cohesion of bronchiolar walls. This is particularly important in diving mammals and reptiles, as the collapse of part of their lungs is important for their diving and expiratory cycles.[9]

In addition to its surface tension reducing capabilities, the lung surfactant is known to have protective functions. It can be very significant in protection of epithelial cells from damage by air thrusts. Furthermore, the surfactant can protect the alveolar cells from damage by pathogens or bacterial toxins and it has some antibacterial and antiviral activity. It has also been shown that by lowering surface tension at the end of expiration, lung surfactant can enhance the removal of particulates and damaged cells from the alveoli. [10]

1.2.1 Discovery of the Lung Surfactant

The lung surfactant was initially described in the 1920s when von Neergaard demonstrated the importance of interfacial forces involved in lung mechanics. He proposed a theory that molecules existed at the surface of the lung tissue that reduced surface tension to prevent alveolar collapse. However, he was unable to identify the presence of these molecules with the techniques available at that time.[11]

It was rediscovered in the mid-1950's by Pattle and Clements when they found that extracts from the lung rapidly spread and adsorb to form an insoluble film and that surface tension was reduced to small values. Pattle initially assumed that lung surfactant was a protein film, but further studies soon established that phospholipids comprised the major component. [12, 13]

1.2.2 Production of Lung Surfactant

Lung surfactant is a complex mixture of molecules (as discussed below), which are synthesised in the endoplasmic reticulum of alveolar type II cells lining the alveoli, beginning during the lung development of foetuses (approximately 20 weeks gestation). After synthesis, the molecules are trafficked *via* the Golgi

apparatus to higher order phospholipid-rich structures known as Lamellar bodies. The foetal lung produces surfactant in increasing quantity towards the end of gestation.[14]

The surfactant molecules are stored in the Lamellar bodies until an infant takes his or her first breath. It is not yet clear how the contents of the lamellar bodies form the film at the interface but the generally accepted mechanism is shown in Figure 1.2. In this mechanism, the bodies are secreted by exocytosis upon an infant's first breath into the surface water layer lining the alveolar airspace to form a mesh-like structural body known as tubular myelin. Electron microscopy has been fundamental in identifying the presence of lamellar bodies and tubular myelin as stores of surfactant. Other proposed methods for transporting the lung surfactant to the air-water interface include direct transfer of surfactant from secreted lamellar body-like particles touching the interface or rapid movement of surface active species through a continuous network of surfactant membranes, connecting secreting cells with the interface. The mechanisms by which newly secreted surfactant phospholipids are transferred to the air-liquid interface *in vivo* remains disputed because translation of *in vitro* results, which often use model lipid mixtures, is not straightforward.[14, 15, 16]

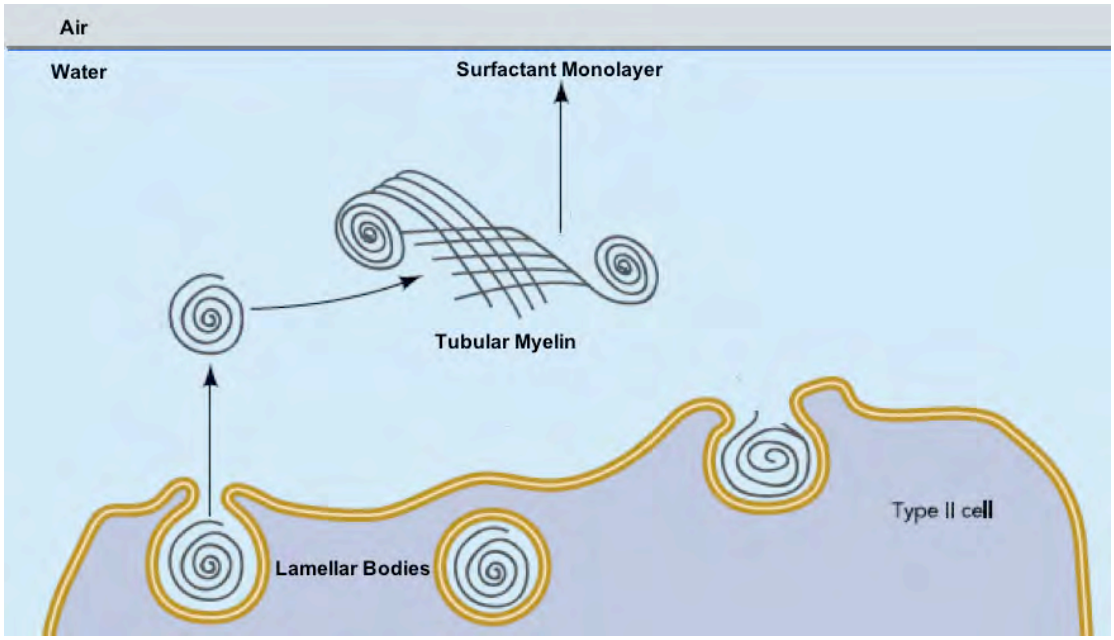

Figure 1.2. Lung surfactant adsorption to the interface and surface film formation.

Processes involving transport of surfactant to the air-liquid interface. [15]

1.3 Composition of Lung Surfactant

Lung surfactant is a complex mixture of phospholipids, neutral lipids and proteins at the air-water interface. It is represented by several structural entities: lamellar bodies, tubular myelin and monolayers. The monolayer is the surface-tension reducing feature of the surfactant at the air-water interface. It has been shown that lung surfactant exists in all air-breathing vertebrates, although the composition can vary across species.[7] However, the composition of mammalian species is similar even in very diverse species. The components of human lung surfactant are shown in Figure 1.3. The exact percentages can vary in the literature, particularly the proportions of different lipids, this is probably due to the differences in methods used to analyse the surfactant, e.g. liquid or gas chromatography. [8]

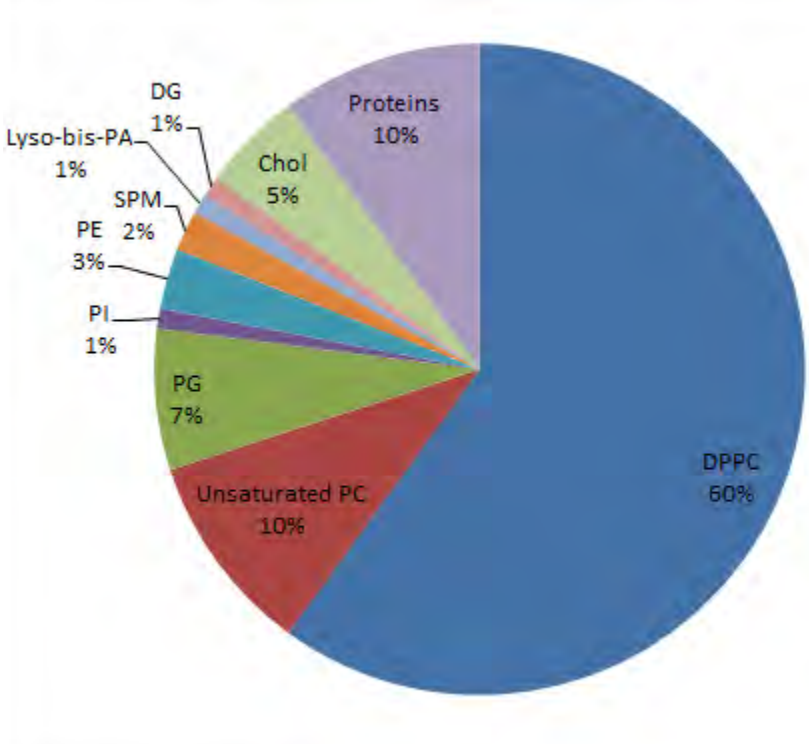

Figure 1.3. The percentage composition of molecules within human lung surfactant.

This pie chart represents the weight percentage composition of the molecules found in the surface monolayer of the lung surfactant. DPPC: dipalmitoyl phosphatidylcholine; PC: phosphatidylcholine; PG: phosphatidylglycerol; PI: phosphatidylinositol; PE: phosphatidylethanolamine; Lyso-*bis*-PA: lyso-*bis*-phosphatidic acid; SPM: sphingomyelin; DG: diacylglycerol; Chol: cholesterol.[8]

1.3.1 Phospholipids

Phospholipids are the main components of the lung surfactant, comprising 90-95 wt.% of all lipids, or 80-85 wt.% of all surfactant components. Phosphatidylcholines (PC) are the predominant class of phospholipids, accounting for approximately 70% by weight of all lung surfactant components. In humans, the most prevalent PC is the saturated dipalmitoylphosphadylcholine (DPPC- 60% by weight of all surfactant components). The other prominent PC species are mainly unsaturated PC such as 1-palmitoyl–2-oleoyl phosphatidylcholine (POPC). Examples of PC molecules are shown in Figure 1.4.[8, 17]

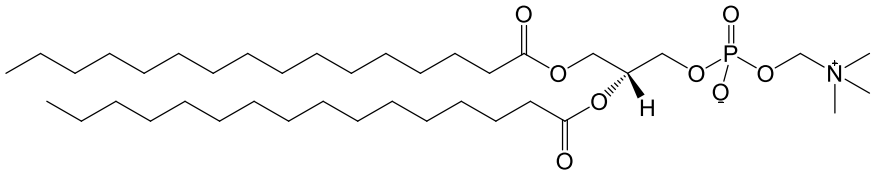

DPPC

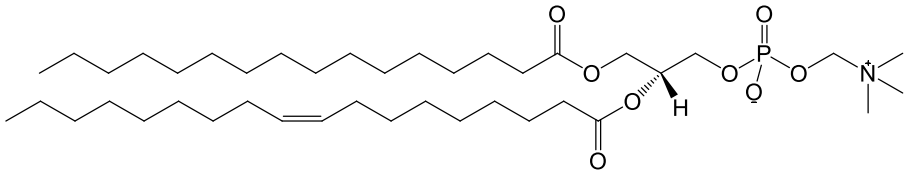

POPC

Figure 1.4. The chemical structure of the phosphocholines DPPC and POPC.
The phosphocholines that are significant components of the lung surfactant.

The remaining 20% of phospholipids are primarily unsaturated, the majority of which are anionic lipids such as phosphatidylglycerol (PG), phosphatidylinositol (PI), and lyso-bis-phosphatidic acid. The anionic phospholipids constitute approximately 15% of total phospholipids. Other phospholipids include the zwitterionic lipids phosphatidylethanolamine (PE) and sphingomyelin. Examples of other phospholipids are shown in Figure 1.5.[7, 14]

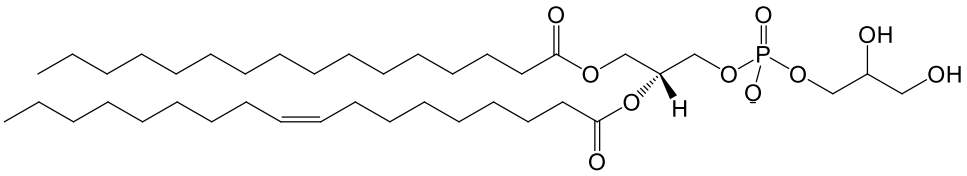

POPG

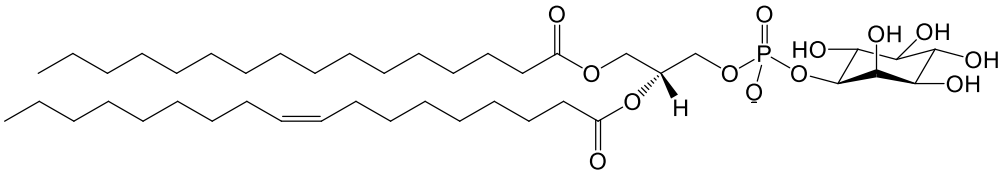

POPI

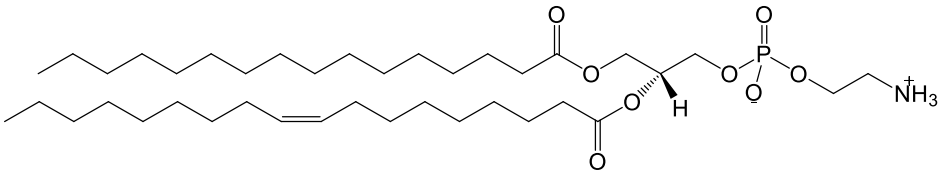

POPE

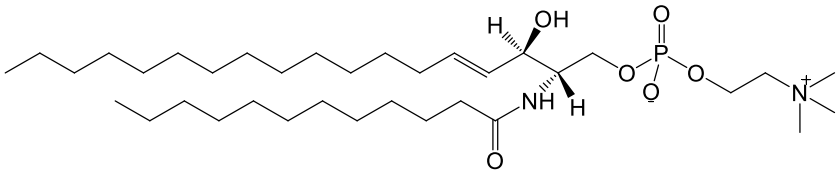

Sphingomyelin

Figure 1.5. The chemical structure of phospholipids POPG, POPI, POPE and Sphingomyelin.

1.3.1.1. Functions of the Phospholipids within Lung Surfactant Monolayers

Phospholipids have a hydrophilic "head", for example the choline or glycerol part of PC or PG, and a hydrophobic "tail", for example one or more alkane chains. Therefore, at the air-water interface it is energetically more favourable for these amphiphiles to form a monolayer where the heads are associated with the water and the tails form an insoluble layer above the surface. A monolayer of phospholipid can exist in different phases, depending on several properties including number of molecules per area (surface pressure), hydrocarbon length, unsaturation, charge and headgroup. Monolayers could exist in phases ranging from the solid phase, where hydrocarbon chains are fully extended and closely packed, to the disordered gas phase, where hydrocarbon chains are randomly oriented and fluid (Figure 1.6).[18]

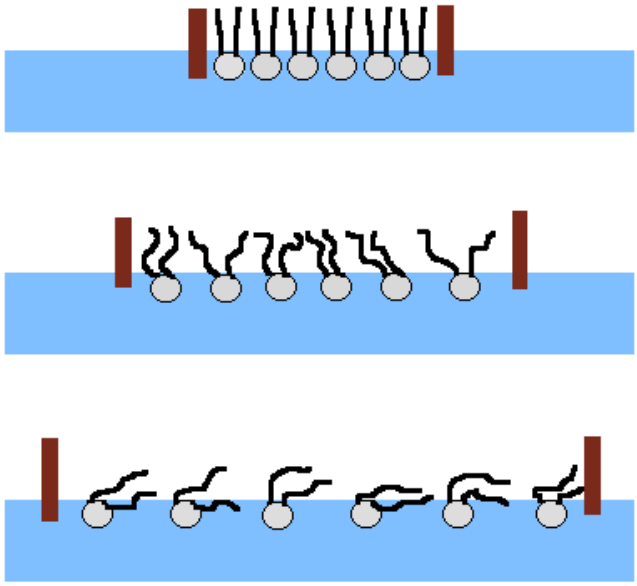

Figure 1.6. A monolayer of phospholipids at different areas per lipid showing different phases.

As the area per molecule increases, the phospholipid monolayer goes from solid phase (top) to liquid-expanded phase (middle) to gas phase (bottom).[22] Grey balls represent the lipid heads and the black lines represent the lipid tails. The diagrams are for a monolayer at the air-water interface, where the blue box represents the water.

The primary phospholipid, DPPC, is the main surface-tension reducing agent. It has been shown that DPPC is the only major component that is capable of generating surface tension levels lower than 2 mN m^{-1} as required for the full function of the lungs.[19] This can be achieved because the saturated tails can pack very closely together, therefore the effective concentration at the surface can be very high. It has been shown to be capable of retaining a continuous low surface tension at a constant area for several hours.[20]

The unsaturated phospholipids within the surfactant monolayer are not able to reduce the surface tension to such low levels since such films cannot pack as tightly in the monolayer as DPPC, as a double carbon bond introduces rigidity to the conformation. Monolayers of these unsaturated phospholipids alone can lower surface tension to only 15-20 mN m^{-1}. At low lung volumes, the lung would not be

stabilised at these surface tension levels.[21] Therefore, the lung contains a film rich in DPPC to maintain low enough levels. The presence of unsaturated phospholipids is assumed to be for an alternative function.

At physiological temperature, DPPC would form a surface monolayer extremely slowly and would therefore be incapable of adequately replacing surfactant during lung compression and expansion cycles. It can be observed that continuous compression and expansion of a monolayer of DPPC leads to increasing surface tensions during subsequent cycles because DPPC is forced out of the monolayer in a collapsed state and the monolayer can not respread rapidly.[19] Although unsaturated lipids do have some surface-tension reduction capabilities, it is thought that their presence is also to enhance adsorption and fluidity of the lipid monolayer, by introducing a "kink" in the tails of the DPPC monolayer at small areas. This is particularly important in lungs of colder-blooded animals, for example the ratio of DPPC to total surfactant components in reptiles of 37°C is mammalian-like at approximately 50%, whereas the ratio of DPPC to total surfactant in colder reptiles of 23°C is approximately 25%. There is a greater fraction of unsaturated lipids with lower phase transition temperatures than DPPC in the cold-blooded reptiles.[23] However, the presence of unsaturated phospholipids alone is not sufficient for the full adsorption required of the surfactant monolayer, as described in section 1.3.1.1.[19]

Lung surfactant consists of a significant amount of acidic/anionic phospholipids, such as PG and PI, suggesting a specific function. It has been shown using fluorescence probes that PG interacts specifically with positively charged moieties on the surfactant proteins (see section 1.3.3).[24] Mixtures of DPPC, PG and surfactant protein B show very surface-active films, i.e. low surface tension is maintained during compression and expansion cycles with minimal loss of DPPC.[25] Therefore, in addition to decreasing surface tension and improving fluidity of lipid films, some phospholipids are necessary for interaction with surfactant proteins.

The role of minor phospholipids that are present in relatively low amounts in the lung surfactant is not clear. From a surface tension perspective, these lipids should have minimal effect on surfactant activity but there is no specific evidence for this. It has been proposed that the presence of some of these lipids could be

related to metabolism of the surfactant, although this has not been determined.[12]

The surfactant film mechanism is often disputed. It is generally accepted that DPPC is required to maintain the low surface tension required to prevent collapse of the alveoli but the organisation of the components to maintain this enrichment is not known. Many authors in the literature describe a model where the mixed film is compressed during exhalation leading to unsaturated lipids being squeezed out of the surface monolayer to form a DPPC rich monolayer of very low surface tension. The unsaturated lipids remain associated with the monolayer in a vesicle-like structure that can re-enter the monolayer upon expansion of the alveoli.[12] Another model is where the surfactant forms multilayers at the surface instead of squeeze-out occurring.[8]

1.3.2 Other Lipids

There is less information available about non-phosphorus containing lipids involved in the lung surfactant. Cholesterol is the main non-phosphorus lipid in mammalian species, with levels of about 3-7% in humans. Glycerides are also present, such as diacylglycerols. Some examples of neutral lipids are shown in Figure 1.7. [8, 12]

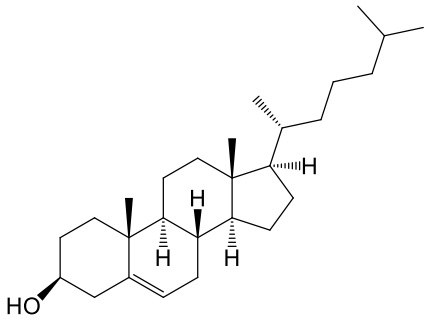

Cholesterol

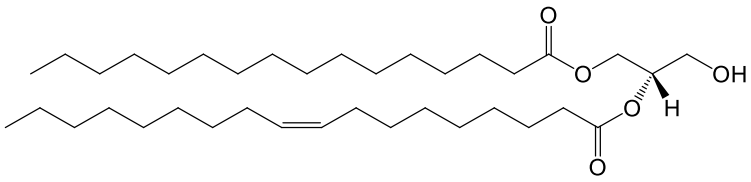

1-palmitoyl-2-oleoyl-*sn*-glycerol (PODG)

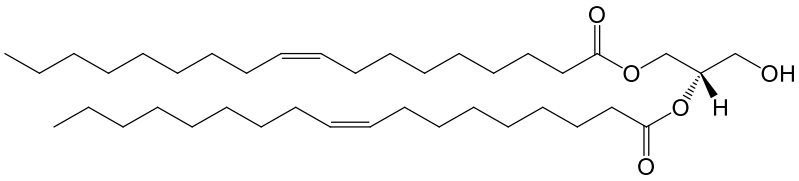

1-2-dioleoyl-*sn*-glycerol (DODG)

Figure 1.7. The chemical structures of the lipids cholesterol, PODG and DODG.

1.3.2.1 Functions of Neutral Lipids in Lung Surfactant

Although neutral (non-phosphorus containing) lipids are present in the lung surfactant at significant levels, there has been much less experimental research investigating their function compared to phospholipids. Addition of glycerides to DPPC or DPPC/PG mixtures has been shown to increase the adsorption rate of the lipids to the air-water interface, possibly by affecting the packing of the lipid components.[26]

Cholesterol has also been shown to enhance the adsorption of DPPC lipid

vesicles to the air-water interface by increasing fluidity and improving film respreading. However, cholesterol limits the minimum surface tensions achievable during compression as it cannot be readily squeezed out from the monolayer, causing a reduction in the packing of the DPPC layer. It has not yet been established whether cholesterol, therefore, has a more important role in the function of the lung surfactant.[27]

1.3.3 Surfactant Proteins

Surfactant-specific proteins contribute to about 10% by weight of the surfactant material. These are separated into 2 subgroups: the Ca^{2+} dependent carbohydrate-binding hydrophilic proteins, surfactant-protein A (SP-A) and surfactant-protein-D (SP-D); and the hydrophobic proteins, surfactant protein-B (SP-B) and surfactant protein-C (SP-C).[17]

1.3.3.1 Hydrophilic Surfactant Proteins

SP-A and SP-D are structurally characterised by an N-terminal collagen-like domain connected by a neck domain with globular C-terminal domains. These proteins are assembled in complex structures consisting of 3 subunits.

The most abundant surfactant by weight is SP-A (32 kDa), constituting 5-7% of the total weight of surfactant. It is associated with some structural membranes in the surfactant, but does not exist as part of the surfactant monolayer.[27] In contrast, SP-D constitutes about 0.5 weight % and is not associated with lipids in the surfactant. SP-D is a 43 kDa protein that has sequence homology with SP-A. [28]

1.3.3.2 Functions of Surfactant Protein A

Surfactant protein A exists below the surface of the interface in the lungs and so does not specifically cause a decrease in the surface tension within the

lungs. It does however enhance the rate of formation of a phospholipid surface film at the air-water interface *in vitro*. It has been proposed to do this by binding to DPPC lamellar bodies or vesicles below the surface.[32, 33]

It has also been shown that SP-A can aid regulation of surfactant homeostasis within the alveolus either by binding to receptors to promote recycling of the phospholipids [34] or by inhibiting the secretion of phospholipids.[35,36] However, lung function is not altered when the SP-A gene is deleted in mice. [36]

Plasma proteins have been shown to inhibit surfactant activity *in vivo* and *in vitro*.[37] It has been shown that bovine SP-A reduces the inhibition caused by plasma proteins.[38] Additionally, surfactant from SP-A knockout mice is more amenable to inhibition by plasma proteins than surfactant obtained from wild type mice. [39]

SP-A is also proposed to have a protective function against bacteria and viruses. It is known to bind to endotoxin in the walls of gram-negative bacteria to facilitate their aggregation, phagocytosis and killing by macrophages. Furthermore, SP-A can up-regulate and activate macrophages to induce phagocytosis.[33] For example, SP-A has been shown to enhance the binding and phagocytosis of *Mycobacterium tuberculosis* by human macrophages.[40] Human SP-A has also been shown to bind the herpes simplex and influenza A virus *via* its carbohydrate moiety, increasing their phagocytosis by human macrophages.[41,33]

1.3.3.3 Functions of Surfactant Protein D

Although homologous with SP-A, SP-D is the only surfactant protein that does not interact with the lipids that form the surfactant monolayer. It does, however, have a similar protective function against bacteria and viruses as SP-A. SP-D has also been shown to interact with *Mycobacterium Turberculosis*[42] and gram-positive bacteria [43] to induce the killing of the bacteria by macrophages.

For example, SP-D has been shown to inhibit the infectivity and activity of influenza A virus *in vitro* [44] and other respiratory viruses such as the Rous sarcoma virus G and rotaviruses.[45] It can do this by calcium-dependent attachment to the major viral glycoprotein.

1.3.4 Hydrophobic Surfactant Proteins

SP-B and SP-C are extremely hydrophobic proteins that form part of the surfactant monolayer. They are described separately below.

1.3.4.1 Surfactant Protein B (SP-B)

SP-B (8 kDa per monomer) is an unusually hydrophobic, positively charged protein, found mainly in a dimeric form, linked *via* disulphide bonds. It is synthesised in the cell as a 42 kDa proprotein. This is cleaved at the amino terminus by cathepsin D resulting in a 25 kDa intermediate protein. Finally, the C terminal is removed to produce the mature, active protein in order for it to reside at the air-water interface within the surfactant monolayer.[46]

The three-dimensional structure of the full-length protein is not known, but high-resolution structures of synthetic peptide fragments (e.g., N-terminal 1–25[47] or 34-residue mini-B [48]) are available. A detailed description of these peptide fragments is given in Chapter 3.

Homology analysis of the SP-B protein sequence (Figure 1.8) has revealed that it belongs to the family of saposin-like proteins. It has been predicted that SP-B structure might have a characteristic saposin fold with four amphiphilic α-helices connected by unstructured loops and linked by three intramolecular disulfide bridges, as presented in Figure 1.8.[49] It is thought that SP-B inserts into the monolayer of phospholipids with its amphipathic helical segments aligned parallel to the plane of phospholipid layers.[50, 51]

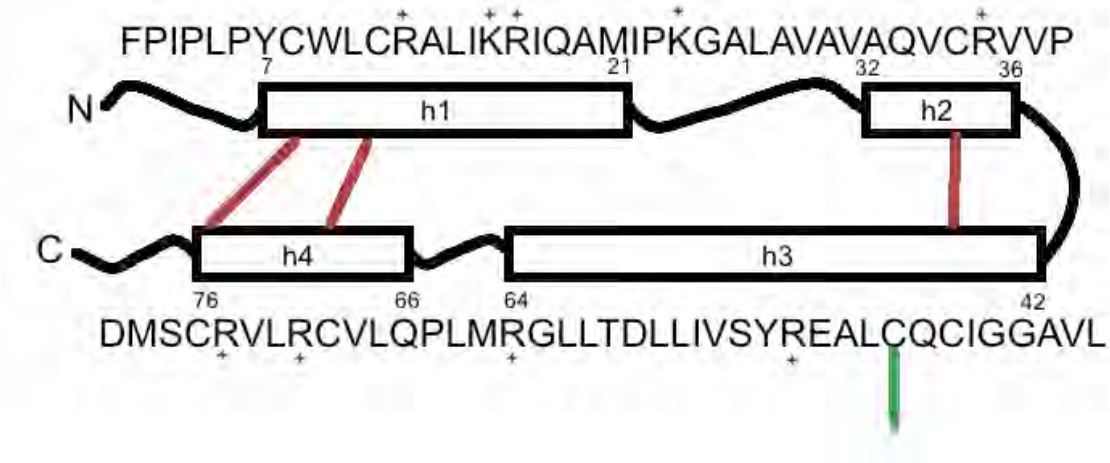

Figure 1.8. The amino acid sequence of human SP-B.

The secondary structure of the protein obtained from homology modelling is also shown. SP-B contains four α-helices (h1–h4) connected by unstructured loops (solid black lines) and linked by disulfide bridges (red lines) forming a hairpin shape. The intermolecular disulphide bond that would form the dimer is shown in green. The positively charged residues are also indicated.

1.3.4.2 Functions of Surfactant Protein B

Genetic manipulation studies of SP-B have shown that the protein is vital for the function of the lungs. Homozygous knockout mice did not survive after delivery unless rescued with SP-B proprotein or continually managed with liquid fluorocarbon ventilation (liquid breathing).[56] Heterozygous mice showed decreased lung function and air trapping following airway collapse.[57] In both sets of mice, other surfactant proteins were present in normal amounts. However, very little is known about the functions of SP-B considering its great importance to breathing.

SP-B has several proposed functions primarily related to surface tension reduction and metabolism of lung surfactant.[58] Experiments have indicated that addition of small amounts of SP-B greatly increase the surface tension reducing properties of surfactant lipids.[46]

An evident function of SP-B is to enhance the rate of adsorption of

phospholipids from an aqueous subphase to the air-water interface.[46] *In vitro* studies suggest that SP-B participates in organisation and turnover of phospholipids. Addition of SP-B to liposomes results in their lysis and fusion and formation of films of phospholipids at the air-water interface.[59] This suggests that SP-B acts to maintain a surface layer of surfactant at the air-water interface.

As a positively charged protein at physiological pH (7+ on human SP-B), the protein is proposed to interact with anionic phospholipids such as PG in order to promote the formation of monolayers of the lipids at the air-water interface. When monolayers of PG at the air-water interface are compressed (mimicking exhalation), lipid molecules will squeeze out of the film. If no SP-B is present in the monolayer, the PG lipids will not re-enter the monolayer upon expansion and they remain permanently suspended in the aqueous subphase. Addition of a small amount of SP-B eliminates this irreversible squeeze-out of anionic phospholipids. Fluorescence microscopy and atomic force microscopy experiments have shown that SP-B alters the monolayer phase behavior and morphology of the surfactant lipids, eliminating the need for squeeze-out of phospholipids.[60]

Further evidence from neutron and X-ray reflectivity suggests that during compression of the surfactant, SP-B undergoes changes in its tertiary structure at the air-water interface under the influence of surface tension. X-ray scattering length density profiles suggest that SP-B unfolds at high surface tension at the air-water interface, with its α-helices lying in the plane of the interface. As the molecules are squeezed together, the protein folds to form a globular shaped protein. As the monolayer is compressed further, the protein monolayer collapses but remains associated with the interface so that when the monolayer expands it can re-enter the interface to reform the monolayer. This observation is thought to be vital for its function as the conformational flexibility of the protein can provide a mechanism by which cycling of phospholipids could occur.[61]

1.3.4.3 Surfactant Protein C (SP-C)

SP-C is one of the most hydrophobic proteins known and consequently lacks homologous proteins. It is a 4.2 kDa protein, as shown in Figure 1.9, and incorporates two palmitoyl chains covalently bound to adjacent cysteines, significantly contributing to its extreme hydrophobicity. The protein is synthesised in the cell as a 21 kDa proprotein that undergoes post-translational processing to liberate the biophysically active 35-amino acid protein.

FGIPC(-Pal)C(-Pal)PVHLKRLLIVVVVVVLIVVIVGALLMGL

Figure 1.9. The amino acid sequence of human dipalmitic SP-C.
Where (-Pal) is a Palmitoyl chain.

A three-dimensional structure of SP-C has been determined in chloroform/methanol/0.1M HCl (32:64:5 by volume) by 2-D ^{1}H-NMR.[62] This showed a regular α-helix over the poly-valine section of the protein chain in positions 9-34. The N-terminal 8 residues, including the two palmitoyl chains, and the C-terminal residue are flexibly disordered in solution. This is shown in Figure 1.10.

Figure 1.10. The structural features of SP-C as determined by NMR.

The hydrophobic α-helix between positions 9 and 34 is 3.7 nm and is shown in ribbon. The palmitoyl residues (not shown) form thioester bonds with the two adjacent cysteines. Sulphur atoms are shown in yellow, nitrogen in red and oxygen in blue. [62]

The FTIR and CD spectroscopies of SP-C with and without the palmitoyl chains have shown that the presence of the palmitoyl chains has a large impact on the conformation of the protein and therefore its function. This is discussed further in Chapter 5.[63]

1.3.4.4 Functions of Surfactant Protein C

Unlike for SP-B, in homologous SP-C knockout mice, there were few adverse effects on health, reproduction or lung function. However, there were abnormalities in lung mechanics and instability of SP-C deficient surfactant during expiration, which could lead to inflammation of lung tissue (pneumonitis).[64,65]

Similarly to SP-B, addition of SP-C to a monolayer of phospholipids at the air-water interface significantly accelerates film formation by enhancing adsorption and spreading of the lipids. It is thought to be play an important role in maintaining a functional interfacial monolayer by recruiting phospholipids into the expanding film, promoting respreading of a compressed film, and modulating film

composition during dynamic compression and expansion.[66] Although SP-C is not as important for lung function as SP-B, there is extensive overlap in their abilities to promote and maintain a functional surfactant monolayer.

The structural basis for the mechanism whereby SP-C modulates formation and function of the surface film is unclear. Synthetic protein studies for SP-C indicate that the membrane-spanning domain is critical for biophysical activity and that the helical structure rather than the actual amino acid sequence seems to be more important for activity. A section of the research in this thesis investigates the orientation and helical properties of the SP-C protein lying in a phospholipid monolayer using molecular dynamics simulations. This is a useful technique to study this protein as it is difficult to study experimentally due to its high hydrophobicity and difficulty to isolate. [67-70]

1.4 Diseases of the Lung Surfactant

Lung surfactant in not produced until the later stages (approximately 20 weeks) of gestation. Very premature infants are commonly born with an insufficient amount of surfactant, causing infant respiratory distress syndrome (IRDS). The incidence of this disorder decreases with gestational age, from about 50% in babies born at 26-28 weeks, to about 25% at 30-31 weeks.[71]

IRDS causes difficulty breathing and as the disease progresses the baby may develop ventilatory failure and prolonged periods of apnea. IRDS can often be treated with an exogenous preparation of surfactant, either synthetic or extracted from animal lungs, given through the breathing tube into the lungs. Even though the number of IRDS cases in the United States is growing, the infant mortality rate from IRDS has dramatically declined from about 25,000 deaths per year in the 1960s to 860 deaths in 2010 because of surfactant replacement therapy.[72]

Lung alveolar proteinosis (PAP) is a rare lung disease characterised by excessive accumulation of surfactant materials within alveolar spaces. The cause of the disease is relatively unknown. It causes lung problems such as shortness of breath, coughing and fever. It can be treated by physically removing the accumulated alveolar material using sterile fluid to lavage the excess material. [73]

Surfactant Protein B (SP-B) deficiency is an uncommon, autosomal recessive lung disorder in term infants. The inability to produce SP-B leads to progressive, lethal, respiratory failure in the first year of life. It is caused by a mutation on the SFTPB gene leading to partial or complete loss of mature SP-B, resulting in abnormal composition of surfactant and decreased surfactant function. In addition, lamellar body formation is impaired. The lack of normal lamellar bodies leads to abnormal processing of SP-C, resulting in a reduction of mature SP-C and a buildup of unprocessed forms of SP-C. The loss of functional surfactant raises surface tension in the alveoli, causing difficulty breathing and collapse of the lungs. The combination of SP-B and SP-C dysfunction may explain why the signs and symptoms of SP-B deficiency are so severe. The only current treatment options available include lung transplantation or constant manual breathing.[74]

Genetic deficiency in SP-C can cause severe breathing problems in newborns or gradual onset of milder breathing problems in children or adults. Mutations in the SFTPC gene results in a reduction or absence of mature SP-C and a buildup of abnormal forms of SP-C. It is unclear which of these outcomes causes the signs and symptoms of SP-C dysfunction. Lack of mature SP-C can lead to abnormal composition of surfactant and decreased surfactant function. Research suggests that abnormally processed SP-C proteins form the wrong three-dimensional structure and accumulate inside lung cells. These misfolded proteins may trigger a cellular response that results in cell damage and death. This damage may disrupt surfactant production and release, leading to the breathing problems associated with surfactant dysfunction.[75]

1.5 Air Pollution and Lung Surfactant

The lung is the only inner-organ that is in direct contact with the outer atmosphere, and consequently the first point of contact between the air and the inside of the body is with the lung surfactant. Any air pollutants in the atmosphere will therefore also enter the lungs and interact with the lung surfactant. It is well established that air pollutants can contribute to respiratory problems and amplify other diseases such as cardiovascular problems. This section describes the types of

air pollution that can affect the lung surfactant, focussing principally on the oxidising pollutant ozone, and the proposed damage that it can cause.

1.5.1 Air Pollutants

Air pollution is defined as contamination of the atmosphere by gaseous, liquid and/or particulate waste (or its by-product) that can cause harm or discomfort to humans or other living organisms, and/or cause damage to the environment.[78] The main contaminants are:

- Sulphur Dioxide: emitted during the combustion of sulphur-containing fossil fuels, such as crude oil and coal
- Nitrogen oxides (NO_x): emitted in traffic and combustion of installations such as power plants and industries. They are also released from farmland and agriculture
- Ammonia: formed during agricultural activities
- Volatile organic compounds (VOC): usually derived from petrol and gasoline reservoirs, industrial processes and fuel combustion
- Methane: mainly from agriculture and natural gas extraction
- Carbon Monoxide: produced during incomplete combustion of fuels and cigarette smoke
- Particles: complexes of organic compounds and minerals. They derive from human activities such as industrial combustion or traffic
- Ozone: created through photochemical reaction of oxygen and is described in more detail in the next section. [79-82]

1.5.2 Ozone Air Pollution

Ozone air pollution is created in the lower atmosphere under the influence of UV light and is aided by VOCs and NO_x (Figure 1.11). The mechanism of this reaction is shown in Figure 1.12. Since the formation of this pollutant requires the presence of nitrogen oxides and VOCs as well as sunlight, ozone is often produced

in excess in urban areas with large amounts of traffic combustions or industrial processes when the weather is sunny.[79-82]

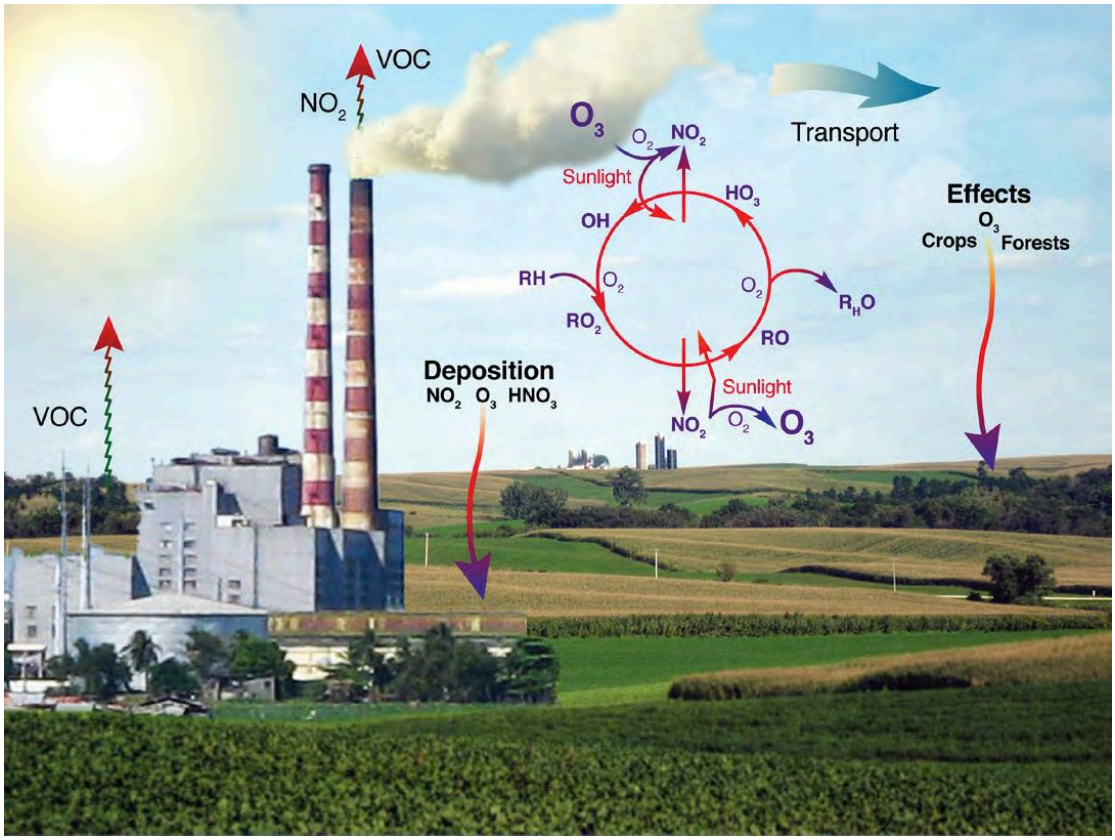

Figure 1.11. The process of ozone formation in the atmosphere.

Ozone is produced in a reaction between volatile organic carbons, nitrogen dioxide and oxygen in the presence of sunlight. Taken from www.nasa.gov. [81,87]

$$OH + C_3H_8 \rightarrow H_2O + C_3H_7$$

$$C_3H_7 + O_2 \rightarrow C_3H_7O_2$$

$$C_3H_7O_2 + NO + O_2 \rightarrow C_2H_5CHO + NO_2 + HO_2$$

$$HO_2 + NO \rightarrow OH + NO_2$$

$$NO_2 + h\nu\ (\lambda \leq 400\ nm) \rightarrow NO + O$$

$$O + O_2 + N_2 \rightarrow O_3 + N_2^*$$

Figure 1.12. The mechanism of formation of O_3 from propane.

A similar reaction scheme applies for the formation from other VOCs. Note that energy of only $\lambda \leq 400$ nm is required for photolysis of nitrogen dioxide, whereas $\lambda \leq 320$ nm is required for photolysis of molecular oxygen.[83]

In comparison to many other countries, ozone pollution levels in the UK are low. The National Air Quality Objectives of ozone exposure for the UK are a maximum of 0.1 ppm over an 8 hour period. Levels can, however, be problematic in or near to major cities, particularly near busy roads, as petrol and diesel from motor vehicles can emit a variety of pollutants such as nitrogen oxides and volatile organic carbons. Quite often in the immediate vicinity of very large emissions of NO (e.g. power plants), ozone concentrations are supressed through reaction with NO (to produce NO_2 and O_2). Therefore, sub-urban areas near to cities with large NO_x emissions often have elevated ozone levels as the production of O_3 exceeds the supression *via* reaction with NO.[81]

Cities normally considered to have the worst levels of pollution are Beijing (China), Bangkok (Thailand) and Mexico City (Mexico). However, it has been shown that some small smaller cities in Iran (e.g. Ahwaz, Sanadaj and Kermanshah), Mongolia (e.g. Ulan Bator), India (e.g. Ludhiana and Kanpor), Pakistan (e.g. Quetta) and Botswana (e.g. Gaberone) have levels much higher than recommended by the World Health Organisation (WHO). It has been proposed that this could be because many of these cities are relatively poor, therefore residents often resort to cheaper and less "green" fuels for heat and energy, such as firewood, and old, diesel powered cars are common, which can produce high levels

of VOCs.[85,86]

Data from the NASA Aura spacecraft have shown that global ozone levels are seasonally dependent and that the pollution can travel significant distances forming "streams" that cover much greater regions than just urban cities. This is shown in Figure 1.13 and high levels of ozone are indicated by darker shades of orange. Levels are higher in the summer months for each hemisphere and the ozone is transported by weather patterns forming pollution rivers.[87]

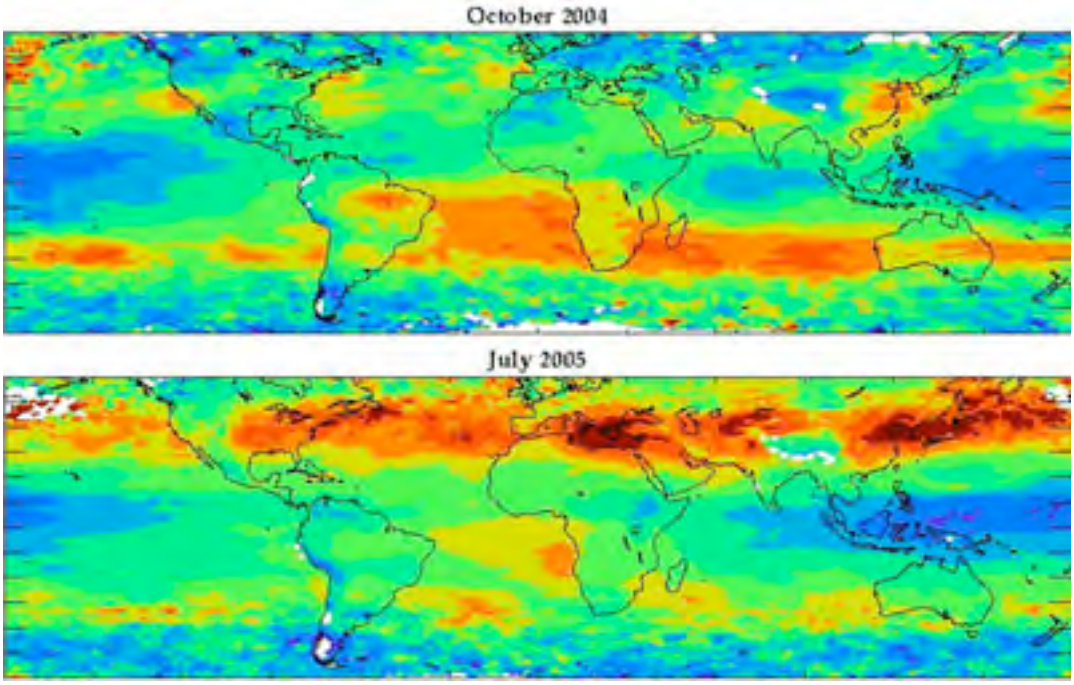

Figure 1.13. A global map of ozone pollution from October 2004 (top) and July 2005 (bottom).

Darker orange colours indicate greater levels of ozone pollution. The map is taken from www.nasa.gov.[87]

1.6 Ozone Pollution and Lung Health

Pollutants can be inhaled with air and may cause long-term or short-term lung health problems. Long-term problems arise from breathing polluted air over several years. Evidence has shown that this can reduce the rate at which children's lungs grow and can prompt worsening of asthma or chronic obstructive lung

disease (COPD, the collective term for bronchitis and emphysema).[81, 88]

Short-term problems from exposure to high levels of air pollution include lung irritation, coughing and shortness of breath. This is particularly prevalent in people with diseases such as asthma or COPD.[89-92] Anderson *et al.* investigated the link between air pollution levels and daily hospital admissions for COPD in 6 European cities. It was found that increases in ozone and particulates were closely linked to increased hospital admissions.[93] Nitrogen oxides, particulates and ozone are particularly harmful to the lungs in relatively low concentrations. In high doses, ozone is irritating to the airways of even healthy people. For those with asthma and COPD, ozone can cause coughing, difficulty breathing and chest tightness.

Evidence strongly implies that higher daily ozone concentrations are associated with increased asthma attacks, hospital admissions and even death. A recent study of the U.S. population by Bell *et al.* investigated the link between daily mortality count and ground ozone concentration for 95 large communities between 1987-2000. It was found that there was an overall (average) 0.5% excess risk in non-accidental daily mortality for each 0.02 ppm increase in 24-hour ozone concentration.[93,94] A study by Jerrett *et al.* in 2009 showed that increased levels of ozone were significantly associated with an increased risk of death from cardiovascular causes. In this study, there was a strong positive association of ozone with respiratory mortality for a 10 ppb increment in ozone.[95]

An important issue in ozone exposure is whether repeated episodes of damage, inflammation and repair caused by years of recurrent short-term ozone exposures results in adverse health effects in addition to short-term lung function changes. Bronchoalveolar lavage and mucosal biopsies have indicated that repeated short-term exposures show the presence of markers of cell injury that is cumulative over time.[92,96] Additionally, animal studies have shown that long-term exposure to ozone results in small structural changes to the airways, including an increase in fibrous tissue, which can be an early indication of chronic respiratory disease.[97]

1.7 Air Pollution Damage to the Lung Surfactant

Interactions between toxic aerosols or gases and the lung surfactant are thought to influence the structure and function of the surfactant system, inducing the lung health problems described above. Pollutants expected to significantly interact with the lung surfactant are ozone, nitrogen dioxide and ultrafine particles.[98-101]

The damaging effects of the pollutant depend on its solubility, size, chemical reactivity and concentration/duration of exposure. For instance, ozone is very reactive but relatively insoluble in water so will readily interact with molecules in the surfactant and will not enter the alveolar cells. However, nitrogen dioxide is less reactive so may penetrate the alveoli.[102-107]

1.7.1 Interactions between Ozone and Lung Surfactant

Ozone is an extremely reactive oxygen species (ROS) and is of high interest as a pollutant due to its known capability to cause irritation in the lungs. Additionally, since ozone has only limited solubility in water, the upper respiratory tract is less effective at removing ozone from inhaled air than for more soluble pollutants such as SO_2. As a result, the majority of ozone reaches the respiratory tract and therefore interacts with the lung surfactant.

Ozone is highly oxidising and reacts readily with carbon-carbon double bonds or triple bonds as shown in Figure 1.14. The mechanism of this reaction was proposed in 1953 by Rudolf Criegee.[108] Ozone adds to the alkene group to form the cyclic molozonide. In solution this initial addition product rapidly isomerises to the trioxolane shown in Figure 1.14. The carbon-carbon bond is completely cleaved during the reaction. The trioxolane can collapse *via* an oxidative or reductive hydrolysis process, depending on the chemical environment, to form a variety of potential oxidised products such as ketones, aldehydes or acids. There is dispute over whether the molozonide collapses *via* a concerted or radical process, although this is thought to be dependent on the environment. It has also been proposed that in the gas-phase ozonolysis reaction the hydroxyl radical can form following

collapse of the molozonide, which is discussed further in Chapter 4.[109]

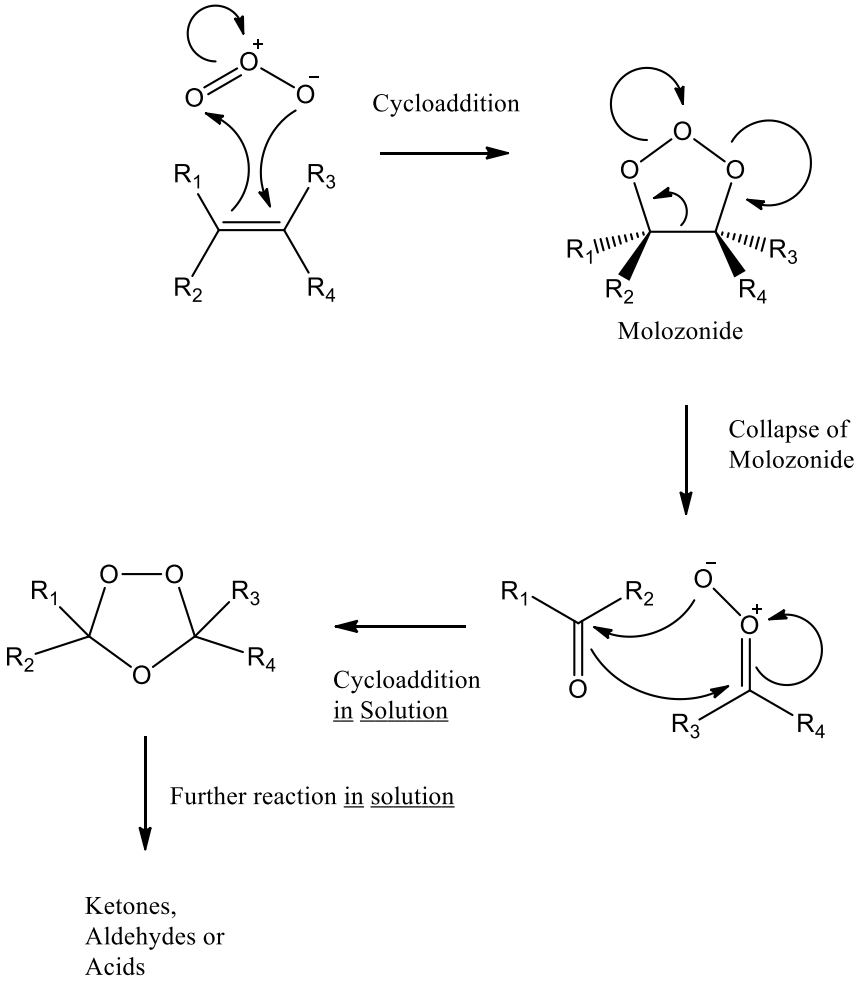

Figure 1.14. The mechanism of ozonolysis.

After the initial collapse of the molozonide, the oxidised species will react further in solution as shown. The secondary ozonide will not form in the gas phase.

Many components of the lung surfactant could potentially react with ozone such as unsaturated phospholipids, other lipids with a carbon-carbon double bond, such as cholesterol, and amino acid residues within the surfactant proteins. However, the extent or mechanisms of these reactions at the air-water interface are not understood.

1.7.2 Research Investigating Ozone Damage to Lung Surfactant

Relatively little research has attempted to determine the damage caused by ozone to lung surfactant. Balis *et al.* attempted to identify the changes to surfactant secretion in response to ozone. Adult rats were exposed to high levels (3 ppm) of ozone for 1-8 hours and lung fluid was collected. It was found that there was a significant (22%) decrease in tubular myelin but an increase in lamellar bodies. Electron micrographs of lavage fluid surfactant from control and ozone exposed rats indicated that ozone stress inhibits unfolding of secreted lamellar bodies to prevent formation of tubular myelin, thus reducing the proportion of lung surfactant available for adsorption to the surface monolayer.[110]

Putman *et al.* exposed rats to ozone at 0.8 ppm for 2 and 12 hours.[111] The surfactant was isolated and it was found that SP-A was significantly degraded after 12 hours of exposure and there was also an inflammatory response in the lungs. This was not observed in lungs that were exposed to ozone for 2 hours. This damage to SP-A has been studied several times *in vivo*. It has been suggested that the change in structure and function of SP-A after ozone exposure reduces its ability to enhance formation of the monolayer. Since SP-A does not exist on the surfactant monolayer, it is thought that SP-A is damaged by the products formed in ozonolysis rather than ozone itself, which is relatively insoluble in water.[111]

It was later shown by Putman *et al.* that surfactant extracted from rat lungs exposed to ozone, containing phospholipids, SP-B and SP-C, had a significantly lower surface adsorption rate than the control lung surfactant. It was suggested that the activity of one or both surfactant proteins was affected by ozone.[112, 113]

Several studies have investigated the specific changes to the surfactant lipids *in vitro*, demonstrating significant damage to the components. These studies are described in more detail in Chapter 4.

1.7.3 Ozonolysis of Amino Acid Residues within Proteins

Ozone can react with the alkene or aromatic group within the amino acids tryptophan, tyrosine, histidine and phenylalanine. It can also oxidise the sulphide of cysteine and methionine. Full length human SP-B contains 1 tryptophan, 2 tyrosines, 1 phenylalanine, 3 methionines and 8 cystines. Human SP-C contains 1 histidine, 1 phenylalanine, 1 methionine and 2 cysteines (each bonded to a palmitic acid chain). The susceptibility of the amino acids to reaction with ozone have been determined to be cysteine > methionine > tryptophan > tyrosine > histidine > cystine > phenylalanine. Other amino acids are unaffected by ozone.[114]

Enami *et al.* have investigated the ozonolysis of cysteine on the surface of aqueous cysteine microdroplets. The intermediates and products formed in the reaction at the interface were determined by thermospray MS. It was established that cysteine sulphenate ($CySO^-$), cysteine sulphinate ($CySO_2^-$) and cysteine sulphonate ($CySO_3^-$) species formed on the surface of the droplets. The sulphur can be oxidised at the interface to form a variety of oxidation states. Notably, negatively charged residues are formed, which could change the steric requirements and therefore the structural integrity of proteins.[115] It has also been shown that ozonolysis of cystine leads to the production of the same oxidation products as for cysteine but after slightly longer reaction times.[116]

The breaking and ozonolysis of carbon-carbon double bonds in residues that contain an alkene group, or ozonolysis of cysteines, would produce more acidic structures, therefore potentially altering the structural integrity of proteins. A number of research groups have explored the damage caused to the lung surfactant protein B by ozone by various techniques. These are discussed in detail in Chapter 3.

1.7.4 The Consequences of Lung Surfactant Oxidation by Ozone

Oxidised products of lung surfactant, such as oxidised phospholipids, have been thought to cause cellular damage to the alveolar cells. The ozonides and hydroperoxides formed during oxidation are more soluble in aqueous media

therefore they could dissolve in the fluid lining of the lungs and diffuse readily across lipid membranes. It is thought that the ultimate cell damage caused by ozone exposure is mediated by free radicals and other oxidant species formed from the initial reaction between lung surfactant and ozone. These species react with lipid membranes in the epithelial cells, which can then lead to the formation of more oxidised lipids, such as peroxidised lipids, aldehydes, ketones and acids. These oxidised species are highly reactive and can cause DNA damage, disruption to signal transduction pathways, interference to expression of genes and cell signaling, activation of tumour-supressor protein p53, aging and apoptosis.[117,118]

1.8 Oxidation of Lipid Bilayers by Reactive Oxygen Species (ROS)

The lung surfactant is not the only part of the body that is at risk of damage by oxidative species. Reactive oxygen species are formed constantly in the body as a result of normal metabolic processes, or as a result of exposure to exogenous sources, such as ozone pollution (as described above), radiation or drugs. An excess of these ROS could cause damage to components of the cell, such as membrane lipids and proteins. The following sections describe lipid membrane arrangement in cells and how these membranes could be affected by oxidative damage by ROS.

1.8.1 Lipid Bilayers and Lipid Rafts

The lipid bilayer is a universal component of all cells in the form of the cell membrane. Membranes are vital to distinguish intra and extracellular components. The bilayer acts as a barrier to keep ions, proteins, water and other molecules where they are required, therefore they are vital for cell function.[119]

The main components of natural bilayers are phospholipids such as phosphatidylcholines, phosphatidylethanolamines, phosphatidylserines, phosphatidylinositols and phosphatidic acid. PCs account for >50 % of the phospholipids in most eukaryotic membranes, and most of these are unsaturated. PEs have small headgroups, therefore inclusion of PE in PC bilayers imposes

curvature stress onto the membrane, which is utilised in budding, fission and fusion. Sphingolipids are also present in lipid membranes, mainly sphingomyelin and the glycosphingolipids. Sphingolipids have saturated tails so are able to pack more tightly and with a larger thickness than unsaturated PCs of the same chain length, adopting the solid (gel) phase. This phase can be fluidised by sterols, predominantly cholesterol in mammals.

These molecules are amphiphilic and when exposed to an aqueous environment they will arrange themselves into a two-layered sheet,[119] driven by the hydrophobic effect as shown in Figure 1.15. Phospholipids can also arrange in water to form micelles or vesicles (Figure 1.15), and the latter can be used to study the behaviour of bilayers in the laboratory. Micelles form when the concentration of the lipid is greater than the lipid's critical micelle concentration (CMC) and the temperature of the system is greater than the critical micelle temperature. The formation of micelles is dependent on the molecular architecture of the lipid, for example single tailed lipids have a higher propensity to form micelles than double tailed lipids, which would more likely form vesicles.[120]

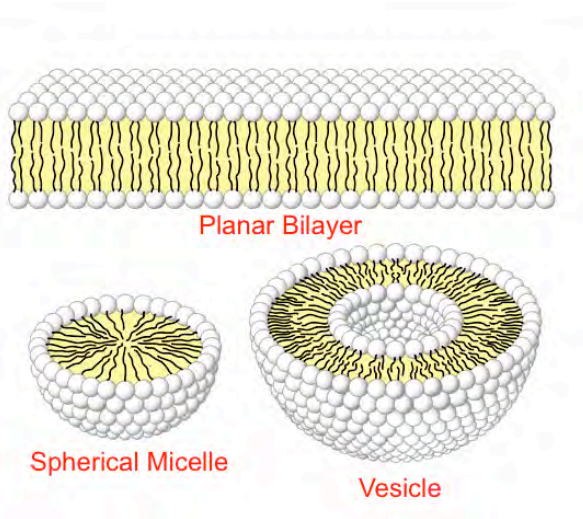

Figure 1.15. The structure of planar bilayers, vesicles and micelles.

Phospholipid molecules have a hydrophilic head and hydrophobic tails. When exposed to water these molecules arrange themselves into a two-layered sheet with all of their tails pointing toward the centre of the sheet. The self-assembly of such sheets is driven by the hydrophobic effect. Depending upon the geometry and characteristics of the amphiphilic molecules, micelles and vesicles can form during self-association.

At a given temperature a lipid bilayer can exist in either a liquid or a gel (solid) phase. All lipids have a characteristic temperature at which they transition (soften) from the gel to liquid phase. In the gel phase the lipids have a high degree of order and have a more rigid structure, whereas in the liquid phase the lipids have more free space to move, usually due to some disruption in packing (such as unsaturation). Cell membranes are generally considered to be in a fluid phase since most biological phospholipids have a low acyl melting temperature (T_m). Some membranes are, however, rich in sphingolipids with elevated T_m, and sterols, which can significantly affect the phospholipid bilayer phase. These lipid mixtures can lead to complex phase behaviour in membranes.[120]

It has more recently been shown that membranes can be partially in a liquid –ordered (L_o) phase, characterised by a high degree of acyl chain order of saturated phospholipids when mixed with cholesterol, and partially in a liquid-disordered (L_d) phase, characterised by low lipid tail order and fewer cholesterol molecules. This leads to formation of lipid rafts (Figure 1.16), which are discrete,

highly dynamic microdomain structures. In general, these rafts contain 3-5 times more cholesterol than the surrounding bilayer, while the saturated lipid in this region is elevated by approximately 50%.[121,122]

As well as enrichment in certain lipids, lipid rafts are enriched in particular classes of proteins, such as glycosylphosphatidylinositol (GPI)-anchored and acylated proteins. This led to the "raft hypothesis" described by Simons and Ikonen,[121] which describes that membrane rafts have functional significance in a number of key biological processes including cell signalling and membrane trafficking.[123]

Experimentally lipids rafts can be formed by reducing the temperature of a multicomponent lipid bilayer or monolayer sample as it causes some of the lipids to phase separate to form an ordered phase (composed of dispersed L_o saturated lipids and cholesterol) in a fluid-like phase (comprised of L_d unsaturated lipids) rather than the fluid phase present at higher temperature.

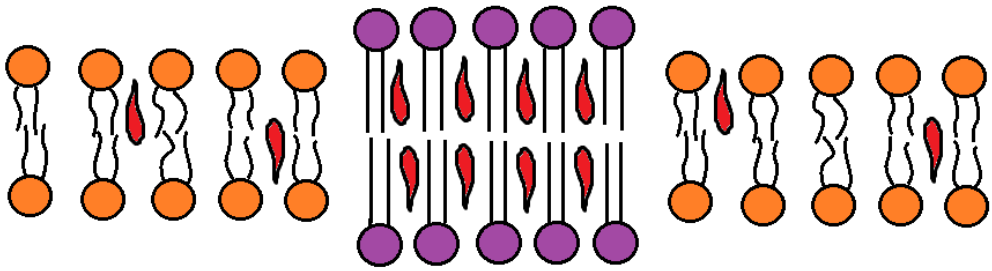

Figure 1.16. Schematic representation of a cell membrane showing a lipid raft.

The lipid raft is rich in saturated phospholipid (purple head group) and cholesterol (small red molecule) in a liquid ordered (L_o) phase, floating in a "sea" of predominantly unsaturated phospholipid (orange head group) in a liquid disordered (L_d) phase.

1.8.2 Oxidation of Lipid Bilayers

Reactive oxygen species (ROS) have been shown to react with lipid bilayers, changing their structure and physical-chemical properties. Examples of such species include peroxide ions, hypochlorite ions, hydroxyl radicals and superoxide anions.[124] It has been estimated that one human cell is exposed to approximately 1.5×10^5 oxidative hits a day from hydroxyl radicals and other reactive species.[124]

ROS can be produced from both endogenous and exogenous sources. Mitochondria have been known to generate significant amounts of hydrogen peroxide from a superoxide radical precursor involved in electron transfer reactions. Other endogenous sources of ROS include xanthine oxidase, which catalyses hydroxylation of purines, neutrophils, macrophages and cytochrome P450.[117] Exogenous processes that produce ROS include environmental agents as well as xenobiotics such as chlorinated compounds, metal ions, radiation (UV, X-rays, gamma rays) and barbiturates.[125-127]

ROS are implicated in causing cell damage, as well as interfering with the expression of genes and cell signalling. High concentrations of ROS can cause apoptosis. Alternatively, ROS can cause a positive response at low concentrations by stimulating cell proliferation. Signalling molecules formed during lipid peroxidation can lead to the upregulation of signalling cascades such as growth factor kinase-dependent signalling pathways resulting in the activation of redox-regulated transcription factors.[117] Abnormalities in signalling cascades, such as growth factor receptors are associated with the development of many cancers.[128] Additionally, the tumour-supressor protein p53 is inactivated by radicals produced in lipid peroxidation. Disruption of this protein causes uncontrollable cell-division and is associated with more than half of all human cancers.[129]

According to the free-radical theory of aging, organisms age because cells accumulate free-radical damage over time. This is because there is a strong correlation between chronological age and levels of ROS and oxidative damage. Aging is also associated with an increase in the levels of oxidatively damaged lipids.[130]

Membrane reorganisations can occur following oxidation of lipids. These

changes can include the alteration of the packing of membrane components, fluidity of the bilayer, molecular redistributions or increased permeability. This can change the structure and function of some membrane proteins, which will in turn characterise pathological conditions, as described above.[117] In particular, membrane lipid rafts could be greatly affected by oxidation of lipids by reactive oxygen species due to changes in the lateral segregation into L_o and L_d phase domains, or it could alter the size of existing domains.

Considering the fact that many studies have examined the pathological conditions resulting from oxidation reactions occurring at lipid membranes, the understanding of the early sequences that lead to membrane remodelling is still very poorly understood. Specifically, little is known about the influence of the oxidation products on the structure of the membrane after oxidation, and how lipid raft formation is affected.

1.8.3 Examples of Reactive Oxygen Species

Phospholipids within the body could potentially be exposed to numerous ROS. The research presented in this thesis focuses on several of these endogenous and exogenous ROS, which are described in more detail below.

1.8.3.1 Singlet oxygen

Molecular oxygen in the ground state is in a triplet state as the LCAO (linear combination of atomic orbitals) model maintains that the unpaired electrons occupy different molecular orbitals. In the singlet oxygen excited state, these two electrons occupy the same molecular orbital (and are therefore no longer unpaired). This excited state has a lifetime of 45 minutes in low pressure gas, and in water the lifetime is approximately 2.5 μs. [131]

Singlet oxygen can be produced in several types of reactions, a number of these being biochemical processes, including enzyme catalysed oxidations of halide ions, unsaturated fatty acids and hydroperoxides. Additionally, singlet

oxygen can be produced in photosynthetic organisms when more light is absorbed than used by photosynthesis.[132,133] It can also be generated in the lower atmosphere as an air pollutant by the action of sunlight on polycyclic aromatic hydrocarbons.

Singlet oxygen reacts with many organic compounds, including alkenes, aromatics, proteins, vitamins and inorganics such as phosphates. Importantly, singlet oxygen can react with phospholipids and proteins in cell membranes causing significant membrane damage.[133] The membrane damage could occur from direct reactions between the phospholipids and singlet oxygen, while chain reactions could also occur from other ROS intermediates formed. Reaction with singlet oxygen leads to the addition of oxygen to the molecule.

1.8.3.2 Hypochlorite

Hypochlorite is produced in the body when the enzyme myeloperoxidase is secreted into the cell in response to the activation of phagocytes. Hypochlorite ($HOCl/ClO^-$) is a strong oxidant that can react with a variety of molecules, in particular chlorohydrins are formed when HOCl is added to a double bond in a lipid. Chlorohydrins can form epoxides in some conditions, but it has been observed that this does not occur during reaction with phospholipids in aqueous media.[134,135]

1.8.3.3 Hydroxide radicals

The hydroxide radical, ·OH, can be produced *in vivo* during the action of some enzymes such as peroxidases, and macrophages often produce the radical when exposed to pathogens. The hydroxide radical is a strong electrophilic species and can react rapidly, meaning it has a very short lifetime *in vivo*. It can readily abstract hydrogens from phospholipids, initiating a chain reaction where the radical formed can readily be oxidised.

1.8.3.4 Ozone

The production and reactions of the pollutant ozone have been discussed earlier in this chapter.

1.9 Conclusion

The lung surfactant is vital for lung function as it prevents collapse of the alveoli due to high surface tensions. Although the existence and composition of the lung surfactant is now understood, less is known about the mechanism of action of the lung surfactant, and the exact function of all of the components such as the surfactant proteins B and C. In particular, the presence of the palmitoyl chains attached to SP-C are thought to be important but it is not known how they aid the function of the lung surfactant.

Exposure to the air pollutant ozone is known to cause damaging health effects, and several *in vivo* and *in vitro* experiments have provided more evidence for damage to the lungs, however little is known about the mechanisms and kinetics of the reactions between ozone and the lung surfactant molecules. Also, little is known about the products that are formed at the interface and the resulting structure and function of the monolayer.

Experiments have attempted to elucidate these mechanisms, many of which are limiting in their capability to provide the full picture. In the case of *in vivo* studies, although the pathology of damage to the lung surfactant can be monitored, the need to extract the surfactant following exposure limits the mechanistic details. Furthermore, *in vitro* experiments are often limiting due to the lack of techniques available to analyse the lung surfactant at the air-water interface. Molecules at an interface have very different physical and chemical properties than in solution. Therefore, studies done in solution may have little relevance or transferability to interfacial reactions.

It is thought that the products formed in ozonolysis reactions at the air-lung interface could lead to the formation of further reactive oxygen species that could then react with lipids comprising the cell membrane of nearby cells. Other

processes in cells, such as metabolism, could also produce these ROS. Exposure of cells to an excess of ROS could lead to significant damage to lipids within cell membranes, therefore compromising the structural integrity of the cell, or a change in the organisation of lipid rafts could alter important processes such as membrane trafficking.

1.10 Research Objectives

The aims of this research are to identify the chemical and physical changes (damage) to the air-water interface of lung surfactant and its components that occur following exposure to the ubiquitous environmental pollutant ozone. Little is known about the structure, physical properties and chemical composition of the components of lung surfactant during and after exposure to ozone pollution at the air-water interface. This project intends to observe these changes under controlled laboratory conditions so that the chemical mechanisms leading to surfactant damage and the physical and chemical properties of the products can be determined.

The challenges faced in this research arise from the lack of techniques available to monitor ozone reactions at the air-water interface. The Thompson group has recently established a method using neutron reflectivity combined with surface tension measurements using a Langmuir Trough/ Wilhelmy plate to analyse the structure and physical properties of lung surfactant components at the air-water interface.[136] Information about these techniques is given in Chapter 2. This research will continue the previous work performed in the Thompson group by exploring the interfacial reaction between ozone and lung surfactant components in Chapters 3 and 4.

Furthermore, molecular dynamics simulations will explore the structural features of SP-C, the lung surfactant protein that is particularly difficult to study due to its difficulty to isolate or synthesise and its extreme hydrophobicity. This research will begin to understand the interaction between the protein and the phospholipids in the lung surfactant monolayer, in particular the structural effects of the presence of the palmitoyl chains bonded to its cysteine residues.

The research then extends to investigate various techniques that can be used to study the damage caused to lipid bilayers by reactive oxygen species, which, as described above, could be produced in secondary reactions resulting from the oxidation of lung surfactant by ozone as well as from other sources such as UV radiation. Since reactions between lipid bilayers and ROS occur at the bilayer-liquid interface, neutron scattering and reflectivity techniques would be employed to explore these reactions, the products formed and the structural changes to the bilayers.

Chapter 2 Background to Neutron and X-ray Reflectivity and Small-Angle Neutron Scattering Techniques

2.1. Introduction

The neutron is now well established as a unique probe for studying the nature of surfaces and interfaces and has significant advantages over other forms of radiation in the study of structure and dynamics. Neutrons have been a vital tool for the research presented in this thesis, in combination with other experimental procedures; therefore the background to the techniques used will be explained here.

2.2 The Neutron

A neutron is an uncharged subatomic particle with a mass of 1.67495×10^{-27} kg. Neutrons are stable when bound in an atomic nucleus, but have a mean lifetime of approximately 1000 s as a free particle before it undergoes beta decay to form a proton, electron and antineutrino. The mass and lifetime features are important for its use in experiment.[137,138]

2.2.1 History of the Neutron

Ernest Rutherford first described the neutron in 1920 by considering that the disparity found between the atomic number of an atom and its atomic mass could be explained by the existence of a neutrally charged particle within the nucleus.[137,138]

In 1932, Bothe and Becker noticed that a very penetrating non-ionising radiation was emitted when beryllium was bombarded with α-particles.[138] Additionally, in 1932, Iréne and Frédéric Joliot-Curie allowed this non-ionising

radiation to hit paraffin wax, and found it caused the emission of protons. The speed of these protons implied that this radiation would be extremely energetic.[138]

These results encouraged James Chadwick, who was working with Rutherford, to investigate further, believing that this "radiation" was in fact the presence of neutrons. He performed experiments to show that the new radiation was a neutral particle with a mass similar to that of the proton.[138]

Enrico Fermi was an iconic figure in neutron research. He developed "Neutron Transport Theory", showing that thermal neutrons (slow) were much more reactive than fast neutrons. This is because they have kinetic energies (MeV range) that are similar to vibrational frequencies of atoms and have much larger fission cross sections than fast neutrons. This is a significant property for structural research. From this, in 1942 Fermi discovered fission, showing that neutrons from fission of the uranium nucleus could support a controlled chain reaction.[139]

After many difficulties in neutron structural research, Clifford Shull and Bertram Brockhouse were awarded the Nobel Prize for their pioneering contributions to development of neutron scattering techniques in 1994. Shull was key in the development of neutron diffraction and from this he discovered the structure of ice and hydrides. He also measured the neutron cross-sections for atoms; an important tool for structural analysis.[140] Brockhouse played a major role in the development of inelastic scattering and development of spectroscopy equipment.[141]

2.2.2 Uses of Neutrons

Neutrons interact with the nucleus of an atom, *via* the strong intranuclear forces. Their scattering cross sections (the ability to "see" nuclei) are not directly related to atomic number, in fact isotopes of the same element can have very different cross-sections. Neutrons are advantageous in structural research compared to X-rays as small atoms are much more easily "seen" in the presence of heavier ones. Also, neighbouring elements in the periodic table have substantially different cross-sections and can therefore be distinguished.

The properties of the neutron have important consequences. The interaction of a neutron with the nucleus of an atom is weak, meaning they are highly penetrating. Therefore they can be used in the investigation of the interior of materials, rather than just surface layers. It also means that they are non-destructive, which is beneficial for samples, including the biological samples used in this study.[142,143]

2.3 Neutron Sources

The mass of the neutron has significant consequences. At a practical level it means that highly energetic neutrons produced by either fission or spallation of heavy nuclei can be slowed or moderated to a point at which they have the same energy as the atoms in the moderating medium. Energies of neutrons are then suitable to study a wide range of dynamic phenomena in solids and liquids as they can then be scattered or absorbed. [143]

2.3.1 Reactor Sources

Typically since the 1940s, neutron scattering experiments have been performed using a beam of neutrons from a reactor source. In thermal reactor sources, neutrons are formed by the fission of heavy (normally ^{235}U) nuclei. When the nucleus absorbs a slow neutron, the nucleus splits into two or more lighter fragment nuclei, releasing kinetic energy, gamma radiation and free neutrons. These neutrons may be absorbed later by other fissile nuclei, triggering further fission events and sustaining a nuclear chain reaction.[144]

The cross section for neutron-induced fission of ^{235}U is only high for slow neutrons with meV energies, whereas the neutrons produced by fission are fast with MeV energies. Therefore, the neutrons must be moderated in order to sustain the fission process. The moderator contains large numbers of low mass nuclei (usually hydrogen) because the energy transferred in the inelastic collisions (where kinetic energy is not conserved) is maximised when the mass of the colliding nucleus is as close as possible to the neutron mass.[144]

In order to use neutrons to study molecular properties, a neutron spectrometer is required. A neutron spectrometer uses a beam of neutrons that is obtained by viewing a moderator through a beam-tube or neutron guide, which passes through the shielding around the neutron source. High flux reactors, such as the Institut Laue-Langevin in Grenoble, France[145] produce a high flux of thermal neutrons distributed around 25 meV.

The neutron flux produced by a normal nuclear reactor is unchanging with time and covers a wide range of neutron wavelengths. In order to perform a neutron experiment it is necessary to monochromate the neutron beam so that it covers a narrow range of neutron wavelengths. Unfortunately, this means that the majority of the flux is lost at this stage.[144]

2.3.2 Accelerator/ Spallation Based Neutron Sources

Recently, neutron experiments are increasingly being performed using neutrons formed from a spallation source. In accelerator based neutron sources, a beam of charged particles is accelerated to a high energy (typically 500-800 MeV) and then fired at a target. Interactions between the particle beam and the target nuclei produce highly excited nuclear states that decay by emitting nuclear radiation, such as neutrons, γ particles, neutrinos etc. These neutrons are of very high energy and are then slowed down by a moderator.[144]

Early accelerator-based sources use an electron linear particle accelerator to accelerate an electron beam to relativistic energies (~50 MeV). The electron beam is fired at a dense target made of a heavy element, such as uranium, and neutrons are produced in two stages. Electrons are firstly slowed down extremely rapidly due to the strong interaction with the electromagnetic field of the target nuclei, producing a cascade of Bremsstrahlung photons. Following this, some of these photons go forth to produce neutrons by photo-neutron reactions where the photon excited a target nucleus, which subsequently decays with the emission of a neutron. Approximately 20 electrons must be accelerated for each neutron produced.[145]

More recent neutron sources combine a linear accelerator with a

synchrotron to accelerate protons to high energy (~800 MeV). The protons are fired at a heavy metal target, e.g. tantalum, uranium or tungsten, and neutrons are produced by spallation. The initial interaction between the proton and the target nucleus is very violent and mainly causes the emission of neutrons and light nuclear fragments. Typically, each proton produces approximately 15 neutrons for a non-fissile target, or 25 neutrons for a fissile target.[144]

Accelerator sources are normally pulsed, producing a pulsed neutron flux that is ideally suited to time-of-flight experiments. This technique involves measuring the time-of-flight t taken for a neutron to travel the total flight path L from the moderator to the detector, *via* the sample. In elastic scattering (where the energy of the final neutron is equal to the initial neutron):

$$t = \frac{m_n}{h} L\lambda \qquad (2.1)$$

Where m_n is the mass of the neutron, λ is the neutron wavelength and h is Planck's constant. From this, the neutron wavelength can be calculated. The use of this technique prevents the necessity of monochromating the beam; therefore there is no loss of flux. The world's most intense pulsed neutron source is the ISIS spallation source at the Rutherford Appleton Laboratory, UK.[146] Here, an ion source produces H^- ions using an electric discharge. A proton linear accelerator transports 70 MeV H^- ions into the outside of the main 800 MeV 163 m circumference synchrotron ring. As the ions enter the synchrotron, thin alumina foil strips away the electrons leaving a beam of protons. Once sufficient protons have been collected into the synchrotron, they are accelerated by radio-frequency electric fields in ten accelerating cavities. After almost 10,000 revolutions, the protons have separated out into two large bunches travelling at 84% of the speed of light. Each bunch is extracted from the synchrotron by fast kicker magnets that rise to 5000 amps in 100 nanoseconds. The proton bunches are then transported and collide with a tungsten target. The spallation neutrons that are produced are moderated to useful speeds using various hydrogenous moderators around the target and are then directed to the instruments. [147]

2.4 Interactions of Neutrons with Matter

Neutrons interact with the strong nuclear forces within a nucleus. The total scattering of a single nucleus is:

$$\sigma = 4\pi b^2 \qquad (2.2)$$

where σ is the neutron cross section of a system, i.e. its ability to "see" or scatter neutrons. The units of σ are in barns where 1 barn = 10^{-24} cm^2. b is the scattering length, which has units of length. The sign of b is arbitrary and a negative scattering length implies a change in the phase of the scattered wave. The scattering length is dependent on the nucleus, therefore isotopes of the same element can have very different scattering lengths. It is also dependent on the spin state of the nucleus.[142]

The value of b does not vary systematically along the period table. An example of how neutron scattering lengths vary across the periodic table is shown in Figure 2.1.

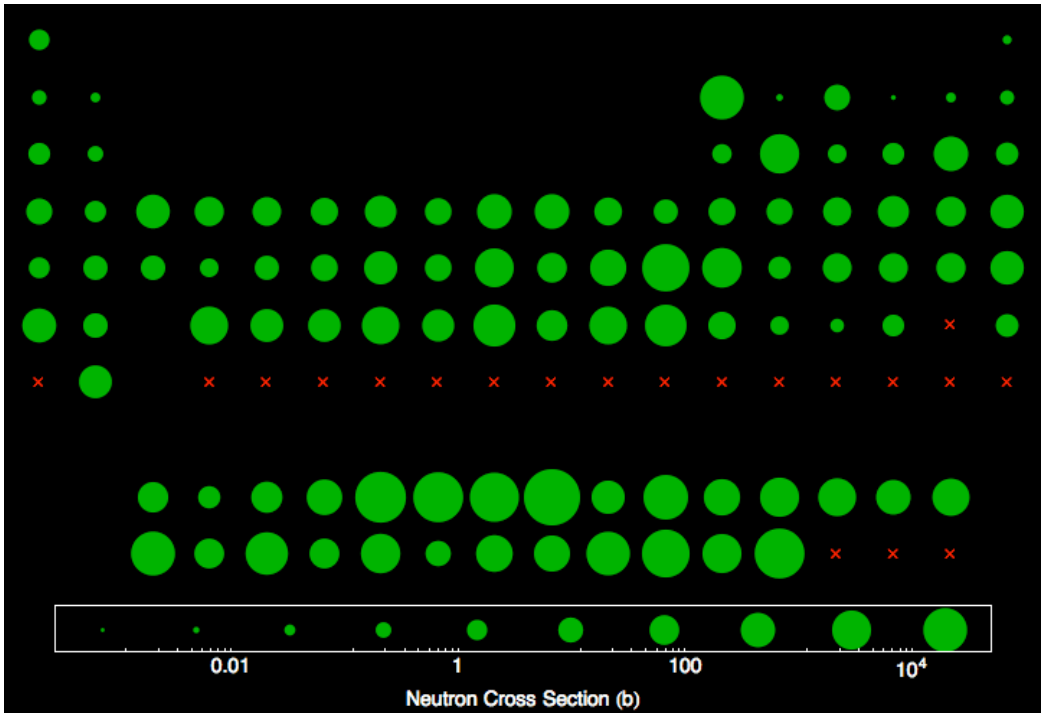

Figure 2.1. Neutron cross sections for elements in the periodic table.

The neutron scattering lengths are shown as an average over isotopes. [143]

This variation leads to advantages over X-ray scattering as X-rays interact with the electrons of an atom. Therefore, X-ray scattering lengths increase with atomic number. This means that light atoms such as hydrogen are difficult to detect with X-rays whereas with neutrons it is possible to "see" lighter elements in the presence of heavy ones. Also, it is beneficial to distinguish between ions with the same number of electrons, such as K^+ and Cl^-.[142]

The dependence on isotopes for neutron scattering length (for example Table 2.1) can be advantageous to introduce contrast into the structure of a molecule. For example, deuterium has a much higher scattering length than hydrogen, which has a negative scattering length. Substituting hydrogens with deuteriums would significantly increase the scattering of neutrons from a

molecule, without significantly changing its chemical properties.

Hydrogen Isotope	Scattering Length, *b* / fm
^{1}H	-3.741
^{2}D	6.674
^{3}T	4.792

Table 2.1. The coherent scattering length for the isotopes of hydrogen. [142]

2.4.1 Coherent and Incoherent Scattering

When considering more than one nuclei, the neutron waves will be scattered from each nucleus, causing interference of the scattered waves. In coherent scattering, all the atoms scatter in phase and produce constructive interference. The scattered neutrons therefore carry information on the correlations of one atom with respect to its neighbours. In incoherent scattering, the scattering is not in phase and there is no constructive interference. Thus, the scattered neutron only carries information about individual atoms. Coherent scattering lengths are useful for structural analysis, whereas incoherent scattering of a nucleus can lead to background noise. This gives rise to an equation for neutron cross-section:

$$\sigma_{tot} = \sigma_{coh} + \sigma_{inc} \qquad (2.3)$$

2.4.2 Scattering Length Densities

The scattering length density is the ratio of the scattering length per molecule and the molecular volume. Scattering lengths can be added together for each atom within a molecule to give the total scattering length of a molecule. Therefore, the scattering length density, ρ_{AmBm}, for an A_mB_n molecule is:

$$\rho_{AmBn} = \left(\frac{b}{v}\right)_{AmBn} = \frac{mb_A + nb_B}{v} \qquad (2.4)$$

where v is the volume of the molecule, b_A is the scattering length of A and b_B is the scattering length of B.

2.4.3. Contrast Variation

Deuterium has a positive scattering length whereas hydrogen has a negative scattering length. Therefore, by adjusting the amount of deuteration in a sample or solvent it is possible to adjust the scattering length density of the material so that the sample or solvent dominates or is removed from the total scattering. This is known as contrast variation. For example if water is used as a solvent, H_2O can be mixed with increasing amounts of D_2O to linearly increase its scattering length density. The scattering length densities of H_2O and D_2O are -0.55 x 10^{-6} Å^{-2} and 6.35 x 10^{-6} Å^{-2} respectively. By mixing 8% (by volume) of D_2O with 92% H_2O achieves a scattering length density of 0.0 Å^{-2}. This is known as null reflecting water. This is a useful feature because neutrons detected in scattering experiments using this system will only have been scattered from the sample of interest, not the solvent.

2.5 Neutron Reflectivity

A beam of neutrons can be reflected from a surface, similarly to the phenomenon of the specular reflection of light (Figure 2.2). Specular reflection is the mirror-like reflection of a wave from a surface, in which the angle of incident wave is equal to the angle of the reflected wave. A thin film on a surface reflects light and the reflected light may experience strong interference depending on the wavelength of the light, the thickness of the layer and the refractive indices of the media. Thus, the reflectivity pattern of the reflected light can give information about the thickness of the layer.[147,148]

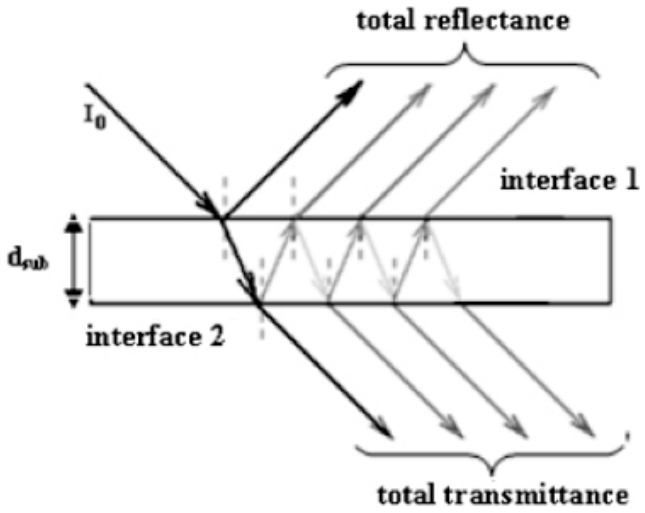

Figure 2.2. A schematic of neutron reflection experiments from an interface with a film of thickness *d*.

Neutrons are reflected from a surface and detected at the same angle as the angle of incidence. The amount of neutrons reflected is dependent on the scattering length density of the material at the interface.

Specular neutron reflection provides information about structure and inhomogeneities normal to an interface or surface. In neutron reflection, the simplest model is of a layer of uniform refractive index with a different refractive index to that of the bulk media above and below the layer. The neutron refractive index is in fact close to unity so reflection is usually defined in terms of the scattering length density, which is related to refractive index by:[147]

$$n^2 = 1 - \frac{\lambda^2}{\pi}\rho \quad (2.5)$$

where n is the refractive index, λ is the neutron wavelength, and ρ is the scattering length density of the material in the film.

In neutron reflection experiments, the incident neutron beam, containing a range of wavelengths, is collimated and inclined to a small angle of incidence, θ, to the horizontal of the air-liquid interface. The ratio of reflected intensity to incident intensity, known as the reflectivity, R, is measured as a function of the momentum transfer vector, q_z:

$$q_z = \frac{4\pi sin\theta}{\lambda} \quad (2.6)$$

where q_z describes the change in momentum of a neutron after reflecting from the material. Conventionally, z is defined to be the film normal direction and for specular reflection, the scattering vector has only the z-component.

For most materials, the neutron scattering lengths, b, are positive and therefore n is less than unity (Equation 2.5), giving rise to total external reflection below the critical angle. The refractive index for neutrons is just smaller than unity ($1 - n < 10^{-4}$) so critical glancing angles for total reflection are very small. Therefore, measurements require highly collimated beams. [147]

Specular neutron reflection experiments involve measuring the specular reflectivity as a function of momentum vector transfer, q, perpendicular to the surface or interface. This can be achieved either by using a single monochromatic

wavelength and varying the grazing angle of incidence, or by using a fixed angle of incidence and a range of wavelengths sorted by time of flight. Using a range of grazing angles would often involve rotating the sample on an axis. This is impractical for liquid interfaces, therefore horizontal, time of flight instruments, such as FIGARO at ILL are more suitable. All of the neutron reflectivity experiments performed in this thesis have used a time-of-flight instrument. [148,149]

The neutron reflectivity of the samples is measured as a function of neutron wavelength. The wavelength of the detected neutrons is calculated from the "time-of-flight" i.e. the initial position and velocity of a pulse of neutrons is fixed, and the time after the pulse that the neutrons are detected is measured. Assuming conservation of momentum, the wavelength, λ, can be calculated from the de Broglie relationship (Equation 2.1).[143] The neutron wavelengths can then be converted to momentum transfer vector using Equation 2.6. The reflectivity curve is produced from the reflectivity of the neutrons over the momentum transfer vectors. An example of neutron reflectivity of a D_2O-air interface is shown in Figure 2.3. [143]

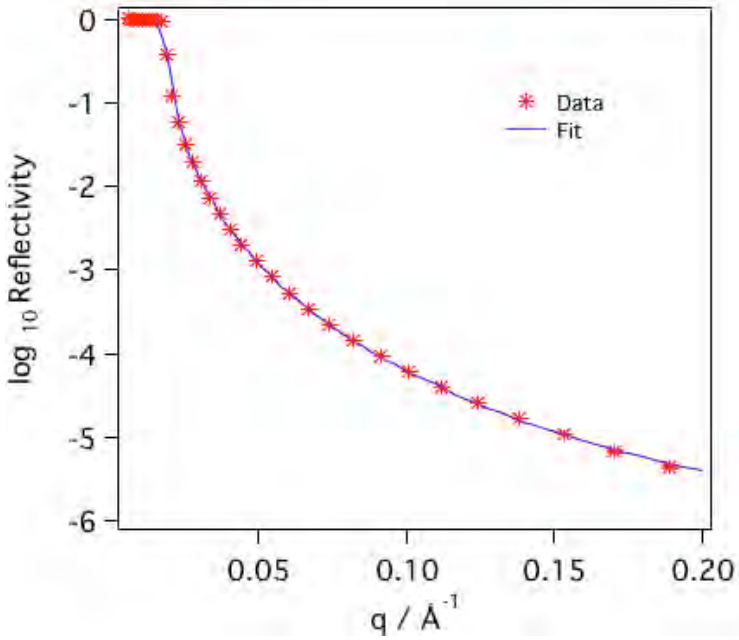

Figure 2.3. A neutron reflectivity curve of D_2O at the air-liquid interface.

Reflectivity is the reflected intensity relative to the incident intensity. The measured data is shown by the red markers and the fit is shown by the solid purple line.

For the air-liquid or solid-liquid interfaces studied in this thesis, the reflectivity curve can provide information about the material at the interface. The resulting reflectivity profile is characterised by its thickness, δ, and scattering length density, ρ. The profile can be fitted by using a least-squares fitting procedure to compare to a model reflectivity profile in order to optimise these features.

The thickness of the layer can be calculated using Fresnel's Law. As neutrons are reflected from each parallel interface (e.g. air-monolayer and liquid-monolayer), the multiple reflected neutron waves will interfere with each other, which will cause fringes on the reflectivity curve. The fringe spacing can be approximated by π/δ, therefore a lipid or surfactant monolayer or bilayer will have large fringe spacing due to its small thickness.[143]

A benefit of neutron reflectivity is that measurements on a sample can be taken continuously; therefore the kinetics of reactions at interfaces can be

monitored in real-time. This is useful in this research for investigating the reaction between gas phase pollutants and lung surfactant at the air-water interface.

2.5.1 Off-Specular Neutron Reflectivity

Off-specular neutron reflectivity can be used to probe surface features on a micrometre scale (600 nm – 60 μm). Off-specular scattering defines neutrons that are detected at a different angle to the angle of incidence. It is caused by any local deviation from the average layering structure as shown in Figure 2.4.

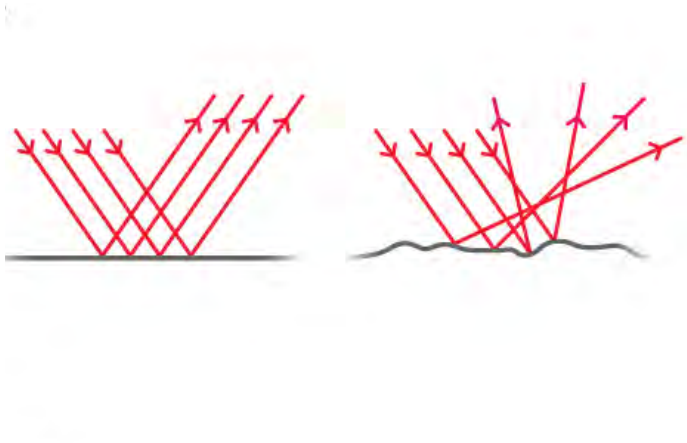

Figure 2.4. A shematic representation of specular reflection (left) and off-specular (right) reflection from a rough interface.

This technique has previously primarily been used to describe magnetic domains in multilayers since the discovery that the spin dependent electric transport properties depend sensitively upon the local spin-spin correlations. To our knowledge, this technique has not previously been used to investigate roughness of phospholipid systems. The theoretical treatment of off-specular neutron scattering is not as advanced as the theory of specular neutron scattering and has mainly focused on handling magnetic off-specular neutron scattering.

2.6 X-ray Reflectivity

X-ray reflectivity is a complementary technique to neutron reflectivity. The principles of measurement are the same, however the signal to background ratio is much higher than neutron reflection. This is because X-rays are absorbed by the liquid subphase, leading to lower background scattering and also because X-ray sources are more intense than neutron sources. This allows measurements of reflectivity to higher values of q.

The usefulness of X-ray reflection is limited by the lack of manipulation of contrasts of different components in the layer. X-rays are scattered by the electrons of the molecules, rather than the nuclei, therefore X-ray scattering lengths increase with increasing atomic number. Hydrogen has a very low signal in X-ray reflection and this will not increase with isotopic substitution to deuterium. Furthermore, there is a risk of X-ray damage, while neutrons are non-destructive.[150]

However, X-ray reflectivity has been utilised in this research when it has not been possible to selectively deuterate samples as it can aid structural analysis due to the benefit of lower background scattering, thus providing an additional method for examining difficult samples, along with neutron scattering. The ability to measure to high q is also important as it can allow the more accurate measurement of thickness of monolayer films, as the characteristic fringes are present towards higher q.

2.7 Combining Neutron or X-ray Reflectivity with Surface Tension Measurements

Much of the research in this thesis investigates the changes to the properties of lung surfactant samples during exposure to ozone pollution; therefore it is useful to measure the surface tension in real-time along with neutron reflectivity measurements. To do this, a monolayer of the compounds of interest can be formed on an aqueous subphase inside a Langmuir trough. A

solution of an amphiphile in a water insoluble solvent, such as chloroform, is carefully placed onto the surface of an aqueous subphase using a microlitre syringe, and the solution rapidly spreads across the available area. As the solvent evaporates, a monolayer of the amphiphile is formed and the molecules are free to move in a two-dimensional plane (Figure 2.5). The molecules orientate themselves so that the hydrophilic groups (e.g. lipid heads) are in the water subphase and the hydrophobic groups (e.g. lipid tails) are in the air above the subphase. For macromolecules such as proteins, the situation is more complex because in any molecule there may be numerous hydrophilic and hydrophobic residues distributed evenly or in blocks along the chain length. Therefore, parts of the macromolecule will be attracted to water and other parts repelled, and the resulting chain configuration will depend on how the hydrophilic and hydrophobic groups are distributed.[151]

The Langmuir trough barriers (see Figure 2.5) can be controlled to compress and expand the monolayer. The monolayer molecules are contained within the barriers. The characteristics of a monolayer on the water surface are studied by measuring changes in surface tension upon compressing the monolayer. The surface tension, γ, is measured as the surface pressure, Π, a two dimensional analogue of the force, where $\Pi = \gamma_0 - \gamma$: the difference between the surface tension in the absence of a monolayer γ_0 and the surface tension in the presence of a monolayer γ. This can be monitored on the Langmuir trough using the Wilhelmy-plate method. A measurement is made by determining the force due to surface tension on a plate suspended so that it is partially immersed in the subphase (see Figure 2.6). This force is then converted into surface tension (mN m^{-1}) utilising the dimensions of the plate. The force is determined by measuring the changes in the mass of the plate, which is directly coupled to a sensitive electrobalance. When a surface active material is added to the interface, the surface tension decreases, hence the force pulling down on the Wilhelmy plate is reduced and the change in surface tension can be detected.

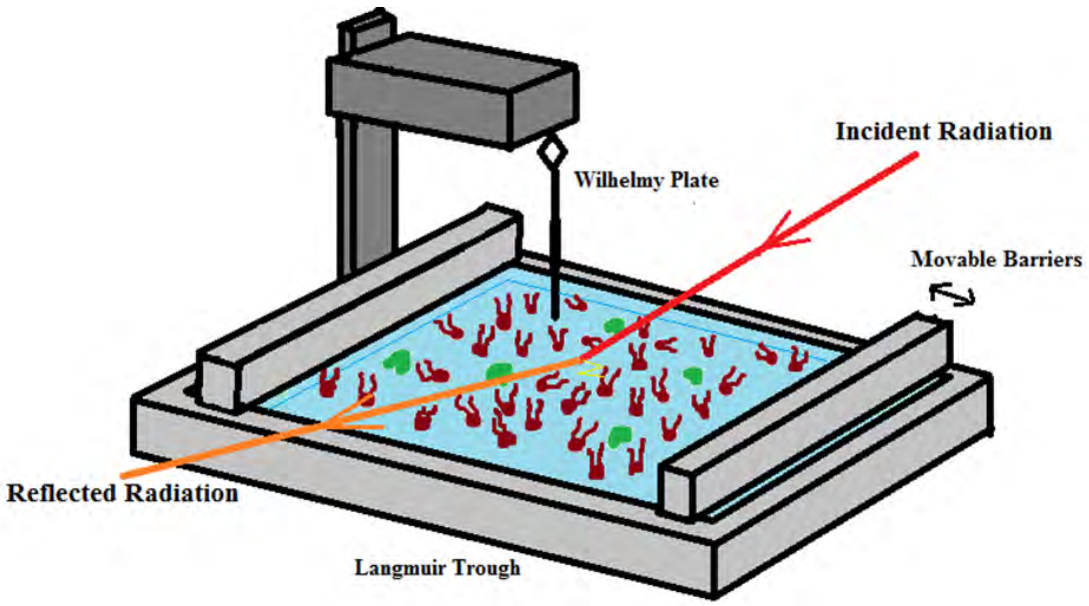

Figure 2.5. The Langmuir trough.

The Langmuir trough is filled with aqueous subphase and a monolayer is formed on the surface in the area enclosed by the movable barriers. The Wilhelmy plate dips into the subphase and is attached to a sensitive microbalance that detects any changes in the forces exerted onto it, calculating the surface pressure. At the same time the neutron or X-ray reflectivity can be measured.

When the trough area is decreased, the available surface area to the monolayer is decreased and the molecules exert a repulsive effect on each other. This leads to a decrease in the surface tension at the interface (or increase in surface pressure). The characteristics of a monolayer on the water surface can be studied by measuring the changes in surface tension upon compressing the monolayer. The plot of surface pressure *versus* area per molecule is known as a pressure-area isotherm, the shape of which is characteristic of the molecules within the film. The rate of change of surface pressure with decrease in area per molecule can aid identification of the phases of the monolayer, e.g. gas, liquid expanded or solid (Figure 1.6, Chapter 1).[136]

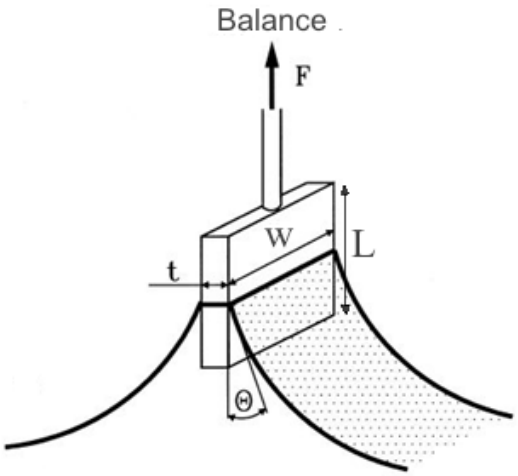

Figure 2.6. The Wilhelmy plate partially immersed in the subphase and its dimensions.

The net downward force on the wilhelmy plate (and therefore surface pressure) can be calculated for a rectangular plate from its dimensions of width w, length L and thickness t and contact angle Θ and immersed depth h.

Combining surface pressure measurements simultaneously with neutron reflectivity measurements is beneficial as it allows understanding of how the changes in surface pressure are linked with the changes in neutron reflectivity (and therefore structure of the monolayer). The set-up for these experiments can be seen in Figure 2.5.

2.8 Methods for Studying Lipid Bilayers

In this thesis two techniques were used to study the structure of lipid bilayers. The first is using neutron reflectivity at the solid-liquid interface, which involves forming a supported bilayer of the lipid on a quartz slab by spreading vesicles over the surface. This set-up is described further in Chapter 6. The second technique uses small angle neutron scattering (SANS), which is discussed in more detail below.

2.8.1 Small Angle Neutron Scattering

SANS can be used to study the bulk properties of a particle such as its size, polydispersity, structure and particle interaction. In SANS, different length scales are explored in reciprocal space by detecting the number of scattered neutrons as a function of the wave vector, q. SANS can help to determine structural information about samples due to differences in neutron scattering length densities within the sample.

The geometry set-up for a SANS experiment is shown in Figure 2.7. In this research a spallation neutron source was used to perform experiments, therefore the incident beam consists of a range of neutron wavelengths.

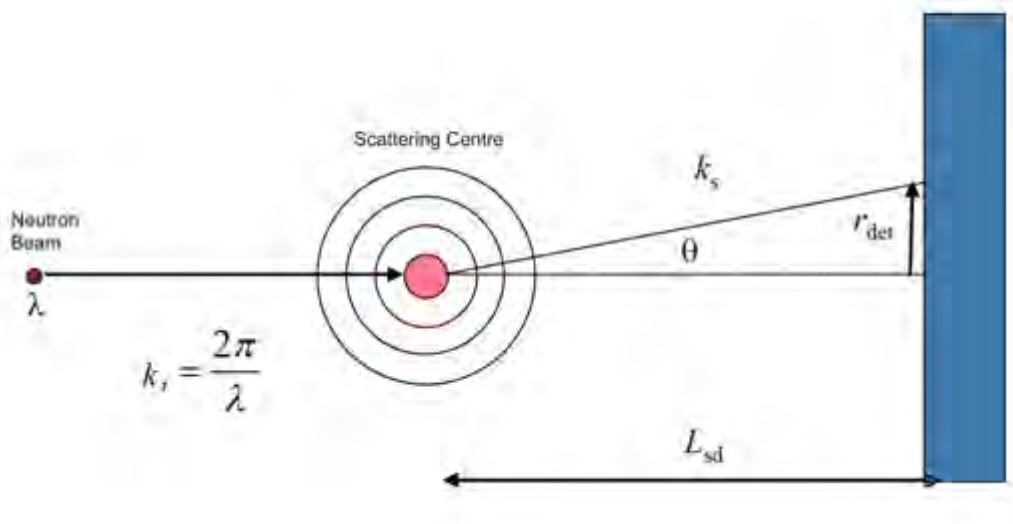

Figure 2.7. Typical geometry set-up for a SANS experiment.

Neutrons of wavelength λ are scattered by nuclei in the sample. A proportion of neutrons scattered through an angle, θ, are recorded on a 2-D detector at a distance, L_{sd}, from the sample at a radial distance, r_{det}. $\boldsymbol{k}_i$ and $\boldsymbol{k}_s$ are the wave vectors of the incident and scattered neutrons respectively. [19]

The scattering of thermal soft neutrons by matter can be described by the coherent scattering cross-section per unit volume:

$$I(q) = \frac{1}{V} \langle \sum_{i=1}^{N} \sum_{j=1}^{N} f_i f_j e^{iq(r_i - r_j)} \rangle \qquad (2.8)$$

where N is the total number of particles in the scattering volume V, and r_i and r_j are the space positions of the particles i and j. f_i and f_j are the scattering amplitudes of particles i and j. The angular bracket represents an ensemble average.

For a collection of particles in a system (e.g. vesicles), equation 2.8 is summed for all pairs i and j both within and between the particles. For convenience, scattering contributions are expressed using a form factor *P(q)* and a structure factor *S(q)*:

$$I(q) = n_P P(q) S(q) \qquad (2.9)$$

where n_p represents the average number density of particles in scattering volume V.

The form factor, *P(q)*, is a function that describes how the neutron scattering cross section is adjusted by interference effects between neutrons scattered by different parts of the same particle. It describes the scattering observable from an isolated body in the absence of interference effects and depends on the particle size and shape. The larger the size of particle, the more steeply *P(q)* falls off with q.

The structure factor, *S(q),* represents the effect of interference due to neighbouring particles, the extent of which depends on their relative positions. *S(q)* is equal to one for sufficiently dilute, non-interacting systems. Information on the particle size and shape determined by neutron scattering can be found using mathematical modelling.[155]

2.8.2 Modelling Vesicles and Micelles from SANS

In this thesis, vesicles were analysed using the monodisperse oriented sheet model described by Kotlarchk *et al.*[154] This model uses a form factor describing scattering from a thin interface and includes a Lorentz factor to allow for small Gaussian distribution of surface normals around q:

$$L_N(q) = \frac{1}{1+\frac{1}{2}q^2(R\sigma)^2} \qquad (2.10)$$

where Rσ describes the "flatness" of the bilayer sheet. This model is fitted to give the thickness of the bilayer as well as $R\sigma$. It also includes terms for the polydispersity of the bilayer ($\sigma(L/L)$), which is assumed to be small in this study due to the sample preparation technique, therefore is kept at a low value.

In order to model micelles, a core-shell model was used where the core was assumed to consist of the hydrophobic tails of the lipid while the shell contains the hydrophilic head groups. Sphere or ellipsoid form factors were used to describe scattering between particles. Figure 2.8 shows schematics of the various form factors investigated in this study.

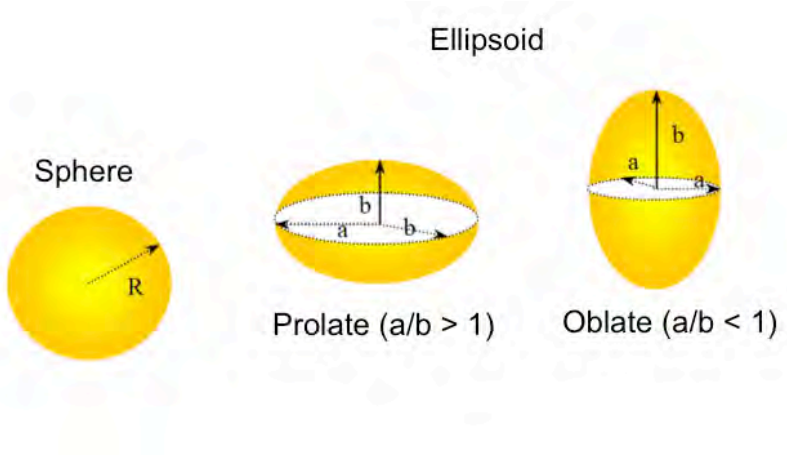

Figure 2.8. Schematic of the various form factors for SANS data fitting of micelles and mixed samples in this study.

The Hayter-Penfold (H-P) structure factor was applied to the micelle model, which includes parameters of potential for charges on the particles.[155,156] When

combined with the core-shell model with an ellipsoid form factor, this allows for inclusion of the interparticle interference effects due to screen coulomb repulsion between molecules. This model slows determination of the micellar charge and inverse Debye screening length. For full details of the models, please refer to the referenced papers.

Chapter 3 Ozone Initiated Oxidation of Surfactant Protein B Monolayers at the Air-Water Interface

3.1 Introduction

Surfactant protein B is vital for lung function as an absence of the protein can lead to lung failure and death.[56,57] Breathing in ozone air pollution could expose the protein to this reactive oxidant, reacting to cause damage to its structure at the air-water interface. Since the lung surfactant function is so sensitive to levels of SP-B, any damage to the protein could be detrimental to the function of the lungs. This chapter examines the structural and chemical damage to SP-B by ozone at the air-water interface, and how this damage leads to changes in its interaction with surrounding phospholipids in a monolayer.

3.1.1 SP-B in Research

The effect of ozone exposure on two peptide mimics of SP-B: SP-$B_{1\text{-}25}$ and Super Mini B (SMB), was studied at the air-water interface. These peptide mimics were used as there are no current methods for chemical synthesis of the full-length protein, and no protein expression system is available. Attempts have been made to synthesise the full-length protein, but the configuration of the disulphides within the protein were incorrect, therefore the protein was non-functioning.[157] Additionally, the full-length protein has not yet been expressed in the laboratory, presumably because its synthesis is so specific to type II alveolar cells and requires post-translational modifications to cleave the pro-protein into the functional surfactant protein. Therefore, mimicking the synthesis in order to correctly produce and fold the protein is difficult, even more so considering the insolubility of the protein in water.

Therefore, for research requiring highly pure samples of SP-B, these two peptide mimics are often used. The amino acid sequences of the full-length protein SP-B and the peptide mimics SMB and SP-B_{1-25} are shown in Figure 3.1. The three-dimensional structure of the full-length protein is not known, but high-resolution structures of these synthetic protein fragments are available.

SP-B

FPIPLPYCWLCRALIKRIQAMIPKGALAVAVAQVCRVVPLVAGGICQCLAERYSVILLDTLLGRMLPQLVCRLVLRCSM

SMB

FPIPLPYCWLCRALIKRIQAMIPKG_____ GRMLPQLVCRLVLRCS

SP-B_{1-25}

FPIPLPYCWLCRALIKRIQAMIPKG

Figure 3.1. The primary structures of full-length human SP-B, SMB and SP-B_{1-25}.

3.1.2 SP-B_{1-25}

SP-B_{1-25}, is formed from the first 25 residues of the full-length protein, representing the N-terminal helix of the protein. Circular dichroism (CD) and Fourier transform infrared (FTIR) spectroscopy of this synthetic peptide indicate a dominant helical content with minor β- and disordered components.[53,54] 2D-NMR of the SP-B_{11-25} protein showed an α-helix was present consisting of residues 14-21.[55] The structure of SP-B_{1-25} predicted from FTIR studies is shown in Figure 3.2.

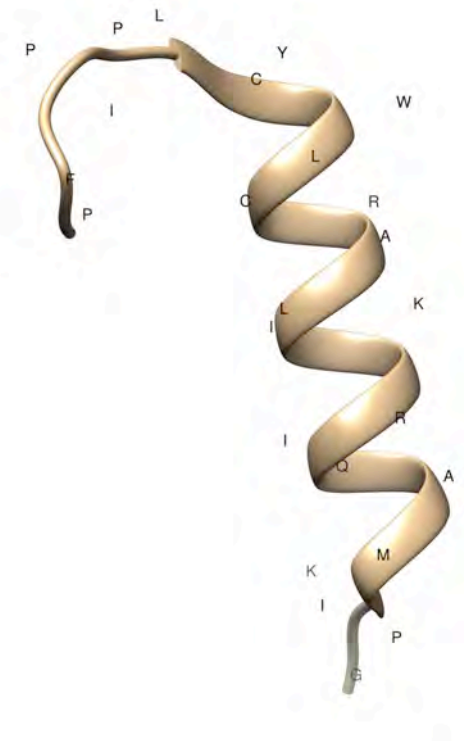

Figure 3.2. The 3-D structure of the synthetic peptide mimic SP-B_{1-25}.

The structure was determined by ^{13}C-enhanced Fourier Transform FTIR spectroscopy in POPG liposomes at a protein/lipid ratio of 1:70 (mol/mol)[54] (PDB reference 1DFW). The amino acid residues are indicated.

Figure 3.2 demonstrates that the peptide has α-helical residues (residues 8 –22), and random residues (residues 1-7, 23–25). These conformations are close to those predicted for the full-length protein, as discussed in Chapter 1. Additionally, they are analogous to the structural motifs observed in the corresponding homologous N-terminal regions of the saposin family of proteins.[54]

Shanmukh *et al.* investigated the structure of monomeric SP-B_{1-25} at the air-water interface.[158] Using polarisation modulation infrared reflectance absorption spectroscopy (PM-IRRAS) they were able to show that the secondary structure of the protein was dependent on the ratio of protein to phospholipids. In a monolayer of 4:1 DPPC/DOPG (1,2-dioleoyl-*sn*-glycero-3-phospho-glycerol) plus 10 weight % SP-$B_{1–25}$, there was a lack of any significant *α*-helix detected, but as the percentage of SP-B_{1-25} was decreased to physiological concentrations, the α-helical content

significantly increased. In phospholipid monolayers containing 1 wt.% SP-B_{1-25}, results indicated predominant presence of α-helix.

3.1.3 Super Mini-B (SMB)

Super mini-B is composed of the N (residues 1-25) and C (residues 63-78) terminal helical regions of SP-B.[159,47] The solution 2D-NMR structure of a slightly shorter version of this synthetic protein, Mini-B (residues 11-25 and 63-78), has been determined. Two α-helices were detected, connected *via* two intramolecular disulphide bonds. The proposed structure is shown in Figure 3.3. [160]

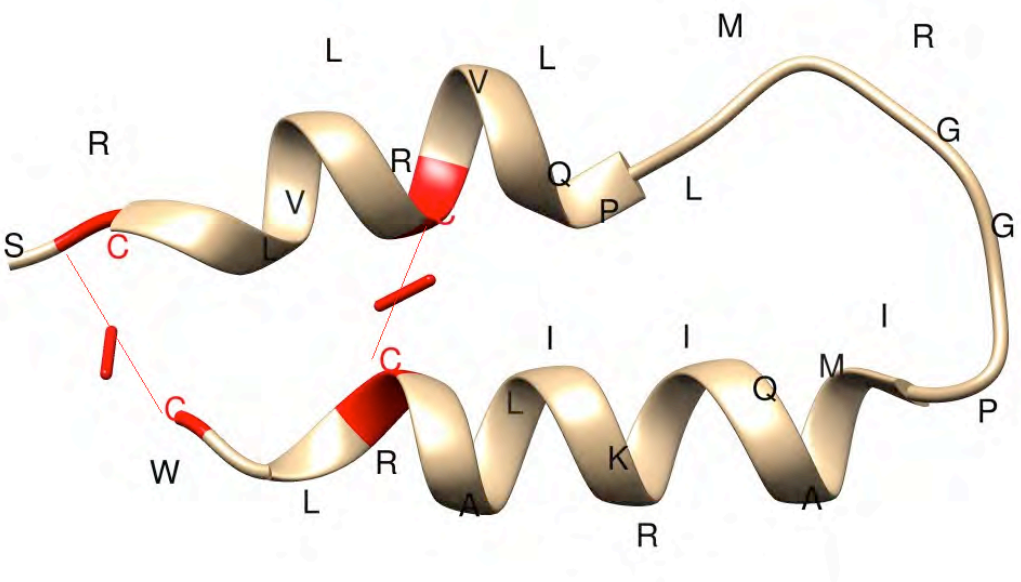

Figure 3.3. The representative structure of the synthetic peptide mini-B.

($SP\text{-}B_{11\text{-}25,\ 63\text{-}78}$) as determined by NMR in SDS micelles (PDB reference 2DWF).[160] Amino acid residues are indicated by their one letter code and the intramolecular disulphide bonds are shown in red.

3.1.4 Potential Function of Protein Mimics

Both SP-B_{1-25} and SMB have been shown to fulfil the same function as the full-length protein. Captive bubble surfactometry of dimeric SP-B_{1-25} in a phospholipid mixture (2 mol% SP-B_{1-25}) indicates that it has enhanced dynamic respreading properties relative to pure lipid monolayers, and properties similar to that of whole extracted calf surfactant.[161] Monomeric SP-B_{1-25}, in a phospholipid mixture with DPPC:POPG:Palmitic Acid (69:22:9 wt/wt/wt), quickly improves lung function in both premature rabbits and lavaged, surfactant-deficient rats.[162] Additionally, when monomeric and dimeric SP-B_{1-25} were compared in the premature rabbit and lavaged rat models, dimeric SP-B_{1-25} was more efficient in improving lung function than monomeric SP-B_{1-25}.[163,164]

The surface activity of SP-B fragments built around the C-terminus have been tested *in vitro* and *in vivo* with an isolated lung system. Results from these studies indicate that lengthening the sequence toward the N-terminus of SP-B increases the surfactant activity of the peptide fragment, indicating the functional importance of the N-terminal helix.[165, 166]

3.2. Ozone Pollution Damage to SP-B

It has been shown that the presence of SP-B is vital for lung function, and the conformation of the protein is also important.[57] This work explores the damage that could be caused to this vital protein when it is exposed to ozone pollution at the air-water interface. The peptide mimics in this study are sufficient representatives of the full-length protein due to their structural and functional similarity as described.

3.2.1 Previous Research in the Literature

There are currently no studies in literature looking at the exposure of the full-length surfactant proteins to ozone. However, Kim *et al.* have previously studied the chemical changes of SP-B_{1-25} due to reaction with ozone using field-induced droplet ionisation (FIDI) mass spectrometry at the air-water interface. The spectra were compared before and after exposure to ozone and it was found that the main product after this time had the mass of SP-B_{1-25} plus 3 oxygen atoms. Collision induced dissociation (CID) indicated that the oxidised amino acids were methionine (Met_{21}+1O) and tryptophan (Trp_9 + 2O, N'-formylkynurenine), as shown in Figure 3.4. Kim *et al.* then suggested that the oxidised form of SP-B_{1-25} might be lost entirely from the interface, given the weak signal they observed for the triply oxygenated product.[167]

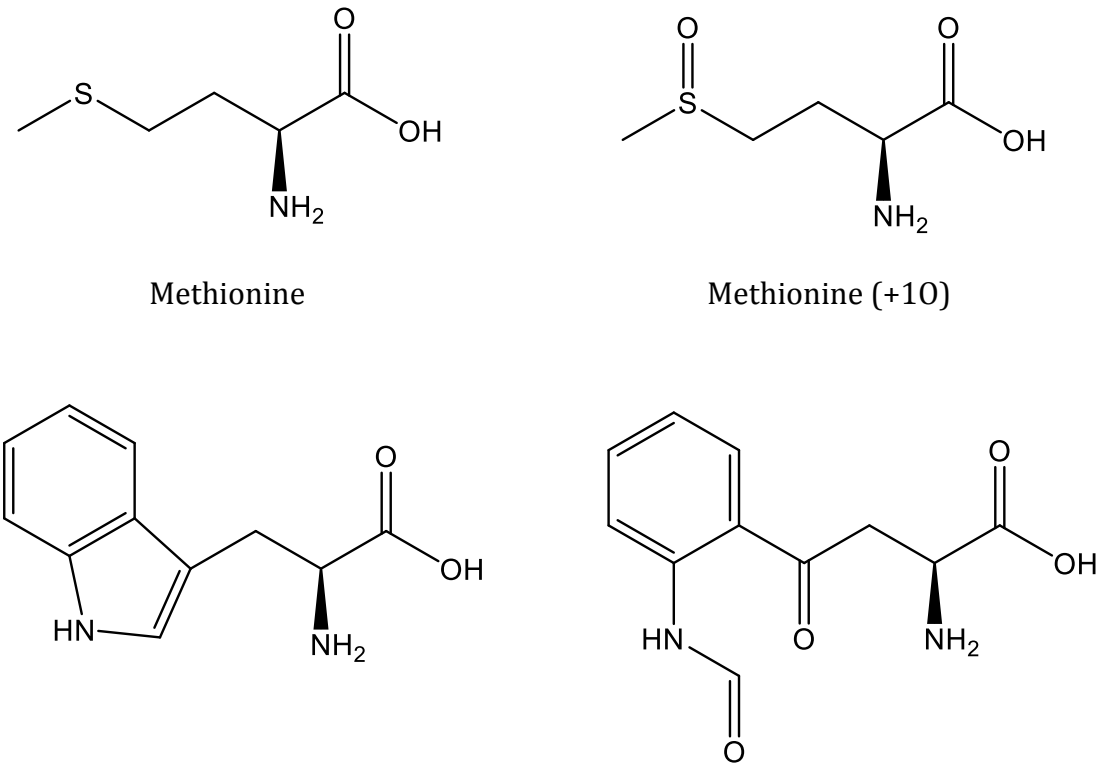

Figure 3.4. The chemical structures of Met, Met (+1O), Trp and Trp (+2O).

These are the proposed amino acids that are oxidised by ozone in the reaction with SP-$B_{1\text{-}25}$ at the air-water interface, and the chemical structures of the products, as determined using MS.[167]

Sarker *et al.* have modified the tryptophan residue of SP-$B_{8\text{-}25}$ to one of its oxidised forms (kynurenine-Figure 3.5).[168] In this case the tryptophan has only one additional oxygen atom added, whereas Kim *et al.* had proposed that tryptophan was oxidised to a form with two oxygen atoms added.[167] The nuclear magnetic resonance (NMR), circular dichroism (CD) and molecular dynamics (MD) of the oxidised form were compared to the unmodified form. It was shown that oxidation leads to significant decrease in helical content from approximately three helical turns to only one or less. MD showed that the oxidised protein has a very different orientation in lipid monolayers indicating that its interactions with lipids, which are thought to be vital for its function, are severely affected. If the tryptophan was

oxidised to a greater extent, as suggested by Kim *et al.*, the structure of the protein and interaction with phospholipids could be affected to an even greater level. [168]

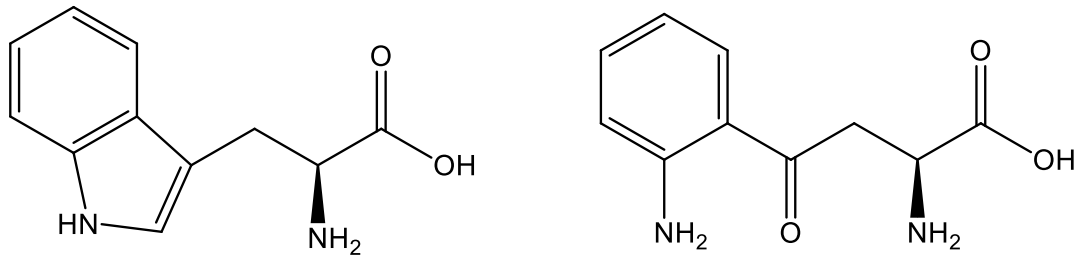

Tryptophan Kynurenine (Trp +1O)

Figure 3.5. The chemical structure of tryptophan and kynurenine, Trp (+1O).

The tryptophan residue in SP-B_{1-25} was replaced with kynurenine by Sarker *et al.* and the structural properties of the peptide in a lipid monolayer were investigated.[168]

The research presented in this chapter aims to investigate the reactions between monolayers of SP-B_{1-25} and ozone and monolayers of SMB and ozone at the air-water interface using a variety of techniques such as surface pressure measurements combined with neutron and X-ray reflectivity, SDS-PAGE, HPLC and fluorescence microscopy. These experiments can provide information about the damage caused to the peptides at the interface and whether the oxidative damage causes the peptides to fragment, to leave the interface (as proposed by Kim *et al.*) or change their orientation (as suggested by Sarker *et al.*). Furthermore, research on the interaction between the peptides and phospholipids before and after exposure was performed, in order to determine how the function of the peptide might change after oxidation, as it has been suggested that SP-B interacts with phospholipids, potentially *via* its positively charged residues. Therefore, both Zwitterionic and anionic phospholipids will be examined.

3.3 Experimental Details

3.3.1 Chemicals and Reagents

SP-B_{1-25} and SMB were synthesised by Peptide Synthetics (Peptide Protein Research Ltd, UK) using solid-phase synthesis and purification by reverse phase HPLC. The protein purity for both was >90% and masses were obtained using LC-MS.

The details of all other chemicals used in this study are presented in Table 3.1 and the chemical structures of the deuterated lipids d_{62} DPPC, d_{62} DPPG and d_{31} POPG and the lipid ^{1}H DPPG are shown in Figure 3.6. The structures of ^{1}H DPPC and ^{1}H POPG have been presented earlier in Figures 1.4 and 1.5 respectively.

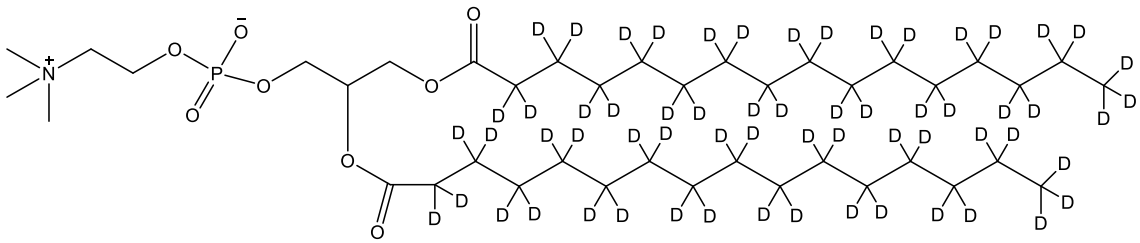

d_{62} DPPC

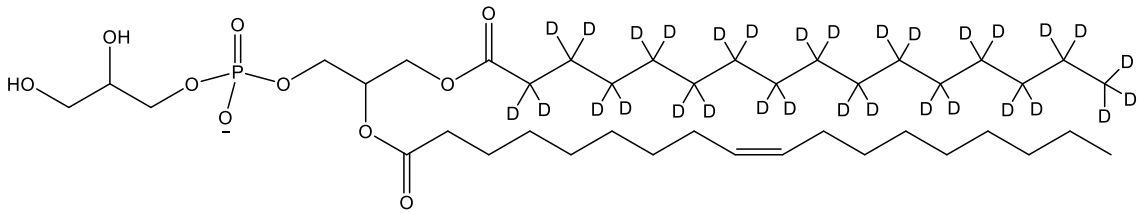

d_{31} POPG

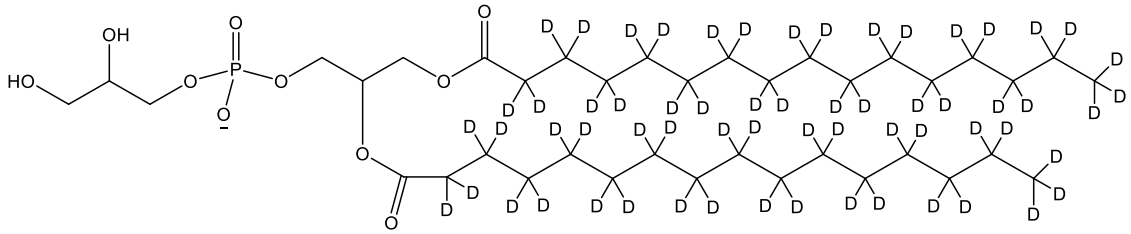

d_{62} DPPG

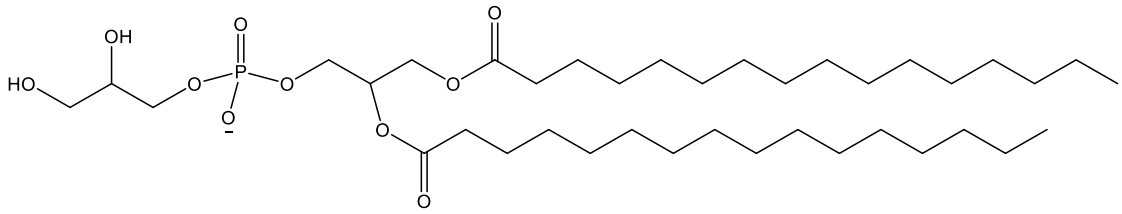

^{1}H DPPG

Figure 3.6. The chemical structures of the phospholipids d_{62} DPPC, d_{31} POPG, d_{62} DPPG and ^{1}H DPPG.

These phospholipids were used in mixed peptide/lipid monolayer research in this study.

Compound	Details	Manufacturer
Ethanol	99.9% purity	Fisher
Acrylamide/ bis-Acrylamide 19:1	40% w/v, 99% purity	Sigma-Aldrich
Acrylamide/ bis-Acrylamide 29:1	40% w/v, 99% purity	Sigma-Aldrich
Ammonium Persulphate	>98% purity	Sigma-Aldrich
Chloroform	≥99.9% purity with 0.5-1.0% ethanol stabiliser	Sigma-Aldrich
DL-dithiothreitol (DTT)	1M , ≥99.0 % purity	Sigma-Aldrich
Glutaraldehyde	25% w/v, >99.95% purity	Sigma-Aldrich
Methanol	≥99.9% purity	Fisher
Formaldehyde	37-41% w/v, >99% purity	Fisher
Propan-2-ol	Min. 99.7% purity	Sigma-Aldrich
Sodium chloride	Min. 99.5% purity	Sigma-Aldrich
Sodium dodecyl sulphate (SDS)	99% purity	BDH Chemical Ltd.
Silver nitrate	99.9% purity	Sigma-Aldrich
TEMED (N, N, N', N' - Tetramethylethylenediamine	99% purity	Sigma-Aldrich
Tricine	≥99.8% purity	Fisher
Tris(hydroxymethyl)methylamine	99.8% purity	BDH Chemical Ltd.
Sodium Carbonate	99.99% purity	Fisons
Ethylenediaminetetraacetic acid (EDTA)	99.5% purity	BDH Chemical Ltd.
Sodium thiosulphate-5-hydrate	99% purity	BDH Chemical Ltd.
Sodium phosphate monobasic dihydrate	≥99.0% purity	Sigma-Aldrich
Sodium phosphate dibasic dihydrate	≥99.0% purity	Sigma-Aldrich
Glycerol	≥99.0% purity	Sigma-Aldrich
Cholesterol	≥99.0% purity	Sigma-Aldrich
d_{62} DPPC	≥99.0% purity	Avanti Polar Lipids
d_{62} DPPG	≥99.0% purity	Avanti Polar Lipids
d_{31} POPG	≥99.0% purity	Avanti Polar Lipids
^{1}H DPPC	≥99.0% purity	Avanti Polar Lipids

Table 3.1. Details and stated purities of the materials used in this study.

3.3.2 Surface Pressure Measurements

In all Langmuir trough experiments that were combined with neutron or X-ray reflectivity, a 50 mM phosphate buffered aqueous subphase was used. This was formed by weighing 1.68 g of sodium phosphate monobasic, 5.11 g of sodium phosphate dibasic and making up to 1 L with pure water or pure D_2O. When null-reflecting water (NRW) buffer was used, 1.68 g of sodium phosphate monobasic, 5.11 g of sodium phosphate dibasic and 88.3 g D_2O were weighed before making up to 1 L with pure water. The pH of all buffers was adjusted to pH 7 if necessary before use. For all other Langmuir trough experiments, pure water was used as a subphase.

The surface pressure of the peptide or peptide and lipid monolayers was measured by forming monolayers on a Langmuir trough (Nima Technology). Surface pressure measurements where neutron or X-ray reflectivity experiments were performed simultaneously used a Langmuir trough enclosed in an environmental chamber to contain the gasses in order to prevent contamination of the lab atmosphere. All other measurements were performed on a Nima model 102M/INV housed in an AtmosBag (Aldrich) in a fume hood.

The surface pressure (the difference between the surface tension of the air-water interface of pure water and the interface being measured) was determined using a Wilhelmy plate made from chromatography grade filter paper (Whatman). This was attached to a sensitive microbalance that can measure forces acting on the plate.

The Langmuir trough was filled with an aqueous subphase of 50 mM phosphate buffer at pH 7.0. The surface of the subphase was checked for cleanliness by compressing the trough barriers to minimum trough area. If the surface pressure was above 0 mN m^{-1} upon compression, the surface was aspirated to remove impurities. The surface was then re-checked to ensure no more impurities were present.

The SP-B_{1-25} and SMB peptide monolayer solutions were formed by dissolving 1 mg of the peptide in 5 mL of chloroform/methanol (1:5 v/v). The peptide/phospholipid monolayer mixtures were formed by mixing the necessary

volumes of the peptide solutions and 1 mg mL^{-1} lipid solutions to give the required weight ratio. The mixed peptide/lipid monolayers studied in this research are presented in Table 3.2. The monolayers were prepared by touching droplets of the monolayer solution of interest to the subphase surface using a Hamilton syringe. The monolayer was slowly added until a surface pressure of approximately 5 mN m^{-1} was achieved at the maximum trough area. Before experiment, the monolayer was exposed to a constant flow rate of 1-4 L min^{-1} oxygen gas for 15 minutes to allow for total evaporation of the monolayer solvent.

Monolayer Mixture	Weight Ratio	Molar Ratio
SP-B $_{1\text{-}25}$ / ^{1}H DPPC	1.0 : 1.5	1.0 : 6.1
SMB / ^{1}H DPPC	1.0 : 1.0	1.0 : 6.4
SMB / d_{62} DPPC	1.0 : 1.0	1.0 : 6.0
SMB / d_{31} POPG	1.0 : 2.0	1.0 : 12.2
SMB / d_{62} DPPG	1.0 : 2.0	1.0 : 12.1

Table 3.2. Details of the peptide/phospholipid monolayer mixtures studied at the air-water interface.

Before and after ozone or control experiments, an isotherm (plot of surface pressure *versus* trough area performed at constant temperature) of the monolayer was measured by decreasing the trough area until a surface pressure of 30 mN m^{-1} was achieved and then increasing the trough area to maximum area. This was repeated twice. Before experiment, the film was compressed to a surface pressure of 5 mN m^{-1} above the desired surface pressure and then re-expanded to the desired surface pressure. The surface pressure was monitored continuously during the experiment, while the trough surface area and temperature were held constant.

3.3.3 Ozone Reactions

Ozonolysis experiments were performed by continuously flowing a dilute (~2 ppm) mixture of ozone in oxygen at a constant flow rate of 1 or 2 L min^{-1} through the environmental chamber or AtmosBag. Ozone was generated by passing dry oxygen through a commercial ozone generator (UVP) containing a mercury Pen-Ray lamp, producing ozone from the photolysis of molecular oxygen at 185 nm as shown below.

$$O_2 \xrightarrow{\lambda=185nm} 2O^{\cdot} \quad \textbf{(3i)}$$

$$O^{\cdot} + O_2 \longrightarrow O_3 \quad \textbf{(3ii)}$$

Monolayers were exposed to ozone for varying lengths of time as described. During exposure, an outlet from the chamber allowed the unreacted ozone to flow out and enter a container of water to prevent contamination of the lab atmosphere.

3.3.4 Fluorescence Microscopy of Monolayers of SMB at the Air-water Interface

Monolayers of SMB were formed in a petri dish with a glass bottom (MatTek, MA, USA) by adding 1 drop of SMB in chloroform/methanol (1:5 vol/vol, 0.2 mg mL^{-1} SMB) to the surface of a small volume of water (approximately 300 µL). The fluorescence was monitored using the Octopus cluster at the Central Laser Facility at Rutherford Appleton Laboratory, Oxfordshire. Fluorescence microscopy was performed using an inverted confocal microscope (Leica), and objective lens with long working distance capable of transmitting the UV fluoresced light at 380 nm. The excitation of the tryptophan residue in SMB was achieved by two photon excitation in the visible at 566 nm. Tryptophan fluorescence was measured before ozone exposure and then after 5 and 10 minutes of exposure (2 ppm at 1 L min^{-1}) *in situ*. Additionally, tryptophan fluorescence was measured using a different SMB monolayer before and after 10 minutes of oxygen exposure (1 L min^{-1}).

3.3.5 Collection of Monolayers of SP-B_{1-25} and SMB for Analysis

SP-B_{1-25} or SMB monolayers were formed on a Langmuir trough. The oxidised or un-oxidised monolayers were extracted by collecting all of the subphase into a glass separating funnel, using a 20 mL glass pipette. The pipette was hydrophilised beforehand by drawing up dilute sulphuric acid followed by pure water, to prevent adsorption of the protein to the pipette. The protein was then extracted by washing the subphase three times with chloroform and collecting the chloroform fraction. The majority of the chloroform was evaporated using a rotary evaporator followed by drying the remaining 1-2 mL under a flow of dry nitrogen gas. The extracted protein was then diluted appropriately for the techniques described below.

3.3.6 Tris-Tricine SDS-PAGE of SP-B_{1-25} and SMB Samples

The SDS-PAGE method used was based on the Tricine-SDS-PAGE protocol described by Schagger *et al.,*[169] which is a procedure that has been optimised for the separation of very small proteins (< 30 kDa). Silver staining was used in this case due to the very low concentration peptide monolayers collected from the Langmuir trough, as well as the hydrophobic nature of the peptides, which is not ideal for Coomassie use.

3.3.6.1 Preparation of Buffers and Gels for SDS-PAGE and Silver Staining

Tris-SDS sample buffer was prepared by mixing pure water (2.92 mL), glycerol (2 mL), SDS (10% w/v, 1.6 mL), Tris (0.5 mM, pH 6.8, 1 mL) and bromophenol blue (1% w/v, 0.08 mL). For sample buffer with DTT, a fresh aliquot of DTT (0.1 M, 1 mL) was added.

3M Tris-HCl with 0.4 % SDS, pH 8.45 was formed by dissolving Tris (36.3 g) and sodium dodecyl sulphate (400 mg) in water (up to 50 mL). The pH was

adjusted to 8.45 with concentrated hydrochloric acid and water added to 100 mL. This buffer was used to create the protein gels and was formed within 1 day of use.

10X Tris-tricine-SDS running buffer was formed by dissolving Tris (12.1 g), tricine (17.9 g) and SDS (1 g) in water (up to the 1 L line) and pH was adjusted to 8.3 accordingly. Prior to electrophoresis, the buffer was diluted 1:10 to form 1X buffer.

The resolving gel (18%) was prepared by mixing deionised water (4.8 mL), 3 M Tris-HCl buffer, pH 8.45 (4 mL), acrylamide/bis-acrylamide (40%, 19:1, 7.2 mL), ammonium persulphate (40 %, 16 μL) and tetramethylethylenediamine (TEMED, 24 μL). The mixture was immediately added between glass and aluminium plates with 0.75 mm spacers, leaving ~2 cm at the top of the plates. This was left for 1 hour to set.

The stacking gel (5%) was prepared by mixing deionised water (5 mL), 3M Tris-HCl buffer, pH 8.45 (2 mL), Acrylamide/bis-acrylamide (40%, 1 mL, 29:1), ammonium persulphate (40 %, 8 μL) and tetramethylethylenediamine (TEMED, 32 μL). This was immediately added to the top of the set resolving gel and a comb (5 mm spacings) was inserted. This was left to set for a further hour at room temperature before electrophoresis.

3.3.6.2 SDS-PAGE

The peptide samples were dried under a flow of nitrogen gas and dissolved in Tris-SDS sample buffer, with or without DTT. The samples were then heated at 95 ^{o}C for 10 minutes and cooled to room temperature prior to electrophoresis.

The gel was filled with running buffer and loaded with samples (10 μL per well) and molecular weight standard (BioRad polypeptide SDS-PAGE standard #161-0326 containing an unstained mixture of 6 polypeptides ranging from 1400-26600 Da). Electrophoresis was run for 2 hours at 200 V. The gel was removed, washed twice with water and incubated in 5% glutaraldehyde fixation buffer (50 mL x 2) for 2 x 30 minutes.

The fixation buffer was removed and the gels washed twice in water. The gels were then sensitised in sodium thiosulphate (0.005% w/v, 50 mL) for 1 hour.

This solution was removed and the gels were incubated in silver nitrate solution (0.1%, w/v, 50 mL) for 1 hour. The solution was removed and the gels were washed in water and incubated in developer (0.036% w/v formaldehyde, 2% w/v sodium carbonate, 50 mL) for 2 minutes. After, stop solution was added (50 mM EDTA, 50 mL) and the gel was incubated for 1 hour.

The bands were readily visualised using white light and photographed with a standard digital camera.

3.3.7 HPLC of Extracted Peptide Monolayers

Extracted peptide monolayers were dissolved in 100 μL of propan-2-ol. HPLC was performed by injection of 10 μL of each sample on a 30 x 2 mm C_5 column (Phenomenex) with 5 μm particle size and pore size of 100 Å. Ethanol/ water (75/25 v/v) and propan-2-ol were used as mobile phases, both with 0.1% TFA. A linear gradient of 0-50% propan-2-ol over 40 minutes and a flow rate of 0.5 mL min^{-1} were used. The absorption of the eluent at a wavelength of 254 nm was monitored throughout.

3.3.8 Neutron and X-ray Reflection of SP-B_{1-25} and SMB Monolayers, and Mixed Peptide/Phospholipid Monolayers at the Air-Water Interface

Monolayers of the peptide or peptide/phospholipid mixture were formed at the air-water interface on a Langmuir trough inside an environmental chamber. For some experiments the trough was warmed to 37^{o}C. Throughout the reflectivity experiments the trough area was held constant and the surface pressure was monitored continuously. The reflectivity of the interface was measured under oxygen alone prior to ozone being switched on.

3.3.9 Neutron Reflectivity Experiments

Neutron reflectivity experiments of monolayers of SMB alone, SP-B_{1-25} alone and mixed monolayers of SMB and DPPC were performed on the FIGARO

reflectometer at the Insitut Laue Langevin, Grenoble, France.[149] Neutron reflectivity of mixed monolayers of SMB and DPPG, SMB and POPG and monolayers of POPG alone were performed on the SURF reflectometer at ISIS, Rutherford Appleton Laboratory, Didcot, UK.[170]

In all experiments the neutrons entered and exited the environmental chamber *via* fused quartz windows. For experiments at FIGARO, which were performed above room temperature, the windows were heated to prevent the condensation of water vapour. The reflection of visible laser light was used to regularly check the height alignment of the interface with respect to the neutron beam.

The incident beam contained neutrons with a range of wavelengths, λ. On FIGARO the range was from $2.2 \leq \lambda \leq 25$ Å, and on SURF the range was $0.5 \leq \lambda \leq 6.5$ Å. The neutron beam was collimated and inclined to fall at a grazing angle of incidence to the horizontal of the air-liquid interface depending on the instrument. On FIGARO the angles were 0.624^{o} and 3.78^{o} to the horizontal and on SURF the angle was 1.5^{o} to the horizontal. The reflected neutrons were detected and processed to give neutron reflectivity data as a function of momentum transfer normal to the interface, *q*, as described in Chapter 2.

The reflectivity of a monolayer was measured for varying time lengths during the experiment to give reflectivity curves at regular timepoints. The time length of acquisition was dependent on the instrument, the angle of incidence and the monolayer/subphase, i.e. a deuterated sample or D_2O subphase would have greater signal so data would be acquired for a shorter length of time than a non-deuterated sample.

In general, for experiments on FIGARO with peptide-only on D_2O subphase, 8 minutes at 0.624^{o} and 25 minutes at 3.78^{o} of reflected neutrons were detected for analysis, alternating each angle during the experiment. For peptide-only on NRW experiments on FIGARO, neutron reflectivity was measured for 8 minutes at 0.624^{o} and 30 minutes at 3.78^{o}. For peptide/ ^{1}H DPPC on D_2O experiments on FIGARO, neutron reflectivity data was acquired for 8 minutes at 0.624^{o} and 40 minutes at 3.68^{o}. In peptide/ d_{62}-DPPC on NRW experiments on FIGARO, reflectivity was measured for 6 minutes at 0.624^{o} and 10 minutes at 3.68^{o}. At each timepoint, the reflectivity curves for both angles were stitched together after

normalisation. During peptide/deuterated phospholipid on NRW experiments on SURF, neutron data was collected for 5 minutes at 1.5°. For d_{31}-POPG monolayers on NRW, 5 minutes of neutron data were collected for each timepoint.

The measured reflectivity of a sample of pure D_2O contained in the Langmuir trough was used to obtain a scale factor with which to normalise for the intensity spectrum of the incident beam.

3.3.10 Neutron Reflectivity Data Fitting

The reflectivity as a function of q was modelled, assuming a single uniform layer between two semi-infinite media. The reflectivity data was fitted using the separate fitting procedures, *mono*[171] *drydoc*[172] and *motofit*.[173] These fitting programs use a least-squares fitting process to compare modelled reflectivity data as a function of q, calculated according to Abeles optical matrix method[174] with each experimental data set measured in a time sequence.

The model *mono* was designed to allow kinetics of changes in interfacial layer to be followed. The simple model uses the area per molecule at the interface and the thickness as fittable parameters. For the reflectivity curve at each timepoint, the thickness, area per molecule, background and surface roughness were fitted using the least-squares procedure. This program has advantages as it assumes that the contrast from the single interfacial layer arises solely from the adsorbate molecules described by scattering length, area per molecule and thickness without significant mixing with the adjacent bulk phases, except as described by the interfacial roughness at each boundary. This is useful as the area per molecule and thickness of the monolayers are of primary interest in the study of reactions at the interface, so obtaining the statistical uncertainty on this quantity is beneficial.

This model requires prior knowledge of the system as the scattering length density of the aqueous subphase, air and scattering length of the molecules are defined and held constant during the fit. The coherent neutron scattering lengths, b, and scattering length densities, ρ, (calculated using Equation 2.4) for the

molecules used in this study are shown in Table 3.3. Values are shown for each molecule when present on H_2O, D_2O or null reflecting water (NRW) subphase. This is to take into consideration deuterium-hydrogen exchange between the subphase and any exchangeable hydrogens within the molecule. Exchangeable hydrogens are hydrogen atoms that can readily be replaced with deuteriums, such as those in N-H groups, for example the amides on protein backbones. When on D_2O subphase, it is assumed that all exchangeable hydrogens are deuteriums, and on NRW approximately 8% of hydrogens have exchanged. However, the actual extent of the deuteration of the exchangeable hydrogens is unknown as some will exchange more rapidly than others. Therefore, the actual values for *b* could be lower than those quoted on NRW and D_2O.

Calculation of the scattering length density, *ρ,* required a value of the volume of the molecule of interest. The peptide volumes were taken from the calculations of Fisher *et al.*[175], which estimates the protein specific volume from its molecular weight using an exponential function. This gave volumes of 3178 Å^3 for a molecule of SP-$B_{1\text{-}25}$ and 5270 Å^3 for a molecule of SMB. These volumes are only estimates as the actual volume of the peptide at the interface would not be known as the volume is dependent on the conformation of the peptide, which would change with area per molecule at the interface. The volumes for the phospholipids were taken from Armen *et al.,*[176] which used molecular dynamics simulations to calculate the volumes of fragments of the phospholipids. This gave a DPPC volume of 1262 Å^3, a DPPG volume of 1218 Å^3 and a POPG volume of 1257 Å^3. However, these volumes represent a value for the lipid in a bilayer, therefore at small area per lipid. The values for scattering length density, *ρ,* in Table 3.3 might be acceptable for monolayers of the lipid at very small areas per lipid (small trough area), but as the area per lipid increases the values for *ρ* would significantly change. These values of scattering length density are not used in the fitting of the neutron reflectivity curves, but are useful for illustrating the effect of deuteration on the scattering length density of molecules, and the differences in scattering length density between the subphase, monolayer and air.

Compound	Formula (assuming maximum exchange)	Subphase	b / fm	ρ / 10^{-6} Å^{-2}	Volume / Å^3
SP-B_{1-25}	$C_{139}N_{35}O_{28}S_3H_{223}$	H_2O	588	1.85	3178
	$C_{139}N_{35}O_{28}S_3H_{177}D_{47}$	D_2O	1067	3.36	
	$C_{139}N_{35}O_{28}S_3H_{219}D_4$	NRW	629	1.98	
SMB	$C_{217}N_{61}O_{46}S_6H_{363}$	H_2O	938	1.78	5270
	$C_{217}N_{61}O_{46}S_6H_{284}D_{79}$	D_2O	1762	3.35	
	$C_{217}N_{61}O_{46}S_6H_{357}D_6$	NRW	1002	1.9	
^{1}H-DPPC	$C_{40}H_{80}NO_8P$	All	27	0.21	1262
d_{62}DPPC	$C_{40}H_{18}D_{62}NO_8P$	All	673	5.4	1262
d_{31}POPG	$C_{40}H_{46}O_{10}PD_{31}$	H_2O	356	2.95	1257
d_{62}DPPG	$C_{38}H_{13}O_{10}PD_{62}$	H_2O	684	5.49	1218

Table 3.3. The formulae, coherent neutron scattering lengths and scattering length densities of the peptides and lipids used in this work.

The scattering length of some species can vary depending on the subphase if exchangeable hydrogens are present on the molecules. Only NRW and D_2O were used as subphases in neutron reflectivity experiments but values for H_2O are shown for comparison.

The programs *drydoc* and *motofit* are similar to *mono,* except that the scattering length density of the interface is fitted rather than area per molecule. This requires only prior knowledge of the scattering length density of the air and aqueous subphase in order to fit the thickness and scattering length density of the layer at the interface. These programs can therefore be beneficial when the scattering length of the molecules in the layer is not known, therefore the area per molecule cannot be accurately calculated using *mono*. Additionally, if the scattering length of the molecule changes significantly during reaction (e.g. loss of deuterated material from the interface) *drydoc* or *motofit* can be useful in determining the extent of loss of material.

An interfacial roughness is an additional feature of the reflectivity curve that arises from surface irregularities. Roughness leads to a reduction in measured

reflectivity, an effect that is increasingly more pronounced with increasing momentum transfer, q. This reduction in intensity is fitted along with surface coverage and thickness. Roughness in these programs is calculated according to the method of L. Nevot and P. Croce.[177] This uses an approximation that is valid for values of the roughness that are small compared to the thickness of the adjacent layer.

The neutron reflectivity background is present due to the incoherent neutron scattering component of nuclei. Hydrogen has a particularly high incoherent scattering length, therefore experiments performed when the subphase contained relatively more H_2O than D_2O gave a high background signal.

In these neutron experiments, all peptide-only reflectivity data was fitted using *mono*, *motofit* and *drydoc*. The mixed peptide/phospholipid films were fitted using *motofit* and *drydoc*. Multiple programs were used to ensure that suitable parameters were fitted. To ensure similar appropriate values were fitted, area per molecule and thickness values from *mono* were converted to scattering length density using:

$$\rho_t = \frac{b}{A_m \times \delta} \qquad (3.1)$$

where ρ_t is the scattering length density at the interface from the reflectivity curve at time t, b is the scattering length of the molecules in the layer, A_m is the area per molecule determined using *mono* and δ is the monolayer thickness as determined using *mono*. If the values for scattering length density and thickness were the same (within error) using each fitting procedure, the fitted parameters were deemed suitable.

Following this, the relative amount of material at the interface at time t was calculated using:

$$Relative\ amount\ of\ material\ at\ the\ interface = \frac{\delta_t \rho_t}{\delta_t \rho_0} \qquad (3.2)$$

where δ_t is the thickness at time t, ρ_t is the scattering length density at time t, both

obtained from fitting the neutron reflectivity curve at time *t*. δ_0 is the thickness at time 0, ρ_0 is the scattering length density at time 0, both obtained from fitting the neutron reflectivity curve at time 0 (the neutron reflectivity curve of the initial film).

When a decrease in $\delta_t\rho_t$ was observed during reaction with ozone, the decrease *versus* time was fitted to a single exponential decay function

$$\frac{(SLD \times thickness)_t}{(SLD \times thickness)_0} = Ae^{-t/\tau} + B \qquad (3.3)$$

where τ is the lifetime of the lipid, A is a constant, and B represents the fraction of monolayer material left at the interface when t = infinity, also referred to as the y-offset.

3.3.11 X-ray Reflectivity Experiments

All X-ray reflectivity experiments were performed on the I07 beamline at Diamond Light Source, Harwell Science and Innovation Campus, Didcot, UK.[178] The X-rays had a wavelength, λ, of 1.0 Å (12.4 KeV) and entered the chamber *via* a mica window and exited the chamber *via* a Kapton window. The incident X-ray beam on I07 can be deflected to fall at a range of angles of incidence to the air-liquid interface, allowing the reflectivity to be measured as a function of q. In this work the reflectivity was recorded between values of q of 0.015 $Å^{-1}$, below the critical edge where total reflection occurs, and 0.8 $Å^{-1}$.

A fast shutter was used to block the X-ray beam from hitting the sample at all times except when reflectivity measurements were being carried out. Also, the beam footprint was regularly moved by 1 mm between runs to change the region of monolayer that is being measured during the experiment. Both of these procedures prevented X-ray beam damage to the sample as tested by observing a monolayer under oxygen alone for several hours, where no drop in reflectivity was seen when the above procedure was followed.

The reflectivity at each timepoint was generally measured for 5 minutes

and the height alignment of the interface with respect to the X-ray beam was checked after every 3 runs and realigned if necessary.

The X-ray reflectivity is dependent on the X-ray scattering length density of the material at the interface, ρ, and the thickness of the material, δ. The X-ray scattering length density is:

$$\rho = \frac{\sum Z\, r_e}{V} \qquad (3.4)$$

where Z is the atomic number of the individual nuclei in the compound, r_e is the classical radius of an electron (2.817940 x 10^{-15} m) and V is the volume occupied by one molecule. The volumes used for SP-$B_{1\text{-}25}$ and SMB were the same as those detailed in section 3.3.10. The X-ray scattering lengths, b, and scattering length densities, ρ, for the peptides in this study are shown in Table 3.4.

Molecule	Formula	$\sum Zr_e$ / fm	ρ / 10^{-6} Å^{-2}
SP-$B_{1\text{-}25}$	$C_{139}N_{35}O_{28}S_3H_{223}$	4435	8.4
SMB	$C_{217}N_{61}O_{46}S_6H_{363}$	7293	13.8

Table 3.4. The X-ray scattering lengths and scattering length densities of the peptides SP-$B_{1\text{-}25}$ and SMB.

As described in section 3.3.10, the volumes of the peptide molecules are likely to change as the trough area increases and therefore area per molecule increases and the conformation of the molecule will change. The X-ray scattering length density of water is 9.40 x 10^{-6} Å^{-2} therefore the scattering length density of the monolayers at the air-water interface will be sensitive to the area per molecule.

The fitting programs *motofit* and *drydoc* were used to obtain values for

thickness, δ, X-ray scattering length density of the material at the interface, ρ, and background, as described in section 3.3.10. A roughness of 3 Å was used to optimise fitting of these parameters. The relative amount of material at the interface was calculated as described in Equation 3.2.

3.4. Results: Oxidation of Monolayers of SP-B Peptide Mimics by Gas-Phase Ozone at the Air-Water Interface

Monolayers of two synthetic forms of SP-B; SP-B_{1-25} and super mini B (SMB), at the air-water interface were exposed to the gas-phase oxidant ozone and the structural and chemical changes of the peptides were examined using surface pressure measurements, neutron and X-ray reflectivity experiments, HPLC, SDS-PAGE and fluorescence microscopy. Following this, oxidation of mixed monolayers of peptides and the phospholipids DPPC, DPPG and POPG by ozone at the air-water interface was examined using surface pressure measurements and neutron reflectivity experiments, in order to determine whether oxidation of the peptides affects the phospholipids, and if the interactions between the peptide and the phospholipids are affected after oxidation.

3.4.1 Surface Pressure of Monolayers of SP-B_{1-25} and SMB Exposed to Gas-Phase Ozone at the Air-Water Interface

The surface pressure of monolayers of SP-B_{1-25} and SMB at the air-water interface was measured during exposure to ozone in order to determine if there was any change in the surface properties of the films, suggesting the peptides are oxidised by ozone. Initially the peptide monolayers were exposed to oxygen only as a control to ensure the monolayers were not affected by oxygen gas at the air-water interface.

The exposure of a monolayer of SP-B_{1-25} or SMB on phosphate buffered water revealed no significant change in surface pressure over time when exposed to pure oxygen for 7 hours, as shown in Figure 3.7. A small drop in the surface pressure is often observed in all Langmuir trough/Wilhelmy plate experiments, which can be attributed to a slow loss of material at the trough barriers, as described by Hardy *et al.*[179]

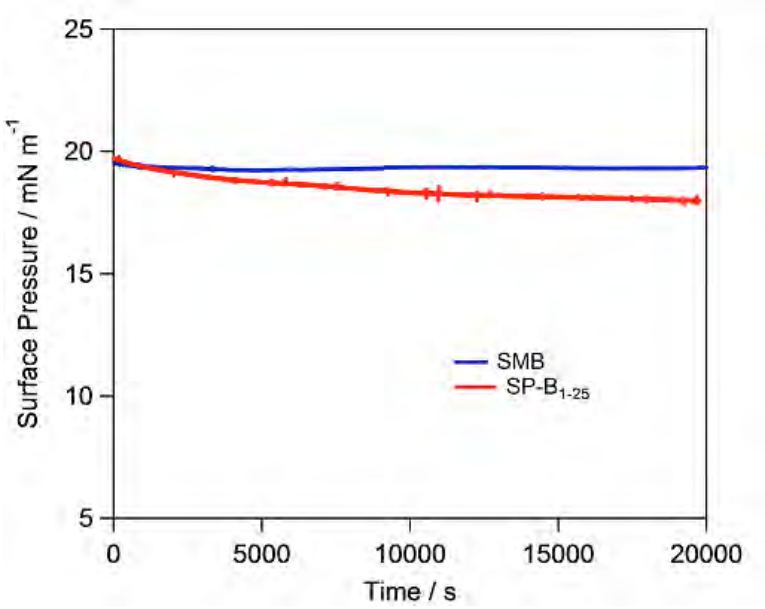

Figure 3.7. The surface pressure *versus* time of a monolayer of SP-B$_{1-25}$ (red) or SMB (blue) on buffered water exposed to oxygen only for 7 hours.

Data was recorded at 37^{o}C

When monolayers of SP-B $_{1-25}$ or SMB on an aqueous subphase at 37 ^{o}C were exposed to ozone at 2 ppm there was a rapid reaction, indicated by a rapid, sharp drop in surface pressure, corresponding to a rise in surface tension, for both peptides. Figure 3.8 shows that a drop occurs from approximately 20 mN m^{-1} to 15 mN m^{-1} over 10 minutes when both peptide monolayers were exposed to ozone. The drop is slightly more significant upon exposure to SMB compared to SP-B$_{1-25}$. This rapid drop is followed by a much slower decrease in surface pressure over several hours.

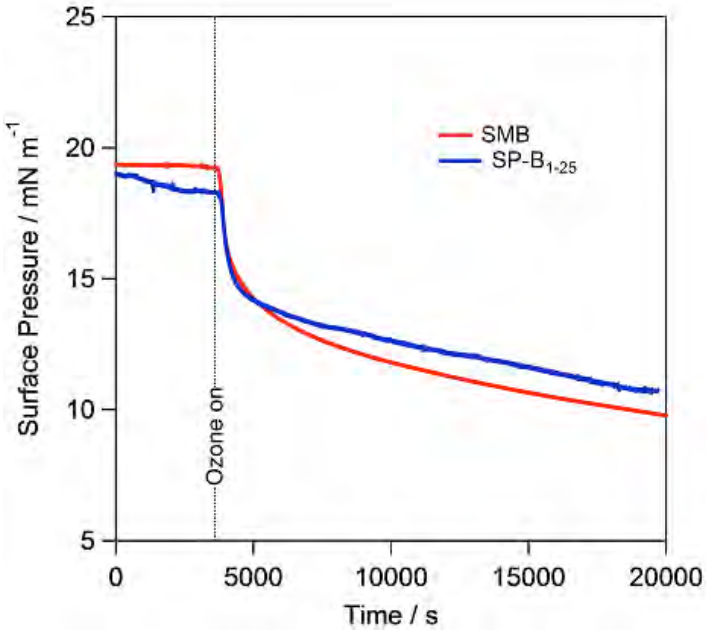

Figure 3.8. The surface pressure *versus* time of a monolayer of SP-$B_{1\text{-}25}$ (blue) or SMB (red) on buffered water exposed to 2 ppm ozone for 4 hours.

Data was recorded at 37 °C. The time at which ozone was switched on is indicated by the dotted vertical line at ~4000 s.

Figure 3.8 suggests that an oxidation reaction is occurring between the peptides and ozone at the air-water interface. Since the reaction occurs at the interface, few techniques are available to look at structural changes during the reaction, as methods such as NMR and MS cannot easily be used. To investigate this further, some experiments were done to looks at changes to the properties of the molecules within the monolayer. Fluorescence microscopy of peptide monolayers during ozone exposure was used to investigate whether the tryptophan residues are damaged by ozone exposure. Furthermore, HPLC was performed in order to determine how the hydrophobicity of the peptides changes after exposure to ozone and SDS-PAGE was utilised to investigate whether any fragmentation of the peptides occurs.

3.4.2 Fluorescence Microscopy of Monolayers of SMB during Ozone Exposure at the Air-Water Interface

A monolayer of SMB on water was excited using two-photon absorption at 566 nm (thus exciting at 283 nm). This wavelength excited the tryptophan residues and the fluorescence was detected between 310-380 nm. Fluorescence of the tryptophan residues within the SMB monolayer was measured before and after 5 and 10 minutes of dilute ozone exposure (2 ppm). The fluorescence image taken prior to exposure is shown in Figure 3.9. After 5 minutes of ozone the fluorescence of the monolayer has significantly decreased as shown in the second image in Figure 3.9. No fluorescence was detected at all after 10 minutes of ozone. This suggests that all of the tryptophan residues had reacted to form a residue that does not fluoresce at 310-380 nm after only 10 minutes of ozone exposure at 2 ppm. This loss in fluorescence was not observed when fluorescence microscopy of a SMB monolayer was performed before and after 10 minutes of exposure to an oxygen-only atmosphere, therefore it is not an artefact of photobleaching.

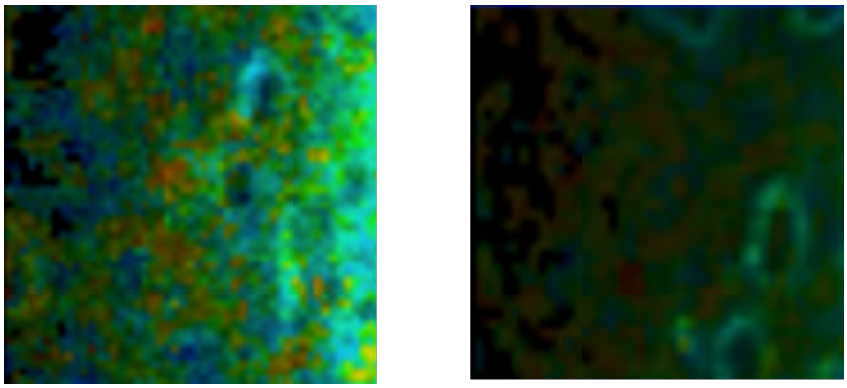

Figure 3.9. Fluorescence microscopy image of tryptophan residues within a monolayer of SMB at the air-water interface before ozone exposure (left) and after 5 minutes of ozone exposure (right).

Tryptophan was excited by two-photon absorption at 566 nm (leading to excitation at 283 nm) and fluorescence was detected from 310-380 nm. The brightness of the pixels in the images indicates the amount of fluorescence detected, therefore in the right-hand image there is significantly less fluorescence from the tryptophan residues.

3.4.3 Sodium Dodecyl Sulphate-Polyacrylamide Gel Electrophoresis (SDS-PAGE) of SP-B_{1-25} and SMB

SDS-PAGE of both SP-B_{1-25} and SMB was performed directly from the stock solutions in chloroform/methanol (i.e. prior to any monolayer formation). The solvent was removed from the peptides and electrophoresis was run both in normal sample buffer and in reducing conditions (sample buffer with DTT). The resulting protein gel is shown in Figure 3.10. It is evident that the peptides are both in a monomer and oligomer form. SMB is mainly dimer and monomer, whereas SP-B_{1-25} is mainly in the monomer and pentamer form, with some other further oligomers. After reduction by DTT, only the monomer was present in the case of both peptides.

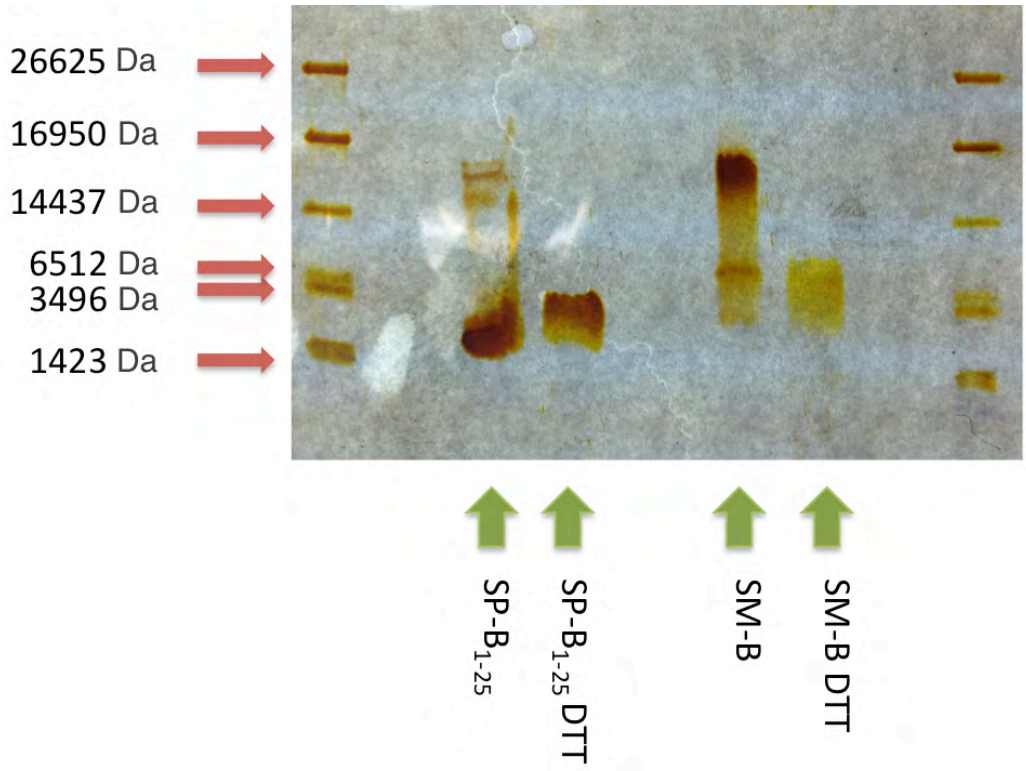

Figure 3.10. The SDS-PAGE gel of (from left to right) molecular weight ladder, SP-B_{1-25}, SP-B_{1-25} after treatment with DTT, SMB, SMB after treatment with DTT and molecular weight ladder.

The molecular weights of the species in the ladder are indicated on the left and the samples in each lane are indicated below. The gel has been stained using a silver staining procedure.

To see whether possible fragmentation or changes in oligomer state of the protein occurred after reaction with ozone, monolayers of SP-B_{1-25} were collected before any ozone exposure, after 10 minutes of ozone and after 60 minutes of ozone exposure at the air-water interface. SDS-PAGE was performed on the extracted monolayers, as shown in Figure 3.11.

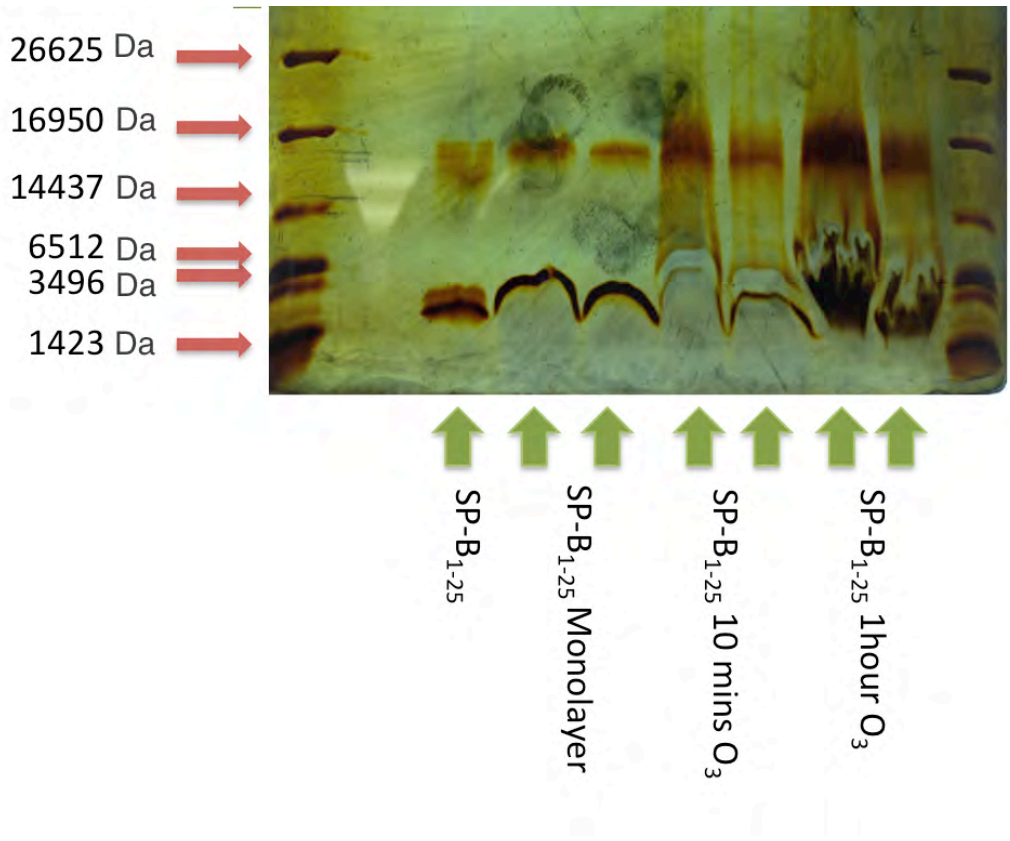

Figure 3.11. The SDS-PAGE gel of SP-B_{1-25}, a collected monolayer of SP-B_{1-25} with no ozone exposure, a collected monolayer of SP-B_{1-25} after 10 minutes of ozone exposure and a collected monolayer of SP-B_{1-25} after 60 minutes of ozone exposure.

The molecular weights of the species in the ladder are indicated on the left and the samples in each lane are indicated below. Each of the extracted monolayer samples was run in two adjacent lanes. Gels were stained using a silver staining procedure.

The gel of the SP-B_{1-25} monolayer before any ozone exposure shows the same bands for the monomer and oligomer as the bands obtained when the peptide was analysed without first spreading and recovering from a monolayer, therefore showing that the peptide prior to ozone can successfully be collected from the subphase. Both the monolayers exposed to 10 minutes of ozone and to 60 minutes of ozone show no noticeable change in the molecular weight of the bands and in both cases the oligomers are present as well as monomer. From oxidation of

the reactive amino acids, the peptides would only vary in mass by addition of between 16 Da and ~144 Da, therefore less than 5 % change, so a visible change in the mass of the bands would not be expected.

Reaction with ozone could lead to formation of other ROS, such as ·OH, which could then react further with the peptide, possibly cleaving the chain to give smaller fragments. There are no bands formed at smaller molecular weight after ozone, suggesting that smaller fragments of the peptide are not present in the monolayers after these timescales, therefore ozonolysis has not led to cleavage of the peptide chain. However, it does seem that with increasing ozone exposure, the band for the oligomer becomes more pronounced. This could either be due to more oligomer being formed in the reaction, or more likely that oxidation causes a change in the hydrophobicity of the protein, altering its interaction with SDS. This means that less of the monomer could be dissolving in the sample buffer after oxidation. Oligomerisation could have occurred from disulphide bond formation between the cysteine residues of different SP-$B_{1\text{-}25}$ molecules.

3.4.4 HPLC of SP-$B_{1\text{-}25}$ and SMB Monolayers Before and After Exposure to Ozone at the Air-Water Interface

Monolayers of SP-$B_{1\text{-}25}$ were spread at the air water interface, exposed to ozone for 0, 10 and 60 minutes and then collected and extracted into chloroform. Reverse-phase HPLC of the collected monolayers was performed using isocratic elution on a C_5 hydrophobic column and the chromatograms are shown in Figure 3.12. The peaks have been normalised to the intensity of the SP-$B_{1\text{-}25}$ peak in order to compare the peak heights. Normalisation was necessary as the recovery of the monolayers varied significantly between samples. This is probably due to the small concentration of peptide to be recovered from the large subphase volume (~6 μg of peptide on 50 mL of subphase) and also possibly due to the solubility of the peptide in chloroform changing after oxidation by ozone. Furthermore, an internal standard could not be used to measure the actual recovery efficiency as an additional compound in the monolayer solution could effect the spreading and ordering of the peptide at the interface, therefore compromising the way in which it will react with ozone.

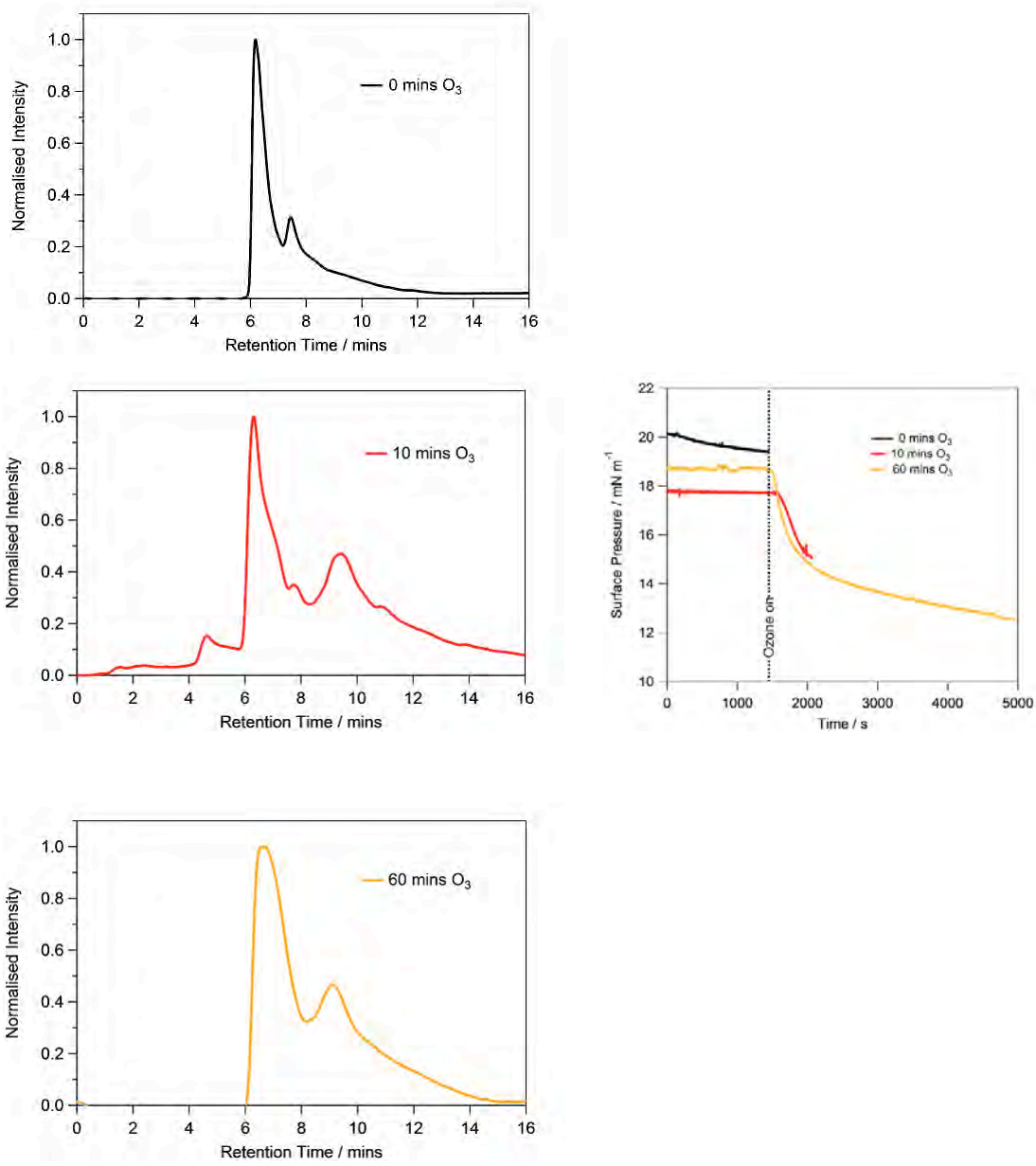

Figure 3.12. HPLC of extracted monolayers of SP-$B_{1\text{-}25}$ before ozone and after 10 and 60 minutes of ozone.

The panels on the left show chromatograms of material extracted into chloroform for monolayers on an aqueous subphase of SP-$B_{1\text{-}25}$ (top), SP-$B_{1\text{-}25}$ after exposure to ozone for 10 mins (middle) and SP-$B_{1\text{-}25}$ after exposure to ozone for 60 mins (bottom). All peaks have been background subtracted and normalised to the absorption, at 254 nm, of the SP-$B_{1\text{-}25}$ peak at ~6.5 mins. The panel on the right shows the data for surface pressure *versus* time for the monolayer immediately before extraction with chloroform with no ozone (black line) after 10 minutes exposure to ozone (red line) and 60 minutes exposure to ozone (orange line).

Figure 3.12 shows that oxidation of SP-B_{1-25} by ozone at the air-water interface leads to changes in the HPLC profile of the peptides after collection from the interface. The SP-B_{1-25} peak at approximately 6.5 minutes is present in all the chromatograms, but after ozone exposure additional peaks at longer retention times are present in the chromatograms. A peak at around 9 minutes appears in the chromatogram of the peptide monolayer exposed to ten minutes of ozone and is present in the chromatogram of the peptide monolayer exposed to sixty minutes of ozone at the same relative intensity. This additional peak after exposure to ozone, not present in the unreacted monolayer, suggests that a product is formed in the reaction between SP-B_{1-25} and ozone that is more hydrophobic than the starting peptide since it is eluted more slowly under the reverse-phase chromatographic conditions employed.

HPLC of extracted SMB monolayers was also performed. Monolayers of SMB were spread at the air water interface, exposed to ozone for 0, 10 and 60 minutes and then collected and extracted into chloroform. The chromatograms of these samples run on a reverse phase HPLC column are shown in Figure 3.13. The SMB peak is present in all chromatograms. After ten minutes of ozone exposure there is also a small peak at a retention time of 10 minutes, which increases relative to the size of the SMB peak by sixty minutes of ozone exposure. These additional peaks are implying that a reaction product is formed slowly and, as it is eluted more slowly than SMB under the reverse-phase chromatographic conditions employed, this slow forming product must be more hydrophobic than the starting material SMB. It should be noted that no products that are more hydrophilic than the starting material for both SP-B_{1-25} and SMB were detected using this collection method and analysis.

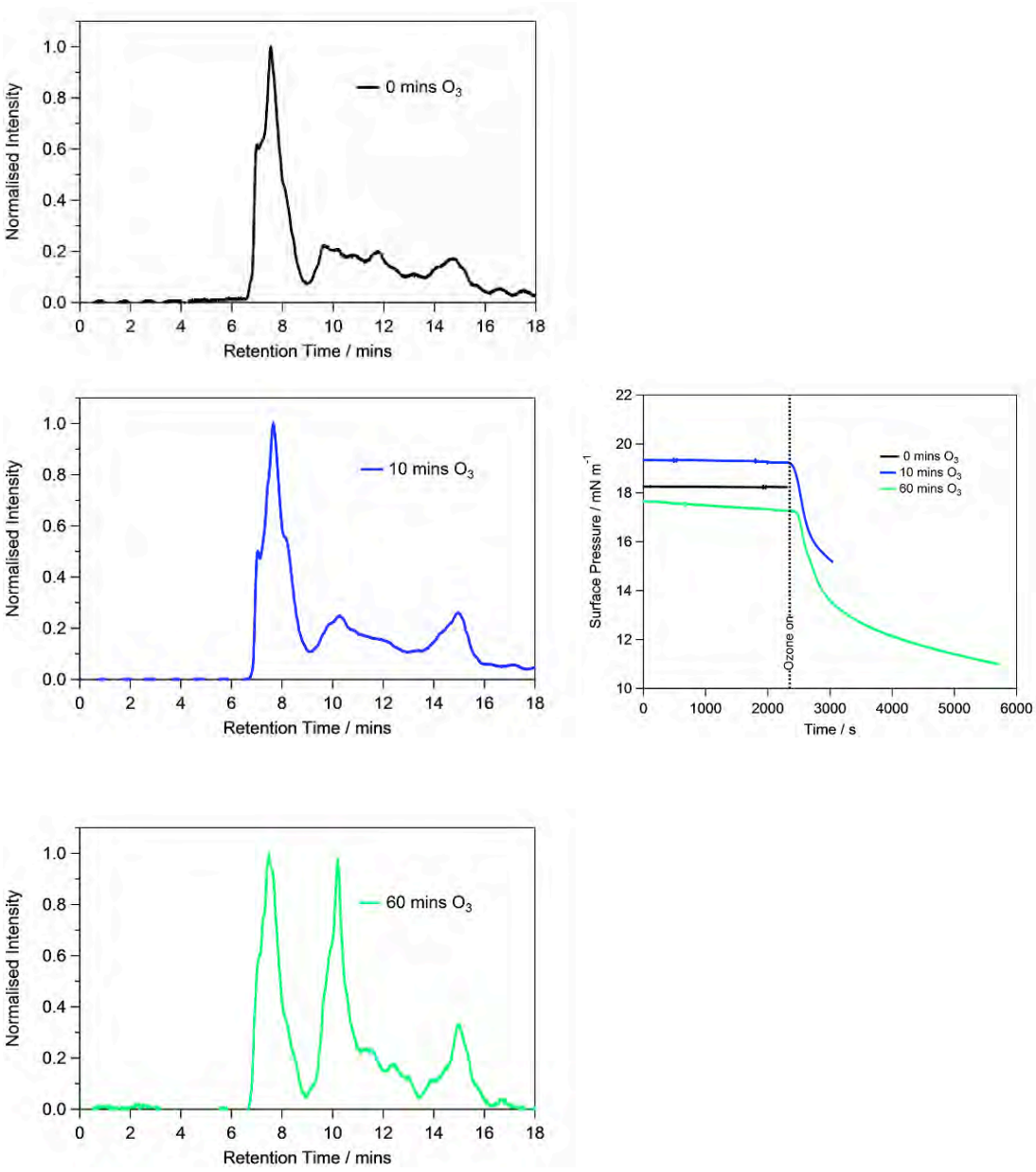

Figure 3.13. HPLC of extracted monolayers of SMB before ozone and after 10 and 60 minutes of ozone.

The panels on the left show chromatograms of material extracted into chloroform for monolayers on an aqueous subphase of SMB (top), SMB after exposure to ozone for 10 mins (middle) and SMB after exposure to ozone for 60 mins (bottom). All peaks have been background subtracted and normalised to the absorption, at 254 nm, of the SMB peak at ~7.5 mins. The panel on the right shows the data for surface pressure *versus* time for the monolayer immediately before extraction with chloroform with no ozone (black line) after 10 minutes exposure to ozone (blue line) and 60 minutes exposure to ozone (green line).

3.5 Results: Neutron and X-ray Reflectivity of SP-B_{1-25} and SMB at the Air-Water Interface

Surface pressure measurements of monolayers of SP-B_{1-25} and SMB and fluorescence microscopy of monolayers of SMB indicated that the peptides react with ozone gas at the air-water interface. HPLC experiments revealed changes in the hydrophobicity of both peptide monolayers after oxidation by ozone. Neutron and X-ray reflectivity was employed to elucidate any changes in the area per molecule and thickness of the surface peptide films during oxidation and the results are presented in this section.

3.5.1 Neutron and X-ray Reflectivity of Monolayers of SP-B_{1-25} at the Air-Water Interface

Monolayers of SP-B_{1-25} on a Langmuir trough were monitored using neutron reflectivity during exposure to ozone in order to elucidate any changes in the area per molecule and thickness of the surface film during oxidation. The neutron reflectivity of the peptide on D_2O buffer was recorded as well as the reflectivity on NRW buffer, due to the relatively weak reflectivity of the non-deuterated peptides on NRW buffer. Furthermore, X-ray reflectivity of monolayers of SP-B_{1-25} was measured before and after ozone. As explained in Chapter 2, X-rays can measure to higher q more accurately than neutrons due to significantly lower backgrounds. The thickness of the film can therefore be more accurately measured using X-rays as the fringe spacing feature indicating the monolayer thickness will extend to higher q in the case of thin monolayers.

As a control, the neutron reflectivity of monolayers of the peptide on buffered NRW was measured for several hours under a flow of oxygen gas at 37^{o}C. The neutron reflectivity curves were fitted to determine values of the surface scattering length density and thickness at each timepoint, while background and surface roughness were held constant. The roughness was held at 3 Å for the fitting

of each curve. The relative amount of material at the interface was calculated from these fitted values at each timepoint and is presented in Figure 3.14. Also, the X-ray reflectivity of a monolayer of SP-$B_{1\text{-}25}$ at the air-water interface was measured continuously for 10 hours under a flow of oxygen at 37^{o}C. The reflectivity, and therefore amount of material at the interface did not change over this time, as shown in Figure 3.14. It is clear that the monolayer is stable at the interface under a flow of oxygen for a significant length of time, as demonstrated by both neutron and X-ray reflectivity. Furthermore, the peptide sample is not damaged by the X-ray beam under these time scales.

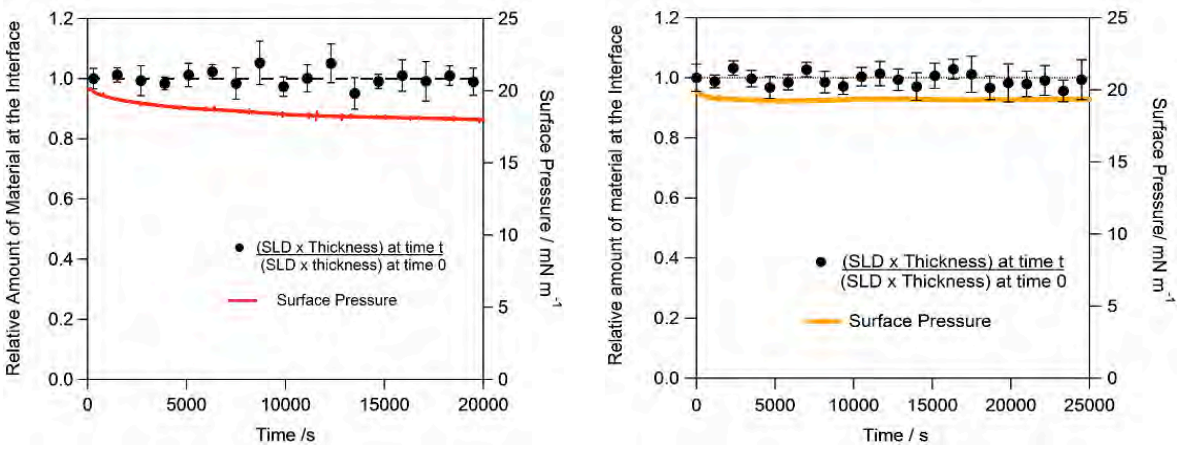

Figure 3.14. The surface pressure and relative amount of material at the interface of a monolayer of SP-$B_{1\text{-}25}$ exposed to oxygen only: neutron (left) and X-ray (right) reflectivity data.

Left panel: The surface pressure *versus* time (red line) for a monolayer of SP-$B_{1\text{-}25}$ on buffered NRW exposed to oxygen gas for 6 hours. The markers represent the relative amount of material at the interface, calculated from the fitted neutron scattering length density (ρ_t) multiplied by the thickness (δ_t) of the monolayer at time t divided by the fitted neutron scattering length density (ρ_0) multiplied by the thickness (δ_0) at time 0. The dashed line represents a constant amount of material at the interface.
Right panel: The surface pressure *versus* time (orange line) for a monolayer of SP-$B_{1\text{-}25}$ on buffered water exposed to oxygen gas for 9 hours. The markers represent the relative amount of material at the interface, calculated from the fitted X-ray scattering length density (ρ_t) multiplied by the thickness (δ_t) of the monolayer at time t divided by the fitted X-ray scattering length density (ρ_0) multiplied by the thickness (δ_0) at time 0. The dashed line represents a constant amount of material at the interface.

The reaction between SP-$B_{1\text{-}25}$ monolayers on buffered NRW and gaseous ozone (2 ppm) at 37°C was then studied at the air-water interface. Figure 3.15 shows the neutron reflectivity of a SP-$B_{1\text{-}25}$ monolayer before and after exposure to ozone. There is no discernible change in reflectivity after 3 hours of exposure. Also presented in Figure 3.15 is the relative amount of peptide at the interface *versus* time, calculated from the individual neutron reflectivity curves at each timepoint (as described above), along with surface pressure data. There is no measurable change in the relative amount of material at the interface *versus* time upon

exposure to ozone when measuring the neutron reflectivity on NRW. Since only the peptide would be responsible for the neutron reflectivity at the interface, as the NRW would not reflect neutrons, the constant reflectivity shows that the peptide is remaining at the interface during reaction with ozone.

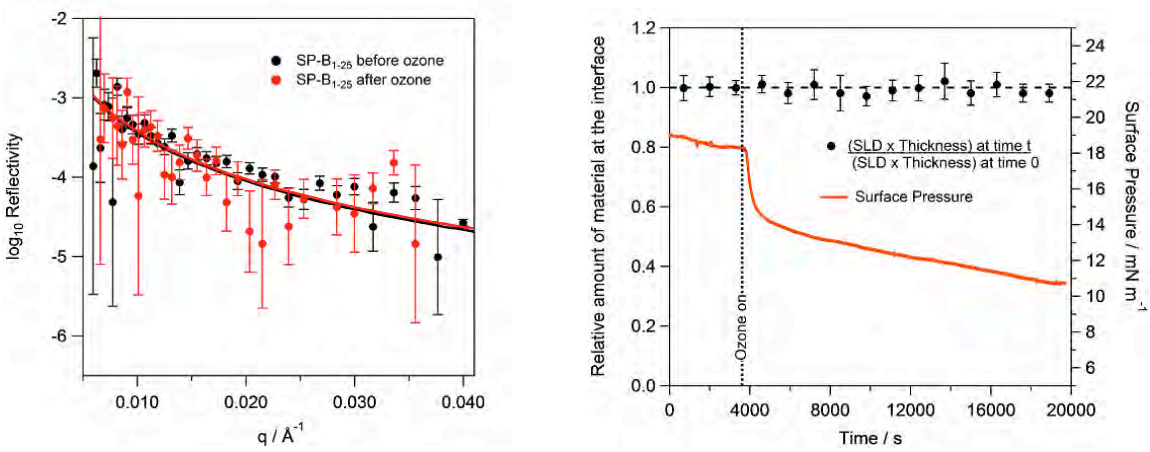

Figure 3.15. Neutron Reflectivity at the air-water interface of a monolayer of SP-B$_{1\text{-}25}$ on NRW during exposure to ozone.

Left panel: The neutron reflectivity curves of a monolayer of SP-B$_{1\text{-}25}$ on buffered NRW before ozone (black) and a monolayer of SP-B$_{1\text{-}25}$ on buffered NRW after ozone (red). The measured data is represented by the round markers and the best fit of the curves is shown by the solid lines. The fits were calculated by varying the thickness and scattering length density of the monolayer at each timepoint, whilst keeping surface roughness and background constant.
Right panel: The surface pressure *versus* time (red line) for a monolayer of SP-B$_{1\text{-}25}$ on buffered NRW exposed to 2 ppm ozone gas for 4.5 hours. The dotted line represents the time at which the ozoniser was switched on. Black markers represent the relative amount of material at the interface, calculated from the fitted neutron scattering length density (ρ_t) multiplied by the thickness (δ_t) of the monolayer at time t divided by the fitted neutron scattering length density (ρ_0) multiplied by the thickness (δ_0) at time 0. The dashed horizontal line represents a constant amount of material at the interface.

Monolayers of SP-B$_{1\text{-}25}$ on a buffered D_2O subphase were also exposed to ozone and neutron reflectivity of the films was measured. Experiments on NRW revealed that all of the peptide remained at the interface during reaction with ozone, however this does not give an indication of whether the position of the

peptide at the interface changes. Experiments on D_2O would show changes in the disruption of the D_2O surface by the peptide, and if this changed significantly upon oxidation, for example if the peptide would become considerably more hydrophilic it could be more hydrated, increasing the contribution of D_2O to the reflectivity.

The exposure of monolayers of SP-$B_{1\text{-}25}$ on D_2O to ozone caused negligible change in neutron reflectivity over time as shown in Figure 3.16. The neutron reflectivity curves were fitted to determine values of the surface scattering length density and thickness at each timepoint, while background and surface roughness were held constant. The roughness was held at 3 Å for the fitting of each curve. The relative amount of peptide material at the interface was calculated for each reflectivity curve at each timepoint and is also presented in Figure 3.16 along with the surface pressure of the monolayer *versus* time. There is no significant change in the scattering length density at the surface or thickness of the film after exposure to ozone for 60 minutes, even after the rapid drop in surface pressure, therefore oxidation of the peptide by ozone does not lead to changes in its hydration at the surface.

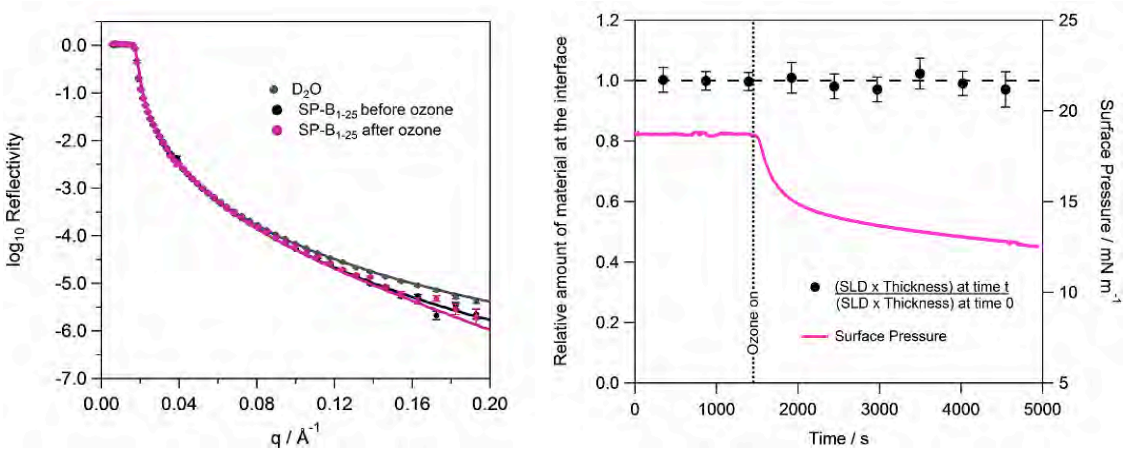

Figure 3.16. Neutron Reflectivity at the air-water interface of a monolayer of SP-B_{1-25} on D_2O during exposure to ozone.

Left panel: The neutron reflectivity curves of a monolayer of SP-B_{1-25} on buffered D_2O before ozone (black) a monolayer of SP-B_{1-25} on buffered D_2O after ozone (pink), as well as the neutron reflectivity curve for buffered D_2O only (grey). The measured data is represented by the round markers and the best fit of the curves is shown by the solid lines. The fits were calculated by varying the thickness and scattering length density of the monolayer at each timepoint, whilst keeping surface roughness and background constant.
Right panel: The surface pressure *versus* time (pink line) for a monolayer of SP-B_{1-25} on buffered D_2O exposed to 2 ppm ozone gas for 1 hour. The dotted line represents the time at which the ozoniser was switched on. Black markers represent the relative amount of material at the interface, calculated from the fitted neutron scattering length density (ρ_t) multiplied by the thickness (δ_t) of the monolayer at time t divided by the fitted neutron scattering length density (ρ_0) multiplied by the thickness (δ_0) at time 0. The dashed horizontal line represents a constant amount of material at the interface.

Neutron reflectivity experiments indicated that there was no change in the reflectivity of SP-B_{1-25} monolayers upon exposure to ozone. However, it is possible that the neutron reflectivity curves of SP-B_{1-25} before and after ozone (Figures 3.15 and 3.16) could differ at higher *q*. Therefore, to investigate to higher *q,* X-ray reflectivity of monolayers of this peptide was performed.

Figure 3.17 shows the X-ray reflectivity of a monolayer of SP-B_{1-25} before ozone and after 5 hours of exposure to ozone. There is no discernible change in

reflectivity, even at high q, after exposure. The X-ray reflectivity curves were fitted to determine values of the surface scattering length density and thickness at each timepoint, while background and surface roughness were held constant. The roughness was held at 3 Å for the fitting of each curve. The relative amount of material at the interface *versus* time is also presented in Figure 3.17. This also indicates that there is little significant change over time, therefore the protein remains at the interface following reaction with ozone. Furthermore, there was no detectable change in the thickness of the SP-$B_{1\text{-}25}$ monolayer during exposure to ozone as shown in Figure 3.18, demonstrating that any changes in the conformation of the peptide at the interface following oxidation do not lead to a significant change in the thickness of the surface film.

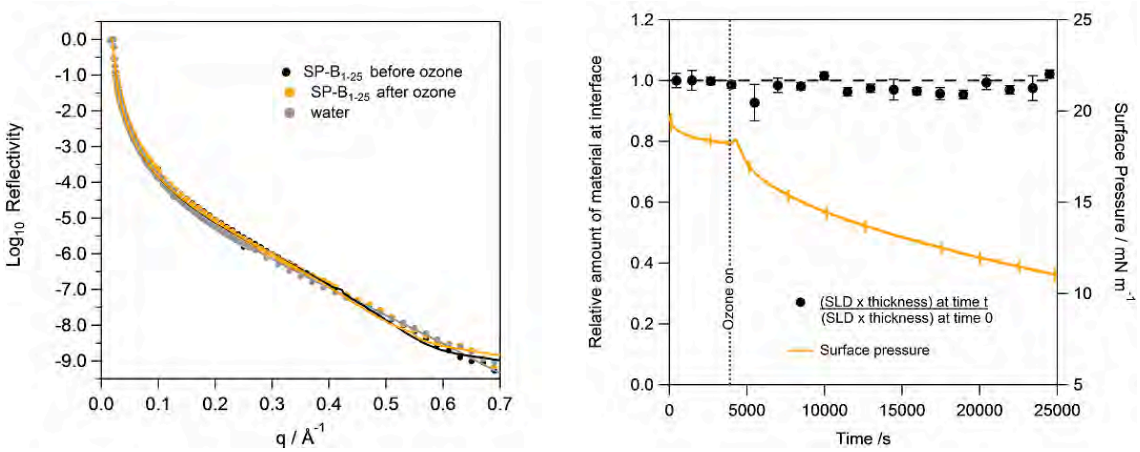

Figure 3.17. X-ray Reflectivity at the air-water interface of a monolayer of SP-B$_{1\text{-}25}$ on water during exposure to ozone.

Left panel: The X-ray reflectivity curves of a monolayer of SP-B$_{1\text{-}25}$ on buffered water before ozone (black) a monolayer of SP-B$_{1\text{-}25}$ on buffered water after ozone (orange), as well as the X-ray reflectivity curve for buffered water only (grey). The measured data is represented by the round markers and the best fit of the curves is shown by the solid lines. The fits were calculated by varying the thickness and scattering length density of the monolayer at each timepoint, whilst keeping surface roughness and background constant.

Right panel: The surface pressure *versus* time (orange line) for a monolayer of SP-B$_{1\text{-}25}$ on buffered water exposed to 2 ppm ozone gas for 5 hours. The spikes in the surface pressure data are an artefact caused by small trough movements between runs. The dotted line represents the time at which the ozoniser was switched on. Black markers represent the relative amount of material at the interface, calculated from the fitted X-ray scattering length density (ρ_t) multiplied by the thickness (δ_t) of the monolayer at time t divided by the fitted X-ray scattering length density (ρ_0) multiplied by the thickness (δ_0) at time 0. The dashed horizontal line represents a constant amount of material at the interface.

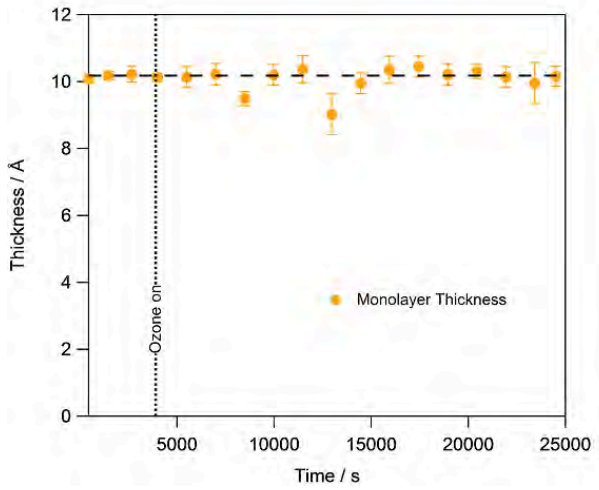

Figure 3.18. The thickness of a SP-B_{1-25} monolayer during exposure to ozone at the air-water interface as determined using X-ray reflectivity.

The thickness *versus* time (orange markers) for a monolayer of SP-B_{1-25} on buffered water exposed to 2 ppm ozone gas for 5 hours at an initial surface pressure of 18 mN m^{-1}. The dotted line represents the time at which the ozoniser was switched on. Thickness was calculated from fitting the X-ray reflectivity curve at each timepoint.

3.5.2 Neutron and X-ray Reflectivity of Monolayers of SMB at the Air-Water Interface

In addition to studies on SP-B_{1-25}, neutron and X-ray reflectivity experiments were also performed on the larger form of synthetic peptide, SMB. As a control, monolayers of SMB were exposed to oxygen only and monitored using both neutron and X-ray reflectivity at the air-water interface. Figure 3.19 shows that there was no change in the neutron or X-ray reflectivity, and therefore amount of SMB at the interface, after over 7 hours of exposure to oxygen. Hence the peptide monolayer is stable under oxygen for significant lengths of time and there is no damage by the X-ray beam in these timescales.

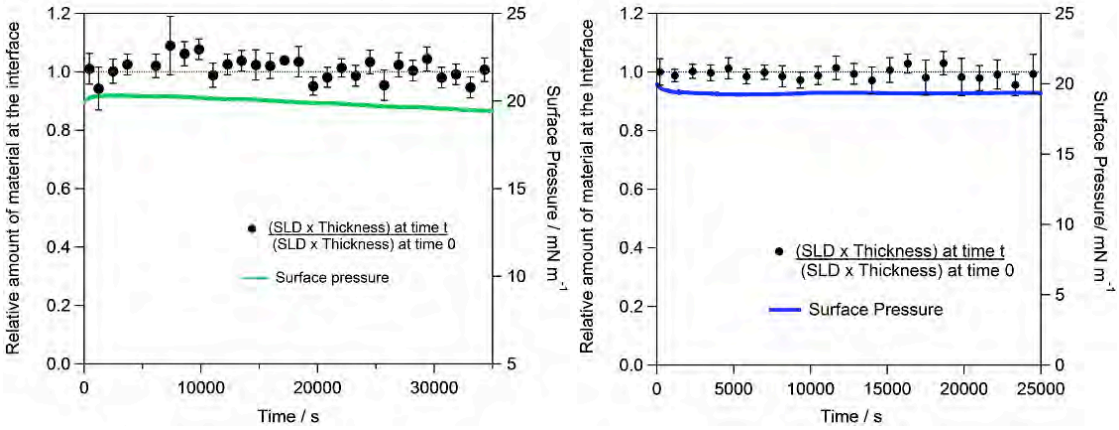

Figure 3.19. The surface pressure and relative amount of material at the interface of a monolayer of SMB exposed to oxygen only: neutron (left) and X-ray (right) reflectivity data.

Left panel: The surface pressure *versus* time (green line) for a monolayer of SMB on buffered NRW exposed to oxygen gas for 9 hours. The markers represent the relative amount of material at the interface, calculated from the fitted neutron scattering length density (ρ_t) multiplied by the thickness (δ_t) of the monolayer at time t divided by the fitted neutron scattering length density (ρ_0) multiplied by the thickness (δ_0) at time 0. The dashed line represents a constant amount of material at the interface.

Right panel: The surface pressure *versus* time (blue line) for a monolayer of SMB on buffered water exposed to oxygen gas for 7 hours. The markers represent the relative amount of material at the interface, calculated from the fitted X-ray scattering length density (ρ_t) multiplied by the thickness (δ_t) of the monolayer at time t divided by the fitted X-ray scattering length density (ρ_0) multiplied by the thickness (δ_0) at time 0. The dashed line represents a constant amount of material at the interface.

Figure 3.20 shows the neutron reflectivity of a monolayer of SMB on NRW before ozone and after exposure to ozone for 8 hours. The neutron reflectivity curves were fitted to determine values of the surface scattering length density and thickness at each timepoint, while background and surface roughness were held constant. The roughness was held at 3 Å for the fitting of each curve. Also presented is the amount of material at the interface *versus* time, and again there is

no discernable change in the reflectivity during ozone exposure using this contrast, and all of the oxidised peptide remains at the air-water interface.

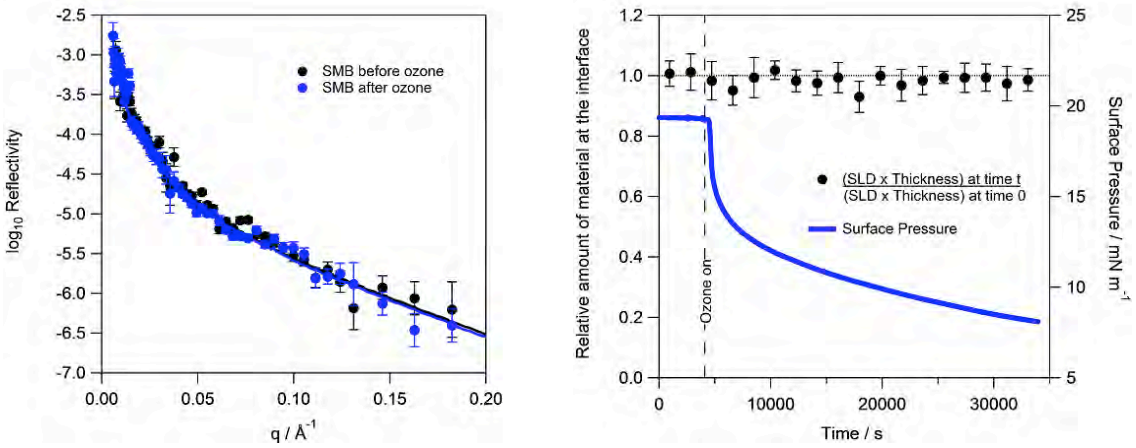

Figure 3.20. Neutron Reflectivity at the air-water interface of a monolayer of SMB on NRW during exposure to ozone.

Left panel: The neutron reflectivity curves of a monolayer of SMB on buffered NRW before ozone (black) a monolayer of SMB on buffered NRW after ozone (blue). The measured data is represented by the round markers and the best fit of the curves is shown by the solid lines. The fits were calculated by varying the thickness and scattering length density of the monolayer at each timepoint, whilst keeping surface roughness and background constant.
Right panel: The surface pressure *versus* time (blue line) for a monolayer of SMB on buffered NRW exposed to 2 ppm ozone gas for 8 hours. The dotted line represents the time at which the ozoniser was switched on. Black markers represent the relative amount of material at the interface, calculated from the fitted neutron scattering length density (ρ_t) multiplied by the thickness (δ_t) of the monolayer at time t divided by the fitted neutron scattering length density (ρ_0) multiplied by the thickness (δ_0) at time 0. The dashed horizontal line represents a constant amount of material at the interface.

In order to determine whether the hydration of the SMB would change after oxidation, a monolayer of SMB on buffered D_2O was exposed to ozone for 1 hour. The neutron reflectivity of the monolayer before and after ozone exposure is shown in Figure 3.21. The amount of protein at the interface, calculated from the reflectivity curves (in the same way as described above), along with the surface

pressure *versus* time is also shown in Figure 3.21. There is no change in the neutron reflectivity of the interface, suggesting that oxidation of the peptide by ozone does not lead to measureable changes in its hydration at the surface.

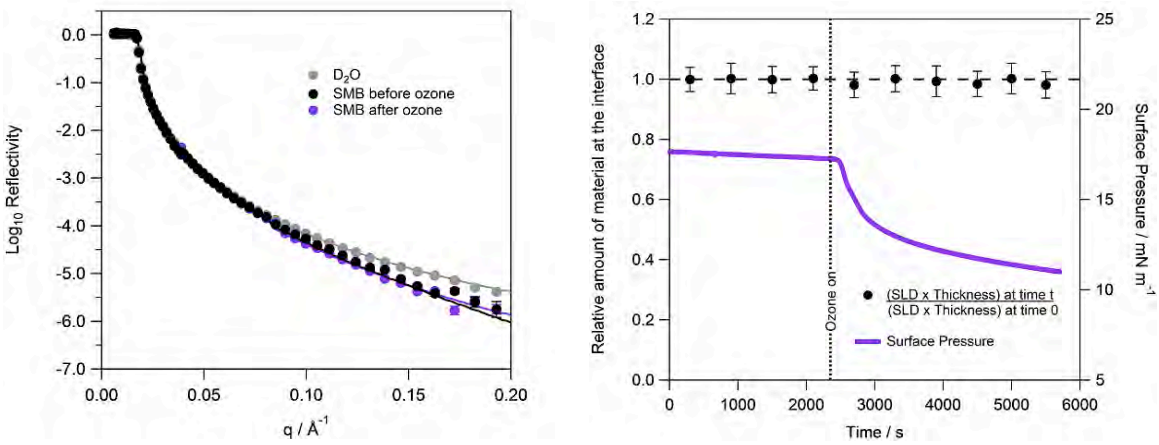

Figure 3.21. Neutron Reflectivity at the air-water interface of a monolayer of SMB on D_2O during exposure to ozone.

Left panel: The neutron reflectivity curves of a monolayer of SMB on buffered D_2O before ozone (black), a monolayer of SMB on buffered D_2O after ozone (purple), as well as the neutron reflectivity curve for buffered D_2O only (grey). The measured data is represented by the round markers and the best fit of the curves is shown by the solid lines. The fits were calculated by varying the thickness and scattering length density of the monolayer at each timepoint, whilst keeping surface roughness and background constant.
Right panel: The surface pressure *versus* time (purple line) for a monolayer of SMB on buffered D_2O exposed to 2 ppm ozone gas for 1 hour. The dotted line represents the time at which the ozoniser was switched on. Black markers represent the relative amount of material at the interface, calculated from the fitted neutron scattering length density (ρ_t) multiplied by the thickness (δ_t) of the monolayer at time t, divided by the fitted neutron scattering length density (ρ_0) multiplied by the thickness (δ_0) at time 0. The dashed horizontal line represents a constant amount of material at the interface.

X-ray reflection of SMB at the air-water interface was also measured to determine any changes in the thickness and spread of the SMB monolayers during exposure to ozone. The X-ray reflectivity of a monolayer before and after ozone

and the amount of material at the interface *versus* time are both shown in Figure 3.22. The curves indicate that there is no significant change in reflectivity after ozone, therefore the protein remains at the interface following reaction with ozone. Furthermore, the thickness *versus* time shown in Figure 3.23 shows that there is no change in the monolayer thickness during ozone exposure.

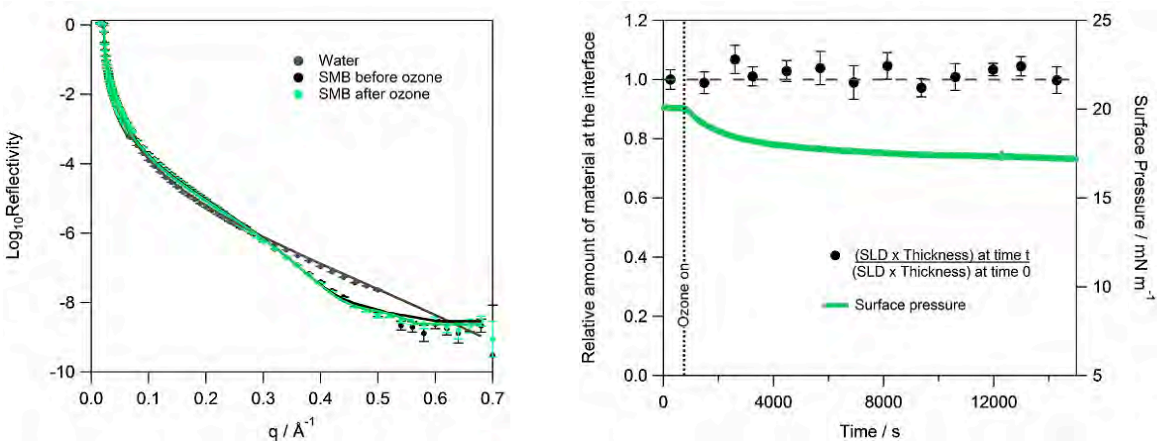

Figure 3.22. X-ray Reflectivity at the air-water interface of a monolayer of SMB on water during exposure to ozone.

Left panel: The X-ray reflectivity curves of a monolayer of SMB on buffered water before ozone (black), a monolayer of SMB on buffered water after ozone (green), as well as the X-ray reflectivity curve for buffered water only (grey). The measured data is represented by the round markers and the best fit of the curves is shown by the solid lines. The fits were calculated by varying the thickness and scattering length density of the monolayer at each timepoint, whilst keeping surface roughness and background constant.
Right panel: The surface pressure *versus* time (green line) for a monolayer of SMB on buffered water exposed to 2 ppm ozone gas for 4 hours. The dotted line represents the time at which the ozoniser was switched on. Black markers represent the relative amount of material at the interface, calculated from the fitted X-ray scattering length density (ρ_t) multiplied by the thickness (δ_t) of the monolayer at time t divided by the fitted X-ray scattering length density (ρ_0) multiplied by the thickness (δ_0) at time 0. The dashed horizontal line represents a constant amount of material at the interface.

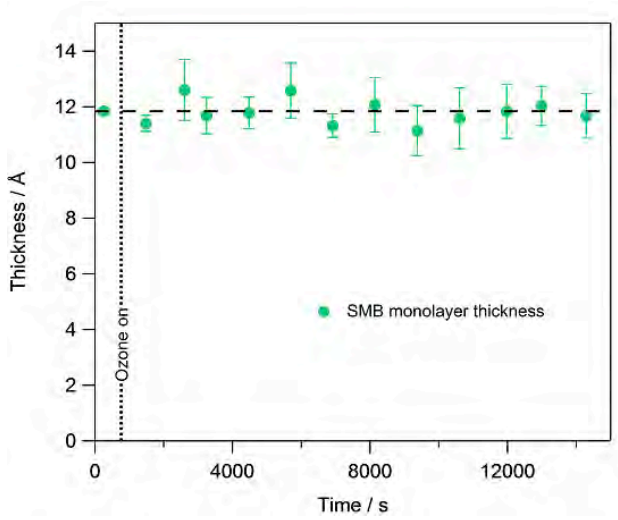

Figure 3.23. The thickness of a SMB monolayer during exposure to ozone at the air-water interface as determined using X-ray reflectivity.

The thickness *versus* time (green markers) for a monolayer of SMB on buffered water exposed to 2 ppm ozone gas for 5 hours. The dotted line represents the time at which the ozoniser was switched on. The dashed line represents a constant thickness. Thickness was calculated from fitting the X-ray reflectivity curve at each timepoint.

3.6 Results: Neutron Reflectivity and Surface Pressure Measurements of Mixed Monolayers of Peptide and Phospholipids at the Air-Water Interface

Sections 3.4 and 3.5 showed that both SP-B peptide mimics, SP-$B_{1\text{-}25}$ and SMB react with ozone at the air-water to form a film of lower surface pressure but both peptides remain at the interface, with no measurable change in the thickness or spread of the films.

SP-B exists in the lung surfactant embedded in a monolayer of surfactant phospholipids. In order to determine how a lipid monolayer is affected by oxidation of the SP-B peptide mimics, or how oxidation of the peptides is affected by the presence of lipids, surface pressure and neutron reflectivity experiments

were performed to establish any changes in the structure and viability of mixed films.

3.6.1 Neutron Reflectivity and Surface Pressure Measurements of Mixed Monolayers of Peptide and the Zwitterionic Phospholipid DPPC at the Air-Water Interface

DPPC is the most abundant component of the lung surfactant, comprising approximately 50% by weight of all components within the monolayer.[7] It has been shown previously by Thompson *et al.* that the phospholipid itself does not react with ozone at the air-water interface.[136] Experiments on mixed monolayers of peptide and DPPC were performed in order to test if the presence of DPPC affected the oxidation of the SP-B_{1-25} and SMB by ozone at the air-water interface, or if the oxidation of the peptides causes damage to nearby lipids, for example if secondary ROS are formed in the reaction.

Mixed monolayers of SP-B_{1-25} and DPPC (1:6, mol/mol) and SMB and DPPC (1:6, mol/mol) were exposed to 2 ppm ozone at the air-water interface and the surface pressure was measured throughout. Figure 3.24 shows that there is a rapid drop in surface pressure upon exposure to ozone, however in both cases the extent of the decrease in much less than for a monolayer of the peptides alone. This is consistent with only the peptides being oxidised within the mixed monolayers.

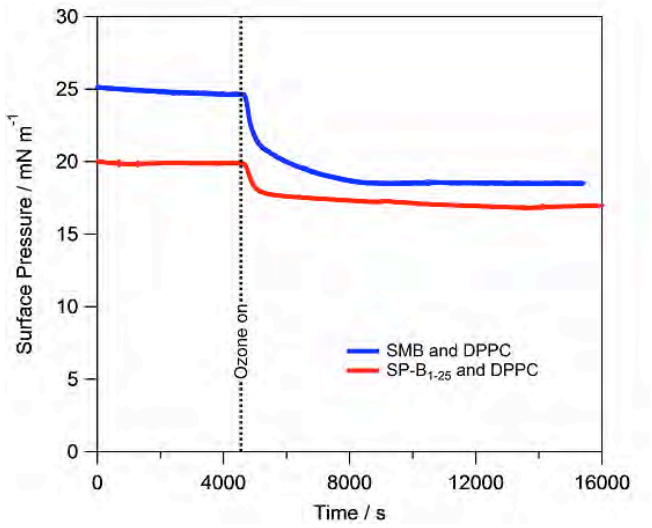

Figure 3.24. The surface pressure *versus* time of a monolayer of SP-$B_{1\text{-}25}$ and DPPC (1:6, mol/mol, blue) or SMB and DPPC (1:6, mol/mol, red) on buffered water exposed to 2 ppm ozone for 3 hours.

Data was recorded at 37 °C. The time at which ozone was switched on is indicated by the dotted vertical line at ~4500 s.

Neutron reflectivity experiments were performed on mixed monolayers of SMB and DPPC at the air-water interface. A mixed monolayer of 1:6 (mol/mol) SMB and ^{1}H DPPC on buffered NRW was exposed to ozone and the neutron reflectivity was measured at regular timepoints. The neutron reflectivity of this monolayer before and after ozone exposure is shown in Figure 3.25. Since the ^{1}H DPPC has a very low scattering length, neutrons are insensitive to the presence of the lipid in the monolayer, therefore most of the reflected neutrons would be as a result of the peptide (SMB has a scattering length of 1002 fm whereas ^{1}H DPPC has a scattering length of 27 fm). The approximate contribution of SMB to the overall scattering length density of the mixed monolayer can be calculated using the scattering lengths and estimated molecular volumes given in Table 3.3, and by using Equation 3.5:

$$\%SLD_{SMB} = 100 \times \frac{SLD_{SMB}}{SLD_{Mix}} \qquad (3.5)$$

where SLD_{SMB} is the scattering length density of the SMB within the mixed monolayer and can be calculated using:

$$SLD_{SMB} = \frac{b_{SMB}}{V_{SMB} + n.V_{lipid}} \qquad (3.6)$$

where b_{SMB} is the scattering length of SMB, V_{SMB} is the molecular volume of SMB, n is the number of lipid molecules for each SMB molecule and V_{lipid} is the molecular volume of the lipid. SLD_{Mix} is the total approximate scattering length density of the mixed monolayer and can be calculated using:

$$SLD_{Mix} = \frac{b_{SMB}+nb_{lipid}}{V_{SMB}+nV_{lipid}} \qquad (3.7)$$

where b_{lipid} is the scattering length of the lipid in the monolayer. Using these equations, the approximate contribution of SMB to the total scattering length density of a mixed monolayer of 1:6 (mol/mol) SMB and ^{1}H DPPC on buffered NRW is 86 %. The neutron reflectivity curves were fitted to determine values of the surface scattering length density and thickness at each timepoint, while background and surface roughness were held constant. The roughness was held at 4 Å for the fitting of each curve. The scattering length density multiplied by monolayer thickness *versus* time is also presented in Figure 3.25. There is no change in neutron reflectivity over time, signifying that all of the peptide material remains at the interface after SMB reacting with ozone.

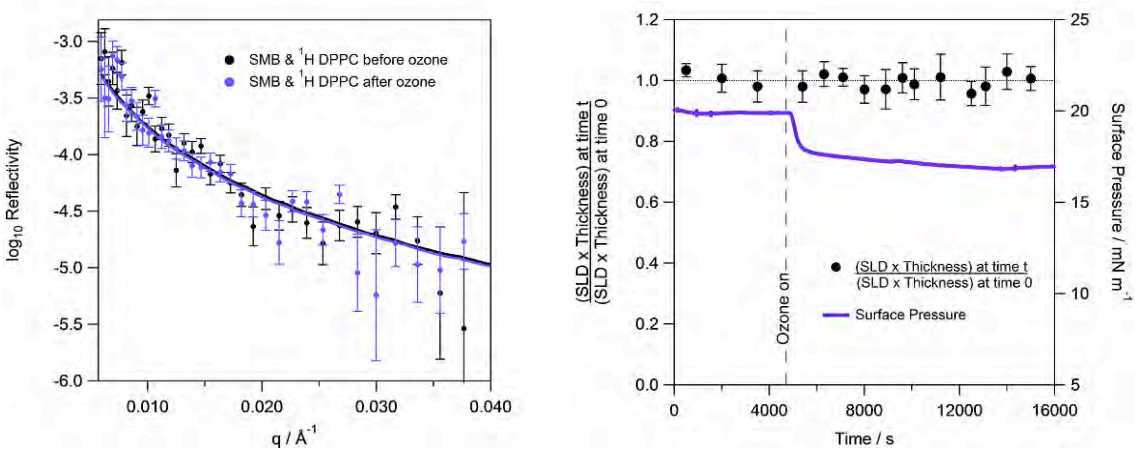

Figure 3.25. Neutron Reflectivity at the air-water interface of a monolayer of SMB and ^{1}H DPPC (1:6, mol/mol) on NRW during exposure to ozone.

Left panel: The neutron reflectivity curves of a monolayer of SMB and ^{1}H DPPC (1:6, mol/mol) on buffered NRW before ozone (black) and a monolayer of SMB and ^{1}H DPPC (1:6, mol/mol) on buffered NRW after ozone (purple). The measured data is represented by the round markers and the best fit of the curves is shown by the solid lines. The fits were calculated by varying the thickness and scattering length density of the monolayer at each timepoint, whilst keeping surface roughness and background constant.
Right panel: The surface pressure *versus* time (purple line) for a monolayer of SMB and ^{1}H DPPC (1:6, mol/mol) on buffered NRW exposed to 2 ppm ozone gas for 3 hours. The dotted line represents the time at which the ozoniser was switched on. Black markers represent the relative amount of material at the interface, calculated from the fitted neutron scattering length density (ρ_t) multiplied by the thickness (δ_t) of the monolayer at time t divided by the fitted neutron scattering length density (ρ_0) multiplied by the thickness (δ_0) at time 0. The dashed horizontal line represents a constant amount of material at the interface.

Figure 3.26 shows the neutron reflectivity of a monolayer of SMB and deuterated d_{62}-DPPC (1:6, mol/mol) on NRW before and after ozone exposure. The approximate contribution of SMB to the overall scattering length density of this monolayer on NRW, calculated using Equations 3.5-3.7, is 20 %. Therefore the deuterated phospholipid would be the main contributor the neutron reflectivity. There is no change in the neutron reflectivity after ozone exposure, and the scattering length density or thickness at the interface does not change over time, as

shown in Figure 3.26, suggesting that all of the lipid material remains at the interface during oxidation of the peptide by ozone.

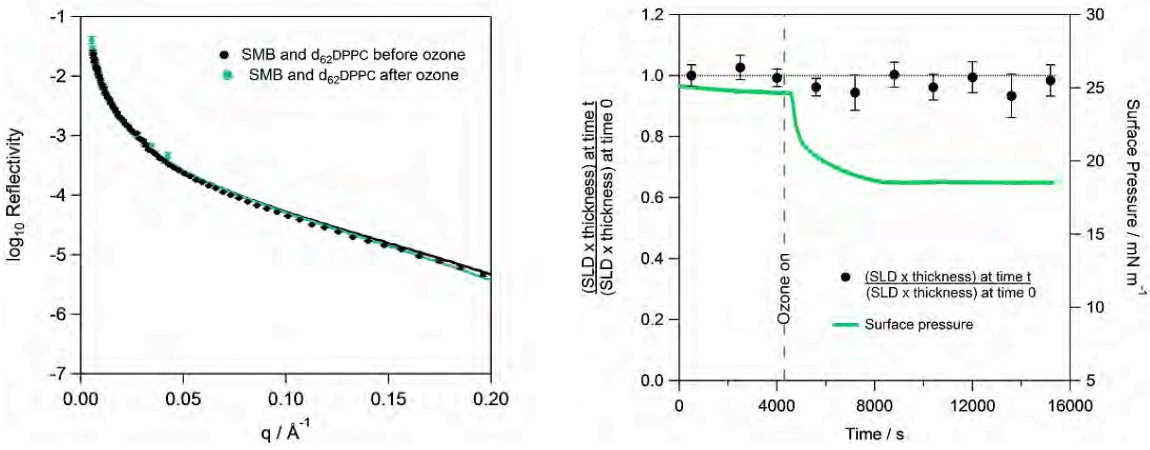

Figure 3.26. Neutron Reflectivity at the air-water interface of a monolayer of SMB and d_{62} DPPC on NRW during exposure to ozone.

Left panel: The neutron reflectivity curves of a monolayer of SMB and d_{62} DPPC on buffered NRW before ozone (black) and a monolayer of SMB and d_{62} DPPC on buffered NRW after ozone (green). The measured data is represented by the round markers and the best fit of the curves is shown by the solid lines. The fits were calculated by varying the thickness and scattering length density of the monolayer at each timepoint, whilst keeping surface roughness and background constant.
Right panel: The surface pressure *versus* time (green line) for a monolayer of SMB and d_{62} DPPC on buffered NRW exposed to 2 ppm ozone gas for 3 hours. The dotted line represents the time at which the ozoniser was switched on. Black markers represent the relative amount of material at the interface, calculated from the fitted neutron scattering length density (ρ_t) multiplied by the thickness (δ_t) of the monolayer at time t divided by the fitted neutron scattering length density (ρ_0) multiplied by the thickness (δ_0) at time 0. The dotted horizontal line represents a constant amount of material at the interface.

It has been shown in the neutron experiments above that oxidation of SMB in a DPPC monolayer at the air-water interface does not lead to loss of either species at the interface. It is thought that SP-B functions by facilitating the transfer of lipids in the lungs at the interface during compression and expansion cycles.[157] Some experiments were performed in order to examine how the DPPC monolayer

is affected by compression in the presence of, first unoxidised, and then oxidised SMB.

The neutron reflectivity of mixed monolayer of SMB and d_{62}-DPPC (1:6, mol/mol) on buffered NRW, under oxygen only, was measured at a surface pressure of 20 mN m^{-1}. This monolayer was then compressed by reducing the trough area until a surface pressure of 35 mN m^{-1} was reached, and re-expanded to the initial trough area. The surface pressure at this initial trough area following a compression was slightly lower at 17.5 mN m^{-1}. The neutron reflectivity of the monolayer was measured again and the reflectivity before and after this compression is shown in Figure 3.27. There is a small drop in reflectivity after a compression, showing a loss of 8% of deuterated DPPC from the interface. When the same procedure is implemented for a monolayer of only d_{62} DPPC on NRW, a similar reduction in neutron reflectivity is observed after a compression, as shown in Figure 3.28. This corresponds to a 7% decrease in deuterated material from the interface, therefore the loss upon compression of a SMB/DPPC monolayer is the same as a DPPC monolayer alone.

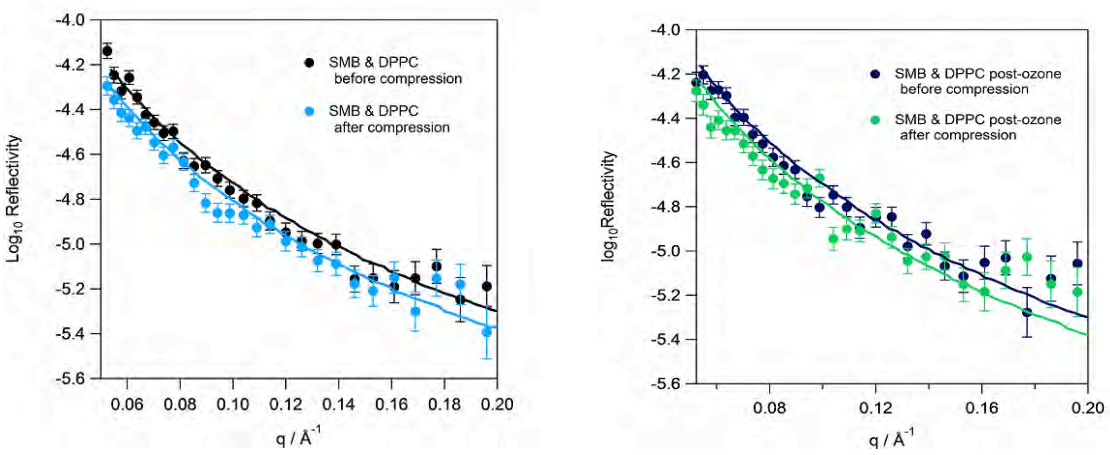

Figure 3.27. The neutron reflectivity curves of a mixed monolayer of SMB and d_{62} DPPC before and after compression to high surface pressures and the neutron reflectivity curves of a mixed monolayer of SMB and d_{62} DPPC after oxidation by ozone before and after compression to high surface pressures.

Left panel: The neutron reflectivity of a mixed monolayer of SMB and d_{62} DPPC (1:6, mol/mol) on NRW before (black) and after (blue) a compression to high surface pressure. The neutron reflectivity curves were measured at the same trough area, under a flow of oxygen gas. The surface pressure before compression was 20 mN m^{-1} and after compression it was 18.5 mN m^{-1}.The measured data is represented by the round markers and the best fit of the curves is shown by the solid lines.

Right Panel: The neutron reflectivity of a mixed monolayer of SMB and d_{62} DPPC (1:6, mol/mol) on NRW after oxidation by 2 ppm ozone for 1 hour before (black) and after (green) a compression to high surface pressure. The neutron reflectivity curves were measured at the same trough area, under a flow of oxygen gas. The surface pressure before compression was 18 mN m^{-1} and after compression it was 16 mN m^{-1}.The measured data is represented by the round markers and the best fit of the curves is shown by the solid lines.

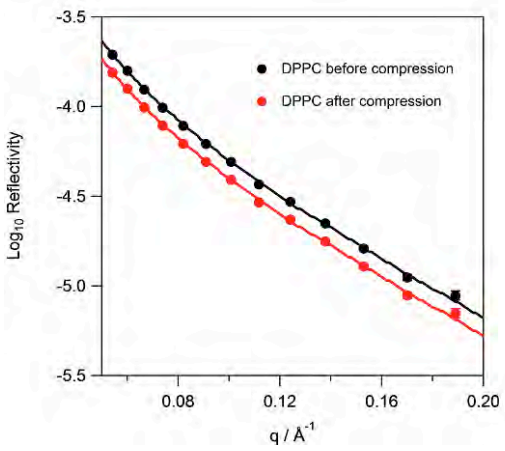

Figure 3.28. The neutron reflectivity curves of a monolayer of d_{62} DPPC before and after compression to high surface pressures.

The neutron reflectivity of a mixed monolayer d_{62} DPPC on NRW before (black) and after (red) a compression to high surface pressure. The neutron reflectivity curves were measured at the same trough area, under a flow of oxygen gas. The surface pressure before compression was 20 mN m^{-1} and after compression it was 18 mN m^{-1}.The measured data is represented by the round markers and the best fit of the curves is shown by the solid lines. This data was collected on FIGARO whereas SMB/d_{62} DPPC data was recorded on SURF.

A different monolayer of SMB and d_{62} DPPC (1:6, mol/mol) was then exposed to 2 ppm ozone for 1 hour, at the same trough area, and the ozone was then switched off. The neutron reflectivity was again measured under a flow of oxygen (at a surface pressure of 18 mN m^{-1}) before compressing the monolayer to 35 mN m^{-1} and re-expanding to the initial trough area. The neutron reflectivity was measured after this compression (at a surface pressure of 16 mN m^{-1}). The neutron reflectivity of the monolayer before and after compression after exposure to ozone is also shown in Figure 3.27. There is a significant decrease in the reflectivity after a compression, showing a loss of approximately 8% of the deuterated lipid material from the interface, but this is the same loss that was observed when the monolayer was compressed and re-expanded before exposure to ozone. The oxidation of the SMB in the presence of the Zwitterionic phospholipid DPPC does not appear to have changed the tendency of the lipid to remain at the interface.

3.6.2 Neutron Reflectivity and Surface Pressure Measurements of Mixed Monolayers of SMB and the Anionic Phosphoglycerols at the Air-Water Interface

SP-B is thought to function by interacting with anionic phospholipids to enhance the respreading of the pulmonary surfactant during exhalation cycles. Monolayers of SMB and phosphoglycerol (PG) mixtures were exposed to ozone and observed using neutron reflectivity coupled with Wilhelmy surface pressure measurements. The respreading and viability of the monolayers were then monitored before and after ozone exposure.

3.6.2.1 Neutron Reflectivity and Surface Pressure Measurements of Mixed Monolayers of SMB and the Anionic Phospholipid POPG at the Air-Water Interface

The anionic, unsaturated phospholipid 1-palmitoyl-2-oleoyl-*sn*-glycero-3-[phospho-rac-(1-glycerol)] (POPG, Figure 1.5) is present in the lung surfactant and thought to interact with SP-B. Similarly to POPC, POPG has been shown to react rapidly and significantly in the presence of ozone as described in detail in Chapter 4.

A mixed monolayer of SMB and POPG (1:12, mol/mol) was formed at the air-water interface and exposed to 2 ppm ozone. The surface pressure was measured continuously and the results are shown in Figure 3.29. It is evident that when ozone is switched on, a rapid reaction is occurring. The surface pressure changes are very different to the reaction between a monolayer of SMB alone and ozone. However, the changes are very similar to the reaction between monolayers of POPG alone and ozone. There is an initial rise in surface pressure by over 10 mN m^{-1} within 10 minutes, followed by a decrease to a value lower than the initial surface pressure. This initial rise in surface pressure was explained previously by Thompson *et al.* to be due to a change in the arrangement of the phospholipid at the surface upon oxidation, causing increased repulsion between head groups of the lipids (see Chapter 4 for more details).[136] The following

decrease in surface pressure was explained by a further loss of lipids material from the interface over time. Therefore, although the surface pressure of a monolayer of SMB alone decreases under ozone, an initial increase in surface pressure is observed for a mixed film of SMB and POPG, due to the significant, prominent oxidation of POPG by ozone.

A mixed monolayer of SMB and d_{31} POPG (1:12, mol/mol) was formed on NRW, exposed to 2 ppm ozone and neutron reflectivity was measured. Using Equations 3.5-3.7, the SMB would approximately contribute 19 % to the scattering length density of this monolayer. The neutron reflectivity of this monolayer on NRW was measured at various timepoints during exposure to ozone, and some of these reflectivity curves are shown in Figure 3.29. There is a continuous decrease in reflectivity during the exposure, indicating a decrease in the deuterated material at the interface. The neutron reflectivity curves were fitted to determine values of the surface scattering length density and thickness at each timepoint, while background and surface roughness were held constant. The roughness was held at 3 Å for the fitting of each curve. Figure 3.29 also shows the calculated scattering length density multiplied by the thickness of the film at the interface *versus* time. The decrease in SLD x thickness is similar to the results seen for POPG alone (as presented in Chapter 4), therefore the presence of a small amount of SMB does not appear to significantly affect the reaction between ozone and POPG. The decrease in SLD x thickness could be fitted to a single exponential function as described by Equation 3.3, giving a lifetime of the material at the interface of 145 (± 9) minutes with a y-offset, of 0.51 (± 0.02) , i.e., 51% of the surface material is expected to remain at the air-water interface after the reaction has gone to completion.

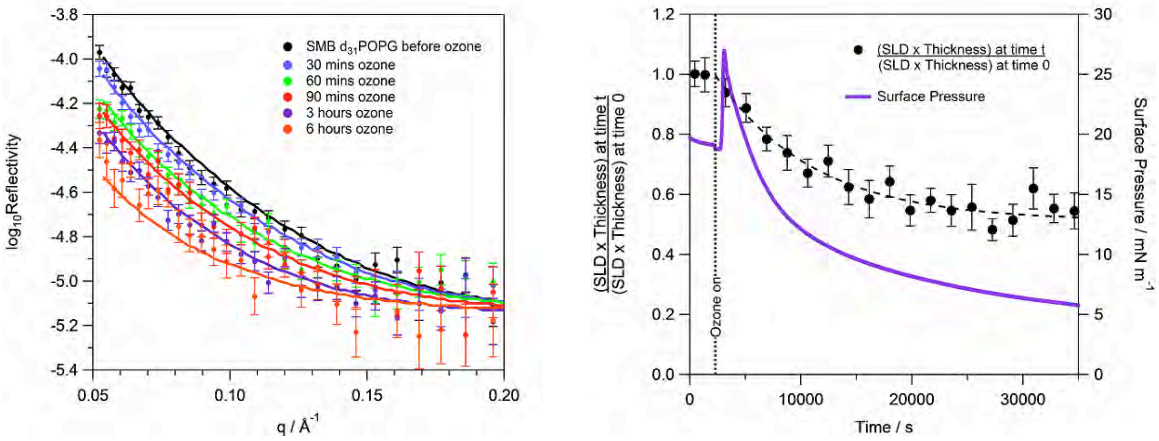

Figure 3.29. Neutron Reflectivity at the air-water interface of a monolayer of SMB and d_{31} POPG on NRW during exposure to ozone.

Left panel: The neutron reflectivity curves of a monolayer of SMB and d_{31} POPG on buffered NRW before ozone (black) and then at regular timepoints during ozone exposure. The measured data is represented by the round markers and the best fit of the curves is shown by the solid lines. The fits were calculated by varying the thickness and scattering length density of the monolayer at each timepoint, whilst keeping surface roughness and background constant.
Right panel: The surface pressure *versus* time (purple line) for a monolayer of SMB and d_{31} POPG on buffered NRW exposed to 2 ppm ozone gas for 9 hours. The dotted line represents the time at which the ozoniser was switched on. Black markers represent the relative amount of material at the interface, calculated from the fitted neutron scattering length density (ρ_t) multiplied by the thickness (δ_t) of the monolayer at time t, divided by fitted the neutron scattering length density (ρ_0) multiplied by the thickness (δ_0) at time 0. The dashed line shows the best fit of neutron data after the ozoniser was switched on, to a single exponential function.

It has been proposed that when a monolayer of SP-B and anionic phospholipid is compressed to high surface pressures (above 30 mN m^{-1}), SP-B is squeezed out of the monolayer with unsaturated lipids, but remains associated with the monolayer *via* its charged residues so that when the monolayer re-expands, the protein re-enters the monolayer. It is thought that this is important in

the lungs to prevent the phospholipids from "squeezing out" of the surfactant monolayer during exhalation.[61] The results presented in this thesis have shown that both SMB and POPG undergo oxidation reactions in the presence of a dilute flow of ozone. It is likely that oxidation of the protein and lipids changes the interaction between the negatively charged lipid, and the positively charged residues in the protein, a property thought to be vital for the function of SP-B. This could either occur due to changes in the structure of the peptide, such as the formation of negatively charged residues, or due to changes in the structure of the lipids, for example if the phospholipids would gain a greater overall negative charge. In order to investigate how the interaction is changed, further neutron reflection experiments were performed.

The neutron reflectivity of mixed monolayer of SMB and d_{31} POPG (1:12, mol/mol) on buffered NRW, under oxygen only, was measured at 20 mN m^{-1}. This monolayer was then compressed by reducing the trough area until a surface pressure of 35 mN m^{-1} was reached, and re-expanded to the initial trough area (and a surface pressure of 19.5 mN^{-1}). The neutron reflectivity of the monolayer was measured again. The reflectivity before and after this compression is shown in Figure 3.30. It is evident that there is no change in the reflectivity, hence no loss in the phospholipid from the interface after this compression.

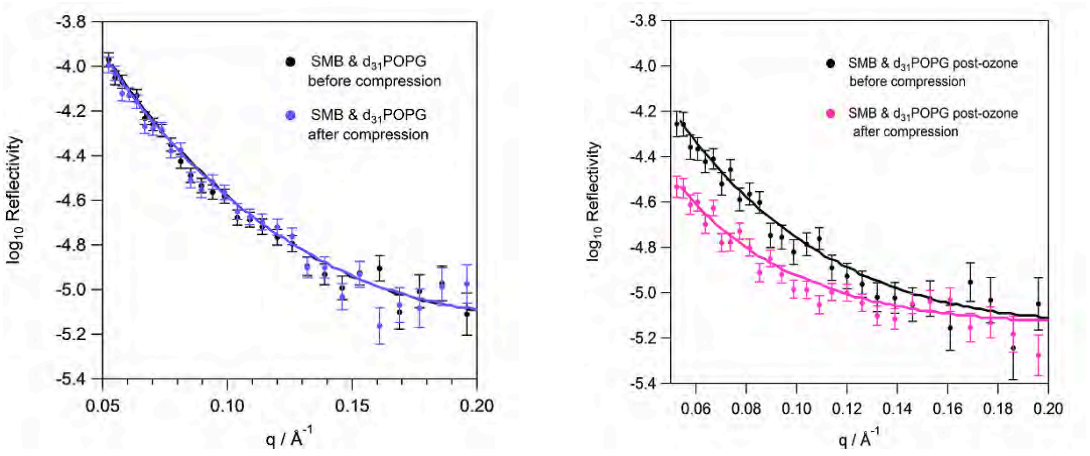

Figure 3.30. The neutron reflectivity curves of a mixed monolayer of SMB and d_{31} POPG before and after compression to high surface pressures and the neutron reflectivity curves of a mixed monolayer of SMB and d_{31} POPG after oxidation by ozone before and after compression to high surface pressures.

Left panel: The neutron reflectivity of a mixed monolayer of SMB and d_{31} POPG (1:12, mol/mol) on NRW before (black) and after (blue) a compression to high surface pressure. The neutron reflectivity curves were measured at the same trough area, under a flow of oxygen gas. The measured data is represented by the round markers and the best fit of the curves is shown by the solid lines.
Right Panel: The neutron reflectivity of a mixed monolayer of SMB and d_{31} POPG (1:12, mol/mol) on NRW after oxidation by 2 ppm ozone for 8 hours before (black) and after (pink) a compression to high surface pressure. The neutron reflectivity curves were measured at the same trough area, under a flow of oxygen gas. The measured data is represented by the round markers and the best fit of the curves is shown by the solid lines.

The same monolayer was exposed to 2 ppm ozone for 8 hours, at the same trough area, and the ozone was then switched off. The neutron reflectivity was again measured under a flow of oxygen at the same trough area, therefore with a low surface pressure of 7 mN m^{-1}. The monolayer was then compressed to 35 mN m^{-1} and re-expanded to the initial trough area and a surface pressure of 2.5 mN m^{-1}. The neutron reflectivity was measured after this compression. The neutron reflectivity of the monolayer before and after compression after exposure to ozone is also shown in Figure 3.30. There is a significant decrease in the reflectivity after one compression, showing a loss of approximately 30% of the deuterated lipid material from the interface. This implies that the interaction

between the protein and the lipid has drastically changed following oxidation as some of the material has become solubilised into the subphase when the monolayer is compressed to high surface pressures.

When a monolayer of d_{31} POPG alone was compressed and re-expanded in the same manner as the SMB/ d_{31} POPG mixed monolayer, different results were observed, as presented in Figure 3.31. Before ozone exposure, a compression of the lipid only monolayer caused a loss of 10 % of the material from the interface. This did not occur when SMB was present in the monolayer, suggesting that SMB provides a mechanism to prevent loss of the phospholipid from the interface, such as charge interactions between the positive amino acids and the negative headgroups. Following ozonolysis of POPG, compressions led to further losses of 20 % of deuterated lipid material from the interface, which was also observed for a mixed monolayer of SMB and POPG.

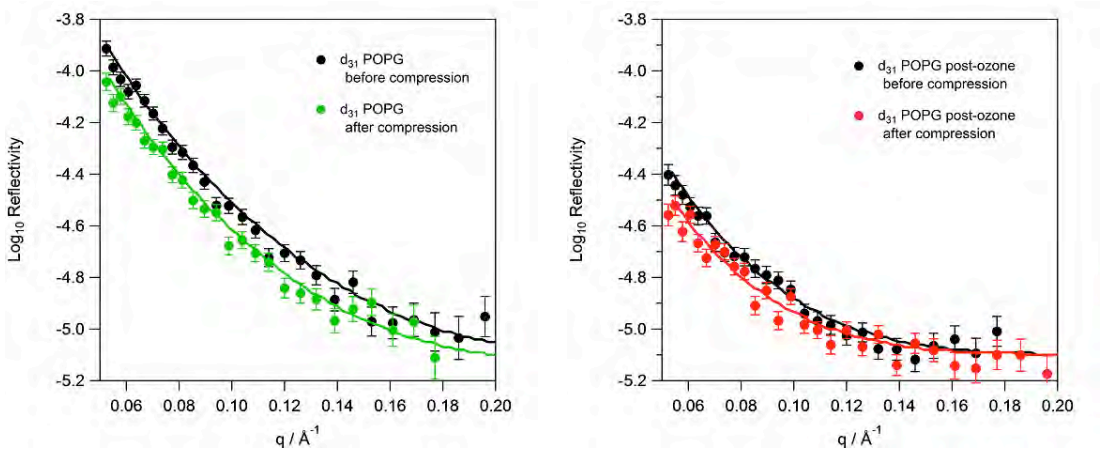

Figure 3.31. The neutron reflectivity curves of a monolayer of d_{31} POPG before and after compression to high surface pressures and the neutron reflectivity curves of a monolayer of d_{31} POPG after oxidation by ozone before and after compression to high surface pressures.

Left panel: The neutron reflectivity of a monolayer of d_{31} POPG on NRW before (black) and after (green) a compression to high surface pressure. The neutron reflectivity curves were measured at the same trough area, under a flow of oxygen gas. The surface pressure before compression was 20 mN m^{-1} and after compression it was 18 mN m^{-1}. The measured data is represented by the round markers and the best fit of the curves is shown by the solid lines.
Right Panel: The neutron reflectivity of a monolayer of d_{31} POPG on NRW after oxidation by 2 ppm ozone for 8 hours before (black) and after (red) a compression to high surface pressure. The neutron reflectivity curves were measured at the same trough area, under a flow of oxygen gas. The surface pressure before compression was 8 mN m^{-1} and after compression it was 2 mN m^{-1}. The measured data is represented by the round markers and the best fit of the curves is shown by the solid lines.

3.6.2.2 Neutron Reflectivity and Surface Pressure Measurements of Mixed Monolayers of SMB and the Anionic Phospholipid DPPG at the Air-Water Interface

Mixed monolayers of SMB and 1,2-dipalmitoyl-*sn*-glycero-3-phosphoglycerol (DPPG) were also exposed to ozone and the neutron reflectivity and the surface pressure were monitored. DPPG is a saturated lipid and a

monolayer of this lipid alone does not react with ozone at the air-water interface, as expected, shown from the surface pressure results in Figure 3.32.

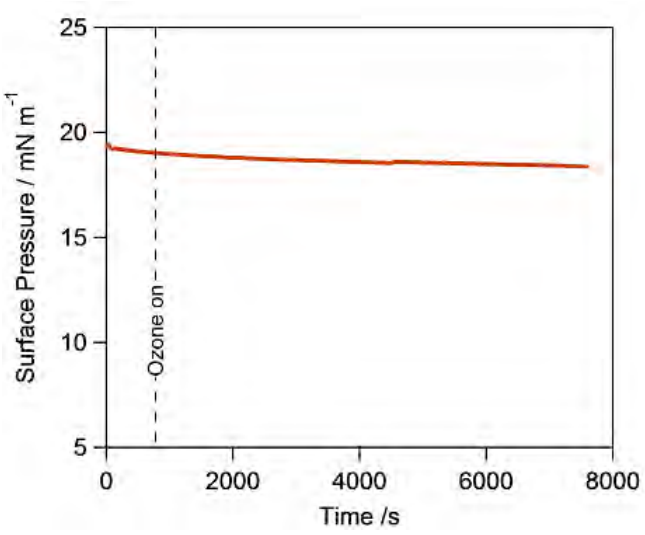

Figure 3.32. The surface pressure *versus* time of a monolayer of DPPG on buffered water exposed to 2 ppm ozone for 2 hours.

The time at which ozone was switched on is indicated by the dotted vertical line at ~800 s.

A mixed monolayer of SMB and DPPG (1:12, mol/mol) was exposed to 2 ppm ozone and the surface pressure measured during exposure. This is shown in Figure 3.33. Results are very similar to the monolayer of SMB and DPPC, in that there is an initial reaction causing a small drop in surface pressure, but this decrease is much smaller than in the reaction between SMB alone and ozone. This decrease in surface pressure is also smaller than in the reaction between a monolayer of SMB and DPPC (1:6, mol/mol) and ozone, presumably because the ratio of lipid to peptide is twice as high.

A mixed monolayer of SMB and d_{62} DPPG (1:12, mol/mol) was exposed to 2 ppm ozone and neutron reflectivity was measured. Using Equations 3.5-3.7, the SMB will contribute to approximately 11 % to the overall scattering length density in this monolayer. The neutron reflectivity of this monolayer on NRW before and after exposure to ozone is shown in Figure 3.33 and there is no discernible change in the reflectivity after ozone exposure. The neutron reflectivity curves were fitted

to determine values of the surface scattering length density and thickness at each timepoint, while background and surface roughness were held constant. The roughness was held at 3 Å for the fitting of each curve. Figure 3.33 also shows that the amount of deuterated material at the interface *versus* time (calculated from the fitted scattering length density and thickness values) does not change in the course of the reaction with ozone. Therefore, oxidation of the peptide at the air-water interface does not lead to observable damage to this saturated anionic phospholipid.

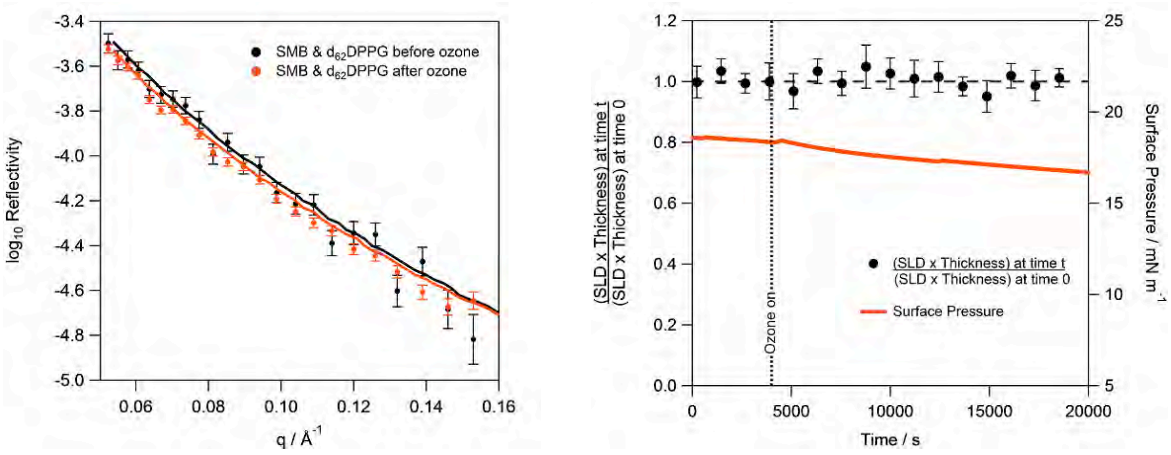

Figure 3.33. Neutron Reflectivity at the air-water interface of a monolayer of SMB and d_{62} DPPG on NRW during exposure to ozone.

Left panel: The neutron reflectivity curves of a monolayer of SMB and d_{62} DPPG (1:12, mol/mol) on buffered NRW before ozone (black), a monolayer of SMB and d_{62} DPPG (1:12, mol/mol) on buffered NRW after ozone (red). The measured data is represented by the round markers and the best fit of the curves is shown by the solid lines. The fits were calculated by varying the thickness and scattering length density of the monolayer at each timepoint, whilst keeping surface roughness and background constant.

Right panel: The surface pressure *versus* time (red line) for a monolayer of SMB and d_{62} DPPG (1:12, mol/mol) on buffered NRW exposed to 2 ppm ozone gas for 4.5 hours. The dotted line represents the time at which the ozoniser was switched on. Black markers represent the relative amount of material at the interface, calculated from the fitted neutron scattering length density (ρ_t) multiplied by the thickness (δ_t) of the monolayer at time t divided by the fitted neutron scattering length density (ρ_0) multiplied by the thickness (δ_0) at time 0. The dashed horizontal line represents a constant amount of material at the interface.

Before any ozone exposure, a monolayer of SMB and d_{62} DPPG on NRW was compressed from 20 mN m^{-1} to 35 mN m^{-1} and then re-expanded to the original trough area (now with a surface pressure of 19 mN m^{-1}). The neutron reflectivity was measured before and after the compression, shown in Figure 3.34. There is no change in the reflectivity, therefore no loss in deuterated lipid from the interface.

The same monolayer was exposed to ozone for 7 hours. The ozone was switched off and the neutron reflectivity was again measured under a flow of oxygen at 16 mN m^{-1}. The monolayer was then compressed to 35 mN m^{-1} and re-expanded to the initial trough area, where the monolayer then had a surface pressure of 12 mN m^{-1}. The neutron reflectivity was measured after this compression. The neutron reflectivity of the monolayer before and after compression following exposure to ozone is also shown in Figure 3.34. There is a significant decrease in the reflectivity after a compression, showing a loss of approximately 20% of the deuterated lipid material from the interface. The SMB contributes to only ~11 % of the total scattering length density of the mixture, therefore it cannot be only peptide lost from the interface. This implies that the interaction between the protein and the lipid has considerably changed following oxidation.

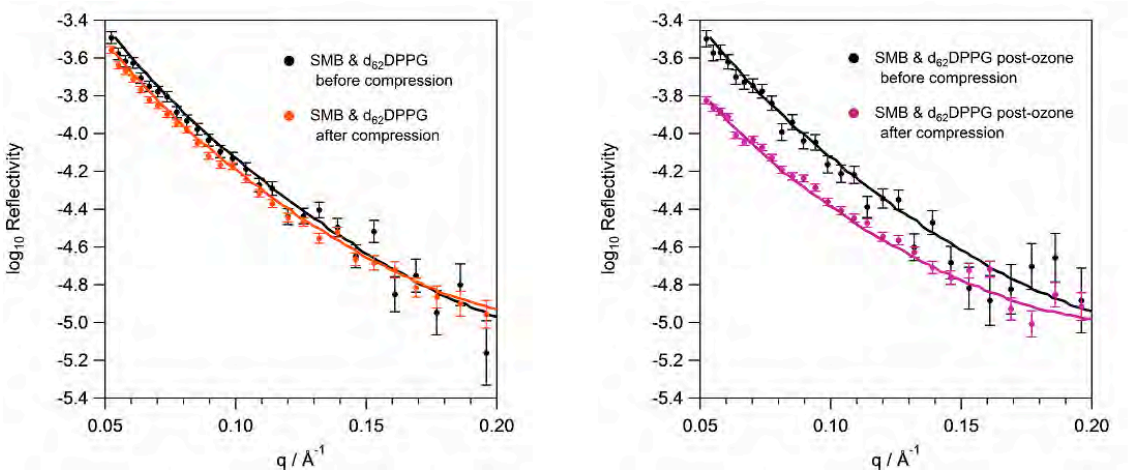

Figure 3.34. The neutron reflectivity curves of a mixed monolayer of SMB and d_{62} DPPG before and after compression to high surface pressures and the neutron reflectivity curves of a mixed monolayer of SMB and d_{62} DPPG after oxidation by ozone before and after compression to high surface pressures.

Left panel: The neutron reflectivity of a mixed monolayer of SMB and d_{62} DPPG (1:12, mol/mol) on NRW before (black) and after (red) a compression to high surface pressure. The neutron reflectivity curves were measured at the same trough area, under a flow of oxygen gas. The surface pressure before compression was 20 mN m^{-1} and after compression it was 19 mN m^{-1}. The measured data is represented by the round markers and the best fit of the curves is shown by the solid lines.

Right Panel: The neutron reflectivity of a mixed monolayer of SMB and d_{62} DPPG (1:12, mol/mol) on NRW after oxidation by 2 ppm ozone for 7 hours before (black) and after (purple) a compression to high surface pressure. The neutron reflectivity curves were measured at the same trough area, under a flow of oxygen gas. The surface pressure before compression was 16 mN m^{-1} and after compression it was 12 mN m^{-1}. The measured data is represented by the round markers and the best fit of the curves is shown by the solid lines.

3.7 Discussion

The oxidation of monolayers of the surfactant protein B peptide mimics, SP-B_{1-25} and SMB, by ozone at the air-water interface has been investigated using a variety of techniques. The surface pressure measurements for the exposure of monolayers of both SP-B_{1-25} and SMB to ozone clearly show that the interaction causes an immediate decrease in the surface pressure of the film when the trough area is held constant, therefore a rapid reaction is occurring. Fluorescence microscopy of monolayers of SMB showed that the total fluorescence of the tryptophan residues within the peptide monolayer had significantly decreased after 5 minutes of ozone exposure and no tryptophan fluorescence was detected at all after 10 minutes of ozone exposure. This suggests that all tryptophan residues had reacted within 10 minutes of ozone exposure to form a residue that does not fluoresce at the wavelength range detected (310-380 nm). The reaction between tryptophan and ozone within 10 minutes corresponds to the same timescale as the rapid drop in surface pressure. Typically, tryptophan has a wavelength of maximum absorption (λ_{ex}) of 280 nm and an emission peak (λ_{em}) at 348 nm. The oxidised forms of tryptophan, kynurenine and N'-formylkynurenine (Figures 3.5 and 3.4 respectively) are more weakly fluorescing than tryptophan. For kynurenine, λ_{ex} = 365 nm and λ_{em} = 449 nm and for N'-formylkynurenine λ_{ex} = 325 nm and λ_{em} = 435 nm,[180] therefore fluorescence emissions from either of these oxidised amino acids would not be detected using this method. It is possible that tryptophan has oxidised to form these species after 10 minutes of ozone exposure, or to another oxidised species, which would explain why no fluorescence is detected.

HPLC of monolayers of SP-B_{1-25} that were collected after 0, 10 and 60 minutes of ozone exposure revealed that a more hydrophobic species was formed after 10 minutes of ozone exposure, that was still present after 60 minutes of ozone exposure. SDS-PAGE of these monolayers revealed that more higher order oligomers of the peptide were present after 10 and 60 minutes of ozone exposure, and also there was a change in the interaction with SDS after ozone, suggesting a

product that is less soluble in aqueous media than the starting material. It is possible that this more hydrophobic residue detected in the HPLC traces could represent an oxidised SP-$B_{1\text{-}25}$ oligomer complex, produced from disulphide bond formation.

HPLC of monolayers of SMB that were collected after 0, 10 and 60 minutes of ozone exposure showed that a major component of the monolayer after an hour of ozone exposure is significantly more hydrophobic than the initial protein. This component is not a significant component after only 10 minutes of ozone, suggesting that further structural changes within SMB are occurring after rapid reaction with tryptophan. Since a more hydrophobic product is formed, it is possible that the peptide could be unfolding or changing its conformation in some way, to expose the hydrophobic core. This hydrophobic product formation is slower than the hydrophobic product formed in the SP-$B_{1\text{-}25}$ reaction with ozone, which could be because it represents a conformational change of SMB rather than an oligomerisation of the peptide. SP-$B_{1\text{-}25}$ is a smaller peptide, therefore such a significant conformational change of this peptide would not occur in the same manner.

For both peptides, only products that are more hydrophobic than the starting peptide were detected after the reaction with ozone. This indicates that the peptide backbones are not cleaved during the reaction with ozone as this would yield some smaller, more hydrophilic fragments. Additionally, SDS-PAGE of the SP-$B_{1\text{-}25}$ monolayers after ozone exposure did not reveal the presence of smaller peptides.

The neutron reflection on NRW and D_2O subphases and X-ray reflection of both peptides show that there is no significant change in the reflectivity after ozone exposure, therefore after reaction with ozone the peptide remains at the interface and there is no measurable change in the hydration or thickness of the peptide monolayer. Kim *et al.* proposed that methionine and tryptophan residues in SP-$B_{1\text{-}25}$ were oxidised after exposure to ozone from mass spectrometry experiments.[167] The neutron and X-ray reflectivity results suggest that addition of these oxygen atoms to the peptides within the monolayers makes no measurable difference to the scattering length density of the peptide monolayers.

Kim *et al.* also proposed that the addition of oxygen atoms to the peptide would lead to a decrease in hydrophobicity, which could mean that the protein loses its surface affinity and is lost to the bulk following reaction with ozone. A decrease in scattering length density of the peptide monolayer at the interface would be observed using neutron or X-ray reflectivity if this occurred. However, the results presented here show unequivocally that the oxidised protein remains at the interface following ozone exposure. Therefore, the results presented in this thesis show that although monolayers of SP-$B_{1\text{-}25}$ and SMB react with ozone at the interface to form films of lower surface pressure, no products of backbone cleavage were detected using SDS-PAGE or HPLC and no change in monolayer thickness or loss of peptide from the interface was observed.

The main component of the lung surfactant, DPPC, does not react with ozone at the air-water interface. When SMB was present in a monolayer of DPPC at the air-water interface, surface pressure results showed that there is a reaction between a mixed monolayer and ozone. Neutron reflectivity of a mixed monolayer of SMB and ^{1}H DPPC on NRW at the air-water interface showed no change during exposure to ozone, indicating that all of the peptide material remained at the interface, therefore the presence of DPPC did not affect the oxidation of SMB by ozone. Furthermore, neutron reflectivity of a mixed monolayer of SMB and d_{62} DPPC on NRW at the air-water interface showed no change during exposure to ozone, showing that the oxidation of SMB does not cause damage to the DPPC molecules in a monolayer. It has been suggested that ozonolysis at the air-water interface can lead to formation of secondary oxidants such as the hydroxyl radical, which could potentially react with other molecules in close proximity.[136] It has been shown in the results presented here that if oxidation of SMB does lead to formation of secondary ROS, they do not react with neighbouring DPPC molecules at initial surface pressures of 20-25 mN m^{-1}.

SP-B is thought to facilitate the transfer and adsorption of lipids during breathing cycles, so oxidation of the protein might affect its function. When a mixed monolayer of SMB and DPPC was compressed to high surface pressures and re-expanded before oxidation, some loss of material from the interface was observed using neutron reflectivity. This 8 % loss could be a result of some protein and/or phospholipid being squeezed out during compression and not readsorbing

upon expansion. This could also be due to a loss of material at the trough barriers as described above.[159] This same loss in material was observed in the compression of DPPC monolayers alone. After oxidation of SMB in mixed monolayer of SMB and DPPC, the loss of material from the interface after a compression is the same as before oxidation. Therefore, the interaction between SMB and DPPC after oxidation of SMB has not changed in a way that is detectable in these experiments.

In the reaction between monolayers of SMB and POPG (1:12, mol/mol) and ozone at the air water interface, similar surface pressure and neutron data were observed as for POPG alone. Since the deuterated POPG contributes to the majority of the neutron reflectivity it is not surprising that similar results were observed. It shows that the presence of SMB does not affect the ozonolysis of the lipid. Before exposure to ozone, there was no loss of material at the interface when the SMB/ POPG monolayer was compressed. Interestingly, when a monolayer of POPG only was compressed, a loss of 10% of the deuterated material from the interface was measured using neutron reflectivity. This demonstrates that SMB is able to aid the re-spreading of the anionic POPG monolayer when it is present in the monolayer.

Notably, the compression of the mixed SMB/POPG monolayer after oxidation led to a loss of a significant amount of the reflectivity from the interface. This suggests that oxidation of both SMB and POPG decreases the ability of the monolayer to re-spread during expansion. This may be due to the lipid being squeezed out at high surface pressures and then being unable to re-adsorb to the surface. Ozonolysis of the alkene in the phospholipid chain could lead to a shortened lipid tail with a more hydrophilic acid or aldehyde group formed at the end of the tail. Therefore the phospholipid would be significantly smaller and more hydrophilic and more soluble in aqueous subphase. Furthermore, oxidation of amino acids within SMB could lead to formation of more negatively charged residues. The residues that could readily be oxidised by ozone are highlighted in Figure 3.35. If oxidation of these residues led to the production of carboxylic acid groups, it could reduce the overall positive charge on the protein. Importantly, some of these amino acids are close to positively charged residues, potentially reducing the effect of their charge. Additionally, reaction could cause a change in the 3-D structure of the peptide, in particular residues such as methionine and tyrosine that form part of the α-helix 1 could disrupt the structure of these

important secondary structure features. These factors could mean that positively charged residues are less accessible to interact with the anionic POPG after reaction with ozone, further reducing the ability of SMB to aid respreading of POPG during compression and expansion cycles. This could be problematic if it occurred during breathing cycles *in vivo*.

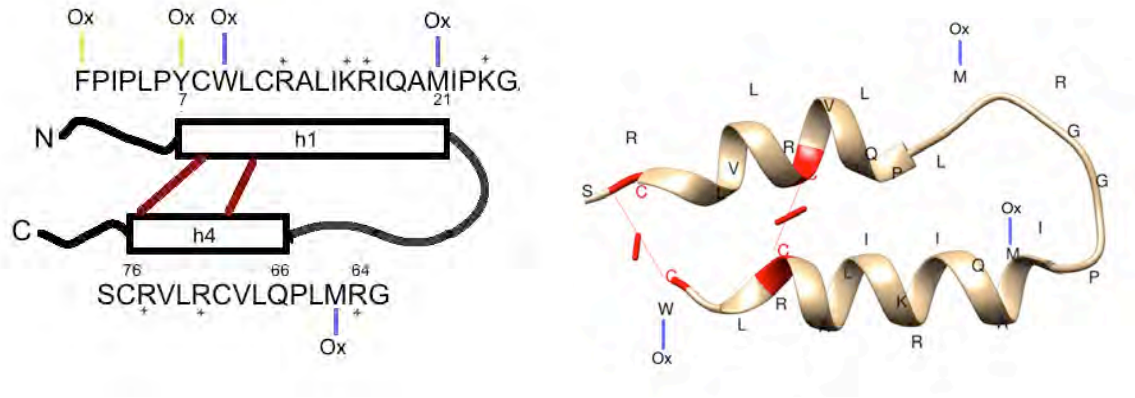

Figure 3.35. The primary structure of SMB and the secondary structure of Mini-B showing the amino acids that are susceptible to ozonolysis.

Left image: The primary structure of the peptide SMB. The peptide contains two α-helices (h1 and h4 from the complete SP-B structure) connected by unstructured loops (solid black lines) and linked by disulfide bridges (red lines) forming a hairpin shape. The positively charged residues are also indicated. The amino acids that were suggested to be oxidised by ozone from Kim *et al.* [167] are indicated by a blue line and other known residues that could react readily with ozone are indicated by a yellow line.

Right image: The structure of Mini-B (SP-B 11-25, 63-78) as determined by NMR in SDS micelles (PDB reference 2DWF).[160] Amino acid residues are indicated by their one letter code and the intramolecular disulphide bonds are shown in red. The amino acids that were suggested to be oxidised by ozone from Kim *et al.* [167] are indicated by a blue line.

The interaction between the anionic phospholipid DPPG and oxidised SMB was investigated and compared to the unoxidised SMB. The surface pressure data shows that the interaction with ozone causes an immediate decrease in surface pressure of the film, similarly to SMB/DPPC mixtures. The level of the drop in surface pressure is much smaller than for SMB alone and the surface pressure

becomes constant much sooner. This is expected, as DPPG does not react with ozone, therefore the surface pressure will remain high after exposure. The neutron reflectivity data shows that there is no change in the amount of material at the interface during ozone exposure.

Compression of a monolayer of oxidised SMB and DPPG caused significant loss of DPPG from the interface, whereas prior to ozone exposure, compression of the monolayer led to no loss of material from the interface. Since DPPG alone does not react with ozone, this must be due to oxidation of SMB. This shows that the function of the protein is affected, as it is no longer interacting in the same way with the anionic phospholipids. It is possible that SMB changes its conformation at the interface upon reaction with ozone, as HPLC of the monolayer showed that more hydrophobic products are formed. The reacted protein could be changing its tertiary structure so that the positively charged residues are no longer readily available to interact with the anionic phospholipids. It could also be due to the oxidation of amino acids within the peptide, forming acidic products, which may reduce the overall charge on the protein, again preventing normal interaction with the negatively charged lipids (as shown in Figure 3.35). This appears to cause phospholipids to be "squeezed out" of the monolayer rather than the peptide. The phospholipids do not re-enter the monolayer upon expansion, presumably forming vesicles or micelles and remaining in the aqueous subphase.

3.8 Conclusion

This study has shown that the two synthetic forms of SP-B; SP-B_{1-25} and SMB, are oxidised by 2 ppm ozone at the air-water interface forming a film that is less able to reduce surface tension, as the surface pressure rapidly dropped when the monolayer was held at constant area. Fluorescence microscopy of SMB monolayers showed that tryptophan residues reacted rapidly with ozone at the air-water interface as the tryptophan fluorescence had significantly decreased after 5 minutes of ozone exposure and no fluorescence was detected after 10 minutes. Therefore, the tryptophan residues had reacted to form a species that does not fluoresce at an emission energy of 310-380 nm. However, surface pressure measurements of SMB monolayers revealed a continuous decrease in surface pressure for several hours after this initial 10 minutes of exposure. This would suggest that after the initial rapid reaction between ozone and the susceptible amino acids, a slower reaction or rearrangement at the interface is observed. This was verified by running HPLC of the extracted monolayers before and after 10 and 60 minutes ozone, where HPLC showed a more hydrophobic product at the interface after 60 minutes of ozone exposure. Additionally HPLC of SP-B_{1-25} monolayers after 10 and 60 minutes of ozone exposure revealed the presence of more hydrophobic products after 10 minutes of ozone exposure. SDS-PAGE of these extracted monolayers revealed that no cleavage of the peptide backbone occurred, but there was a change in the interaction between SP-B_{1-25} and SDS after oxidation, suggesting a product that is less soluble in aqueous media than the starting material. Neutron and X-ray reflectivity of SMB and SP-B_{1-25} monolayers at the air-water interface revealed no change in reflectivity using various contrasts, proving that the oxidised monolayer remains at the interface after oxidation, with no change in the thickness, hydration or spread of the interfacial film.

In mixed monolayers of saturated phospholipids DPPC or DPPG and SMB, no loss of material was seen at the interface when the monolayer was held at

constant area and exposed to 2ppm ozone. Compression of mixed SMB and DPPC monolayers to surface pressures of 35 mN m^{-1} after ozone exposure showed a similar loss in reflectivity as a compression before ozone exposure. This demonstrates that these experiments could not detect a change in the interaction between SMB and DPPC after oxidation of SMB using these methods. However, compression and expansion of the DPPG and SMB monolayers after ozonolysis of SMB caused a loss of 20% of material from the interface, whereas no material was lost from the interface upon compression of the monolayer before ozone exposure, indicating that the SMB could no longer interact *via* its positively charged residues with the anionic lipid head after ozone and so the monolayer was not as capable of re-spreading the phospholipids.

When SMB was present in a monolayer of POPG, similar surface pressure and neutron reflectivity results are seen as with POPG alone. There was an overall decrease in surface pressure during ozone exposure and a loss of deuterated lipid material from the interface, showing that the surface film has very different properties after ozonolysis. Additionally, it was established that oxidised SMB does not prevent the solubilisation of oxidised POPG during expansion and compression cycles. This could be due to the lipids being more hydrophilic, and therefore more soluble in the aqueous subphase, or it could be that the chemical or structural damage to SMB has reduced its positive charges or meant that they were less accessible to interact with the lipids.

The results described in this chapter suggest that peptide mimics of SP-B can rapidly react with ozone at the air-water interface, and reactive amino acids will form residues with different hydrophobicities, leading to changes in their 3-D structure. Therefore, surfactant protein B could be damaged if exposed to ozone pollution in the lungs. It was also shown that the interaction between the peptide mimics and anionic headgroups was changed after ozone damage. If this was to occur to SP-B in the lungs, it could significantly change the function of the protein as it could reduce the ability of the protein to aid respreading of the phospholipids at the interface. These findings present a description for the possible damage to the lung surfactant protein SP-B by ozone exposure and provide an improved understanding of the structure and chemistry of a model lung surfactant system at the air-water interface that is exposed to oxidative stress.

Chapter 4 continues this work by looking at the oxidative damage to various lipids and lipid mixtures by ozone at the air-water interface. The work presented here could be extended by incorporating monolayers of the SP-B peptide mimics with several types of lipids per monolayer that were studied in Chapter 4, such as DPPC, POPG and cholesterol, to determine the effect of ozone exposure on a more elaborate model system. The results can then be compared to those shown in Chapters 3 and 4. Furthermore, the effect of other environmental pollutants, such as ultrafine airborne particles and nitrogen oxides on the SP-B peptide mimics and more extensive lung surfactant models at the air-water interface can be investigated. Additionally, molecular dynamics studies, such as those presented in Chapter 5, of the peptides with oxidised residues could aid clarification of the changes in structure and position of the peptide at the air-water interface after oxidation.

Chapter 4 Ozone Initiated Oxidation of Monolayers of Lipid Components of the Lung Surfactant and Whole Lung Surfactant at the Air-Water Interface

4.1 Introduction

4.1.1 Lipids in the Lung Surfactant

Lipids are the major component of the lung surfactant due to their amphiphilic nature and ability to sufficiently reduce surface tension as a monolayer at the air-water interface. Phospholipids comprise approximately 80-85 % by weight of all the lung surfactant components in humans and the remaining lipids are mainly cholesterol (3-7 % by weight) and glycerides (2-5 % by weight).[8,17] The importance and function of these surfactant lipids has been discussed in Chapter 1.

4.1.2 Lung Surfactant Lipids and Ozone Pollution

This chapter of research presents results that investigate the potential damage caused to lung surfactant lipids, including saturated and unsaturated phospholipids of both the phosphoglycerol and phosphocholine families, and cholesterol. As discussed in Chapter 1, the highly oxidising nature of ozone gas means that it reacts readily with alkene groups, as shown in Figure 1.14, therefore the lipids containing alkenes, i.e. unsaturated phospholipids and cholesterol, could react readily with ozone at the air-water interface.[109]

Following this, ozone pollution damage to whole natural lung surfactant, extracted from animal lungs, will be examined. Using results from ozonolysis of SP-B peptide mimic (Chapter 3) and from ozonolysis of lung surfactant lipids, this can lead to a comparison of ozone damage to the whole surfactant compared to the

individual components in order to envisage the overall oxidative damage to the lung surfactant.

4.1.3 Previous Studies Investigating Ozone Damage to Lung Surfactant Lipids

Several studies have attempted to establish ozone pollution damage caused to both lung surfactant as a whole, and lung surfactant lipids both *in vivo* and *in vitro*. For example, when rats were exposed to 0.5 – 10 ppm ozone and the lung surfactant was then lavaged, Pryor *et al.* determined that the aldehydes hexanal, heptanal and nonanal had formed in the lungs using gas chromatography. This was attributed to the Criegee ozonolysis of the pulmonary surfactant unsaturated lipids such as POPC, POPG, and the C16 unsaturated lipid 1,2-dipalmitoleoyl-*sn*-glycero-3-phosphocholine, to produce 6-9 length aldehydes from scission of the carbon-carbon double bond.[113]

Lai *et al.* measured the surface tension of monolayers of the lung surfactant lipid POPC on a Langmuir trough before and after exposure to ozone. It was shown that the surface tension of the lipid monolayer was substantially higher after ozone exposure. Additionally, using mass spectrometry, it was found that 1-palmitoyl-2(9_0-oxo-nonanoyl)-*sn*-glycero-2-phosphocholine (POnPC- Figure 4.1) was detected after ozonolysis.[105] This oxidised lipid was also detected by Uhlson *et al.* using MS following the reaction between calf pulmonary surfactant and ozone in vitro.[181] With increasing reaction times or ozone concentration, 1-palmitoyl-2-azeloaoyl-*sn*-glycero-3-phosphocholine (PAzPC- Figure 4.1) was also detected. However, the equipment used did not allow for surface tension to be monitored throughout, nor for all products to be analysed.[181]

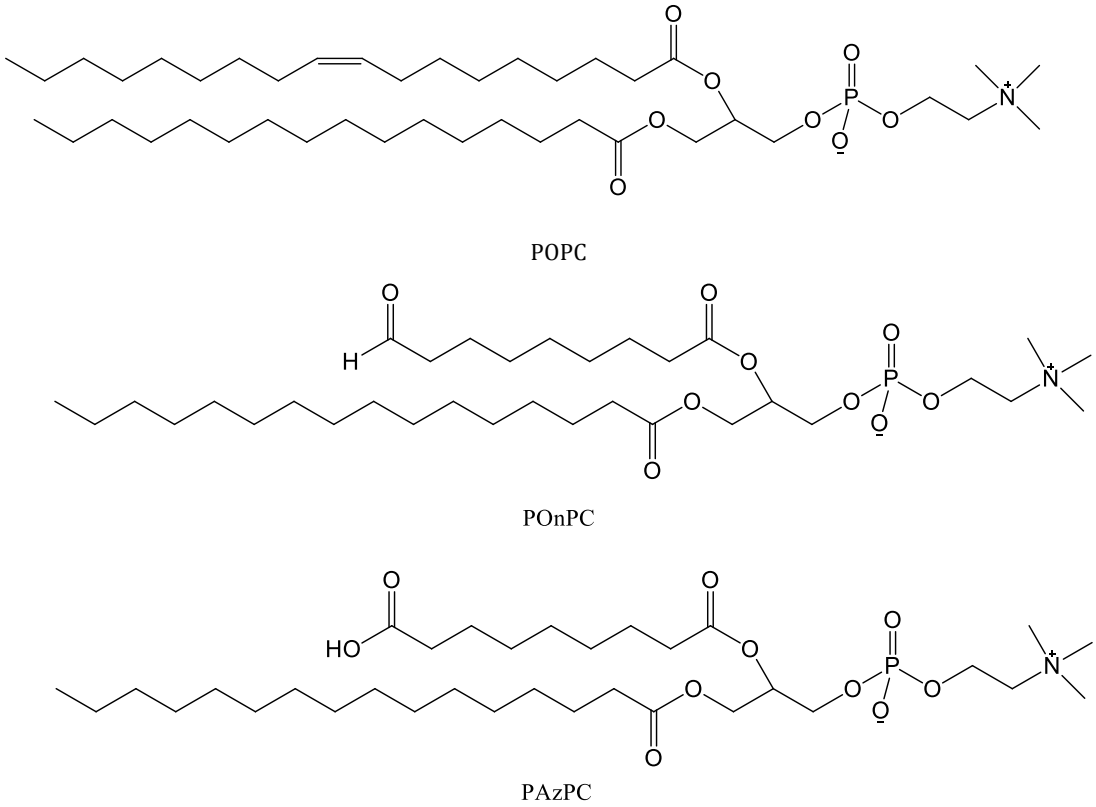

Figure 4.1. The chemical structures of POPC and the oxidised phospholipids POnPC and PAzPC.

Field induced droplet ionization mass spectrometry studies by Kim *et al.* explored the reactions between the pulmonary surfactant lipids POPG, DPPG and DPPC and ozone at the air-water interface. They showed that the unsaturated POPG reacted to form aldehyde and carboxylic acid products from the Criegee intermediate whereas DPPG and DPPC remained intact. [182]

The challenges faced in investigation of ozone damage at the air-water interface arise from the lack of techniques available to monitor these reactions. The Thompson group has recently established a method using neutron reflectivity combined with surface tension measurements using a Langmuir trough/ Wilhelmy plate to analyse the structure and physical properties of pulmonary surfactant components at the air-water interface.[136] Previous work has included investigation of monolayers of POPC reacting with gas-phase ozone, studied in real-time using these techniques. It was found that the lipids were severely degraded during the

reaction leading to a loss of the lipid at the interface. Additionally, surface tensions of the monolayers were significantly higher after oxidation, indicating that oxidation could have a dramatic effect *in vivo*.

Typical surface pressure and neutron reflectivity results observed for exposure of a monolayer of POPC (Figure 4.2) to ~0.1 ppm ozone are shown in Figure 4.3. The initial rise in surface pressure immediately upon ozone exposure was explained by a change in the arrangement of the molecules at the interface after oxidation of the alkene, where the shortened oxidised tail would now be much more hydrophilic and would become associated with the aqueous subphase, causing a tilting or arching of the chain, as shown in Figure 4.4. This increases the effective number of molecules at the air-water interface, leading to an increase in repulsive forces between the surface molecules, therefore an increase in surface pressure.

In these experiments, either palmitoyl deuterated (d_{31} POPC – Figure 4.2) or oleoyl deuterated (Pd_{17}OPC – Figure 4.2) were exposed to ozone and monitored by neutron reflectivity. It was found that loss of deuterated material was observed from the monolayer at the interface in both cases. The loss of deuterated palmitoyl strand was much slower than deuterated oleoyl strand suggesting an intial reaction at the alkene, followed by a slower, secondary reaction causing loss of the palmitoyl strand. It was proposed that the formation of the Criegee intermediate in gas phase could lead to a rearrangement where the very reactive hydroxyl radical would be produced (Figure 4.5). This hydroxyl radical could then react with the palmitoyl strand, causing this observed loss in deuterated material from d_{31} POPC. Additionally, reaction of monolayers of ^{1}H POPC on D_2O subphase with ozone at the air-water interface revealed no change in the spread of the head groups, providing further evidence for reaction of the palmitoyl strand rather than solubilisation of the lipid into the subphase.

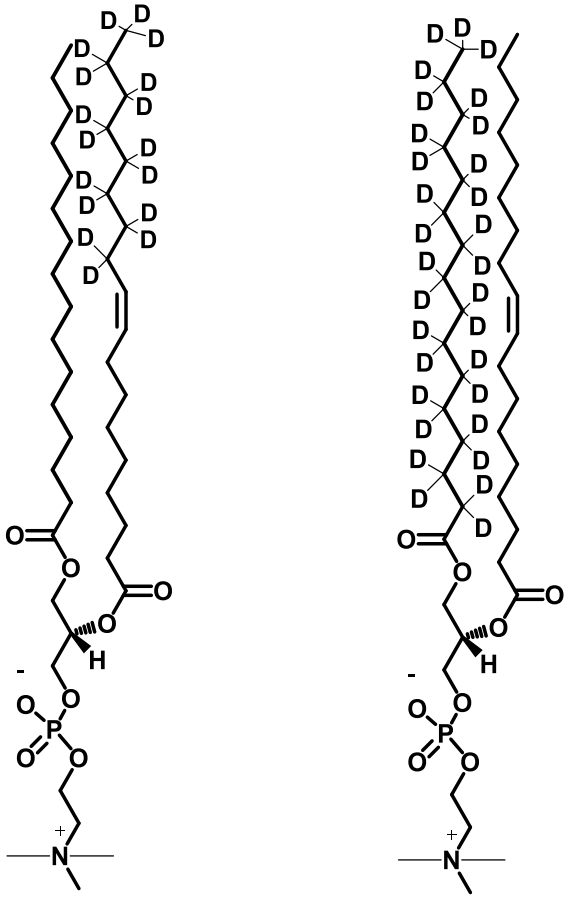

$Pd_{17}OPC$ **$d_{31}POPC$**

Figure 4.2. The chemical structures of $Pd_{17}OPC$ (left) and $d_{31}POPC$ (right).

These chemicals were used to investigate the reaction between POPC and ozone at the air-water interface using neutron reflectivity, both in previous studies in the Thompson group and in the work presented in this chapter. In $Pd_{17}OPC$ the lipid tail above the oleoyl group is fully deuterated. In d_{31} POPC the saturated palmitoyl tail is fully deuterated.

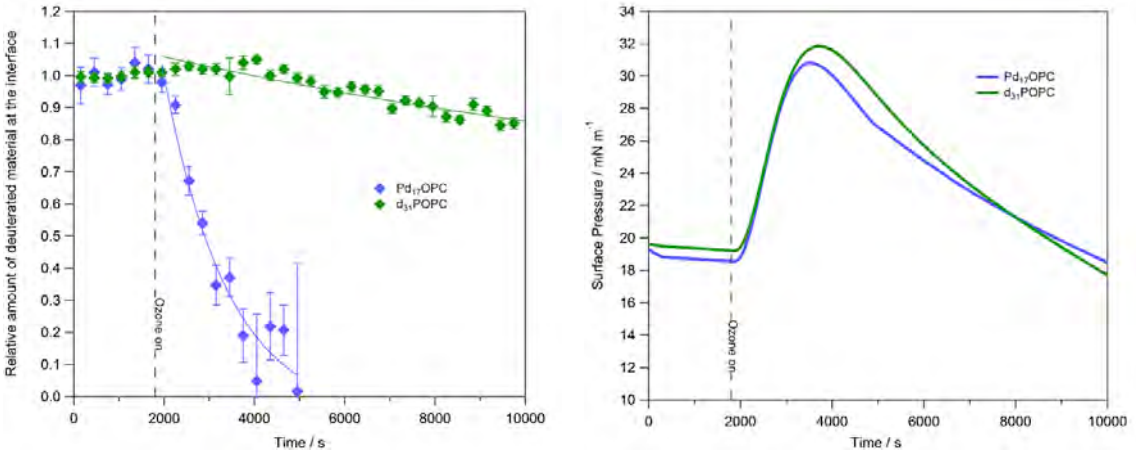

Figure 4.3. A monolayer of Pd_{17}OPC (green) and d_{31}POPC (blue) at the air-NRW interface during exposure to ~0.1 ppm ozone.[136]

Left panel: The relative amount of deuterated material at the interface during exposure of a monolayer of Pd_{17}OPC (blue markers) and d_{31} POPC (green markers) to ozone at the air-water interface. The dashed line represents the time at which the ozoniser was switched on. The solid lines show the best fit, to a single exponential function, of neutron data after the ozoniser was switched on.
Right panel: Accompanying surface pressure data to the neutron data presented in the left panel. The blue line shows the surface pressure of the monolayer of Pd_{17}OPC during exposure to ozone and the green line shows the surface pressure of a monolayer of d_{31}POPC during exposure to ozone. The dashed line represents the time at which the ozoniser was switched on.[136]

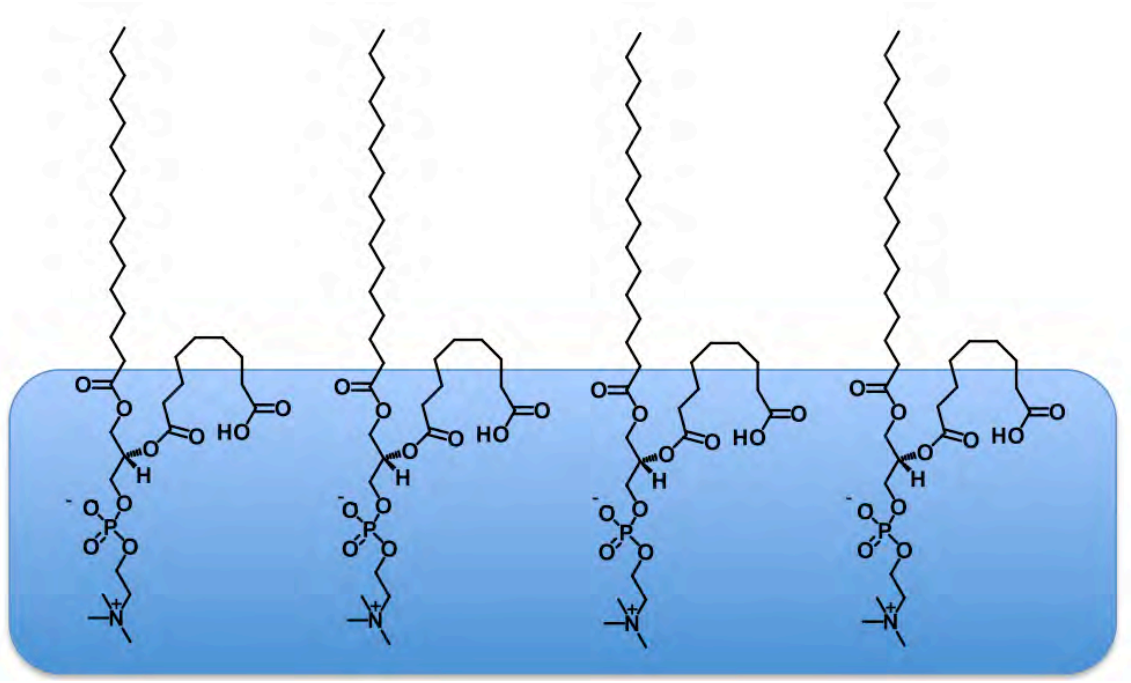

Figure 4.4. The proposed arrangement of PAzPC molecules on an aqueous subphase after reaction with ozone at the oleoyl strand, based on the previous work by Thompson *et al.*[136]

The oxidised tail bends over to become associated with the water causing an increase in the surface pressure.

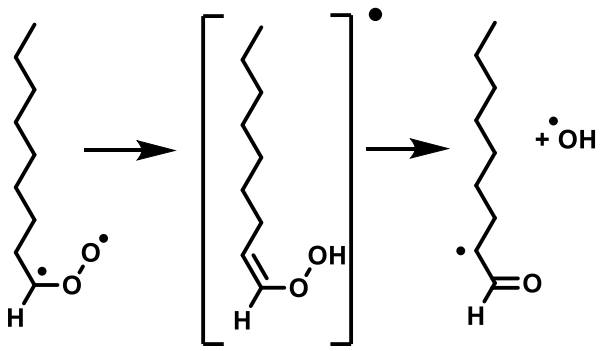

Figure 4.5. The rearrangement of the Criegee intermediate in the gas phase reaction between alkenes and ozone that can lead to formation of the hydroxyl radical.

This chapter will continue the previous work performed in the Thompson group by exploring the interfacial reaction between ozone and lung surfactant lipid components, as well as mixtures of the lipid components and this will extend to investigating the interfacial reaction between ozone and whole lung surfactant. The research aims to investigate the reaction between the unsaturated phospholipids POPC (Figure 4.1) and POPG (Figure 3.6) further by using X-ray reflectivity to provide clearer information on changes in thickness of the monolayers during oxidation. POPG is an anionic phospholipid, therefore has a negatively charged headgroup, and its reaction with ozone at the air-water interface has not previously been studied. Additionally, neutron reflectivity will be used to look at the kinetics of the initial reaction at the oleoyl strand of POPC, and how the reaction is affected by the presence of varying amounts of the saturated phospholipid DPPC (Figure 3.6). The reaction between ozone and the lung surfactant component cholesterol (Figure 1.7) alone and in the presence of POPC at the air-water interface will also be investigated using X-ray reflectivity. Finally, this chapter will end with the analysis of lung surfactant extracted from the lungs of two different species, and the structure of monolayers of the extracted surfactant at the air-water interface will be determined using neutron and X-ray reflectivity. The reaction between the whole surfactant and ozone at the air-water interface will then be examined in order to see how the surface properties of the surfactant are changed by ozone damage.

4.2 Experimental Details

4.2.1 Chemicals and Reagents

The materials used for this study have already been presented in Table 3.1, with the addition of the phospholipids ^{1}H POPC and ^{1}H POPG, which were purchased from Avanti Polar Lipids and had a purity of ≥99.0%. Pd_{17}OPC was obtained from Avanti Polar Lipids as a custom synthesis. Cholesterol was obtained from Fluka (European pharmacopoeia reference standard).

4.2.2 Surface Pressure Measurements

The surface pressure of the lipid or lung surfactant monolayers was measured as described in Section 3.3.2 (Chapter 3). The monolayers studied in this chapter were composed of single lipid components, a mixture of lipid components, or whole extracted lung surfactant. Single component monolayer solutions were prepared by dissolving the synthetic lipids in chloroform to a concentration of 1 mg mL^{-1}. The mixed lipid monolayers studied in this chapter are presented in Table 4.1, and were formed by mixing the single component solutions to achieve the required molar ratio. Whole lung surfactant was also studied, which was extracted in a 3:1 chloroform/methanol (vol/vol) solvent as described in Section 4.2.3. During ozone reaction experiments, the surface pressure was monitored continuously and the trough area and temperature were held constant.

Binary Monolayers	**Concentration / mg mL^{-1}**
Pd_{17}OPC : ^{1}H DPPC	
2.8:1.0 mol/mol	Pd_{17}OPC 0.75
	^{1}H DPPC 0.25
1.9:1.0 mol/mol	Pd_{17}OPC 0.67
	^{1}H DPPC 0.33
1.0:1.1 mol/mol	Pd_{17}OPC 0.5
	^{1}H DPPC 0.5
1.0:2.1 mol/mol	Pd_{17}OPC 0.33
	^{1}H DPPC 0.67
1.0:3.2 mol/mol	Pd_{17}OPC 0.25
	^{1}H DPPC 0.75
Cholesterol : ^{1}H POPC	
7.8:1.0 mol/mol	Cholesterol 0.8
	^{1}H POPC 0.2
2.0:1.0 mol/mol	Cholesterol 0.5
	^{1}H POPC 0.5
1.0:2.0 mol/mol	Cholesterol 0.2
	^{1}H POPC 0.8
2.0:1.0 mol/mol	Cholesterol 0.5
	^{1}H DPPC 0.5

Table 4.1. Details of the mixed lipid monolayers studied in this chapter.

The first column shows the molecular ratio of the binary monolayers and the second column shows the concentration of the components in the monolayer in mg mL^{-1}. These solutions were used to form monolayers on the Langmuir trough.

4.2.3 Extraction of Lung Surfactant from Pig and Sheep Lungs

Pig or sheep lungs from adult animals were purchased freshly from a butcher on the morning of extraction. The lung surfactant was collected using a broncheoalveolar lavage technique where saline solution (0.9 % w/v NaCl, 20-30 mL) was added to the bronchioles of the lungs using a glass pipette and then re-collected for purification.

The procedure for lung surfactant extraction followed the method described by Bligh and Dyer for total lipid extraction and purification.[183] The saline solution containing the surfactant was separated into 1 mL aliquots and centrifuged for 10 minutes at 1000 rpm and room temperature. The supernatant was collected and the pellet containing unwanted cellular debris was disposed of.

The supernatant was separated into 0.2 mL aliquots. To each aliquot 1:2 chloroform/methanol (0.75 mL), chloroform (0.25 mL) and distilled water (0.25 mL) were added sequentially, with vortexing between each addition. The samples were then centrifuged for 5 minutes at 1000 rpm and room temperature. The organic bottom phase, containing the lung surfactant, was removed using a Pasteur pipette, pooled together and stored at -20^{o}C.

4.2.4 Preparation of Lung Surfactant Protein Samples for SDS-PAGE

SDS-PAGE of the extracted lung surfactant samples was performed in order to show that both SP-B and SP-C were present. Due to the low concentration of the proteins within the extracted lung surfactant and the potential interference of the lipid matrix during running the SDS-PAGE, it was necessary to purify and concentrate the proteins from the lung surfactant. Prior to purification, the chloroform/methanol extraction solvent was removed from a 5 mL aliquot of the extracted lung surfactant by evaporation under a stream of nitrogen. The lung surfactant residue was then redissolved in Tris-SDS sample buffer (30 µL), as described in Section 3.3.6.

The PlusOne SDS-PAGE Clean up kit from GE Healthcare was used to remove the lipids from the sample. This is a kit for precipitation of proteins that are difficult to analyse due to their low concentration or the presence of interfering DNA or, in this case, phospholipids.[184] The purification procedure was performed in accordance with the protocol included in the kit. This procedure involves forming a pellet of the protein material within the samples using centrifugation, and washing away remaining lipids and other contaminants. The remaining pellet was then divided into two: to one aliquot 10 μL of Tris-SDS sample buffer with DTT was added, to the other 10 μL of Tris-SDS sample buffer without DTT was added.

4.2.5 SDS-PAGE of Lung Surfactant Proteins Extracted from Animal Lungs

To ensure the presence of both surfactant proteins, the extracted pig lung surfactant was separated using SDS-PAGE and stained using a silver staining protocol to see if proteins at the correct molecular weight could be detected. The SDS-PAGE method used was based on the Tricine-SDS-PAGE protocol described by Schagger *et al.*[169] The same procedure was followed as described in Chapter 3, Section 3.3.6.

The gel shown in Figure 4.6 presents the lung surfactant proteins present, after being treated in 3 different ways. The left sample column shows the whole lung surfactant dissolved in sample buffer, i.e. containing all surfactant lipids, with no reducing agent. There is a significant amount of smearing of the protein bands, showing the interference of the surfactant lipids preventing proper analysis using this method. The middle sample column shows the lung surfactant with the surfactant lipids largely removed using a clean-up protocol, in sample buffer containing no reducing agent. There are three main protein bands, corresponding to the presence of surfactant protein C (<4 kDa), surfactant protein B monomer (9.0 kDa) and surfactant protein B dimer (18 kDa). The third sample column shows the lung surfactant after lipid clean-up after reduction with DTT. There are now two main protein bands corresponding to surfactant protein C and surfactant protein B monomers only. Therefore, it was concluded that the surfactant proteins were successfully extracted from the lung surfactant along with the surfactant

lipids. The extracted sheep surfactant also showed the presence of both SP-B and SP-C.

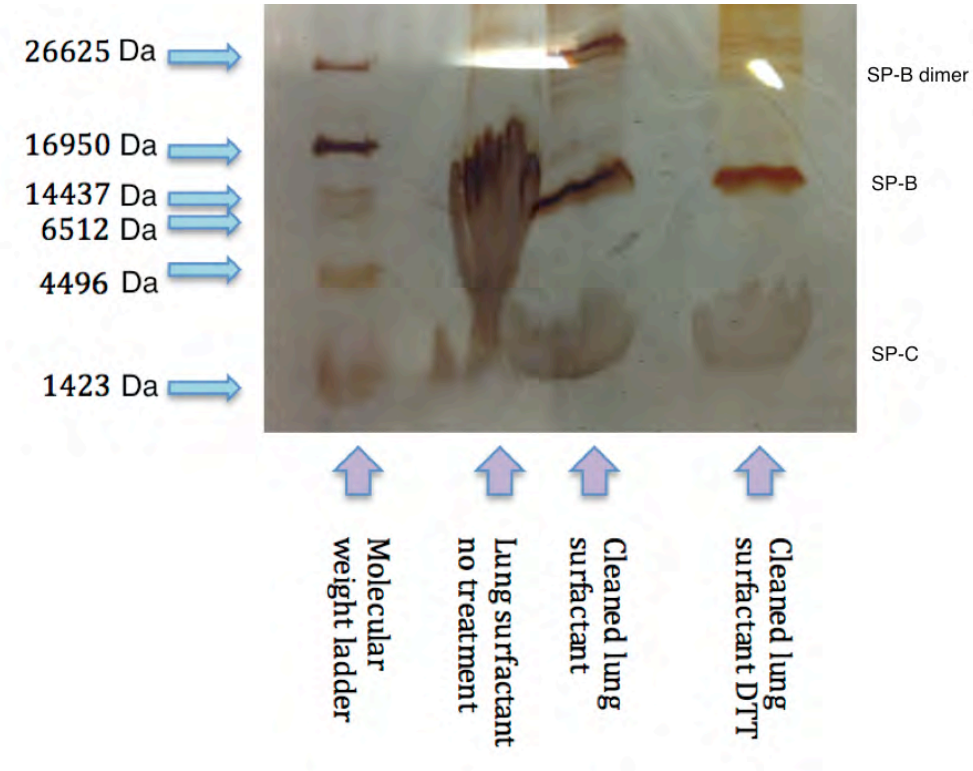

Figure 4.6. Protein gel showing the presence of both SP-B and SP-C in extracted whole lung surfactant collected from pig lungs.

SDS-PAGE protein gel of (i) extracted pig lung surfactant with no treatment, dissolved in sample buffer, (ii) extracted pig lung surfactant after removal of surfactant lipids and (iii) extracted pig lung surfactant after removal of surfactant lipids and reduction of disulphide bonds using DTT to form monomers only. The far left lane shows the molecular weight ladder, which had been reduced using DTT as described in the protocol. The gel is stained using a silver staining method.

4.2.6 Ozonolysis of Monolayers at the Air-Water Interface

The reaction between monolayers and ozone at the air-water interface were performed as detailed in Chapter 3, Section 3.3.3.

The ozone concentrations used were 0.1, 0.25, 0.55, 1.1 and 2 ppm in

oxygen, as specified for each monolayer in the results section, by varying the surface area of the lamp that is exposed to the flow of oxygen during the experiment. Monolayers were exposed to ozone for varying lengths of time as described in the results section.

4.2.7 Neutron and X-ray Reflection of Monolayers at the Air-Water Interface

Monolayers of the synthetic lipids and whole extracted lung surfactant were formed at the air-water interface on a Langmuir trough inside an environmental chamber as previously described in Chapter 3. All experiments were performed at 20 ^{o}C, except for Pd_{17}OPC/DPPC mixtures, where the trough was warmed to 37 ^{o}C. Throughout the experiments the trough area was held constant and the surface pressure was monitored continuously. The reflectivity of the interface was measured under oxygen alone prior to ozone being switched on.

4.2.7.1 Neutron Reflectivity Experiments

Neutron reflection of mixed monolayers of Pd_{17}OPC and DPPC was performed on the FIGARO reflectometer at the Institut Laue Langevin, Grenoble, France. Neutron reflection of POPG monolayers was performed on the SURF reflectometer at ISIS, Rutherford Appleton Laboratory, Didcot, UK, whilst neutron reflection of monolayers of whole, extracted sheep or pig lung surfactant was performed on the INTER reflectometer, also at ISIS. The incident neutron beam for each experiment contained neutrons with a range of wavelengths, λ. On FIGARO the range was from $2.2 \leq \lambda \leq 25$ Å, on SURF the range was $0.5 \leq \lambda \leq 6.5$ Å and on INTER the range was $1 \leq \lambda \leq 16$ Å.

Neutron reflectivity experiments were performed as described in Chapter 3, Section 3.3.9, unless otherwise described. The reflectivity of the monolayer was measured for varying lengths of time during the experiment to give reflectivity curves at regular timepoints. In general, for experiments on FIGARO where NRW was used as a subphase, neutron reflectivity data was acquired for 8

minutes at 0.624° and 30 minutes at 3.78°. For experiments using d_{31} POPG on NRW on SURF, data was acquired for 15 minutes. For whole surfactant experiments on INTER, neutron reflectivity data was acquired for 30 minutes at 0.8° and for 45 minutes at 2.3°. At each timepoint, when two angles were measured, the reflectivity curves for both angles were stitched together following normalisation.

4.2.7.2 Neutron Reflectivity Data Fitting

The coherent neutron scattering lengths used for analysis of the neutron reflectivity data components of the monolayers studied in this chapter are presented in Table 4.2. The approximate scattering length densities and molecular volumes for each phospholipid are also listed in this table. As described in Chapter 3, Section 3.3.10, these volumes, and therefore scattering length density values, are only approximate because they represent a value for the lipid in a bilayer, therefore at small volume. The values for scattering length density, ρ, in Table 4.2 might be acceptable for monolayers of the lipid at very small areas per lipid (small trough area), but as the area per lipid increases the values for ρ would significantly change. The volumes for the phospholipids were taken from Armen *et al.*[176] These values for scattering length density are not used in the fitting of the neutron reflectivity curves, but are useful for illustrating the effect of deuteration on the scattering length density of molecules, and the contribution of each phospholipid to the overall scattering length density of mixed monolayer films. The whole extracted lung surfactant was a multicomponent mixture but of the main components, more than 90 % are hydrogenous lipids, hence a neutron scattering length density of $\sim 0.2 \times 10^{-6}$ Å^{-2} would be expected.

Lipid	Formula	b / fm	ρ / 10^{-6} Å^{-2}	V / Å^3
^{1}H DPPC	$C_{40}H_{80}NO_8P$	27	0.21	1286
d_{31} POPG	$C_{40}H_{46}O_{10}PD_{31}$	356	2.95	1207
Pd_{17}OPC	$C_{42}H_{65}NO_8PD_{17}$	210	1.69	1247

Table 4.2. The formulae, coherent neutron scattering lengths and scattering length densities, appropriate to a bilayer structure, of the lipids studied in this research.

The reflectivity was modelled assuming a single, uniform layer between two semi-infinite media. The data was fitted using the separate fitting procedures *mono*,[171] *drydoc*[172] and *motofit*,[173] as described in Chapter 3, Section 3.3.10.

Mono was used in the fitting of d_{31} POPG monolayer neutron reflectivity curves. The area per head group and monolayer thickness were fitted while background and surface roughness were held constant. The fitted values of area per molecule and thickness were then used to calculate the surface scattering length density using Equation 3.1. *Drydoc* and *motofit* were used to fit all neutron reflectivity data. In these programs the scattering length density and thickness were fitted while background and surface roughness were held constant. For fitting the data of most monolayers, unless otherwise stated, the roughness was held at 3 Å for each synthetic phospholipid neutron reflectivity curve. A roughness of 5 Å was required for fitting the whole extracted lung surfactant data. The relative amount of material at the interface was calculated using Equation 3.2 and when a change in relative amount of material, scattering length density or thickness at the interface was observed during reaction with ozone, the data was fitted to a single exponential decay function given in Equation 3.3.

4.2.7.3 X-ray Reflectivity Experiments

All X-ray reflectivity experiments were performed on the I07 beamline at Diamond Light Source, Harwell Science and Innovation Campus, Didcot, UK, as

described in Chapter 3, Section 3.3.11. The reflectivity at each timepoint was generally measured for 10 minutes and the height of the interface with respect to the X-ray beam was checked every 3 runs and re-aligned if required.

4.2.7.4 X-ray Reflectivity Data Fitting

The X-ray scattering lengths, *b,* scattering length densities, *ρ*, and molecular volumes, *V,* for the lipids investigated in this study are shown in Table 4.3. The volumes of the lipid molecules presented here are valid for a lipid in a bilayer, therefore in a monolayer the volumes are likely to change as the trough area changes. The X-ray scattering length density of water is 9.40 x 10^{-6} $Å^{-2}$ and the scattering length density of the synthetic lipids are very similar to this value, hence the X-ray reflectivity curves of these monolayers will be similar to the curve of water alone and reflectivity of the monolayer could be lower or higher than water alone depending on the trough area. The actual scattering length density of the lipid monolayer therefore depends on the trough area.

Lipid	Formula	b / fm	ρ / 10^{-6} $Å^{-2}$	V / $Å^3$
POPC	$C_{42}H_{82}NO_8P$	1184	9.49	1247
POPG	$C_{40}H_{77}O_{10}P$	1185	9.82	1207
Cholesterol	$C_{27}H_{46}O$	609	9.71	627

.

Table 4.3. The X-ray scattering lengths and scattering length densities of the synthetic lipids studied in this research.

The fitting programs *motofit* and *drydoc* were used to obtain values for thickness, *δ*, and X-ray scattering length density of the material at the interface, ρ, as described in Section 3.3.10. A roughness of 5 Å was used to optimise fitting of these parameters.

4.3 Results

4.3.1 Reactions between Monolayers of POPC and Gas-Phase Ozone at the Air-Water Interface

In the introduction to this chapter, it was described that neutron reflectivity had previously been used to investigate the reaction between the unsaturated phosphocholine POPC and gas-phase ozone at the air-water interface. This section aims to explore this reaction further, firstly by looking more accurately at the thickness changes of the monolayer during the reaction using X-ray reflectivity and secondly by examining how the reaction is affected, in terms of extent of oxidation or reaction kinetics, in the presence of the saturated phosphocholine DPPC.

4.3.1.1 X-ray Reflectivity of a Monolayer of POPC on Buffered Water Exposed to Gas-Phase Ozone at the Air-Water Interface

A monolayer of POPC (Figure 1.5) on water was exposed to 2 ppm ozone at 22 ^{o}C and the surface pressure and X-ray reflectivity was measured continuously during exposure. The surface pressure results are shown in Figure 4.8, and are similar to those described in Section 4.1.

Previously, neutrons were used to observe changes in the POPC monolayer at the surface as deuterated lipids were utilised, meaning that the neutron reflectivity from the deuterated parts was amplified. This allowed us to detect loss specifically from either of the lipid tails from the interface during reaction with ozone. X-ray reflectivity was used here to complement the neutron data and allowed measurement to higher q due to the much higher flux of the X-ray synchrotron beam. X-ray reflectivity is sensitive to all parts of the lipid, i.e. to both heads and tails, because the X-rays interact with the electrons rather than the nuclei.

The X-ray reflectivity curve of a monolayer of POPC is shown in Figure 4.7, showing the reflectivity to a much higher q than previous neutron data. This allows measurement of the changes in the thickness of the monolayer more accurately during ozone exposure. When ozone was switched on, there were evident changes

in the X-ray reflectivity curves of POPC monolayers at the air-water interface as shown in Figure 4.7. Importantly, the fringe spacing at high *q* shifts and becomes wider. The change in fringe spacing can be explained due to a change in the thickness of the monolayer. The fringe spacing is proportional to π/thickness, therefore the increase in width of the fringe in Figure 4.7 indicates a decrease in monolayer thickness. Fitting the X-ray reflectivity curves at each timepoint gave values of scattering length density and thickness of the surface layer. It was found that there was a 20-30% drop in the thickness, which would be expected from the proposed mechanism of reaction, where the ozone reacts at the alkene group to cause a loss of the lipid tail above the double bond. The change in the surface pressure, scattering length density and monolayer thickness *versus* time during the reaction is presented in Figure 4.8. Upon exposure, the thickness decreases rapidly from 22.2 (± 0.4) Å to 19.1 (± 0.4) Å within 15 minutes and then there is a further decrease to 15.8 (± 0.4) Å within another 15 minutes. The thickness does not change significantly after this time. Fitting the scattering length density *versus* time, shown in Figure 4.8, to a single exponential using Equation 3.3 gave a lifetime of 8.3 (± 1.2) minutes with a y-offset of 10.51 (± 0.02) x 10^{-6} $Å^{-2}$, whereas fitting the thickness *versus* time gave a lifetime of 27 (± 1.7) minutes with an offset of 15.5 (± 0.1) Å. Therefore, the decrease in X-ray scattering length density of the film occurs more rapidly than the decrease in monolayer thickness with time.

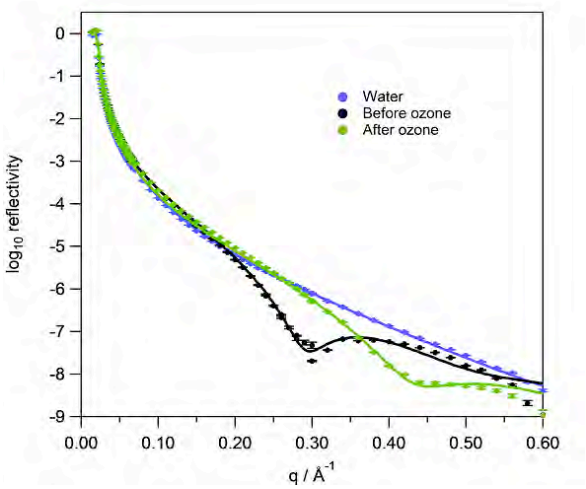

Figure 4.7. X-ray reflectivity of a monolayer of POPC at the air-water interface before and after exposure to ~2 ppm ozone.

The X-ray reflectivity curves of water alone (blue), a monolayer of POPC on water before ozone (black) and a monolayer of POPC on water after ozone (green). The measured data is represented by the round markers and the best fit of the curves is shown by the solid lines. The fits were calculated by varying the thickness and scattering length density of the monolayer at each timepoint, whilst keeping surface roughness and background constant.

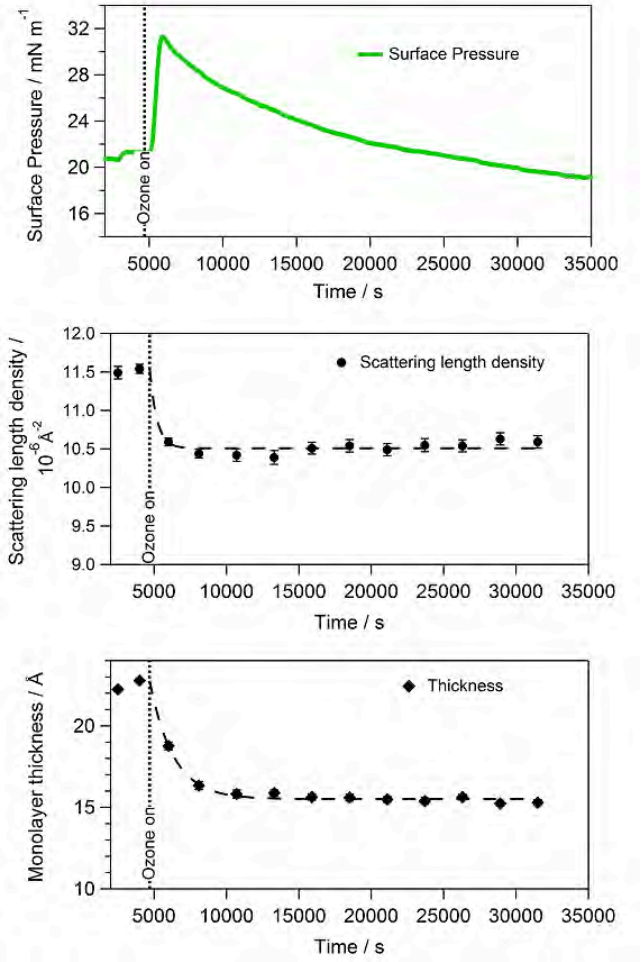

Figure 4.8. The surface pressure, scattering length density and thickness of a monolayer of POPC at the air-water interface during exposure to 2 ppm ozone.

Top panel: The surface pressure *versus* time (green line) for a monolayer of POPC on water exposed to 2 ppm ozone gas for 8 hours.
Middle panel: Black circles show the fitted X-ray scattering length density of a monolayer of POPC on water exposed to 2 ppm ozone gas for 8 hours. The dashed line shows the best fit of X-ray data after the ozoniser was switched on, to a single exponential function.
Bottom panel: Black diamonds represent the fitted thickness of a monolayer of POPC at the air-water interface during exposure to 2 ppm ozone. Thickness was calculated from fitting the X-ray reflectivity curve at each timepoint. The dashed line shows the best fit of X-ray data after the ozoniser was switched on, to a single exponential function.
The dotted line represents the time at which the ozoniser was switched on in all graphs.

4.3.1.2 Neutron Reflectivity of Mixed Monolayers of Pd_{17}OPC and ^{1}H DPPC on Buffered NRW at the Air-Water Interface

It was previously shown that when comparing the reaction between Pd_{17}OPC (Figure 4.2) and 0.1 ppm ozone to d_{31} POPC (Figure 4.2) and 0.1 ppm ozone at the air-NRW interface, loss of the deuterated tail above the alkene (Pd_{17}OPC) was much more rapid (lifetime 24 minutes) than loss of the deuterated saturated tail (d_{31} POPC, lifetime 354 minutes under identical conditions). Additionally, it was proposed that loss of the palmitoyl strand could arise from the production of ozone-generated reactive species, such as the hydroxyl radical, so it was thought that these species could react with DPPC when both POPC and DPPC were present at the air-water interface. However, when a monolayer of d_{62} DPPC and ^{1}H POPC was exposed to ozone, no loss of deuterated DPPC was observed from the interface, showing that if these radicals are formed, they are not present for timescales long enough to attack neighbouring saturated lipids. [185]

It was evident from previous experiments that surface pressure measurements on mixed films of POPC and DPPC show significant differences in the reaction compared to pure POPC monolayers. The initial rise in the surface pressure is disproportionately small and the reduction in surface pressure that follows is only slight. To determine how the presence of DPPC in the lipid monolayer changes the rate of the loss of the POPC oleoyl strand from the monolayer, monolayers of Pd_{17}OPC and DPPC, at a range of ratios of unsaturated to saturated lipids, were exposed to ozone and the surface pressure and neutron reflectivity were monitored.

First, to ensure that the Pd_{17}OPC monolayer was stable under oxygen alone for several hours, a monolayer of this lipid was formed under oxygen at the air-NRW interface and the neutron reflectivity and surface pressure were measured during this time. The results presented in Figure 4.9 demonstrate that the monolayer is stable for at least 5 hours during exposure to oxygen as there is no loss of lipid material from the interface and no significant change in the surface pressure. The small, gradual decline in surface pressure can be attributed to a loss of material at the Langmuir trough barriers as previously described.[179] It was

previously shown by Thompson *et al.*[136] using the same method that a monolayer of DPPC at the air-water interface is stable under oxygen only for several hours.

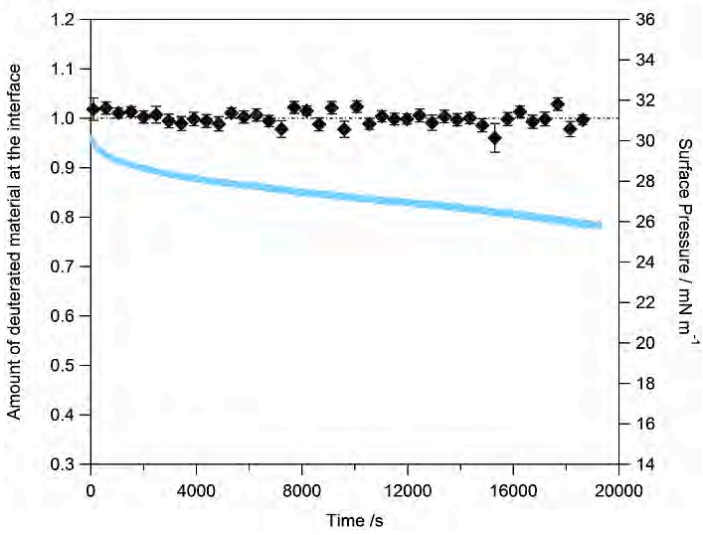

Figure 4.9. A monolayer of Pd_{17}OPC at the air-NRW interface during exposure to oxygen only.

The surface pressure *versus* time (blue line) for a monolayer of Pd_{17}OPC on buffered NRW exposed to oxygen gas for 5 hours. Black diamonds represent the relative amount of deuterated material, calculated from the fitted neutron scattering length density (ρ_t) multiplied by the thickness (δ_t) of the monolayer at time t divided by the neutron scattering length density (ρ_0) multiplied by the thickness (δ_0) at time 0.

Monolayers of Pd_{17}OPC alone and Pd_{17}OPC and ^{1}H DPPC mixtures (2.8:1.0, 1.9:1.0, 1.0:1.1, 1.0:2.1, and 1.0:3.2 mol/mol) were formed on NRW and exposed to 0.1 ppm ozone. The neutron reflectivity and surface pressure was monitored during the reaction in all cases. The neutron reflectivity curves were fitted to determine values of the surface scattering length density and thickness at each timepoint, while background and surface roughness were held constant. The roughness was held at 3 Å for the fitting of each curve. From these values the relative amount of deuterated material at the interface was calculated for each monolayer *versus* time.

Figure 4.10 demonstrates the loss of the deuterated oleoyl strand from a monolayer of Pd_{17}OPC only during the reaction with 0.1 ppm ozone. The left panel

shows that there is a continuous decrease in neutron reflectivity during continuing ozone exposure. Fitting the reflectivity data to give relative amount of material at the interface shows that the product of the scattering length and thickness of the monolayer falls to a factor of <0.4 of its initial value. Using the values given in Table 4.4, the percentage contribution of the deuterated oleoyl strand to the overall scattering length density of the monolayer is approximately 80 %. This would suggest that 20 % of the monolayer material would remain at the interface if all POPC molecules had reacted with ozone. Therefore, the amount of material remaining at the interface in this experiment is higher than expected, and higher than that reported by Thompson *et al.*[136] The current work used the same batch of Pd_{17}OPC lipid as the previous study so it could be possible that the lipid has degraded to form an impurity that still contains the d_{17} strand. If this impurity is saturated and does not react with ozone then it would remain at the interface, explaining the higher proportion of material remaining at the interface compared to previous work. The lifetime of the material at the interface, calculated using Equation 3.3, was 29 (± 5) minutes with a y-offset (B) of 0.35 (± 0.1), so the deuterated strand was lost rapidly from the interface.

Molecule/ Part of molecule	Formula	b / fm	ρ / 10^{-6} Å^{-2}	V / Å^3
^{1}H DPPC	$C_{40}H_{80}NO_8P$	27	0.21	1286
Pd_{17}OPC	$C_{42}H_{65}NO_8PD_{17}$	210	1.69	1247
Deuterated oleoyl (C_9) of Pd_{17}OPC	C_9D_{17}	173	7.49	231
Remaining part of Pd_{17}OPC	$C_{33}H_{65}NO_8P$	37	0.36	1016

Table 4.4. The scattering lengths, approximate scattering length densities and molecular volumes of ^{1}H DPPC and Pd_{17}OPC molecules used in this study.

The contributions from the deuterated oleoyl section of Pd_{17}OPC only and the rest of the Pd_{17}OPC molecule, which is undeuterated, are also presented.

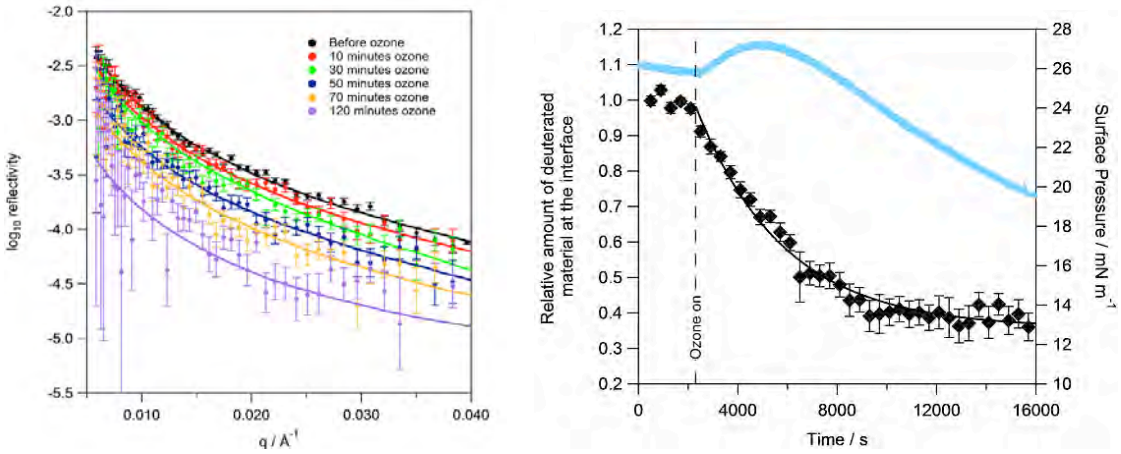

Figure 4.10. A monolayer of Pd_{17}OPC at the air-NRW interface during exposure to 0.1 ppm ozone.

Left panel: The neutron reflectivity curves of a monolayer of Pd_{17}OPC on NRW before ozone exposure (black) and after: 10 minutes (red), 30 minutes (green), 50 minutes (blue), 70 minutes (orange), and 120 minutes (purple) of 0.1 ppm ozone. Right panel: The surface pressure *versus* time (blue line) for a monolayer of Pd_{17}OPC on water exposed to 0.1 ppm ozone gas for 4 hours. The dashed line represents the time at which the ozoniser was switched on. Black diamonds represent the relative amount of material, calculated from the fitted neutron scattering length density (ρ_t) multiplied by the thickness (δ_t) of the monolayer at time t divided by the neutron scattering length density (ρ_0) multiplied by the thickness (δ_0) at time 0.

The experiment was performed with increasing levels of ^{1}H DPPC within the monolayer to see how this lifetime changed in the presence of the saturated lipid. Figure 4.11 shows the surface pressure and neutron reflectivity results for the degradation of Pd_{17}OPC by ozone in the presence of increasing amounts of ^{1}H DPPC. The surface pressure results are different to Pd_{17}OPC alone because there is a smaller initial rise in surface pressure with increasing levels of DPPC in the monolayer. The neutron reflectivity of the monolayers during exposure showed a rapid loss of material from the interface in all cases. It can be assumed that the major contributor to the overall scattering length density in all of the POPC/DPPC mixtures is the deuterated strand of Pd_{17}OPC as shown by the approximate scattering length densities in Table 4.4, therefore the rate of loss of this deuterated strand can be compared.

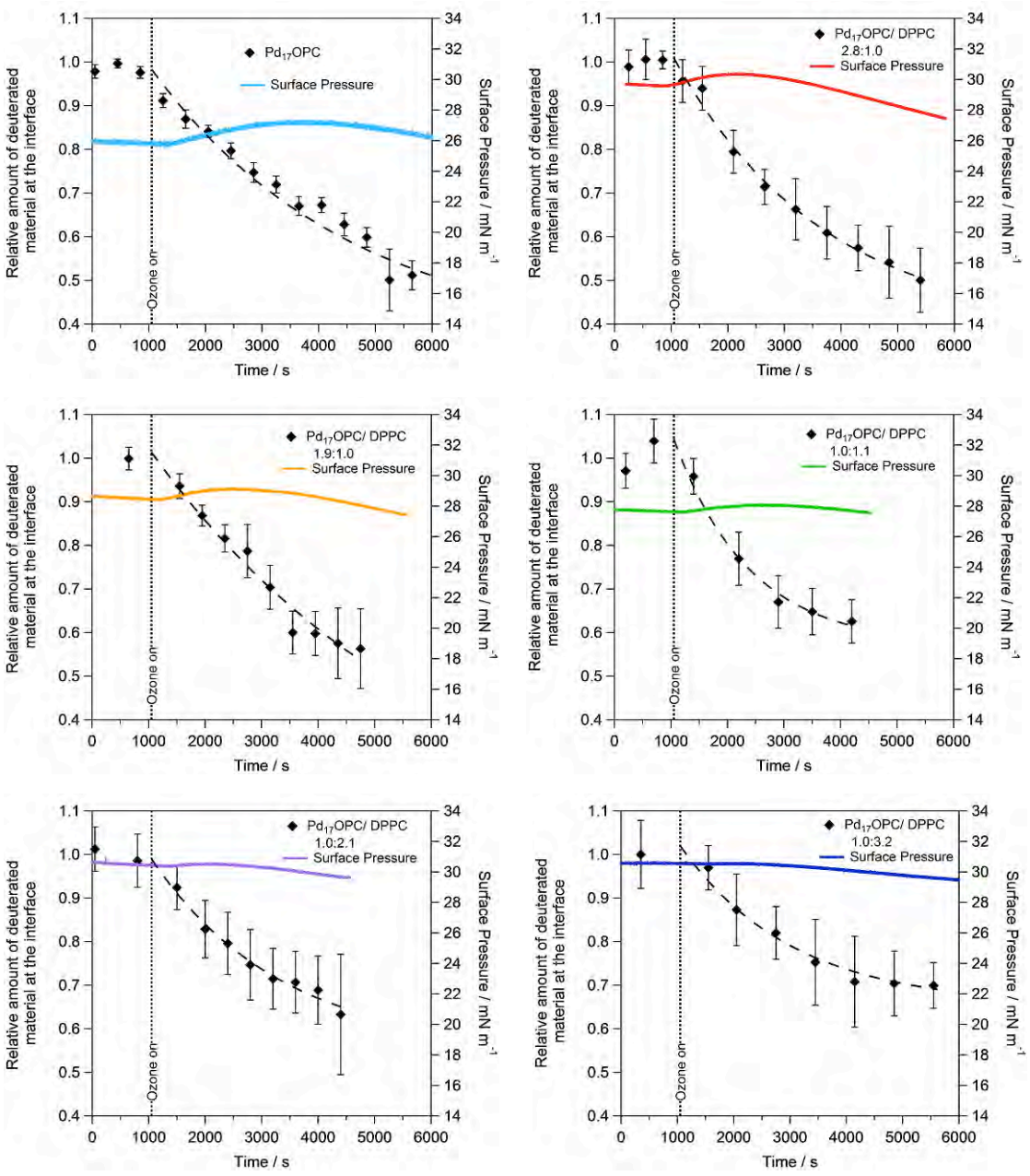

Figure 4.11. Monolayers of $Pd_{17}OPC$ and ^1H DPPC at the air-NRW interface during exposure to ~0.1 ppm ozone.

The surface pressure *versus* time for a monolayer of $Pd_{17}OPC$ and ^1H DPPC on NRW exposed to 0.1 ppm ozone gas for 2 hours. a) 1:0 (light blue), b) 2.8:1.0 (red), c) 1.9:1.0 (orange), d) 1.0:1.1 (green), e) 1.0:2.1 (purple), f) 1.0:3.2 (dark blue) mol/mol. The dotted line represents the time at which the ozoniser was switched on. Black diamonds represent the relative amount of material at the interface, calculated from the fitted neutron scattering length density (ρ_t) multiplied by the thickness (δ_t) of the monolayer at time t divided by the neutron scattering length density (ρ_0) multiplied by the thickness (δ_0) at time 0, determined as described in the main text. The dashed lines show the best fit of neutron data after the ozoniser was switched on, to a single exponential function.

The lifetimes of the material at the interface for each monolayer are presented in Table 4.5. For monolayers where Pd_{17}OPC is the major component, the loss of deuterated material from the interface occurs at the same rate (within error). However, a difference begins to emerge when DPPC becomes the main component of the monolayer, as the loss of material from the interface occurs at an increasingly slower rate. This is evident when comparing the relative amount of material at the interface *versus* time for the mixed monolayers of Pd_{17}OPC and ^{1}H DPPC at 1.0:1.1, 1.0:2.1 and 1.0:3.2 (mol/mol), as shown in Figure 4.12. This suggests that the reaction at the alkene of POPC in monolayers with a higher number of DPPC molecules than POPC molecules occurs at a slower rate. This could be due to the presence of the DPPC molecules preventing the reaction from occurring so rapidly, possibly through shielding the reactive alkene groups in some way.

Monolayer, molecular ratio	Lifetime / min	y offset (B)
Pd_{17}OPC	29.0 (± 5.0)	0.35 (± 0.01)
Pd_{17}OPC & ^{1}H DPPC, 2.8:1.0	27.6 (± 5.4)	0.38 (± 0.05)
Pd_{17}OPC & ^{1}H DPPC, 2.0:1.0	26.5 (± 4.8)	0.33 (± 0.12)
Pd_{17}OPC & ^{1}H DPPC, 1.0:1.1	26.1 (± 5.4)	0.45 (± 0.04)
Pd_{17}OPC & ^{1}H DPPC, 1.0:2.1	30.1 (± 4.0)	0.46 (± 0.06)
Pd_{17}OPC & ^{1}H DPPC, 1.0:3.2	61.2 (± 3.1)	0.61 (± 0.02)

Table 4.5. The lifetimes representing loss of the oleoyl strand of Pd_{17}OPC from mixed Pd_{17}OPC and ^{1}H DPPC monolayers during reaction with ozone at the air-NRW interface.

The lifetimes and y-offset (B in Equation 3.3) values representing loss of the oleoyl strand of Pd_{17}OPC from monolayers of Pd_{17}OPC and Pd_{17}OPC & ^{1}H DPPC during reaction with 0.1 ppm ozone at the air-water interface.

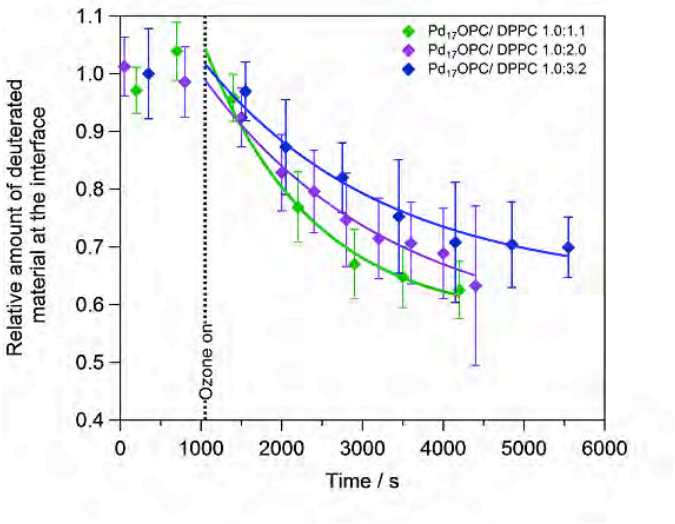

Figure 4.12. Monolayers of Pd_{17}OPC and ^{1}H DPPC (1.0:1.1, 1.0:2.1 and 1.0:3.2, mol/mol) at the air-NRW interface during exposure to 0.1 ppm ozone.

The relative amount of material at the interface *versus* time for monolayers of Pd_{17}OPC and ^{1}H DPPC at 1.0:1.1 (green), 1.0:2.1 (purple) and 1.0:3.2 (blue) (mol/mol) during exposure to 0.1 ppm ozone gas for 2 hours. The relative amount of monolayer material was calculated from the fitted neutron scattering length density (ρ_t) multiplied by the thickness (δ_t) of the monolayer at time t divided by the fitted neutron scattering length density (ρ_0) multiplied by the thickness (δ_0) at time 0. The dotted line represents the time at which the ozoniser was switched on. The solid lines show the best fit of neutron data after the ozoniser was switched on, to a single exponential function.

4.3.2 Reactions Between Monolayers of POPG and Gas Phase Ozone at the Air-Water Interface

The lung surfactant comprises approximately 10% by weight of anionic phospholipids, such as phosphoglycerols. Their presence is believed to be important for interaction with the surfactant proteins. Almost all of the anionic lipids are in the unsaturated form, for example, POPG (Figure 1.5), which is the most common anionic phospholipid in human lung surfactant, comprising approximately 30 mole % of all of the phosphoglycerols.[186] These unsaturated,

anionic phospholipids therefore could possibly react with ozone at the air-water interface.

A monolayer of deuterated POPG where the saturated tail only was deuterated, d_{31} POPG (Figure 3.6), was formed at the air-NRW interface, exposed to ozone at 2 ppm and the surface pressure was monitored over time. This is shown in Figure 4.12. The surface pressure results are very similar to those of a monolayer of POPC exposed to ozone as described in the introduction to this chapter. This suggests that the reaction between the unsaturated chain and ozone does not change in a lipid with a different head group.

The neutron reflectivity of d_{31} POPG monolayers was also measured during ozone exposure. The neutron reflectivity curves were fitted to determine values of the surface scattering length density and thickness at each timepoint, while background and surface roughness were held constant. The fitted data is presented as the amount of deuterated material at the interface against time in Figure 4.13. It is evident that there is an immediate decrease in the neutron reflectivity of the monolayer of POPG upon exposure to ozone, translating as a loss of deuterated material from the interface over time. The overall loss of material is >40% of the saturated deuterated lipid tails. This suggests that POPG reacts in the same manner as POPC, as described in the introduction of this chapter. Fitting the loss of deuterated material from the interface to a single exponential function (Equation 3.3) gives a lifetime of 142 (± 6) minutes and a y-offset of 0.53 (± 0.01), i.e. 53 % of the deuterated material would be expected to remain at the air-water interface after the reaction has gone to completion. These values are similar to those determined for d_{31} POPC reacting with ozone under similar conditions: 184 minutes with a y-offset of 0.58.

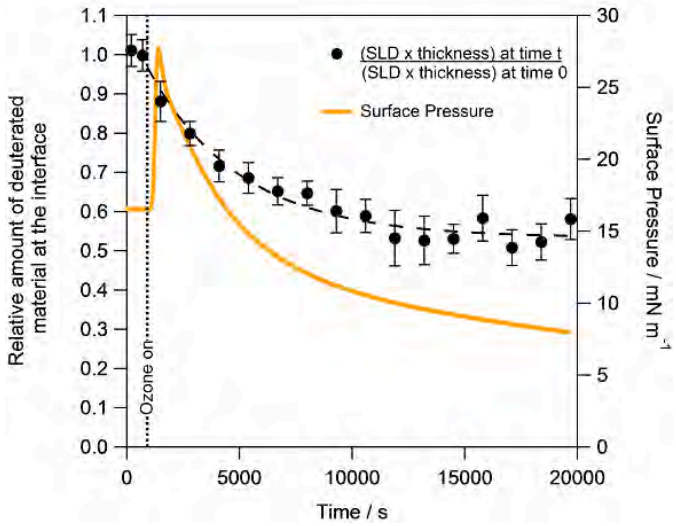

Figure 4.13. A monolayer of d_{31} POPG at the air-NRW interface during exposure to ~2 ppm ozone.

The surface pressure *versus* time (orange line) for a monolayer of d_{31} POPG on NRW exposed to 2 ppm ozone gas for 5.5 hours. The dashed line represents the time at which the ozoniser was switched on. The markers represent the relative amount of deuterated POPG material, calculated from the fitted neutron scattering length density (ρ_t) multiplied by the thickness (δ_t) of the monolayer at time t divided by the fitted neutron scattering length density (ρ_0) multiplied by the thickness (δ_0) at time 0. The dashed line shows the best fit, to a single exponential function, of neutron data after the ozoniser was switched on.

Additionally, X-ray reflectivity of monolayers of POPG on buffered water was measured continuously during 1.1 ppm ozone exposure in order to provide a more accurate way for examining the change in thickness of the monolayer after ozone damage. The X-ray reflectivity curves of a monolayer of POPG on water before and after ozone exposure are shown in Figure 4.14. Similarly to POPC, after ozone there is an increase in width of the fringe spacing after ozone, indicating that a thinner monolayer is present at the interface. The X-ray reflectivity curves were fitted to determine values of the surface scattering length density and thickness at each timepoint, while background and surface roughness were held constant. The change in the surface pressure, scattering length density and monolayer thickness *versus* time during the reaction is presented in Figure 4.15. There was a rapid

change in thickness from approximately 23 Å to less than 14 Å, corresponding to a 40% loss in monolayer thickness.

Fitting the scattering length density *versus* time, shown in Figure 4.15, to a single exponential using Equation 3.3 gave a lifetime of 6.5 (± 1.8) minutes with an offset of 10.68 (± 0.02) x 10^{-6} $Å^{-2}$, whereas fitting the thickness *versus* time gave a lifetime of 16.6 (± 0.6) minutes with an offset of 15.5 (± 0.1) Å. Therefore, the decrease in X-ray scattering length density of the film occurs more rapidly than the decrease in monolayer thickness with time, similarly to the results observed for POPC using X-ray reflectivity.

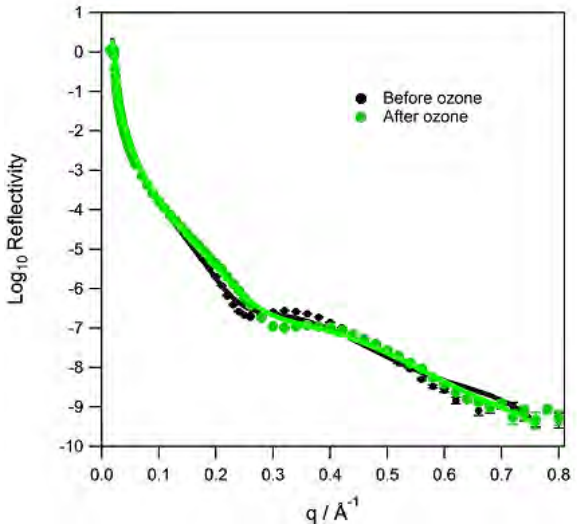

Figure 4.14. X-ray reflectivity of a monolayer of POPG at the air-water interface before and after exposure to ~1.1 ppm ozone.

The X-ray reflectivity curves of a monolayer of POPG on water before ozone (black) and after ozone (green). The measured data is represented by the round markers and the best fit of the curves is shown by the solid lines.

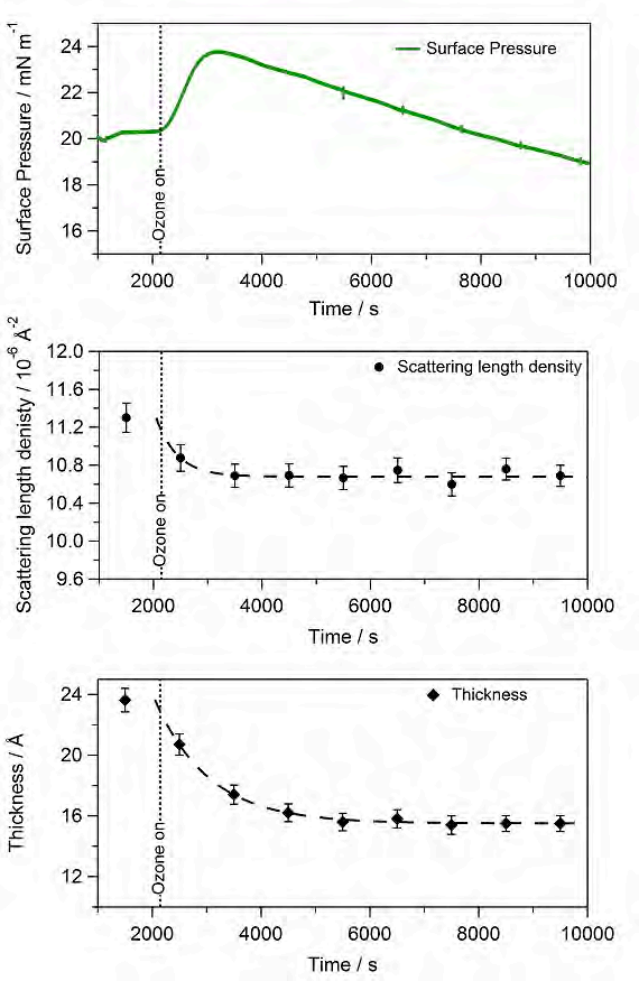

Figure 4.15. The surface pressure, scattering length density and thickness of a monolayer of POPG at the air-water interface during exposure to ~1.1 ppm ozone for 4 hours.

Top panel: The surface pressure *versus* time (green line).
Middle panel: Black circles show the fitted X-ray scattering length density. The dashed line shows the best fit of X-ray data after the ozoniser was switched on, to a single exponential function.
Bottom panel: Black diamonds represent the fitted thickness of the monolayer. The dashed line shows the best fit of X-ray data after the ozoniser was switched on, to a single exponential function.
The vertical dotted line represents the time at which the ozoniser was switched on in all cases.

4.3.3 Reactions Between Monolayers of Cholesterol and Gas-Phase Ozone at the Air-Water Interface

Cholesterol is a significant component of the lung surfactant and although very little is known about its purpose it is thought that its presence at normal levels (3-7 % by weight in humans[8,12]) is important for promoting the fluidity of the lung surfactant. The results presented here aim to characterise changes to monolayers of cholesterol following ozone exposure at the air-water interface using surface pressure and X-ray reflectivity measurements. The structure of the monolayers was compared before, during and after ozone exposure to discover how the molecule could be damaged within the lung surfactant during periods of high ozone. Mixed monolayers of cholesterol and POPC were also investigated.

A monolayer of cholesterol was formed at the air-water interface and the X-ray reflectivity of the surface film was measured at three different surface pressures (representing three different areas per lipid: 32, 34 and 37 $Å^2$) in an oxygen atmosphere. The X-ray reflectivity curves of the monolayer at each surface pressure are shown in Figure 4.16. The X-ray reflectivity curves were fitted to determine values of the surface scattering length density and thickness at each timepoint, while background and surface roughness were held constant. The roughness was held at 5 Å for the fitting of each curve. As the surface pressure of the monolayer increased (and therefore area per lipid decreased), the thickness of the monolayer rose slightly from 12.6 (± 0.2) Å at 10-20 mN m^{-1} to 13.0 (± 0.1) Å at 30 mN m^{-1}.

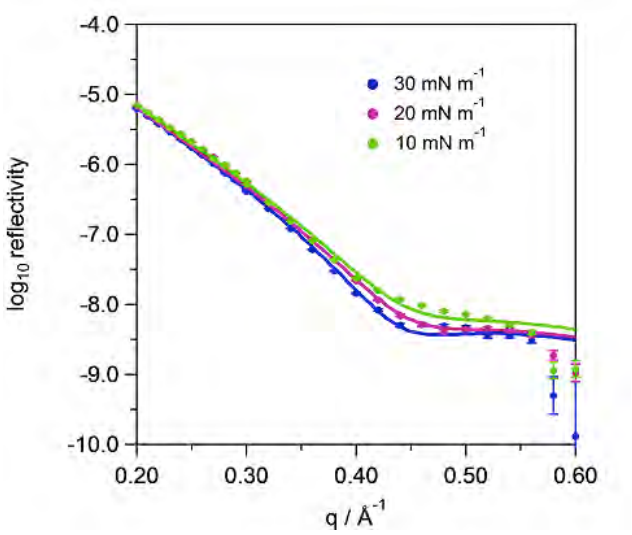

Figure 4.16. X-ray reflectivity curves of a monolayer of cholesterol at 3 different areas per lipid.

The X-ray reflectivity curves of a monolayer of cholesterol on water at: a) 30 mN m^{-1} (blue), b) 20 mN m^{-1} (pink) and c) 10 mN m^{-1} (green). The measured data is represented by the round markers and the best fit of the curves is shown by the solid lines.

To investigate the reaction between monolayers of cholesterol and ozone at the air-water interface, the surface pressure of the monolayers was measured continuously during ozone exposure. Figure 4.17 shows the surface pressure *versus* time of a monolayer of cholesterol exposed to 1.1 ppm ozone and the surface pressure of a monolayer of cholesterol exposed to 0.25 ppm ozone. When ozone is switched on there is an immediate, small decrease in surface pressure followed by a rapid, large increase in surface pressure (decrease in surface tension) for the higher concentration. At the lower concentration of ozone, there is no visible initial decrease in surface pressure. Since an oxidation reaction at the carbon-carbon double bond within cholesterol would cause the molecule to become more hydrophilic overall, this overall increase in surface pressure could be due to a change in the arrangement of the lipid at the interface.

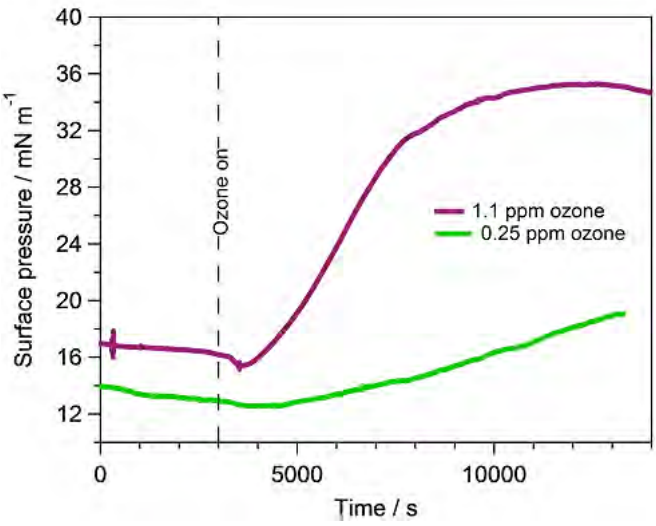

Figure 4.17. The surface pressure *versus* time for monolayers of cholesterol on water exposed to 1.1 ppm ozone (purple line) and 0.25 ppm ozone (green line).

The dashed line represents the time at which the ozoniser was switched on.

To examine this further, X-ray reflectivity of cholesterol monolayers at the air-water interface was measured during 1.1 ppm or 0.25 ppm ozone exposure. Figure 4.18 shows the X-ray reflectivity curves of a monolayer of cholesterol on water before and after 1.1 ppm ozone exposure. After ozone, the reflectivity of the monolayer has increased and the fringe spacing of the curve is slightly narrower, indicating a thicker layer after oxidation. Fitting the reflectivity curves as described above gave values of scattering length density and thickness that are significantly higher after ozone exposure. The change in the surface pressure, scattering length density and monolayer thickness *versus* time during the reaction is presented in Figure 4.19.

Fitting the scattering length density *versus* time, shown in Figure 4.19, to a single exponential using Equation 3.3 gave a lifetime of 324.3 (± 15.5) minutes with an offset of 11.74 (± 0.24) x 10^{-6} Å^{-2}, whereas fitting the thickness *versus* time gave a lifetime of 21.0 (± 4.2) minutes with an offset of 14.31 (± 0.10) Å. Therefore, the increase in thickness was much more rapid than the increase in scattering length density of the monolayer. The thickness rapidly increased by ~20 % upon ozone exposure.

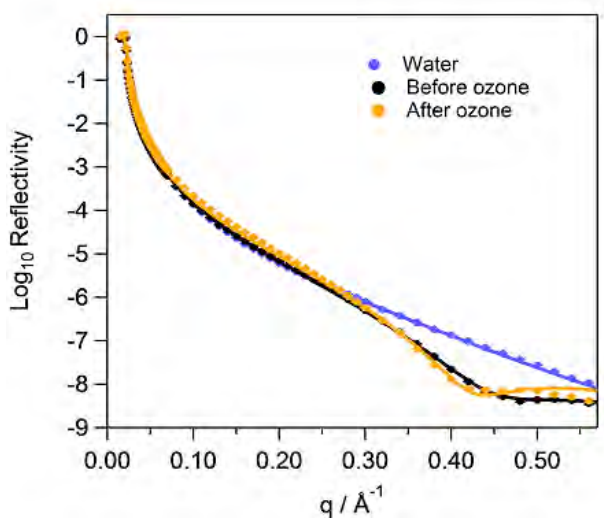

Figure 4.18. X-ray reflectivity of a monolayer of cholesterol at the air-water interface before and after exposure to ~1.1 ppm ozone.

The X-ray reflectivity curves of a monolayer of cholesterol on water before ozone (black) and after ozone (orange). The X-ray reflectivity curve of water alone is also shown in blue. The measured data is represented by the round markers and the best fit of the curves is shown by the solid lines.

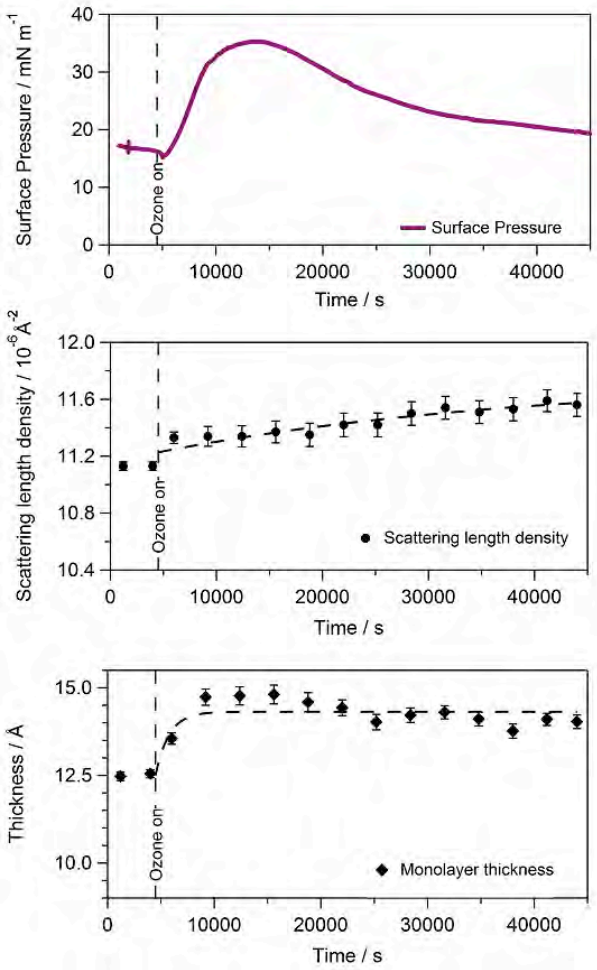

Figure 4.19. The surface pressure, scattering length density and thickness of a monolayer of cholesterol at the air-water interface during exposure to ~1.1 ppm ozone for 11 hours.

Top panel: The surface pressure *versus* time (purple line).

Middle panel: Black circles show the fitted X-ray scattering length density. The dashed line shows the best fit of X-ray data after the ozoniser was switched on, to a single exponential function.

Bottom panel: Black diamonds represent the fitted thickness of the cholesterol monolayer. The dashed line shows the best fit of X-ray data after the ozoniser was switched on, to a single exponential function.

The dashed vertical line represents the time at which the ozone was switched on in all cases.

Figure 4.20 shows the change in surface pressure, scattering length density and monolayer thickness *versus* time for a monolayer of cholesterol exposed to 0.25 ppm ozone at the air-water interface. Similarly to the reaction at 1.1 ppm, there is an increase in surface pressure, scattering length density and thickness upon ozone exposure. Fitting the scattering length density *versus* time, shown in Figure 4.20, to a single exponential using Equation 3.3 gave a lifetime of 504.3 (± 7.5) minutes with an offset of 11.71 (± 0.08) x 10^{-6} $Å^{-2}$, whereas fitting the thickness *versus* time gave a lifetime of 104.3 (± 7.5) minutes with an offset of 11.74 (± 0.24) Å. The rates of increase in surface pressure and thickness of a monolayer of cholesterol are therefore slower, as expected, in a 0.25 ppm ozone atmosphere than a 1.1 ppm atmosphere.

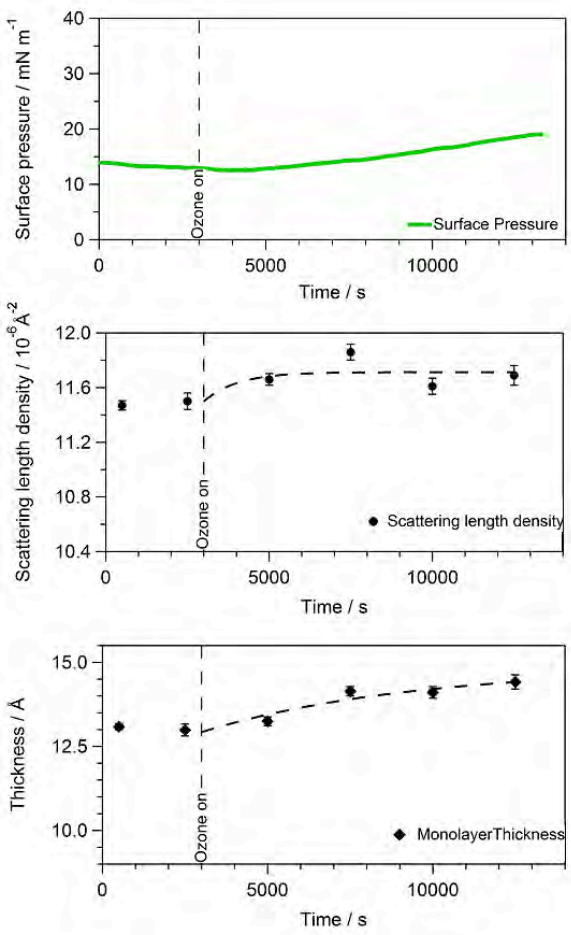

Figure 4.20. The surface pressure, scattering length density and thickness of a monolayer of cholesterol at the air-water interface during exposure to ~0.25 ppm ozone for 3 hours.

Top panel: The surface pressure *versus* time (green line).

Middle panel: Black circles show the fitted X-ray scattering length density. The dashed line shows the best fit of X-ray data after the ozoniser was switched on, to a single exponential function.

Bottom panel: Black diamonds represent the fitted thickness of the cholesterol monolayer. The dashed line shows the best fit of X-ray data after the ozoniser was switched on, to a single exponential function.

The vertical dashed line represents the time at which the ozone was switched on in all cases.

4.3.4 Reactions Between Cholesterol and POPC Mixed Monolayers and Gas Phase Ozone at the Air-Water Interface

It has now been well established above that both of the important lung surfactant components cholesterol and POPC are rapidly oxidised by ozone at the air-water interface. The reaction between ozone and mixed monolayers of cholesterol and POPC has been studied in order to investigate how the kinetics and mechanism of the individual reactions are affected by the presence of the other lipid.

Figure 4.21 shows the surface pressure data of monolayers of cholesterol and POPC at ratios of 1:0, 8:1, 2:1, 1:2 and 0:1 mol/mol during exposure to 2 ppm ozone at the air-water interface. When ozone is switched on, the surface pressure of a monolayer of cholesterol drops initially by ~2 mN m^{-1} and then rises by a large extent of about 15 mN m^{-1}. In the case of a monolayer of pure POPC, when ozone is switched on there is no initial drop in surface pressure but there is a rapid initial increase in surface pressure that occurs at a much quicker rate than the surface pressure increase for a monolayer of cholesterol alone. Increasing levels of POPC within a monolayer of cholesterol causes an increasingly smaller initial drop in surface pressure. Also, the following rise in surface pressure becomes much faster with increasing levels of POPC. When the molecular ratio of POPC exceeds that of cholesterol (cholesterol and POPC, 1:2 mol/mol) there is no initial drop in surface pressure and there are two surface pressure rises, the first increase corresponding to oxidation of POPC and the second corresponding to oxidation of cholesterol. The overall increase in surface pressure increase is much smaller than when more cholesterol is present.

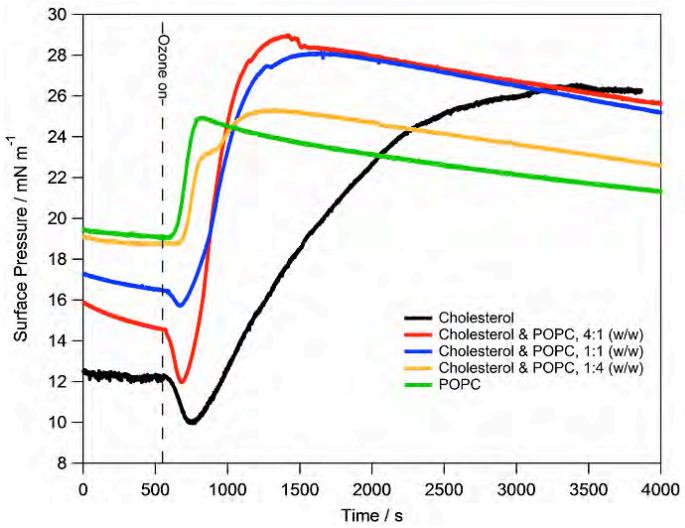

Figure 4.21. Monolayers of cholesterol and POPC exposed to ozone at the air-water interface.

The surface pressure *versus* time for the exposure of 2 ppm ozone to monolayers of cholesterol and POPC at 1:0, 8:1, 2:1, 1:2 and 0:1 mol/mol. The dashed line represents the time at which the ozoniser was switched on.

In order to investigate this further, some X-ray reflectivity experiments were performed to look at changes in the monolayer structure of POPC and cholesterol mixtures during ozonolysis. Figure 4.22 shows the X-ray reflectivity curve of a monolayer cholesterol and POPC at 1.0:2.0 mol/mol before and after ozone exposure. This molecular ratio was chosen for X-ray studies as it represents more closely the ratio of cholesterol to POPC in the lung surfactant.[8] The X-ray reflectivity curve is very different after ozone. The fringe spacing is wider after oxidation suggesting a decrease in monolayer thickness, whereas for cholesterol alone a narrower fringe spacing was observed, indicating a thicker layer after oxidation.

The X-ray reflectivity curves were fitted at each timepoint to determine values of the surface scattering length density and thickness, while background and surface roughness were held constant. The surface pressure, scattering length density and thickness *versus* time of monolayers of POPC, cholesterol and POPC/cholesterol (1:2, mol/mol) are presented in Figure 4.23.

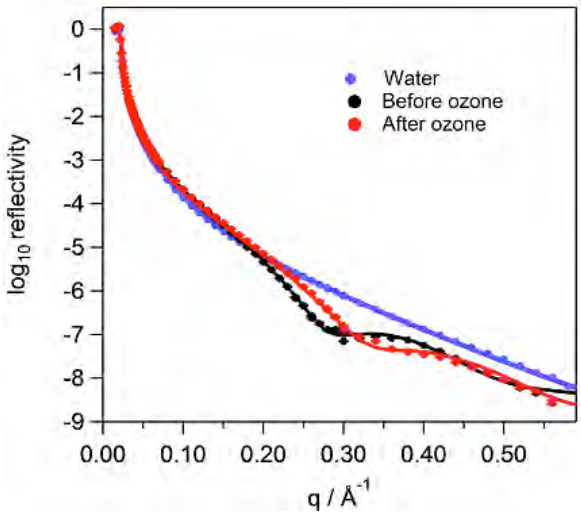

Figure 4.22. X-ray reflectivity of a monolayer of cholesterol and POPC (1:2, mol/mol) at the air-water interface before and after exposure to ~1.1 ppm ozone.

The X-ray reflectivity curves of water (blue), a monolayer of cholesterol and POPC (1:2, mol/mol) on water before (black) and after ozone (red). The measured data is represented by the round markers and the best fit of the curves is shown by the solid lines.

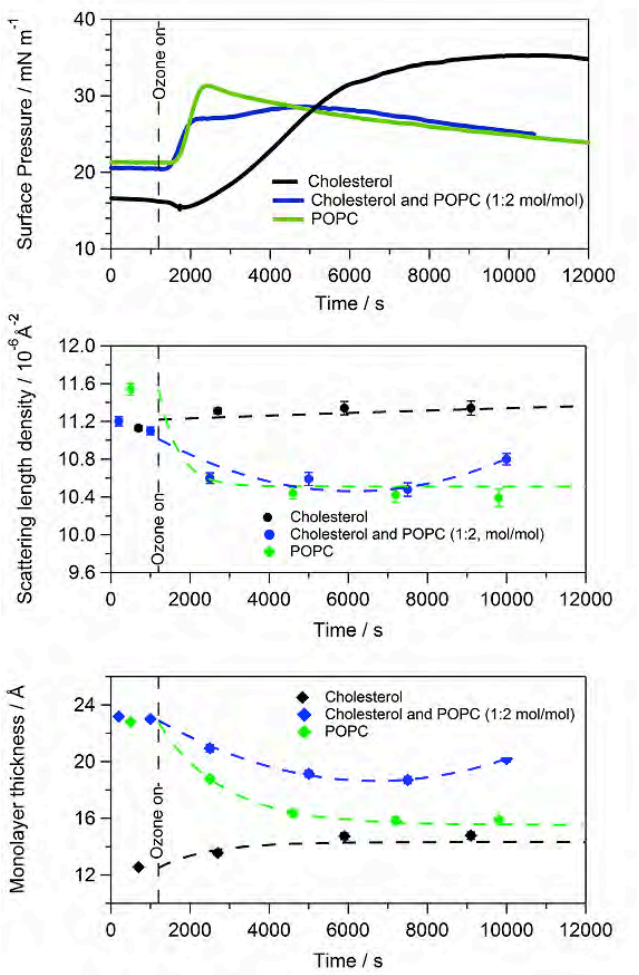

Figure 4.23. The surface pressure, scattering length density and thickness of monolayers of cholesterol, POPC and cholesterol/POPC (1:2, mol/mol) at the air-water interface during exposure to ~1.1 ppm ozone for 3 hours.

Top panel: The surface pressure *versus* time for the monolayers of cholesterol (black), POPC (green) and cholesterol/POPC (blue, 1:2, mol/mol).
Middle panel: The fitted X-ray scattering length density of monolayers of cholesterol (black), POPC (green) and cholesterol/POPC (blue, 1:2, mol/mol). The dashed lines show the best fit of X-ray data after the ozoniser was switched on, to a single or double exponential function, as required.
Bottom panel: The fitted thickness of monolayers of cholesterol (black), POPC (green) and cholesterol/POPC (blue, 1:2, mol/mol). The dashed lines show the best fit of X-ray data after the ozoniser was switched on, to a single or double exponential function, as required.
The vertical dashed line represents the time at which the ozone was switched on in all cases.

The lifetimes for the scattering length densities and thicknesses *versus* time of the monolayers presented in Figure 4.23 are shown in Tables 4.6 and 4.7 respectively. The mixed cholesterol and POPC monolayer reaction with ozone required a double exponential function to suitably fit the data, suggesting two separate reactions were occurring. The scattering length density and thickness of the mixed cholesterol/ POPC monolayer decreased and then increased during oxidation, supporting the surface pressure data that suggested POPC reacted with ozone, followed by cholesterol.

Monolayer	Lifetime 1 / min	Lifetime 2 / min	y offset / 10^{-6} Å^{-2}
Cholesterol	524.3 (± 45.5)		11.74 (± 0.24)
Cholesterol & POPC, 1:2 (mol/mol)	2.4 (± 0.2)	34.0 (± 4.5)	10.76 (± 0.21)
POPC	8.3 (± 1.2)		10.51 (± 0.02)

Table 4.6. The lifetime data for changes in scattering length density *versus* time of monolayers of cholesterol, POPC and cholesterol/POPC (1:2, mol/mol) during exposure to 1.1 ppm ozone.

Monolayer	Lifetime 1 / min	Lifetime 2 / min	y offset / Å
Cholesterol	21.0 (± 4.2)		14.31 (± 0.10)
Cholesterol & POPC, 1:2 (mol/mol)	20.3 (± 2.1)	24.7 (± 3.6)	15.20 (± 0.23)
POPC	27.0 (± 1.7)		15.50 (± 0.10)

Table 4.7. The lifetime data for changes in thickness *versus* time of monolayers of cholesterol, POPC and cholesterol/POPC (1:2, mol/mol) during exposure to 1.1 ppm ozone.

4.3.5 Reactions Between Pig Lung Surfactant Monolayers and Gas Phase Ozone at the Air-Water Interface

It has now been established how monolayers of phospholipids, cholesterol or surfactant protein B analogues, as well as mixtures of the lung surfactant components, are affected and damaged by the air pollutant ozone at the air-water interface. This section aims to investigate how whole lung surfactant, extracted from pig or sheep lungs, is damaged by ozone at the air-water interface, and to compare the surface pressure and reflectivity data to the individual components to provide a clearer picture of how the surfactant becomes damaged when lungs are exposed to ozone pollution.

Natural lung surfactant was extracted from fresh, whole pig lungs and contained both lipids and proteins, as described in Section 4.2. In order to demonstrate how the whole extracted pig lung surfactant is damaged by ozone pollution at the air-water interface, monolayers of the lung surfactant were formed on buffered water and the surface pressure and either neutron or X-ray reflectivity were monitored during ozone exposure. First, to ensure that the lung surfactant is stable under oxygen alone for a significant length of time, the surface pressure and X-ray reflectivity of monolayers of pig lung surfactant were measured during oxygen exposure for several hours. The X-ray reflectivity curves were fitted to determine values of the surface scattering length density and thickness at each timepoint, while background and surface roughness were held constant. There is no significant change in the surface pressure and no change in the X-ray reflectivity during this time, as shown in Figure 4.24, therefore the monolayer is stable under an atmosphere of oxygen only. The same results were observed for the lung surfactant extracted from different pigs. The spikes in surface pressure at regular intervals are a result of an interference from movement of the trough during angle change during X-ray measurements.

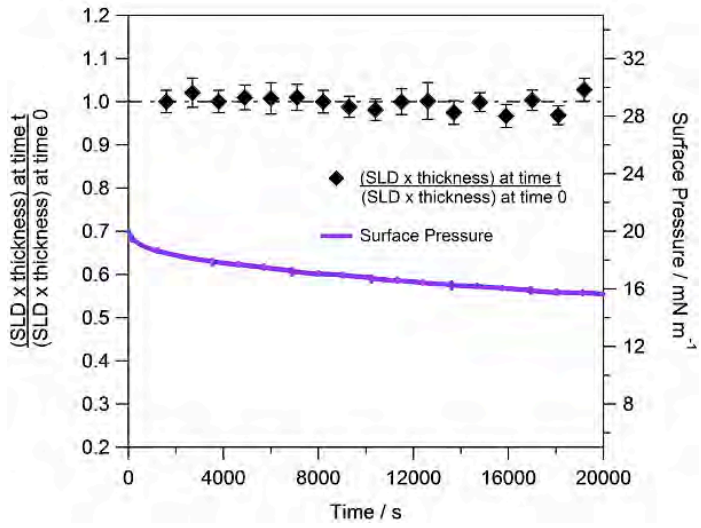

Figure 4.24. A monolayer of pig lung surfactant at the air-water interface during exposure to oxygen.

The surface pressure *versus* time (purple line) for a monolayer of pig lung surfactant on buffered water under oxygen gas for 9 hours. The drop in surface pressure can be attributed to a slow loss of material at the trough barriers. Black diamonds represent the relative amount of pig lung surfactant material, calculated from the fitted X-ray scattering length density (ρ_t) multiplied by the thickness (δ_t) of the monolayer at time t divided by the fitted X-ray scattering length density (ρ_0) multiplied by the thickness (δ_0) at time 0.

Monolayers of pig lung surfactant were formed at the air-water interface at different initial surface pressures and exposed to 1.1 ppm ozone. The surface pressure was measured continuously and is presented in Figure 4.25. The surface pressure of the monolayer changes significantly upon ozone exposure. There is a rapid small peak in surface pressure; followed by a slower rise and then a steady, large decrease in surface pressure over several hours. This change in surface pressure shows that the monolayer is significantly oxidised by ozone at the air-water interface causing changes to the interaction between molecules at the surface. The sequential increases and decreases in surface pressure could be attributed to the different rates of reaction between ozone and the individual components of the lung surfactant. The initial surface pressure of the lung surfactant monolayer appears to slightly alter the rate of reaction with ozone, as the surface pressure falls at a faster rate overall when the initial surface pressure is higher.

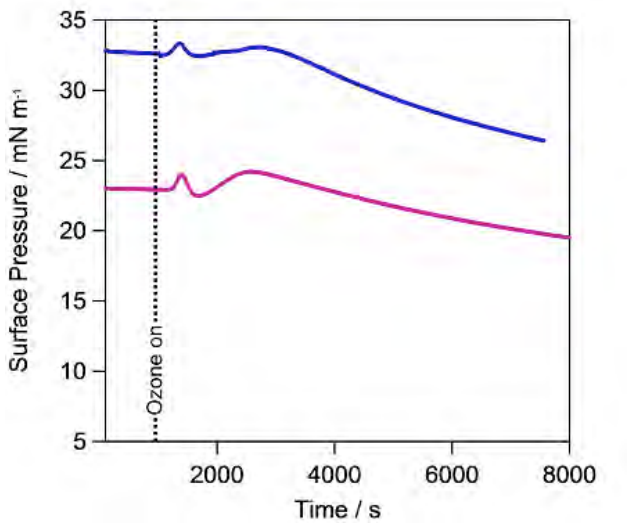

Figure 4.25. Surface pressure measurements of monolayers of pig lung surfactant exposed to ozone at the air-water interface.

The surface pressure *versus* time for the exposure of 1.1 ppm ozone to monolayers of pig lung surfactant at an initial surface pressure of 33 mN m^{-1} (blue) and 23 mN m^{-1} (purple). The dotted line represents the time at which the ozoniser was switched on.

Neutron reflectivity was used to investigate the changes in the interfacial structure of pig lung surfactant monolayers at both the air-NRW and air-D_2O interface. Figure 4.26 presents the relative amount of material, calculated from the neutron reflectivity curves as previously described, of a monolayer of pig lung surfactant on NRW during exposure to 1.1 ppm ozone. Approximately 40% of the monolayer material was lost from the interface during 11 hours of exposure. Fitting the loss of material to an exponential function gave a lifetime of 165.4 (± 4.3) minutes with a y-offset of 0.47 (± 0.06).

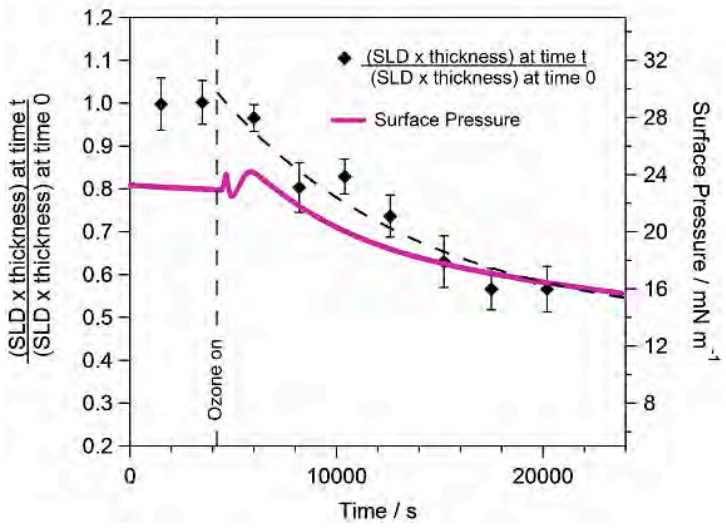

Figure 4.26. A monolayer of pig lung surfactant at the air-NRW interface during exposure to ~1.1 ppm ozone.

The surface pressure *versus* time (pink line) for a monolayer of pig lung surfactant on NRW exposed to 1.1 ppm ozone gas for 11 hours. The dashed line represents the time at which the ozoniser was switched on. The markers represent the relative amount of lung surfactant material, calculated from the fitted neutron scattering length density (ρ_t) multiplied by the thickness (δ_t) of the monolayer at time t divided by the fitted neutron scattering length density (ρ_0) multiplied by the thickness (δ_0) at time 0. The dashed line shows the best fit, to a single exponential function, of neutron data after the ozoniser was switched on.

The neutron reflectivity curves for monolayers of pig lung surfactant on D_2O during ozone exposure were fitted to obtain values of scattering length density and thickness at each timepoint. The fitted values, along with the surface pressure, *versus* time are presented in Figure 4.27. The neutron reflectivity of a monolayer of lung surfactant on D_2O is lower than the neutron reflectivity of the D_2O subphase alone, due to the low scattering length of the hydrogenated molecules within the lung surfactant. After exposure to ozone, there is an increase in the reflectivity of the surface film therefore an increase in the scattering length density at the surface, as shown in Figure 4.27. This could suggest a loss of material from the interface, as shown in the experiments on NRW, or an increase in the hydration of the surfactant monolayer as the molecules become more

hydrophilic. Hence, as more D_2O solvent is incorporated into the monolayer, D_2O would contribute more to the surface reflectivity. Fitting the increase in scattering length density during ozone exposure to a single exponential gives a lifetime of 23.0 (± 1.3) minutes with a y-offset (B) of 1.61 (± 0.17) x 10^{-6} $Å^{-2}$. This short lifetime could suggest that the reaction could be occurring faster than the reaction in Figure 4.26 because the initial surface pressure was higher, however it is unlikely that such an increase in surface pressure from 22 to 32 mN m^{-1} would equate to a large decrease area per molecule. It is more likely, therefore, that the monolayer more rapidly rearranges to become hydrated so that the D_2O contributed more to the scattering length density of the surface upon ozone exposure.

Figure 4.27 also shows that the thickness of the monolayer decreases rapidly and significantly immediately upon ozone exposure: the thickness decreases by approximately 20-30 % after only 15 minutes of exposure. The lifetime of this decrease in thickness was calculated to be 7.8 (± 1.6) minutes with a y-offset (B) of 13.60 (± 0.22) Å from the initial thickness of 18.1 (± 0.3) Å. The thickness calculated for the monolayer on D_2O does, however, gives little information of the tail groups owing to their low scattering length density. Therefore, it better represents the hydrated head regions of lipids.

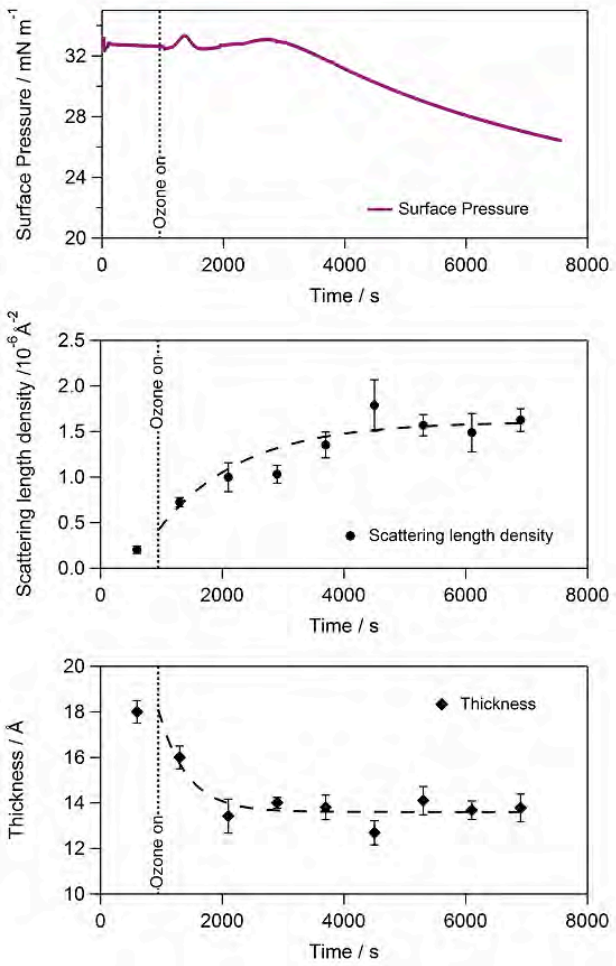

Figure 4.27. The surface pressure, neutron scattering length density and thickness of a monolayer of pig lung surfactant at the air-D_2O interface during exposure to ~1.1 ppm ozone for 2 hours.

Top panel: The surface pressure *versus* time (green line).

Middle panel: Black circles show the fitted neutron scattering length density. The dashed line shows the best fit of X-ray data after the ozoniser was switched on, to a single exponential function.

Bottom panel: Black diamonds represent the fitted thickness of the pig lung surfactant monolayer. The dashed line shows the best fit of X-ray data after the ozoniser was switched on, to a single exponential function.

The dotted line represents the time at which the ozone was switched on in all cases.

To accompany the neutron data, X-ray reflectivity of monolayers of pig lung surfactant during ozone exposure was performed. X-ray experiments were done on multiple pig lung surfactants to ensure the results were consistent, and at 3 different ozone concentrations to investigate the effect on kinetics of the reaction. Firstly, pig lung surfactant was characterised to show how the thickness and scattering length density of the surface film changed at different surface pressures (areas per molecule). This was done using X-rays because of the ability to measure to higher q compared to neutrons, so thicknesses could be more accurately calculated. Additionally, because the natural lung surfactant cannot be manipulated by deuteration of the monolayer, the usefulness of neutron reflectivity can be limited. The X-ray reflectivity of a monolayer of pig lung surfactant at 5 different surface pressures is shown in Figure 4.28. The most striking difference between the reflectivity curves is the decrease in fringe width as the surface pressure of the lung surfactant increases (or area per molecule decreases), in particular from 14-20 mN m^{-1}. This shows that as the monolayer becomes more compressed, the molecules appear to lie in a more ordered, vertical manner. This fitted data is presented in Table 4.8. The thickness values are slightly lower than those fitted using neutron reflectivity above, but this can be attributed to the better accuracy to measure to higher q using X-rays as described above.

Furthermore, since the scattering length density of the monolayer is lower than that of water (9.4×10^{-6} $Å^{-2}$), the reflectivity of the interface with the monolayer present is lower than that of water alone. As the surface pressure increases, the scattering length density of the interface decreases, due to the molecules becoming more densely packed at the surface. This means that the water contributes less to the scattering length density of the molecules at the surface.

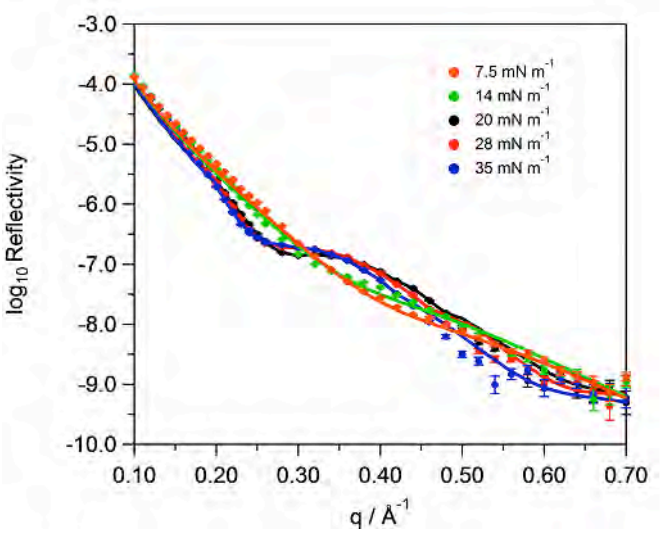

Figure 4.28. X-ray reflectivity curves of a monolayer of pig lung surfactant at different surface pressures.

The X-ray reflectivity curves of a monolayer of pig lung surfactant on water at: a) 35 mN m^{-1} (blue), b) 28 mN m^{-1} (red), c) 20 mN m^{-1} (black), d)14 mN m^{-1} (green) and e) 7.5 mN m^{-1} (orange). The measured data is represented by the round markers and the best fit of the curves is shown by the solid lines.

Surface Pressure / mN m^{-1}	Thickness / Å	Scattering length density / 10^{-6} $Å^{-2}$
7.5	9.7 (± 0.2)	8.64 (± 0.01)
14	11.3 (± 0.3)	8.47 (± 0.03)
20	13.3 (± 0.4)	8.27 (± 0.05)
28	14.0 (± 0.4)	8.27 (± 0.05)
35	14.8 (± 0.5)	8.30 (± 0.06)

Table 4.8. Thickness and scattering length densities of a monolayer of pig lung surfactant at different surface pressures.

The thicknesses and scattering length densities shown were fitted from the X-ray reflectivity curves at each surface pressure, while the background was held constant and roughness was held at 5 Å.

The monolayer of pig lung surfactant was then exposed to three levels of ozone: 1.1, 0.55 and 0.25 ppm and the surface pressure and X-ray reflectivity were monitored continuously. The X-ray reflectivity curve of the pig lung surfactant monolayer before and after 1.1 ppm ozone exposure at the air-water interface is shown in Figure 4.29. Following oxidation by ozone the reflectivity has increased, showing an increase in scattering length density of the film. This suggests a loss of material from the interface as the molecules are now more spread out so the water subphase contributes more to the X-ray reflectivity at the surface. Furthermore, some hydration of the surface film could be occurring. Also, the fringe spacing at high *q* is wider after ozone, suggesting a thinner monolayer film is remaining after oxidation.

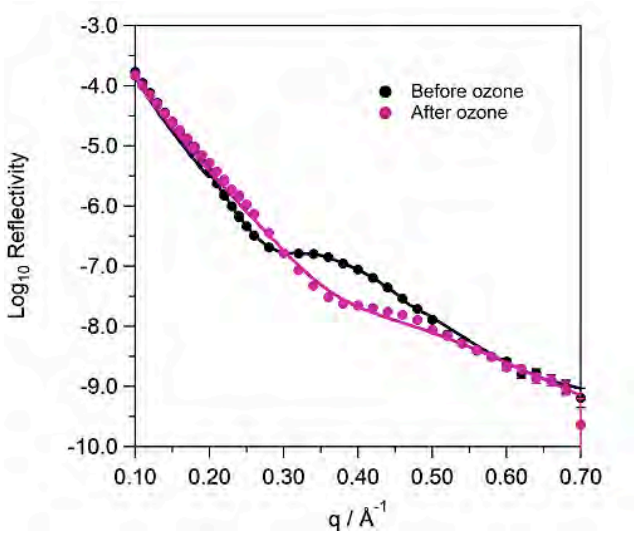

Figure 4.29. X-ray reflectivity of a monolayer of pig lung surfactant at the air-water interface before and after exposure to ~1.1 ppm ozone.

The X-ray reflectivity curves of a monolayer of pig lung surfactant before (black) and after ozone (purple). The measured data is represented by the round markers and the best fit of the curves is shown by the solid lines.

The surface pressure, fitted scattering length density and fitted thickness *versus* time for the exposure of pig lung surfactant to 1.1, 0.55 and 0.25 ppm ozone is presented in Figure 4.30. The surface pressure data shows that as the concentration of the ozone decreases, the rate of change in surface pressure decreases. The surface pressure data for the monolayer exposed to 0.55 ppm

ozone appears to be slightly different, although this is likely to be an experimental issue with the Langmuir trough.

As suggested from the X-ray reflectivity curves shown in Figure 4.29, where reflectivity increased after ozone, the scattering length density of the surface film increases immediately upon ozone exposure at all concentrations. This increase is more rapid with increasing ozone concentration, and this is shown in the lifetimes of the scattering length density, calculated using the exponential function shown in Equation 3.3, as presented in Table 4.9. Also, the thickness of the monolayers *versus* time decreases upon exposure to all three ozone concentrations as shown in Figure 4.29. Table 4.10 demonstrates that the rate of decrease in thickness increases with increasing ozone concentration. This decrease in thickness suggests a change in the orientation of the monolayer at the surface as it reacts with ozone, i.e. a loss of the oleoyl strand from the interface then a partial collapse of the remaining saturated tails.

The lung surfactant from other pigs were exposed to 1.1 ppm ozone at the air-water interface and monitored using surface pressure measurements and X-ray reflectivity. The same results were observed as those shown above.

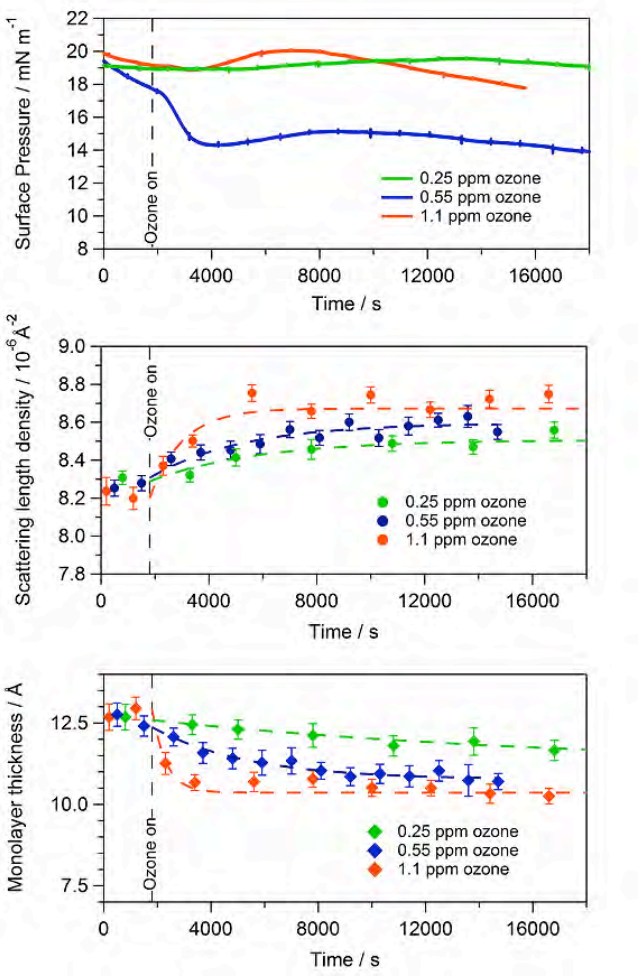

Figure 4.30. The surface pressure, scattering length density and thickness of monolayers of pig lung surfactant at the air-water interface during exposure to ~1.1, 0.55 and 0.25 ppm ozone for 4 hours.

Top panel: The surface pressure *versus* time for monolayers of pig lung surfactant on water exposed to 1.1 (orange), 0.55 (blue) and 0.25 (purple) ppm ozone.
Middle panel: The fitted X-ray scattering length densities of monolayers of pig lung surfactant on water exposed to 1.1 (orange), 0.55 (blue) and 0.25 (purple) ppm ozone. The dashed lines show the best fit of X-ray data after the ozoniser was switched on, to a single exponential function.
Bottom panel: The fitted thickness of monolayers of pig lung surfactant at the air-water interface during exposure to 1.1 (orange), 0.55 (blue) and 0.25 (purple) ppm ozone. The dashed lines show the best fit of X-ray data after the ozoniser was switched on, to a single exponential function.
The vertical dashed line represents the time at which the ozoniser was switched on in all cases.

Ozone concentration / ppm	Lifetime / min	y offset / Å^{-2}
0.25	67.5 (± 3.4)	8.51 (± 0.02)
0.55	57.1 (± 9.7)	8.60 (± 0.03)
1.1	20.1 (± 3.2)	8.67 (± 0.02)

Table 4.9. Lifetimes representing the increase in X-ray scattering length density of pig lung surfactant monolayers during exposure to 1.1, 0.55 and 0.25 ppm ozone.

Ozone concentration / ppm	Lifetime / min	y offset / Å
0.25	276 (± 7.5)	11.13 (± 0.15)
0.55	121.6 (± 9.6)	10.76 (± 0.08)
1.1	8.7 (± 2.3)	10.36 (± 0.07)

Table 4.10. Lifetimes representing the decrease in thickness of pig lung surfactant monolayers during exposure to 1.1, 0.55 and 0.25 ppm ozone.

4.3.6 Reactions Between Sheep Lung Surfactant Monolayers and Gas Phase Ozone at the Air-Water Interface

Lung surfactant is similar across species of land mammals,[8] but to compare how the reaction between ozone and lung surfactant varies with species, monolayers of sheep lung surfactant were exposed to ozone and monitored. Firstly, to ensure that the extracted lung surfactant was stable in oxygen only for a significant length of time, a monolayer of sheep lung surfactant was exposed to an oxygen atmosphere for 9 hours and the surface pressure and neutron reflectivity was measured continuously. The results are presented in Figure 4.31, showing no

significant change in surface pressure or relative amount of material over time, therefore the monolayer is stable under oxygen for this length of time.

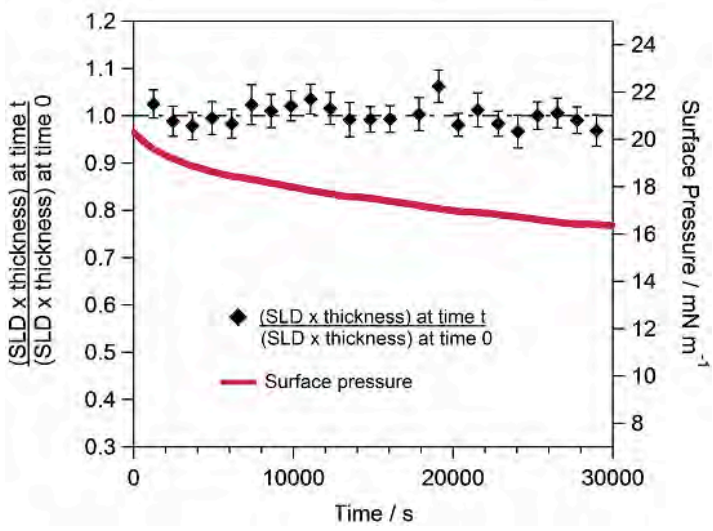

Figure 4.31. A monolayer of sheep lung surfactant at the air-NRW interface during exposure to oxygen.

The surface pressure *versus* time (red line) for a monolayer of sheep lung surfactant on buffered NRW during exposure to oxygen gas for 8 hours. The small drop in surface pressure can be attributed to a slow loss of material at the trough barriers. Black markers represent the relative amount of sheep surfactant material, calculated from the fitted neutron scattering length density (ρ_t) multiplied by the thickness (δ_t) of the monolayer at time t divided by the fitted neutron scattering length density (ρ_0) multiplied by the thickness (δ_0) at time 0.

When a monolayer of sheep lung surfactant on NRW was exposed to ozone at 1.1 ppm, considerable changes in surface pressure and neutron reflectivity were seen over time, as shown in Figure 4.32. Like the pig lung surfactant, the same rapid increase and decrease in surface pressure was observed, followed by a slower increase and decrease to a value much lower than the original film. Also, a decrease in the amount of sheep lung surfactant from the interface was seen when ozone was switched on, corresponding to a ~40 % decrease in the amount of material. The lifetime of this loss is 125.8 (± 9.6) minutes with a y-offset of 0.63 (± 0.02).

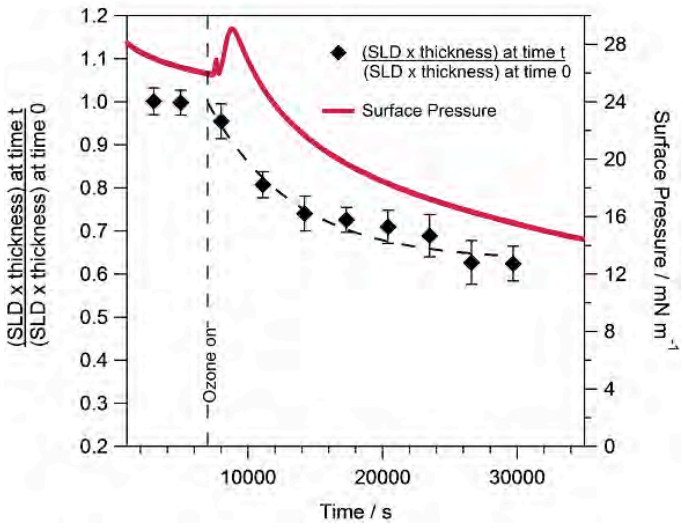

Figure 4.32. A monolayer of sheep lung surfactant at the air-NRW interface during exposure to ~1.1 ppm ozone.

The surface pressure *versus* time (red line) for a monolayer of sheep lung surfactant on NRW exposed to 1.1 ppm ozone gas for 7 hours. A dashed line represents the time at which the ozoniser was switched on. The markers represent the relative amount of lung surfactant material, calculated from the fitted neutron scattering length density (ρ_t) multiplied by the thickness (δ_t) of the monolayer at time t divided by the fitted neutron scattering length density (ρ_0) multiplied by the thickness (δ_0) at time 0. The dashed curve shows the best fit, to a single exponential function, of neutron data after the ozoniser was switched on.

The reaction between sheep lung surfactant and 2 ppm ozone at the air-water interface was also examined using X-ray reflectivity, the results for which are shown in Figure 4.33. The X-ray reflectivity curves before and after ozone exposure show a change in the fringe spacing, where the fringes become wider after ozone, as previously shown for pig lung surfactant. Again, this shows a decrease in monolayer thickness after oxidation.

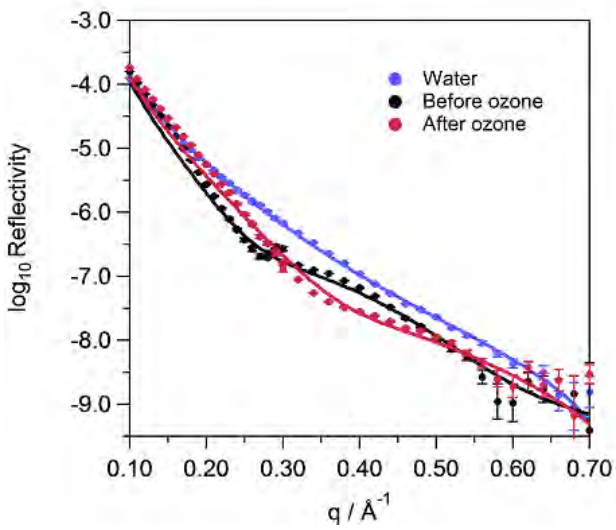

Figure 4.33. X-ray reflectivity of a monolayer of sheep lung surfactant at the air-water interface before and after exposure to ~2 ppm ozone.

The X-ray reflectivity curves of a monolayer of sheep lung surfactant before (black) and after (red) ozone. The X-ray reflectivity curve of water alone is also shown in blue. The measured data is represented by the round markers and the best fit of the curves is shown by the solid lines.

The X-ray reflectivity curves for monolayers of sheep lung surfactant on water during ozone exposure were fitted to obtain values of scattering length density and thickness at each timepoint. The fitted values, along with the surface pressure, *versus* time are presented in Figure 4.34. The X-ray reflectivity of a monolayer of lung surfactant on water is lower than the X-ray reflectivity of the water subphase alone (9.4×10^{-6} Å^{-2}), due to the low X-ray scattering length of the organic molecules within the lung surfactant. After exposure to ozone, there is an increase in the reflectivity of the surface film therefore an increase in the scattering length density at the surface, as shown in Figure 4.34. This is similar to the results observed for pig lung surfactant described above. Fitting the increase in scattering length density during ozone exposure to a single exponential gives a lifetime of 11.0 (± 3.3) minutes with a y-offset of 8.45 (± 0.17) x 10^{-6} Å^{-2}.

Figure 4.34 also shows that the thickness of the monolayer decreases rapidly and significantly immediately upon ozone exposure. The thickness decreases by approximately 30-40 % after only 15 minutes of exposure. The

lifetime of this decrease in thickness was calculated to be 6.4 (± 1.9) minutes with a y-offset of 10.47 (± 0.17) Å.

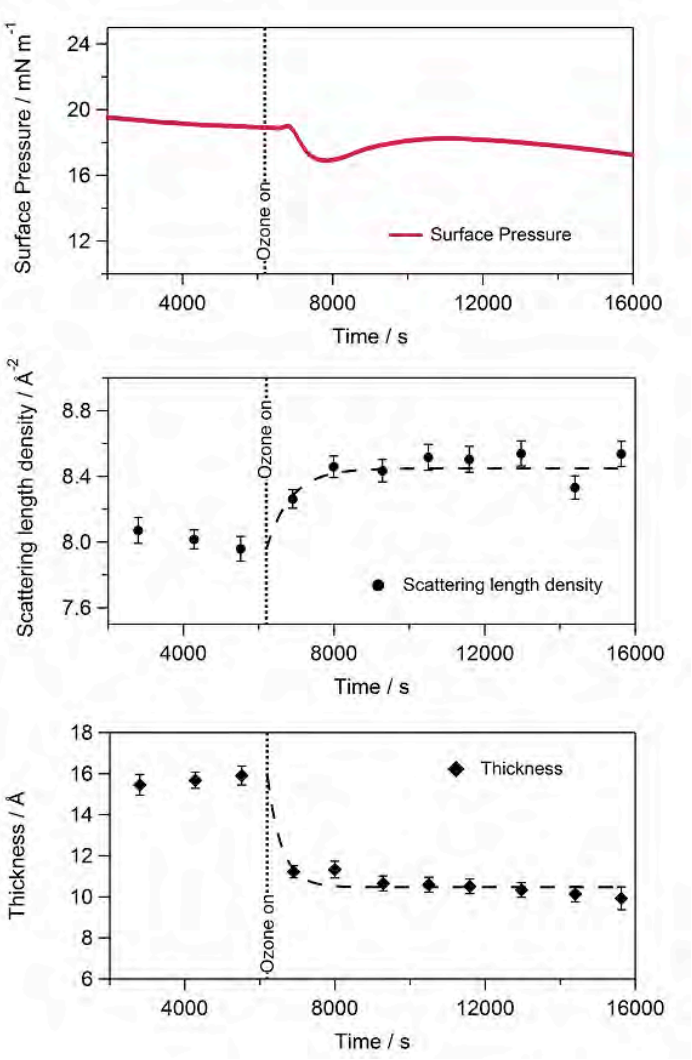

Figure 4.34. The surface pressure, scattering length density and thickness of a monolayer of sheep lung surfactant at the air-water interface during exposure to ~2 ppm ozone for 3 hours.

Top panel: The surface pressure *versus* time (purple line) of the monolayer.
Middle panel: Black circles show the fitted X-ray scattering length density of the The dashed line shows the best fit of X-ray data after the ozoniser was switched on, to a single exponential function.
Bottom panel: Black diamonds represent the fitted thickness of the sheep surfactant monolayer. The dashed line shows the best fit of X-ray data after the ozoniser was switched on, to a single exponential function.
The vertical dotted line represents the time at which the ozone was switched on in all cases.

4.4 Discussion

The aim of this chapter was to investigate and further the previous data researching the damage caused to lipid components of the lung surfactant during times of ozone pollution and then progress to looking at the damage caused to whole extracted lung surfactant by gas-phase ozone.

X-ray reflectivity was used to examine the changes in thickness of the unsaturated phospholipid POPC. The changes in X-ray reflectivity showed a 20-30% decrease in monolayer thickness after exposure to ozone. This correlates well to the previous reported changes in POPC monolayer upon oxidation by Thompson *et al.*,[136] who reported that the POPC showed loss of both lipid tails through damage caused by ozone. Oxidation of the lipid would also cause a change in orientation of the molecules, so it is likely that they would be less vertically ordered after ozonolysis. The oxidised tails would rearrange as they become more hydrophilic, leaving more space for the palmitoyl tails, which would then partially collapse. This would therefore cause a decrease in monolayer thickness. The decrease in thickness *versus* time fitted to an exponential function gave a lifetime of 27 minutes during exposure to ~2 ppm ozone. Thompson *et al.* determined using neutron reflectivity that the loss of the palmitoyl strand during exposure to ~2 ppm had a lifetime of 186 minutes whereas the loss of the oleoyl strand had a lifetime of ~20 minutes during exposure to 0.1 ppm ozone (therefore it would have a much shorter lifetime during exposure to 2 ppm ozone).[136,185] Thus, the lifetime of the decrease in thickness determined using X-ray reflectivity here does not correspond to the timescale of the loss of either the palmitoyl or the oleoyl strand, but somewhere in between these timescales.

Mixed monolayers of Pd_{17}OPC and DPPC were then investigated using neutron reflectivity in order to determine whether the presence of DPPC in a monolayer of POPC affects the oxidation reaction between ozone and POPC in terms of the rate and extent of reaction at the alkene bond. Surface pressure measurements of POPC films containing DPPC showed that the overall surface pressure decrease, normally observed when a POPC monolayer reacts with ozone,

is much smaller with increasing levels of DPPC. This is presumably because the DPPC molecules do not react with ozone under these conditions, therefore the molecules are still fully capable of reducing surface tension within the monolayer to their normal capability. Furthermore, it is possible that the presence of intact DPPC molecules keeps the oxidation products at the interface.

Neutron reflectivity measurements showed that the presence of DPPC within the monolayer of Pd_{17}OPC had little effect on the initial reaction at the carbon-carbon double bond when POPC was the major component of the monolayer mixture. The rate of loss of the oleoyl strand of POPC from the interface was the same until DPPC became the major component of the monolayer. As the molecular ratio of POPC:DPPC increased from 1.0:1.1 to 1.0:2.1 to 1.0:3.2, the rate of loss of the oleoyl strand appeared to decrease. Qiao *et al.* recently showed that the reaction between low levels of ozone and DOPC monolayers was selective in the presence of DPPC molecules (at a ratio of 1:1) as some DOPC molecules remained unoxidised at the interface after oxidation, therefore DPPC affected the oxidation of DOPC.[187] This corresponds well with the results observed for POPC here, although this effect was only observed at higher levels of POPC using this technique. An explanation for this phenomenon could be that the DPPC molecules are "blocking" the reaction between ozone and POPC. The alkene group within the POPC means that the molecules have a "kink" in their tails resulting in monolayers that become less densely packed. DPPC molecules can pack much more closely, hence their prominent role in the lung surfactant at sufficiently reducing surface tension. It could be possible that the presence of DPPC at this ratio prevents the ozone molecules from interacting with the POPC so rapidly, as it is more difficult for the gas molecules to reach them; therefore increasing levels of DPPC in the POPC monolayer slows the rate of reaction between ozone and the alkene. It is also possible that phase separation can occur at some ratios of DPPC:POPC, for example when lower levels of DPPC are present (1:1 or less), more phase separation could be occurring, hence the reaction occurs more quickly because the POPC molecules are more accessible.

The ozonolysis of the anionic, unsaturated phospholipid POPG was also investigated at the air-water interface using both neutron and X-ray reflectivity. The surface pressure increased rapidly upon ozone exposure and then fell to a

level much lower than that of the initial film. These results are the same as shown previously for POPC, as was expected since the molecules have the same lipid tails, which is where the reaction is occurring. Neutron reflectivity of d_{31}POPG revealed that loss of the palmitoyl tail from the air-water interface occured, as previously observed in the case of d_{31} POPC. The overall loss of deuterated material from the interface is approximately 40 %, the same as observed for the loss of deuterated material from a monolayer of d_{31} POPC. The lifetime of the loss of the deuterated palmitoyl strand from d_{31} POPG is 142 minutes when exposed to 2 ppm ozone with a starting surface pressure of 15 mN m^{-1}, which is similar to the stated value for loss of the deuterated strand from d_{31} POPC (186 minutes[136]) in similar conditions. Interestingly, the reaction between monolayers of SMB/POPG and ozone, described in section 3.6.2.1, had a very similar lifetime of loss of deuterated palmitoyl material (145 minutes). This suggests that the presence of the peptide mimic within the POPG monolayer does not affect the rate of reaction between the lipid and ozone.

The X-ray reflectivity of monolayers of POPG at the air-water interface was also performed during ozone exposure. The thickness of the monolayer, calculated from the X-ray reflectivity curves, showed a 40 % decrease in monolayer thickness after oxidation. This decrease in thickness would arise from the degradation of the lipid tails, as was observed using neutron reflectivity measurements, as well as a change in the orientation of the molecules as the amphiphilic nature of the molecules has changed after oxidation and thus the packing of the tails is reduced. The measured decrease in monolayer thickness for POPG is about 10 % more than that of POPC during ozonolysis at the air-water interface. The difference between the molecules is the headgroup, where POPG is negatively charged but POPC is neutral. It is possible that the presence of the charge causes a different rearrangement of the lipids after oxidation, where the molecules lie more flat across the subphase.

Both POPC and POPG are important components of the lung surfactant. It is thought that the presence of unsaturated phospholipids such as POPC and POPG is not only to reduce surface tension but also to enhance adsorption and fluidity of the lipid monolayer. As described above, DPPC molecules can pack tightly within a monolayer, which is why they are so effective at reducing the surface tension

within the lungs. However, at body temperature, the DPPC monolayer alone would enter the liquid-ordered phase when compressed to high surface pressures, so would not spread easily when expanded. Adding unsaturated phospholipids to the DPPC monolayers adds a "kink" in the order of the monolayer, which can help to improve the fluidity and rate of spreading during re-expansion. Oxidation of the unsaturated phospholipids within lung surfactant as shown here would alter the physical properties of the phospholipids, leading to drastic changes in their function. It is likely that their damage by ozone could prevent the fluidity of the monolayer during compression and expansion cycles, which could mean that the surface tension would not be sufficiently reduced. Furthermore, the anionic phospholipids, such as POPG are known to interact with surfactant protein B within the lung surfactant monolayer as they can associate with its positively charged residues.[24,25] This interaction is thought to prevent loss of the phospholipids during breathing when high surface pressures are achieved. Significant oxidation of these phospholipids causes a decrease in the interaction with surfactant protein B due to a change in their chemical structure that could lead to loss of the lipid to the aqueous subphase after compression. This could have negative implications in the lung surfactant.

Cholesterol is also known to be present within the lung surfactant at levels of 3-7 % by weight in humans.[8,12] It is thought to affect the packing of phospholipid monolayers and can increase the respreading properties during monolayer expansion. Although it is not known exactly why cholesterol is important for the lung surfactant, it is known that the correct levels can significantly improve its function.

The data presented in this chapter demonstrates that cholesterol is rapidly oxidised by ozone at the air-water interface. Surface pressure measurements show a small initial drop in surface pressure followed by a large increase in surface pressure by about 10 mN m^{-1}. The rate of this rise in surface pressure increase is dependent on the concentration of ozone, as when a monolayer of cholesterol was exposed to 0.25 ppm, the rate of increase in surface pressure was much slower than for a monolayer exposed to 1.1 ppm ozone.

X-ray reflectivity experiments of cholesterol monolayers showed that immediately upon oxidation there is an increase in both the scattering length

density of the monolayer and the thickness of the film. The increase in scattering length density of the monolayer after oxidation can be explained due to the addition of oxygen atoms to the cholesterol molecules *via* the ozonolysis reaction. The measured increase in scattering length density of the cholesterol monolayer from X-ray reflectivity experiments after ozone exposure was approximately 4 %.

The addition of oxygen atoms to cholesterol would lead to an increase in molecular volume, which would also explain the increase in surface pressure at the interface when the cholesterol monolayer is oxidised by ozone. There is a rise in the concentration of atoms at the surface, increasing the repulsion between the surface molecules, therefore decreasing the surface tension. Isotherms of cholesterol monolayers show that at low areas per molecule, a small decrease in area per molecule can lead to significant increases in surface pressure. Therefore a small decrease in area per molecule upon oxidation of cholesterol could cause this rapid, significant surface pressure increase.

A rise in thickness of the monolayer by ~ 2 Å during ozone exposure suggests a change in the orientation of the molecules at the surface as the cholesterol molecule itself would not have increased in height by this amount during oxidation. This information therefore suggests that the cholesterol molecules lie slightly tilted from the vertical at a surface pressure of 20 mN m^{-1}, and following oxidation by ozone, they become more perpendicular to the aqueous subphase. This could be due to the increase in molecular volume causing the molecules to become more tightly packed, hence the requirement to stand more upright.

Further investigation of this change in molecule orientation could include using X-ray reflectivity to measure the changes in thickness at different starting pressures, as it was shown above that the cholesterol monolayer thickness increases with increasing surface pressure (decreasing trough area). It could be possible that the increase in monolayer thickness during oxidation may not occur at a higher surface pressure.

The ozonolysis of mixed monolayers of POPC and cholesterol at the air-water interface were also investigated. Surface pressure results for ozone exposure to monolayers of cholesterol and POPC at 1.0:0, 7.8:1.0, 2.0:1.0, 1.0:2.0 and 0:1.0 (mol/mol) show that the initial surface pressure increase is much more

rapid for a monolayer of POPC alone and increasing the mole fraction of cholesterol in monolayers of POPC decreases the rate of the initial rise in surface pressure. Furthermore, there appears to be to two separate reactions occurring, where there is an initial rise in surface pressure as the result of the reaction between POPC and ozone and a second, slower rise as the result of the reaction between cholesterol and ozone.

X-ray reflectivity experiments of a mixed monolayer of cholesterol and POPC 1.0:2.0 (mol/mol) showed that the scattering length density of the mixed monolayer decreased during reaction with ozone, although at a slower rate than for a monolayer of POPC alone. This is presumably because cholesterol monolayers alone increase in scattering length density during ozone exposure, therefore the presence of cholesterol in a POPC monolayer prevents the scattering length density from decreasing to the same extent. Additionally, the thickness of the mixed monolayer decreased during ozone exposure, but not to the extent of a monolayer of POPC alone. Since the thickness of a cholesterol monolayer alone is smaller than that of a monolayer of oxidised POPC, the results showing that the thickness of the mixed monolayer does not decrease by the same amount as POPC suggests that the presence of cholesterol within the POPC monolayer changes the orientation of the molecules within the monolayer during oxidation. For example, the presence of oxidised cholesterol could decrease the area per molecule so that the oxidised POPC does not tilt towards the subphase as much as it would do when alone in a monolayer.

Damage caused to cholesterol by ozone pollution within the lung surfactant could lead to significant changes in its function. Although it is not known what the exact function of cholesterol is, it has been shown here that the chemical changes to the cholesterol molecule lead to very different properties at the surface. Oxidised cholesterol can also significantly influence the orientation of the surrounding molecules, such as POPC demonstrated here, and therefore could affect the properties of these molecules too within the monolayer. Further studies could include investigating the reaction of mixed monolayers of cholesterol and DPPC using X-ray or neutron reflectivity to investigate whether oxidation of cholesterol can affect the arrangement of DPPC molecules or reduce the fluidity of

the monolayer. Reflectivity experiments would provide more information on the actual changes in arrangement of the DPPC molecules at the surface, if any.

The results presented in this chapter also demonstrate that whole pig and sheep lung surfactants react significantly with ozone at the air-water interface. The extracted lung surfactant was taken from animal lungs that will have been exposed to air containing various pollutants; consequently they would be likely to have been exposed to some levels of ozone pollution. Therefore even if the lung surfactant had previously been mildly damaged by atmospheric pollutants it was still readily damaged in these experiments by ozone. In all cases, the surface pressure of the lung surfactant monolayers dropped dramatically over time during ozone exposure, therefore the film is damaged by ozone in a way that prevents its full function of reducing surface tension to the required levels. There is usually an initial rapid rise in surface pressure followed by a rapid decrease, then a slower rise in surface pressure, followed by a steady decrease to a value lower than the initial value as previously stated. This surface pressure pattern was observed repeatedly during ozone experiments, although the changes were dependent on the initial surface pressure.

Reaction between individual components of the surfactant and ozone at the air-water interface reveal different changes and rates of change of surface pressure of the monolayers. Therefore, the pattern observed when natural lung surfactant is exposed to ozone could be attributed to the individual reactions occurring at different rates. It was shown above that in a mixed monolayer of unsaturated phospholipid POPC and cholesterol that the surface pressure increases more rapidly with more POPC when the monolayers are exposed to ozone at the air-water interface. Also, when the mole fraction of POPC exceeds that of cholesterol, two distinct “peaks” can be observed in the surface pressure, suggesting that the initial rapid rise in surface pressure could be due to the reaction between ozone and POPC and the second slower increase could arise from the reaction between ozone and cholesterol. Applying this data to the whole lung surfactant, the first peak in surface pressure *versus* time upon ozone exposure could correspond to fast oxidation of unsaturated phospholipids within the lung surfactant. This rapid increase and decrease in surface pressure is much smaller than for a monolayer of unsaturated phospholipid alone as it was shown in the ozone experiments on

mixed monolayers of POPC and DPPC that increasing levels of saturated phospholipids reduced the initial rise in surface pressure. The second rise in surface pressure during exposure of whole lung surfactant to ozone could occur due to the oxidation of cholesterol. However, this rise is much higher than would be expected for the levels of cholesterol normally present in the lung surfactant (~5 %), therefore it could also be attributed to further reactions between other phospholipids and ozone, which might react at a slower rate than POPC. Additionally, the oxidation of the lung surfactant peptide analogues, presented in Chapter 3, leads to a rapid drop in surface pressure, therefore the presence of lung surfactant proteins could influence the surface pressure pattern of the natural lung surfactant during ozone exposure. For example, it is possible that the first rapid drop in surface pressure is a result of oxidation of the proteins.

Neutron reflectivity experiments were also performed on monolayers of pig and sheep lung surfactant during ozone exposure. The reflectivity curves for monolayers on NRW showed that 30-40 % of the lung surfactant material was lost from the interface during long ozone exposure for both species, and the lifetime of loss was at a similar timescale for both species, although it seemed that overall more pig lung surfactant material was lost from the interface than sheep lung surfactant. This could be due to a difference in sample extraction, or a slight difference between the species. Approximately 50 % of the phospholipids in lung surfactant are unsaturated,[18] therefore the majority of the loss of material from the interface could be attributed to the unsaturated lipids. However, this loss of whole lung surfactant material is still higher than expected as it was shown in the POPC and POPG experiments that much of the oxidised material remains at the interface. The lifetime of loss of material from the air-NRW interface was 165.4 (± 4.3) minutes, which is significantly longer than would be expected for the loss of lipid tails above the double bond only, as it was shown at low ozone concentration (0.1 ppm), the oleoyl strand from POPC was lost from the interface with a lifetime of 24 minutes. Therefore, ozonolysis of whole lung surfactant must lead to a loss of more than only lipid tails from the interface, for example solubilisation of whole molecules or further damage as a result of formation of secondary ROS.

For pig lung surfactant on D_2O an increase in neutron scattering length density was observed during ozone exposure, as a loss of material from the

interface causes the D_2O to contribute more to the neutron reflectivity. The lifetime of increase in scattering length density and decrease in thickness are much faster than the lifetime of loss of material from the interface observed for the experiments on NRW. This could be partly because the initial surface pressure of the film on D_2O was higher and this caused a faster solubilisation of some material into the subphase. It could also be because the experiments on D_2O would be sensitive to an incorporation of subphase into the surface layer due to an increase in hydration of the monolayer. As the lung surfactant monolayer is oxidised it would become rapidly more hydrophilic and therefore more hydrated. The faster lifetime, therefore, could correspond to a fast rate of hydration of the monolayer, so this result suggests that the D_2O contributes more rapidly to the reflectivity of the surface than the surface material is lost from the interface.

X-ray reflectivity experiments were also used to investigate the changes in monolayer structure at the air-water interface during ozone exposure. X-ray reflectivity experiments were performed at three different ozone concentrations (1.1, 0.55 and 0.25 ppm) for pig lung surfactant and results indicated that the rate of increase in scattering length density and decrease in monolayer thickness (and consequently the rate of reaction) decreased with decreasing ozone concentration, as expected. It was demonstrated that both pig and sheep lung surfactants become significantly thinner after ozonolysis by approximately 30 %. This is a similar loss of thickness as was observed for the monolayers of POPC and POPG alone reacting with ozone at the air-water interface, therefore this significant decrease in thickness of the whole lung surfactant could be attributed to the loss of phospholipid tails and consequent rearrangement of the monolayer as is becomes less packed.

4.5 Conclusion

Although it is indisputable that the air pollutant ozone has a negative effect on lung health, very little work has been done to investigate the damage caused to the lung surfactant during exposure. In particular, little is known about the specific reactions between the components and ozone at the air-water interface. Some previous work had been done to establish the reactivity of monolayers of POPC with ozone[136, 185] and Chapter 3 of this thesis discusses the reactivity of surfactant protein B with ozone. This chapter aimed to further research the damage caused to lipids within the lung surfactant, as well as the whole surfactant, by ozone pollution, and therefore determine the implications of ozone damage to lung surfactant as a whole.

Neutron and X-ray reflectivity, along with surface pressure measurements were used to confirm that unsaturated phospholipids such as POPC and POPG are rapidly oxidised by ~1.1-2 ppm ozone, as drastic changes in surface pressure and reflectivity were seen when the monolayers were held at constant area. X-ray reflectivity allowed the quantification of the decrease in the thickness of the monolayers after oxidation, showing a change in molecule organisation at the surface.

Neutron reflectivity was also used to investigate the rate of reaction between ozone at the alkene within POPC in the presence of the saturated phospholipid DPPC, which does not itself react with ozone. It was shown that addition of DPPC to a monolayer of Pd_{17}OPC has an effect on the rate of the reaction at the double bond when DPPC is present at a higher ratio than POPC. It was concluded that this could be due to the high concentration of DPPC molecules reducing the accessibility of ozone to the reactive molecules.

X-ray reflectivity measurements of cholesterol monolayers exposed to ozone at the air-water interface showed an increase in both the thickness and scattering length density of the cholesterol molecules after oxidation, owing to the increase in electron density and volume of the molecules at the surface. The thickness increases showed that the molecules changed their arrangement at the

interface to become more upright after oxidation. The surface pressure also increased due to the decrease in area per molecule after oxidation.

It was shown that oxidation of mixed monolayers of cholesterol and POPC by ozone led to a decrease in the scattering length density at the interface, providing evidence for loss of monolayer material from the interface, presumably POPC tails. However, the decrease in thickness of the monolayer was not as much as expected, suggesting that the bulkier oxidised cholesterol molecules can change the orientation of the POPC molecules at the surface so that they are arranged in a more upright manner.

The presence of unsaturated lipids at the correct level in the lung surfactant is important for the full function of the lung surfactant. The damage and loss of unsaturated phospholipids as described here, even in the presence of saturated lipids, will alter the physical properties of the surface monolayer of the lung surfactant, including its fluidity and ability to prevent monolayer collapse at high surface pressure. Ozone-induced oxidation of cholesterol within the lung surfactant could lead to significant changes to the arrangement of molecules in the monolayer as it is thought that cholesterol is able to improve the fluidity of phospholipid monolayers. Oxidised cholesterol could therefore change the properties of the film and arrangement of neighbouring molecules within the lung surfactant.

Exposure of monolayers of whole pig and sheep lung surfactants to ozone at the air-water interface led to drastically altered films that were much less capable of reducing surface tension, its primary function *in vivo*. Additionally, there was a dramatic loss in surface coverage and thickness of the monolayer, thus decrease in relative amount of material at the interface, after 1.1 ppm ozone exposure. Material would be lost to either the aqueous subphase (larger oxidised molecules) or to the atmosphere (small chain organic molecules). This percentage decrease (40 %) was much higher than expected from the individual investigations of the lung surfactant components, as only a loss in material at the interface was previously seen from unsaturated phospholipids reacting with ozone. This suggests that the combination of reactions between the different components within the lung surfactant and ozone changes the properties of the film in such a

significant way that it leads to the loss of more hydrophilic, oxidised molecules to the aqueous subphase.

The correct composition of the lung surfactant is extremely important for maintaining the low surface tensions within the lung and fluidity of the surface monolayer. Thus, it can be concluded that the rapid and significant damage described here to lipid components of the lung surfactant would lead to dramatic changes to the organisation and physical properties of the lung surfactant film, as demonstrated by the substantial damage seen in exposure to whole lung surfactant presented above. Consequently, this study has provided further insights into the reasons why ozone air pollution can cause respiratory problems.

Chapter 5 All-Atom Molecular Dynamics Studies of Surfactant Protein C and DPPC Monolayers at the Air-Water Interface

5.1 Introduction

5.1.1 Surfactant Protein C

Surfactant protein C (SP-C) is one of the two hydrophobic small proteins present within the lung surfactant monolayer at the air-water interface. The structure and supposed function of SP-C was discussed in detail in Chapter 1. As previously described, little is known about the functions of this protein and it is difficult to handle experimentally because of its extreme hydrophobicity (it is one of the most non-polar naturally occurring polypeptides known).

Non-palmitoylated SP-C (nSP-C) is posttranslationally modified by the addition of two (in most mammals) palmitoyl groups *via* thioester bonds to Cys-5 and Cys-6 to form dipalmitoyl SP-C (dpSP-C). These palmitoyl chains have been shown to be important for the function of the protein, possibly because the presence of the chains changes the 3-D structure of the protein.[188] It has been shown using two-dimensional ^{1}H NMR that the structure of dpSP-C in chloroform/ methanol/ 0.1 M HCl, 32:64:5 (v/v/v) has an α-helix encompassing positions 9-34, and the 8 N-terminal residues, that include the two palmitoylcysteines, are flexibly disordered.[31]

Previous research has demonstrated that depalmitoylation of the cysteines in dpSP-C to form nSP-C leads to a decrease in helical content of the protein. Vandenbussche *et al.* demonstrated using FT-IR that the helical content of dpSP-C inserted into lipid bilayers is 20 % higher than the helical content of nSP-C in the same conditions.[189] Johannsen *et al.* later used circular dichroism (CD) experiments of the protein in phospholipid micelles, SDS micelles and in TFE to show that depalmitoylation of dpSP-C to nSP-C leads to a decrease in 20 % of the helical content compared to dpSP-C in all cases.[67] Therefore the extent of this

reduction in helical content upon depalmitoylation appears to be independent of the environment used in the experiment. It is thought that the palmitic acid chains can stabilise the helix in some way, for example by forming hydrogen bonds *via* the carbonyls to the amide hydrogens of the first amino acid within the helix.

It has also been shown that the α-helical content of both dpSP-C and nSP-C is higher in phospholipid bilayers than in a chloroform/methanol solution.[189] Both FT-IR and NMR studies gave a helical content of porcine SP-C in chloroform/ methanol of ~75%,[31,189] whereas FT-IR of SP-C in DPPC/PG gave a helical content of 92%.[189] This suggests that approximately 5 further amino acids become helical in a phospholipid bilayer. However, no research has been performed to investigate the helical content of dpSP-C or nSP-C in a phospholipid monolayer at the air-water interface, which is the environment of this protein within the lung surfactant.

Research has indicated that dpSP-C improves the adsorption and respreading of phospholipids to an air-water interface and increases the mechanical stability of the film when compared to nSP-C.[190, 191] Additionally, the presence of dpSP-C leads to a film that is much better at lowering surface tension when compressed, compared to when the nSP-C form is present, and it has been proposed that this could be due to the ability of the protein to arrange itself into the optimum orientation at the interface in order to do this.[190] Therefore, the palmitoyl chains appear to be vital for optimal surface activity of the protein within a lipid monolayer.

Infrared reflection-absorption spectroscopy (IRRAS) of dpSP-C in a DPPC monolayer at 28 mN m^{-1} surface pressure has shown that the protein is significantly tilted away from the normal to the interface by approximately 70°. However, the tilt of the DPPC molecules was decreased by approximately 16° towards the normal of the interface compared to a monolayer without dpSP-C, thus the molecules were orientated more upright.[68] From this data, it was proposed that SP-C maximises its interaction with the lipid tails *via* its hydrophobic protein helix in order to act as a "hydrophobic lever" to allow the lipids to remain conformationally ordered while being able to spread the maximum number of phospholipid molecules during compression and expansion of a monolayer.[68] Additionally, it has been speculated that the palmitoyl groups are

important because they insert into the phospholipid monolayer tails, essentially "anchoring" the N-terminal residues into the monolayer. It has been proposed that this could be important for its function by disrupting the lipid tail packing of phospholipids at high surface pressures to facilitate spreading of the monolayer.[188]

Research has also shown that the α-helical form of SP-C is metastable and that it can transform to a β-strand conformation, leading to protein aggregates that resemble amyloid fibrils. This transformation is thought to lead to respiratory disorders such as pulmonary alveolar proteinosis. It has been demonstrated that this process is accelerated in the nSP-C form, particularly with increasing pH, and it was proposed that the decrease in helical content from dpSP-C to nSP-C could induce this transformation.[192]

As described above, the unusually high hydrophobicity of this protein means that the knowledge of the structure and function of this protein within the lung surfactant monolayer is largely unknown. In particular, information involving the interactions with surrounding phospholipids and the structural importance of the palmitoylcysteines is particularly lacking. The research presented in this chapter uses atomistic molecular dynamics (MD) simulations to investigate the structure of dpSP-C within a DPPC monolayer at the air-water interface, and compares this to simulations of DPPC monolayers alone and to simulations of non-nSP-C within a DPPC monolayer. The MD was run at various areas per lipid of the monolayers in order to investigate how the orientation of the molecules within the monolayers changes as the monolayers are compressed. This will begin to improve our understanding of the surface activity of this protein and its interaction with the phospholipid monolayer. Additionally, a comparison of the dpSP-C and nSP-C at the air-water interface may increase our knowledge of the structural importance of the presence of the palmitic acid chains.

Previous MD simulations of SP-C mainly investigate the structure of this protein in various solution environments. For example, Kovacs *et al.* ran atomistic MD simulations of nSP-C in chloroform, methanol and water at 300K in order to determine the stability of the α-helix in each solvent. It was concluded that the helix is extremely stable in all environments, but more stable in methanol and water compared to chloroform as the C-terminus began to unfold. This was attributed to the hydrophobic effect, where exposure of the buried moieties of the

poly-valyl helix is more unfavourable in polar solvents.[193] Carvalheda *et al.* have studied the effect of pH and depalmitoylation on protein conformation of SP-C in a chloroform/methanol/water mixture using atomistic MD simulations. It was found that loss of the palmitoyl chains and an increase in pH caused a decrease in helical structure.[194]

MD simulations of SP-C at the air-water interface have not been well studied. There are several simulations investigating the orientations and interactions of SP-B_{1-25} in DPPC monolayers at the air-water interface,[195] as well as the lipids alone.[196] To our knowledge, only one study has investigated mixed monolayers of phospholipids and SP-C at the air-water interface and this study used course-grained MD simulations at 323K to identify mechanisms of monolayer folding. In this study, Duncan *et al.* used nSP-C to show that its presence in a DPPC monolayer promotes the fluidity of the monolayer to induce folding at very high surface pressures to prevent collapse.[197] Therefore, no studies have specifically investigated the orientation of protein in a phospholipid monolayer at an atomistic level at different areas per lipid, nor specifically examined the influence of the palmitic chains.

5.2 Methods for Simulating a Protein/Phospholipid Monolayer System

Molecular simulations are valuable in research for examining the properties of matter that are not yet possible to understand by experimental observation. Using computers to calculate intermolecular forces, it is possible to predict the behaviour of molecules on the atomistic scale. An overview of molecular dynamics techniques is presented here.

5.2.1 Molecular Dynamics Theory

Molecular dynamics (MD) is a computational technique for simulating the temporal evolution of a system of N particles. In classical molecular dynamics, the aim is to predict macroscopic properties of atoms and molecules, such as pressure, energy, heat capacities, etc. from the microscopic properties such as atomic

positions and velocities generated by the simulation. The bridge between macroscopic and microscopic properties is statistical mechanics using the time dependent statistical average. [198]

MD simulations aim to solve Newton's law of motion:

$$F = ma \qquad (5.1)$$

where F is the force acting on the particle, m is the particle mass and a is its acceleration. The force is also equal to the gradient of the potential energy:

$$F = -\frac{dV}{dr} \qquad (5.2)$$

where V is the potential energy of the system and r is the position. The acceleration can be expressed as:

$$a = \frac{d^2r}{dt^2} \qquad (5.3)$$

Combining these 3 equations we can relate the derivative in potential energy to the changes in position as a time function:

$$-\frac{dV}{dr} = m\frac{d^2r}{dt^2} \qquad (5.4)$$

Newton's equations are solved for all atoms at all times separated by a small time step Δt. There are several algorithms to integrate the equations of motion. These are discussed below.

5.2.2 GROMACS

In this research the GROMACS (GROningen MAchine for Chemical Simulations)[199] computer package was used to perform MD simulations. GROMACS is an open-source software package primarily designed for simulations of proteins, lipids and nucleic acids and has consistently been one of the fastest MD codes available.[200,201]

In this research the leap-frog integrator algorithm[202] was used in GROMACS for integrating the Newtonian equations of motion. This algorithm is based on the Verlet algorithm, one of the simplest integrator algorithms. The Verlet algorithm[203] uses positions and accelerations at time t and the positions from time (t - Δt) to calculate new positions at time (t + Δt). It uses no explicit velocities. This algorithm is a two-step method because it estimates $x\ (t + \Delta t)$ from the current position $x(t)$ and the previous position $x(t - \Delta t)$. Therefore it is not self-starting: initial positions $x(0)$ and velocities $v(0)$ are not sufficient to begin a calculation, and a backward Euler method must be done at t = 0 to get $x\ (-\Delta t)$, as shown in the equations below:

$$x(t + \Delta t) = \frac{1}{2}a\Delta t^2 + V(t)\Delta t + x(t) \qquad (5.5)$$

$$x(t - \Delta t) = \frac{1}{2}a(t)\Delta t^2 - V(t)\Delta t + x(t) \qquad (5.6)$$

$$x(t + \Delta t) = a(t)\Delta t^2 - x(t - \Delta t)\Delta t + 2x(t) \qquad (5.7)$$

In the leapfrog algorithm the velocities are first calculated at time $(t + \frac{1}{2}\Delta t)$. By using this as an initial velocity we can calculate the positions, x, at time $(t + \Delta t)$. Thus, the velocities leap over the positions and then the positions leap over the velocities:

$$x(t + \Delta t) = v\left(t + \frac{1}{2}\Delta t\right)\Delta t + x(t) \qquad (5.8)$$

$$v\left(t + \frac{1}{2}\Delta t\right) = v\left(t - \frac{1}{2}\Delta t\right) + a(t)\Delta t \qquad (5.9)$$

$$v(t) = \frac{1}{2}\left[v\left(t - \frac{1}{2}\Delta t\right) + v\left(t + \frac{1}{2}\Delta t\right)\right] \qquad (5.10)$$

5.2.3 Potential Energy Function: The Force Field

The central part of an MD simulation is the potential energy function and its parameters. This description of the atomic interactions of a molecular system is called the force field. The force field is created to cover all relevant molecular interactions that will model the important degrees of freedom describing the multidimensional potential energy surface of a system. For any configuration, r, the potential energy functions give the total configuration energy of the system.

The potential energy, V, can be calculated as bonded (intramolecular) and nonbonded (intermolecular) interactions:

$$V(r) = \sum_{bonded} V_i(r) + \sum_{nonbonded} V_i(r) \qquad (5.11)$$

Bonded interactions include bond lengths and strengths, bond angles, torsions and improper dihedrals. Nonbonded interactions include electrostatic interactions and van der Waals forces.

5.2.4 Nonbonded Interactions

The van der Waals interaction is modelled by the Lennard-Jones potential:

$$V_{LJ}(r) = 4\varepsilon\left[\left(\frac{\sigma}{r}\right)^{12} - \left(\frac{\sigma}{r}\right)^{6}\right] \quad (5.12)$$

where ε is the depth of the potential energy well, σ is the distance between atoms and r is the atomic position, described in Figure 5.1, which can be modified to reproduce experimental data. The potential is attractive at large distances due to the $-1/r^6$ term, which can be derived by averaging dipole-dipole, dipole-induced dipole and induced dipole-induced dipole forces. The potential is repulsive when atoms are brought very close due to the $1/r^{12}$ term.

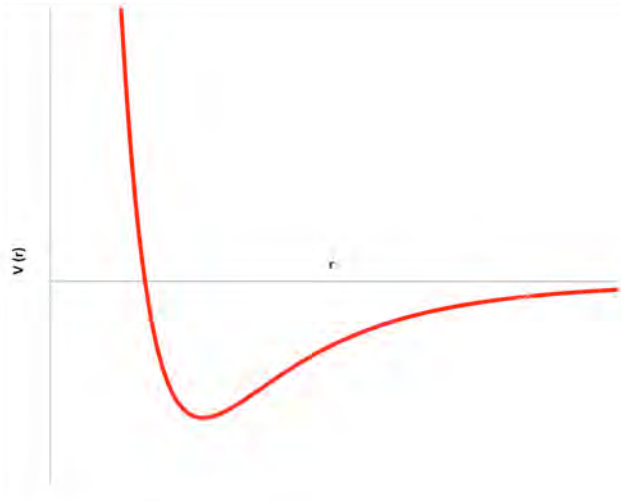

Figure 5.1. A plot representing the Lennard-Jones potential.

At short range (small *r*) the potential energy is very large and positive, revealing that this is a very unfavourable arrangement of the atoms (it indicates that the two atoms are strongly overlapping). At long range the potential energy is small and negative. This indicates that at this range the pair of atoms experiences a stabilising influence. At a separation slightly greater than sigma, the energy is at a minimum. This is where the atom pair is stable, and will be content to remain in this position until some external influence disturbs them.

Electrostatic interactions involve atom charges, so coulombic potentials are incorporated in the potential for charged species:

$$V_{coulombic} = \frac{Q_1 Q_2}{4\pi\varepsilon r} \qquad (5.13)$$

where ε is the permittivity of free space, r is the distance between atoms 1 and 2, and Q_1 and Q_2 are the charges on each species.

Hydrogen bonds are highly directional and can be much stronger than van der Waals interactions. Simulating hydrogen bonding interactions in MD simulations requires the introduction of geometrical criteria. Considering the distance between the donor atom and acceptor atom, *r*, and the hydrogen bond

donor-hydrogen-hydrogen bond acceptor angle, α, a hydrogen bond in MD satisfies both $r < r_{hb}$ and $\alpha > \alpha_{hb}$. These values are chosen based on the water model used in the simulation. Here the SPC water model[201] is used, where r_{hb} = 0.35 nm and α_{hb} = 130°.

In order to make the number of nonbonded interactions manageable, interactions are approximated to 2-body interactions in MD simulations. GROMACS also incorporates a cut-off distance where beyond this value, nonbonded interactions are not considered. In these simulations, a cut-off distance of 1.0 nm was used.

5.2.5 Bonded Interactions

The four types of bonded interactions represent the energy required to stretch or compress, bend or rotate a bond. This energy can be approximated as a simple spring using Hooke's law for stretching or compressing:

$$E_{str} = \frac{1}{2}k(r_i - r_0)^2 \qquad (5.13)$$

where k is the spring constant, r_i is the bond distance and r_0 is the equilibrium bond distance. The energy required to bend a bond from its equilibrium angle, θ_0, is:

$$E_{bend} = \frac{1}{2}k(\theta_i - \theta_0)^2 \qquad (5.14)$$

where k is the bending constant and θ_i is the bond angle. The energy required to deform a planar group of atoms from its equilibrium angle, ω_0 (usually 0), is:

$$E_{improper} = \frac{1}{2}k(\omega_i - \omega_0)^2 \qquad (5.15)$$

where k is the improper constant and ω_i is the improper angle. The energy required to rotate the bonds is modelled by the torsional internal potential:

$$E_{tor} = \sum \frac{1}{2} k(1 + \cos(n\phi - \delta)) \qquad (5.16)$$

where k, δ and n are torsion constants and ϕ is the torsion angle.

Most of these force field parameters are taken from experimental data on small molecules or theoretical calculations on others. In general, crystallographic data is used for bond lengths and angles and spectroscopy for other information.

The force fields used in this study to investigate the protein are the GROningen MOlecular Simulation (GROMOS) force fields. These include terms for harmonic bond stretching and angle bending, torsion energetics, and other bonded and nonbonded interactions described above. The original force field, GROMOS87, was developed by Gusteren *et al.* and released in 1987.[204] The force field was updated in 1996 with the release of GROMOS96.[205]

For simulating lipids, the most widely used parameters are the "Berger lipid", derived by Berger *et al.*[206] These are compatible with GROMOS parameters used to describe proteins. These are a hybrid between GROMOS atom types and OPLS[207] charges, using GROMOS bonded parameters, headgroup Lennard-Jones parameters from OPLS and special Lennard-Jones parameters in the acyl chains. This is because long alkane chains are poorly represented by GROMOS parameters. In this work the GROMOS53A6 force field was used to parameterise the protein and the Berger lipid parameters were used to describe the lipids.

5.2.6 Periodic Boundary Conditions

Molecular dynamics simulations track only a small number of particles in a box of a particular size in order to not slow down the computation. The system size used in MD simulations is far smaller than real-world systems, therefore an unnaturally high proportion of molecules will be interacting with the edge of the box, thus surface effects would dominate the system properties. This would mean that a macroscopic system is not being properly modelled. To avoid this, periodic boundary conditions (PBCs) are used. The system is then assumed to be a unit cell of some ideal crystal that is repeated in 3-D space. If the trajectory of an individual atom takes it outside the boundary of the simulation box, its image simultaneously

enters the box from the point related to the exit location by lattice symmetry. In GROMACS the PBC can be switched off, in the xy plane only, or in x, y and z directions.

5.2.7 Ensembles

A system of particles in thermal equilibrium with the surrounding environment has a microstate that is satisfied by the coordinates and momenta of each particle at a timepoint. The set of microstates that share macroscopic properties, e.g. temperature, pressure, volume or energy, is known as an ensemble. In the isothermal-isobaric (NPT) ensemble, the temperature, pressure and number of atoms are held constant, similarly to the laboratory experiment. In the canonical NVT ensemble, the temperature, volume and number of particles are held constant. This can have advantages over NPT as the system size and geometry are constant so the molecules within the simulation box will not be distorted by the barostat. This can have advantages in simulations of monolayers at the air-water interface as it allows us to simulate at a constant area per molecule at the surface.

The average temperature is controlled using a variety of methods called thermostats. In this thesis the V-rescale thermostat[208] is used. This incorporates the Berendsen thermostat[209], while also scaling particle velocities by a factor every n timesteps to include terms for kinetic energy to ensure a proper canonical distribution.

5.2.8 Running a MD Simulation

Before running a MD simulation, excessively large forces and kinetic energy within the starting configuration must be eliminated to prevent the simulation from crashing. Hence, an energy minimisation simulation is run prior to MD. In this thesis a steepest descent algorithm is used for energy minimisation, where the local minimum for each atom is found by moving stepwise in the negative direction of the gradient and repeated.

The system is then coupled to the required thermostats to equilibrate the solvent and ions within the system using the NVT and/or NPT ensembles in order to stabilise the temperature and pressure of the system. The atoms within the molecule of interest (e.g. lipids and proteins within this project) are normally subjected to position restraints during the energy minimisation.

Following equilibration, the position restraints are released and the final molecular dynamics simulation is run, integrating and solving Newton's equation of motion at each timestep.

5.2.9 Molecular Dynamics Simulations of Monolayers at the Air-Water Interface

MD simulations of lipid monolayers at the air-water interface are not nearly as commonly studied as protein solution or lipid bilayer systems. Much of this previous research into lipid monolayer systems has been to investigate the phase transitions and phase behaviour of lipid monolayers, as well as their self-assembly and collapse, and the physical reasons for these phenomena.[210-213] There have been several described methods for forming lipid monolayers for simulation. The most widely used method is by separation of a bilayer into two monolayer sections exposed to air, as shown in Figure 5.2. The monolayer could also be formed from a random aqueous mixture in the presence of an interface, but this is more computationally demanding. The most common procedure is to take a wide block of water and form a monolayer on either side of the water layer, with a vacuum above and below the layers.[210-213] In order to reduce system size to lead to faster simulations, some studies have formed monolayers on only one side of the water block and either created a vacuum layer below the water surface, or "froze" the bottom layer of water molecules by constraining them.

In this research the double monolayer method was used because trials using the one-monolayer approach revealed that water molecules were not efficiently held in place during the simulation, leading to the movement of water molecules into the vacuum layer.

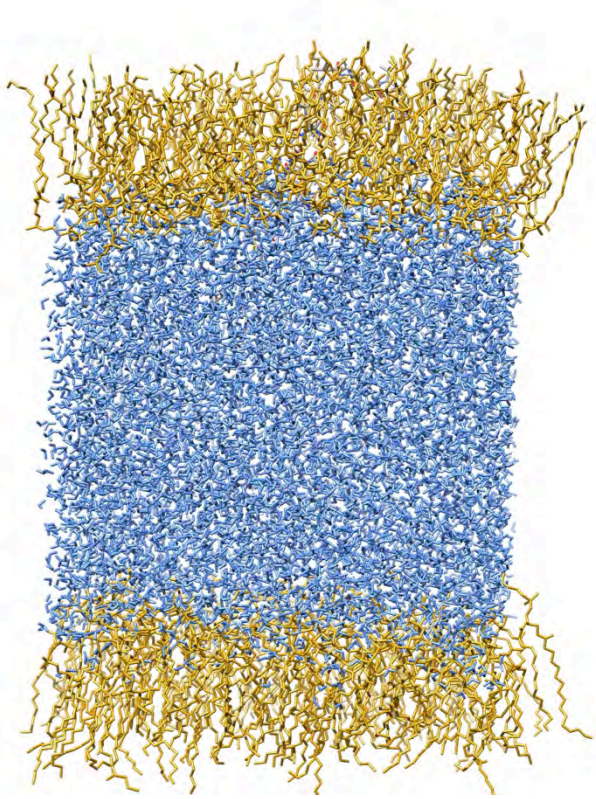

Figure 5.2. A representation of the double monolayer method used in MD simulations in this research.

The blue molecules represent water molecules and the gold colour represents DPPC molecules (79 per layer). The monolayers are formed on two separate edges of a water block. A vacuum layer is created in the simulation box above and below these monolayers.

5.3 Methods

The GROMACS 4.5.4[214] package was used in all simulations in this research and was run on the Asgard supercomputer at Birkbeck College. Further details can be obtained from the package manual. The simulations were visualised using VMD[215] and Molecular graphics and analyses were performed with the UCSF Chimera package. Chimera is developed by the Resource for Biocomputing, Visualisation, and Informatics at the University of California, San Francisco (supported by NIGMS P41-GM103311).[216]

5.3.1 Surfactant Protein C Structure

The starting point structure of both nSP-C and dpSP-C was taken from the palmitoylated isoform of porcine SP-C (PDB 1SPF), which had been obtained by 2-D NMR in chloroform/methanol/0.1M HCl (32:64:5; v/v/v).[31] From the 20 available entries in the PDB file, one was chosen at random to be used as the initial structure. The amino acid sequence of human SP-C compared to porcine SP-C (which was used in this research) is shown in Figure 5.3. The primary structures of the proteins are very similar.

FGIPCCPVHLKRLLIVVVVVVLIVVIVGALLMGL (human)

LRIPCCPV NLKRLLVVVVVVLVVVVIVGALLMGL (porcine)

Figure 5.3. The amino acid sequence of human and porcine SP-C.

The dpSP-C version was formed by adding a palmitic acid chain to the sulphur of each of the cysteines using the Avogadro molecular sketching software[217] to form a thioester linkage. The geometry of the dpSP-C system was optimised firstly within the Avogadro software, and secondly by running a

quantum mechanics calculation using Gaussian 03[218] software using the AM1 semi-empirical method *in vacuo*.[219]

The force field parameters for the palmitoylated cysteines were obtained by modifying the GROMOS 53A6 parameters[220] of a cysteine residue to include the bonded palmitoyl parameters, forming a new "CYP" residue. The parameters for the fatty acid chains were adapted from the GROMOS 53A6 force field parameters of DPPC molecules and the thioester bond was adapted from Carvalheda *et al.* and Olausson *et al.*[194,221] Table 5.1 presents the force field parameters used for the palmitoylated cysteine residues and the corresponding structure is shown in Figure 5.4.

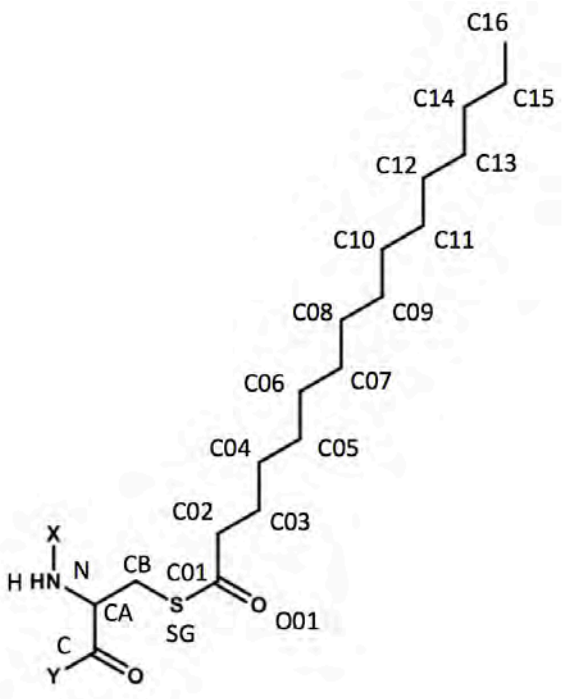

Figure 5.4. The chemical structure and atom labels for the modified (palmitoyl) cysteines used in the parameterisation of dpSP-C.

Atom	Description	Partial Charge
N	N	-0.31
H	H	0.31
CA	CH1	0.00
CB	CH2	-0.16
SG	S	-0.36
C01	C	0.58
O01	O	-0.38
C02,…,C15	CH2	0.00
C16	CH3	0.00

Bond	b_0 / nm	K_b / 10^6 kJ mol^{-1} nm^{-2}
N-H	0.1	18.7
N-CA	0.147	8.71
CA-CB	0.153	7.15
CA-C	0.153	7.15
CB-SG	0.183	5.62
SG-C-01	0.241	2.69
C01-O01	0.123	16.6
C01-C02	0.148	7.64
C02-C03, …., C15-C16	0.153	7.15

Angle	θ / degrees	K_θ / kJ mol^{-1}deg^{-2}
H-N-CA	115	18
N-CA-CB	109.5	13
N-CA-C	109.5	13
CB-CA-C	109.5	13
CA-CB-SG	113	16
CB-SG-C01	104	490
SG-C01-O01	121	750
SG-C01-C02	113	545
O01-C01-C02	121	750
C01-C02-C03,….,C14-C15-C16	111	530

Dihedral	φ / degrees	K_φ / kJ mol^{-1}
N-CA-CB-SG	0	5.9
CA-CB-SG-C01	0	2.9
CB-SG-C01-C02	0	1.0
SG-C01-C02-C03	0	1.0
C01-C02-C03-C04,…, C13-C14-C15-C16	0	5.9

Table 5.1.The details of the force field parameters used for modelling the palmitoyl cysteine residues in this study.

The parameters were adapted from the GROMOS53A6 parameters for DPPC.

5.3.2 Simulations of nSP-C and dpSP-C in Water

The protein was solvated by firstly centring the protein within a cubic box, the edge of which was defined to be at least 1.0 nm from the protein. Water molecules were added to the simulation box using the SPC model, a generic equilibrated 3-point solvent model.[222] The water was added using the genbox program in GROMACS to fill the simulation cell with a density of approximately 1 g cm^{-3}. 3 chloride ions were then added to the box using the GROMACS program genion, replacing some water molecules, to balance the charge of the system. As a result, the nSP-C box of size 348.2 nm^3 was filled with 11360 molecules of water and 3 chloride ions. The dpSP-C simulation box of size 521.1 nm^3 was filled with 17082 water molecules and 3 chloride ions.

The system for each protein was energy minimised with a maximum of 50000 steps of steepest descent with position restraints for the protein and water oxygen atoms. The initialisation phase was composed of two stages: 100 ps in an NVT ensemble with a temperature time constant of 0.1 ps and restraints (1000 kJ mol^{-1} nm^{-2}) in all protein atoms to achieve a temperature of 310 K using V-rescaling thermostat, followed by 100 ps in an NPT ensemble with a temperature time constant of 0.1 ps and a pressure time constant of 2 ps using isotropic Parrinello-Rahman[223] pressure coupling to achieve a pressure of 1.0 bar. In these ensembles two coupling groups were used to increase accuracy: protein and non-protein atoms.

Electrostatic interactions were calculated using the particle-mesh Ewald method.[224] Fourth order (cubic) interpolation was used with a cut-off of 1.0 nm. Van der Waals interactions were also cut-off after a distance of 1.0 nm. The grid neighbour search method was used with cut-off distance for the short-range neighbour list of 1.0 nm. The neighbour list was updated every 5 time steps.

The bonds between atoms were converted to constraints. Otherwise the system was un-constrained. The LINCS[225] constraint algorithm was used for all non-water atoms, and the SETTLE algorithm was used for water atoms. The PBCs were employed in the x, y and z directions.

For running the MD simulation, equations of motion were integrated using the leap-frog integrator with a timestep of 2 fs. The simulations were run for 1 ns.

5.3.3 Modelling the DPPC Phospholipid Monolayer

Simulations of lipid and protein monolayers at the air-water interface were performed using the slab geometry, in which two monolayers containing the same number of DPPC molecules were placed at the two air/water interfaces of the slab, with the headgroups of the lipid molecules immersed in water. In these simulations, one nSP-C or dpSP-C molecule was inserted into only one of the lipid monolayers. This was beneficial as it reduced the computation time and allowed the direct comparison of the DPPC monolayer with or without the protein.

The monolayers were formed using Packmol,[226] a packing optimisation tool for molecular dynamics that employs a geometry-based packing method. Using this program, 4300 water molecules were packed in to a box of size 7.9 x 7.9 x 7.9 nm. 79 DPPC molecules were packed above the slab of water, with the lipid head being inserted no more than 1 nm within the water and the C16 of the lipid tails to be at least 2 nm above the water to ensure the correct orientation. This was repeated for 79 DPPC molecules below the water slab. An energy minimisation was then performed on the system, using the parameters described above.

5.3.4 Insertion of the SP-C Molecule within the DPPC Monolayer

The nSP-C or dpSP-C molecule was inserted into one DPPC monolayer using the InflateGRO methodology.[227] Firstly, the structure files for the protein and the monolayer were concatenated, ensuring that the protein was in a suitable position within a simulation box of the same size. The proteins were orientated in different ways as described below. The system was then “inflated” by scaling the positions of the DPPC lipids by a factor of 4 in the interface (xy) plane (the water molecules are removed by the program). In this stage, one lipid molecule was removed from the interface containing the protein. An energy minimisation of the inflated system was then performed; using very strong position-restraining force on the protein

atoms to ensure the position of the protein did not change. Following this, the energy minimised inflated system was sequentially "compressed" by scaling the lipid positions by 0.95 until an area per lipid of approximately 48 $Å^2$ was achieved (approximately 30 compression steps). An energy minimisation was carried out in between each compression step. This process gave monolayers of a variety of areas per molecule that could be used in various MD simulations. Details of the monolayer surface coverages are described below.

Following energy minimisation, the simulation boxes were solvated using genbox. The water molecules in and above the tail side of the monolayers were manually removed and the box size was adjusted to ensure a vacuum layer of 5 nm above and below the lipid monolayers. Three chloride ions were then added to each system using genion to neutralise the charge on the system.

Since the exact position of the peptide with respect to the interface is unknown experimentally (depth of insertion, tilt of the helix), the simulations were performed in several orientations. The proteins were initially inserted perpendicular to the air-water interface, with either the N-terminus or the C-terminus inserted in the water. The presence of the palmitic acid chains would significantly alter the amphiphilic nature of the protein, so even though the charged and polar amino acids only exist towards the N-terminus, this part of the molecule would be less polar in the presence of the palmitoyl cysteines. Therefore, both nSP-C and dpSP-C were investigated in both orientations to see how they differ. Figure 5.5 represents the different starting positions of the proteins in the simulations, and Table 5.2 shows the various areas per lipid investigated. The areas per lipid were determined using the InflateGro program.

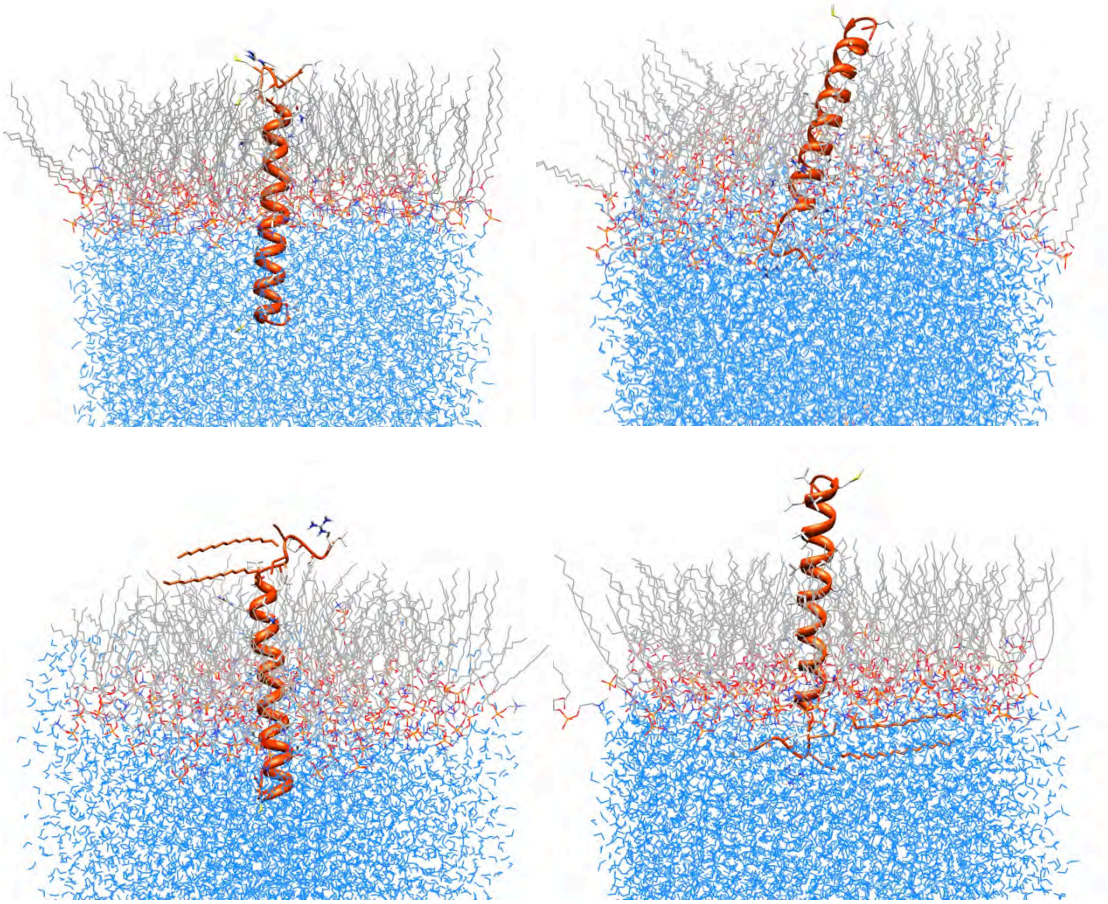

Figure 5.5. The starting systems for simulating nSP-C and dpSP-C in DPPC monolayers.

The top two images show the starting set-up for nSP-C in a DPPC monolayer at the air-water interface, with the C-terminus (left) or N-terminus (right) inserted into the water. The bottom two images show the starting set-up for dpSP-C in a DPPC monolayer at the air-water interface, with the C-terminus (left) or N-terminus (right) inserted into the water. The blue molecules represent water, grey wires shows DPPC tails, whereas red/orange wires show DPPC head groups. The orange ribbon represents the protein molecules.

	nSP-C		dpSP-C	
	C-terminal down	N-terminal down	C-terminal down	N-terminal down
Area per lipid 1 / Å^2	47	47	47	47
Area per lipid 2 / Å^2	52	52	53	53
Area per lipid 3 / Å^2	63	63	65	65
Area per lipid 4 / Å^2	71	71	73	73
Area per lipid 5 / Å^2	80	80	81	80
Area per lipid 6 / Å^2	97	97	101	101

Table 5.2. The areas per molecule of the starting systems for simulations in this study.

5.3.5 Simulations of Protein/DPPC Monolayers at the Air-Water Interface

Each of the systems shown in Table 5.2 was simulated by treating in the same way as the water simulations described in Section 5.3.2 except that in the NVT ensemble three coupling groups were used to increase accuracy: protein, DPPC and solvent. Prior to the final MD simulation, an extra stage was included, which involved a short 10 ps MD simulation using position restraints. Here, the lipids and protein were held in place to allow water molecules to move into the area around the headgroups.

5.3.6 Analysis of MD Simulations

Properties of the SP-C helix were analysed using the g_helix analysis program within GROMACS. This involves checking the protein for the longest helical part as determined by hydrogen bonds and angles. This helical part is then

fitted to an ideal helix around the Z-axis and centred around the origin. The RMS deviation of the helix radius in 2-dimensions for all Cα atoms is calculated as:

$$\sqrt{\sum \frac{x^2+y^2}{N}} \qquad (5.17)$$

where N is the number of backbone atoms. This shows the deviation from the ideal helix radius of 0.23 nm. The RMS deviation of the Cα atoms from ideal helix was also calculated using g_helix.

The protein secondary structure was assigned using the DSSP (define secondary structure of proteins) criterion defined by Kabsch and Sander.[230]

Electron density plots were produced by time averaging the number of electrons in slabs of 0.01 nm during the last 100 ps of the simulation. This was calculated for the DPPC headgroups, DPPC tails, protein and water individually with respect to the Z-axis using the GROMACS g_density program.

The order parameters were calculated for the lipid tails using the g_order program. The order parameter is:

$$S_z = \frac{3}{2}\langle cos^2\theta_z \rangle - \frac{1}{2} \qquad (5.18)$$

where θ_z is the angle between the Z-axis (normal to the monolayer) and the molecular axis under consideration. The brackets indicate a time and molecular average.

5.3.8 Neutron Reflectivity of Monolayers of DPPC and DPPC / nSP-C at the Air-Water Interface

In order to examine MD simulations of DPPC and DPPC/nSP-C monolayers further, results were compared to neutron reflectivity experiments performed on these monolayers. Neutron reflectivity was used to determine monolayer thicknesses at various areas per lipid to compare to those calculated using MD.

nSP-C (Peptide Synthetics) was dissolved in chloroform/methanol (5:1, vol/vol) to a concentration of 0.1 mg/ mL. nSP-C solution and DPPC solution (1

mg/ mL in chloroform) were mixed to form a molecular ratio of 1:25 (250 μL nSP-C solution to 250 μL DPPC solution). Neutron reflection monolayers of deuterated DPPC (d_{62} DPPC) and d_{62} DPPC/nSP-C was performed on the FIGARO reflectometer at the Institut Laue Langevin, Grenoble, France, as described in Chapters 3 and 4. The neutron reflectivity was performed at various areas per molecule at the surface and the reflectivity data was fitted as previously described in Chapters 3 and 4 using the *mono* and *drydoc* programs.

5.4 Results

5.4.1 MD Simulations of nSP-C and dpSP-C in Water

The nSP-C and dpSP-C proteins were initially simulated in water only in order to compare the behaviour of these proteins in free solution. After a 1 ns simulation, the conformations of the proteins are shown in Figure 5.6. Following simulation, the helical content of nSP-C was 71.2 % whereas the helical portion in dpSP-C was 83.2 %. The helical content of the nSP-C input structure was 76.5 %. It is clear from Figure 5.6 that the helix in dpSP-C encompasses more of the amino acid residues than nSP-C, at both the N- and C- terminal sides of the helix.

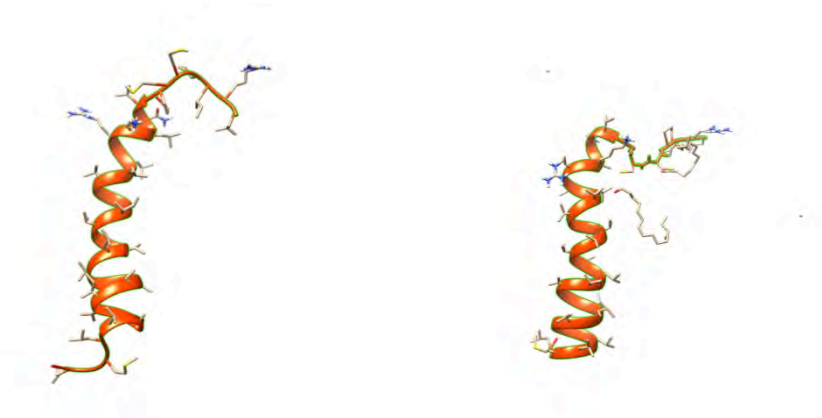

Figure 5.6. A snapshot of the nSP-C molecule (left) and dpSP-C molecule (right) after 1 ns of MD simulation in water.

During the simulation, the RMSD of the structures was calculated, as shown in Figure 5.7. The RMSD of dpSP-C with respect to an ideal helix increased more over time than nSP-C, but during the simulation it was observed that the conformation of the palmitoyl chains varied significantly due to unfavourable interactions with the water, although the conformation of the protein backbone did not change much. The radius of both helices increases slightly to ~0.27 nm from the ideal (0.23 nm) during the simulation as shown in Figure 5.8, but this increase is approximately the same for both proteins.

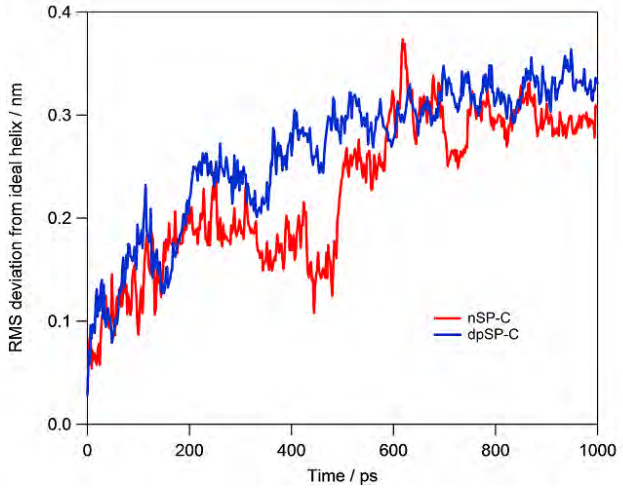

Figure 5.7. The RMS deviation from an ideal helix during simulation of nSP-C (red) and dpSP-C (blue) in water.

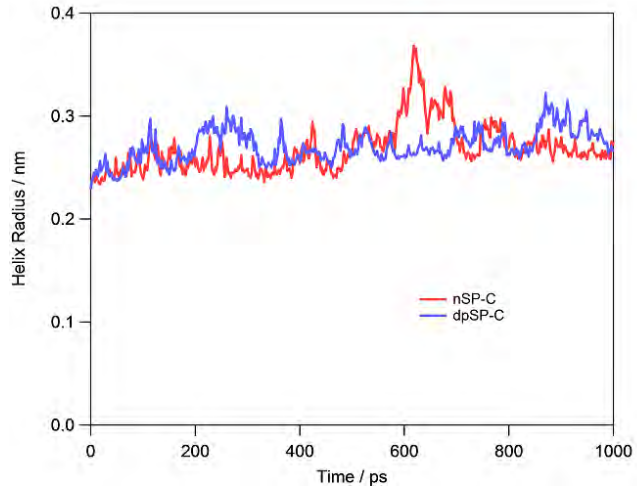

Figure 5.8. The deviation from ideal helix radius of 0.23 nm during simulation of nSP-C (red) and dpSP-C (blue) in water.

5.4.2 MD Simulations of DPPC Monolayers

Simulations of monolayers of DPPC at the air-water interface at various areas per lipid were performed. Snapshots of the DPPC monolayers after 1 ns of simulation are shown in Figure 5.9. As expected, the DPPC molecules become less ordered as area per molecule increases. At smaller area per molecule, the lipid tails are standing more upright, perpendicular to the interface whereas monolayers with a greater area per molecule became deformed quickly during the simulation, with tails tilting towards the interface.

The final configuration is examined in more detail by plotting the electron density profile of the different moieties within the simulation box along the axis perpendicular to the monolayer (z-axis). The headgroup is defined as the hydrophilic part of the molecule: the choline, phosphate group and the ester groups. The tail is defined as the CH_2 and CH_3 groups of the C16 chains only. The electron densities of the monolayers at 47, 58, 63 and 97 $Å^2$ are presented in Figure 5.10. The profiles show that the hydrophilic lipid head groups mix with the water, while the hydrophobic lipid tails project towards the vacuum.

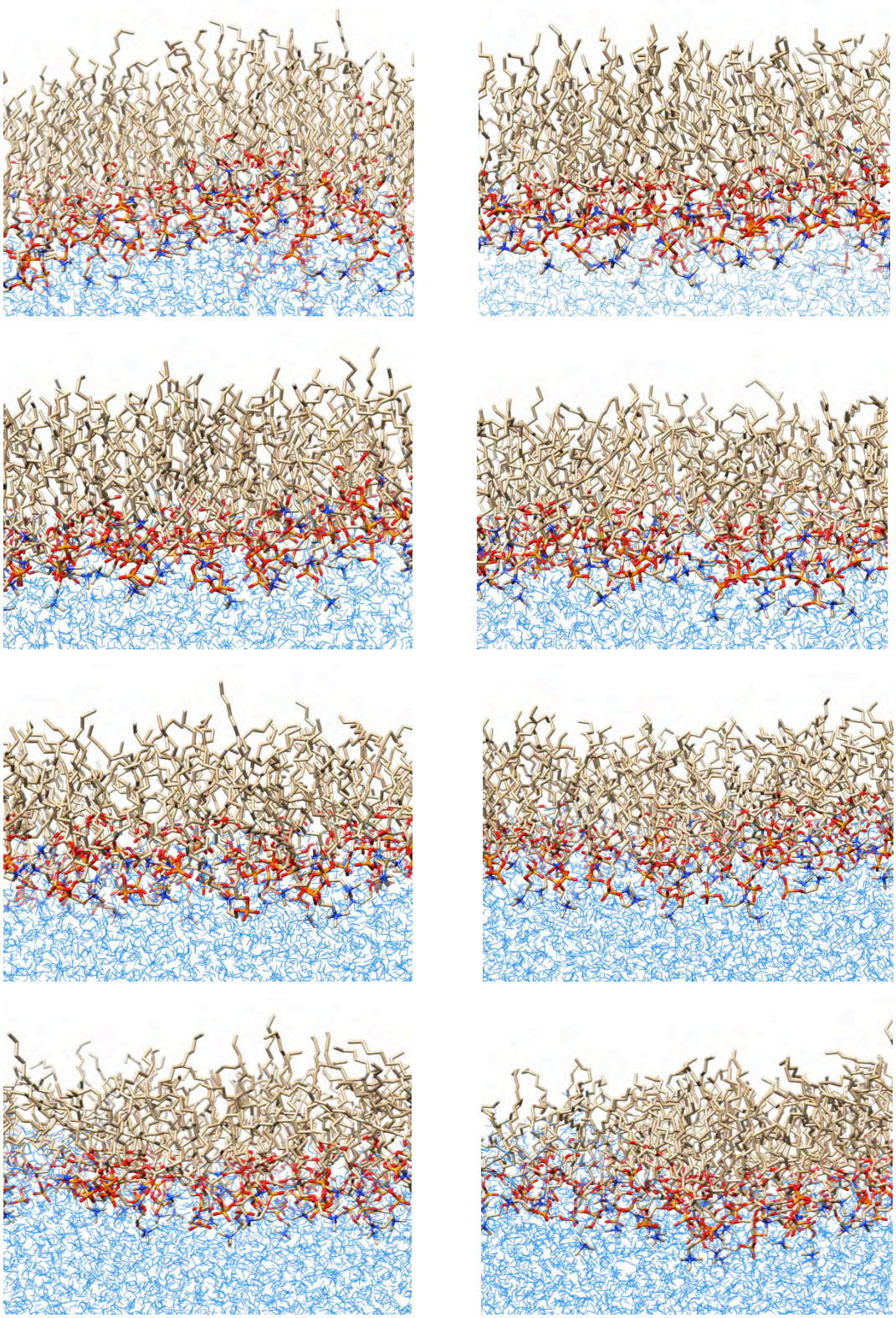

Figure 5.9. Snapshots of monolayers of DPPC at the air-water interface after 1 ns of no constraints, constant area MD simulation.

The areas per molecule of DPPC at the surface from left to right and top to bottom are: 47, 53, 58, 63, 71, 81, 88 and 97 Å^2. In these images: blue = water, gold = lipid tails, red/blue = lipid heads.

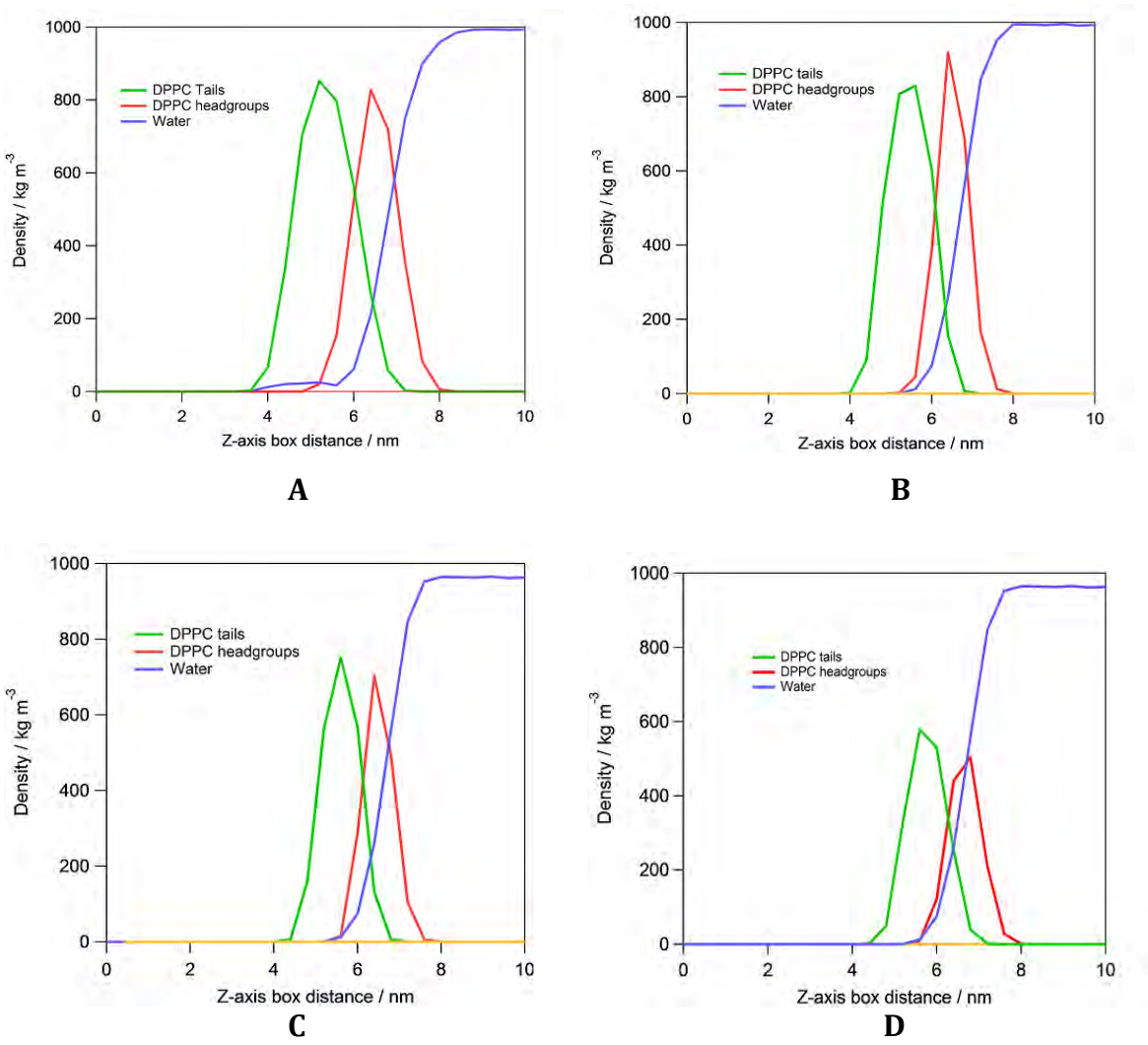

Figure 5.10. Density profiles of DPPC tails (green), DPPC headgroups (red) and water after 1 ns simulation of monolayers of DPPC at the air-water interface.

A is the monolayer at an area per lipid of 47 Å^2, B is at an area per lipid of 58 Å^2, C is an area per lipid of 63 Å^2 and D is an area per lipid of 97 Å^2. The headgroup is defined as the hydrophilic part of the molecule: the choline, phosphate group, glycerol group and the ester groups. The tail is defined as the CH_2 and CH_3 groups of the C16 chains only.

From these plots the average thickness of the phospholipid monolayer was calculated, and compared to thickness values obtained from neutron reflectivity of DPPC monolayers at the air-water interface. The thickness results for both MD

simulation and neutron reflectivity data fitting are shown in Figure 5.11. The minimum area per molecule achievable during the neutron reflectivity experiments was larger than for the simulations due to the experimental restrictions by the Langmuir trough (see Chapters 3 and 4 for details). However, the results suggest that there is good correlation between the monolayer thicknesses obtained during simulation compared to experiment for each area per lipid. In both simulation and experiment, the monolayer thickness increases as area per lipid decreases, which agrees with observations that DPPC molecules tilt more upright as they come closer together.

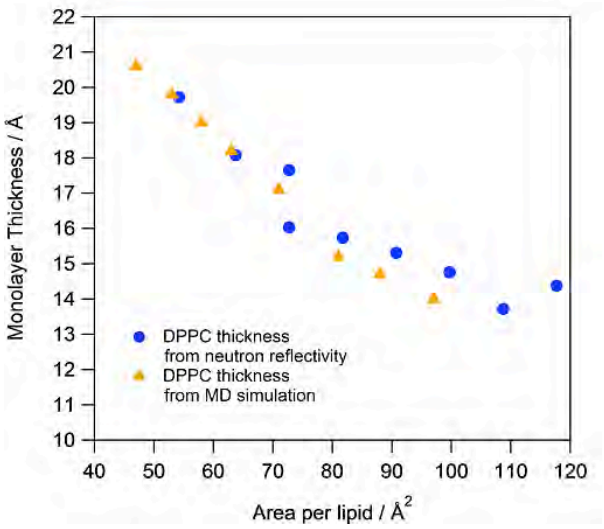

Figure 5.11. The change in thickness *versus* area per lipid in both MD simulation of DPPC monolayers (yellow) and neutron reflectivity of DPPC monolayers (blue).

5.4.3 MD Simulations of nSP-C and dpSP-C in DPPC Monolayers

In order to examine the change in conformation of the nSP-C and dpSP-C and interactions with a DPPC monolayer at different areas per molecule, some MD simulations were performed at constant volume using a canonical NVT ensemble. Snapshots of selected systems after 1 ns simulation are shown in Figures 5.12 (N-terminal initially inserted) and 5.13 (C-terminal initially inserted).

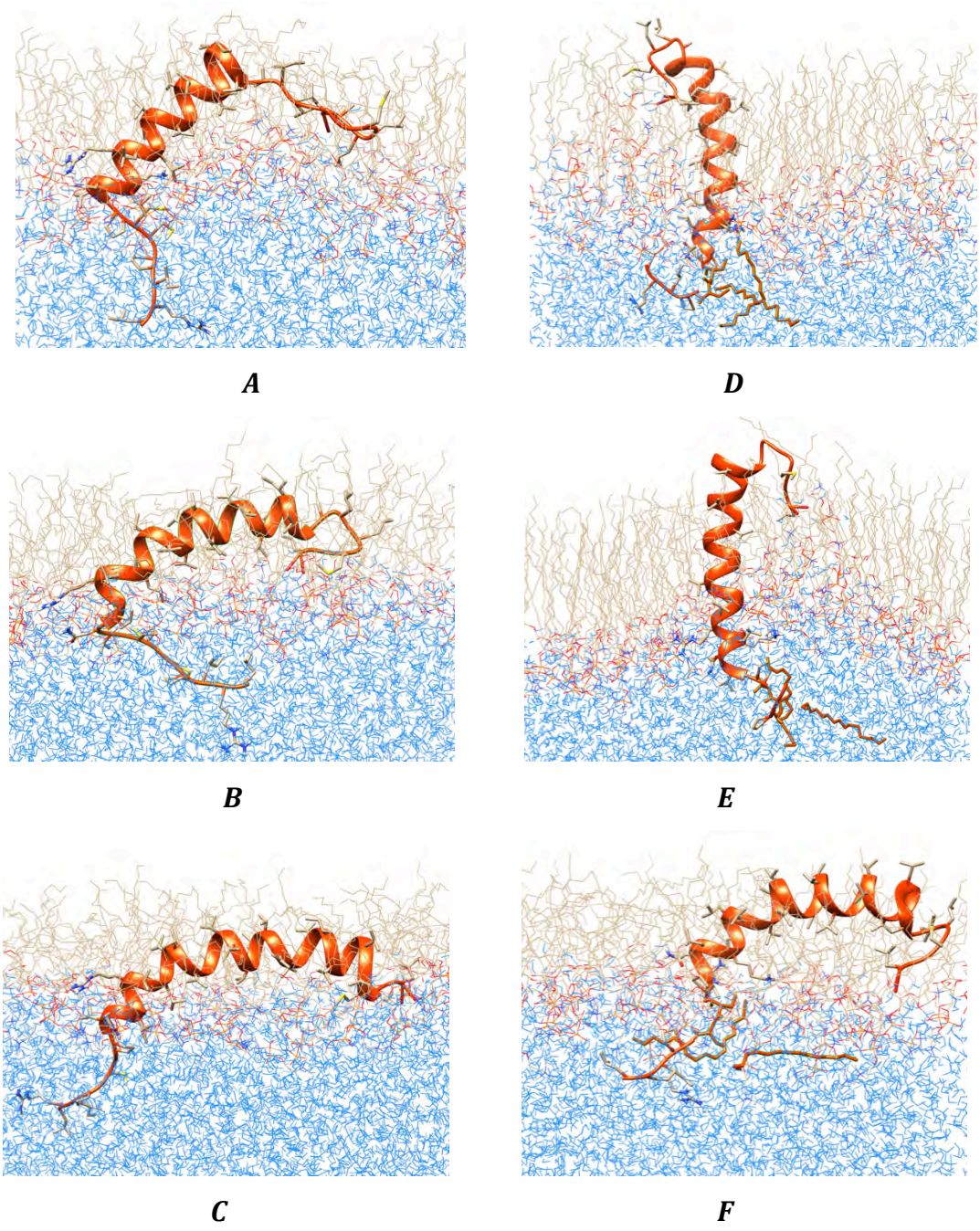

Figure 5.12. Snapshots of monolayers of nSP-C in DPPC (left column, A-C) and dpSP-C in DPPC (right column, D-F) at the air-water interface, with the N-terminal initially inserted into the subphase, after 1 ns of constant area MD simulation.

The areas per lipid at the surface from top to bottom are: ~47 Å^2 (A and D), ~63 Å^2 (B and E), ~80 Å^2 (C and F).

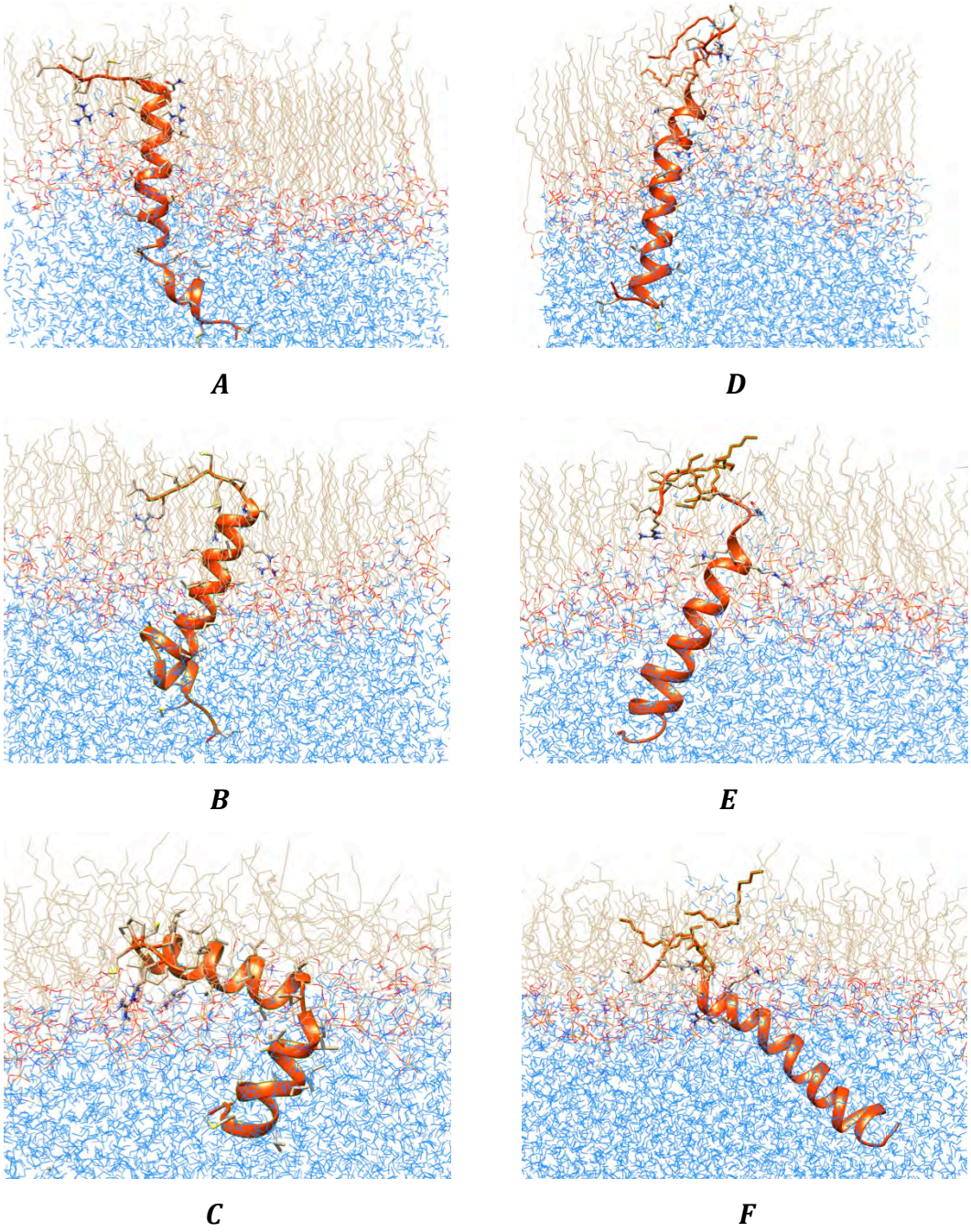

Figure 5.13. Snapshots of monolayers of nSP-C in DPPC (left column, A-C) and dpSP-C in DPPC (right column, D-F) at the air-water interface, with the C-terminal initially inserted into the subphase, after 1 ns of constant area MD simulation.

The areas per molecule at the surface from top to bottom are: ~47Å^2 (A and D), ~65 Å^2 (B and E), ~81 Å^2 (C and F).

Figure 5.12 shows the orientation of the nSP-C and dpSP-C proteins in a DPPC monolayer when the N-terminal residues have been inserted into the water layer. For nSP-C this is the more likely orientation as the more hydrophilic residues are present here (Arg 2, Lys 11, Arg 12), but in dpSP-C the polarity of the molecule would be significantly changed due to the presence of the hydrophobic palmitic acid chains bonded to Cys 5 and Cys 6. Therefore, it is likely that dpSP-C would adopt a different orientation at the interface and so the simulations were performed where the C-terminal residues were inserted into water, shown in Figure 5.13. From these snapshots it appears as though some deformations of the protein within the middle of the helix occur more commonly during simulation of nSP-C than dpSP-C (e.g. Figure 5.13 A-C). Additionally, the nSP-C molecule tilts further towards the parallel of the interface at smaller area per molecule than dpSP-C (e.g. Figure 5.12 A *versus* D, Figure 5.13 B *versus* E).

Analysing the secondary structure of the protein during the simulation revealed that the helical content of dpSP-C was higher in most cases, as shown in Table 5.3. This table also presents the data for average monolayer thickness for each simulation, helix tilt with respect to z-axis and average helix radius during simulation. The data shows the monolayer thickness increasing with decreasing area per molecule in all monolayers, also shown in Figure 5.14. The thickness of the dpSP-C/DPPC monolayers is higher in most cases than nSP-C/DPPC monolayers at comparable areas per lipid. Furthermore, the thicknesses of the dpSP-C/DPPC monolayers are much higher than the thicknesses of DPPC monolayers, whereas the thicknesses of nSP-C/DPPC monolayers are more similar to that of DPPC monolayers.

Table 5.3 shows that the helix tilts to become more parallel with the interface as area per molecule increases. This is also visible in the snapshots of the monolayers in Figures 5.12 and 5.13 as the proteins lie flatter at higher area per lipid. The average helix radius shows very little trend with area per lipid. The nSP-C helix tends to deviate further from the ideal helix radius of 0.23 nm than dpSP-C, which could be due to its higher propensity to unwind and lose helical content.

Protein	Area per molecule / Å^2	Initial orientation (terminus in subphase)	Average helical content / %	Monolayer Thickness / Å	Helix Tilt with respect to z-axis / degrees	Average helix radius / nm
nSP-C	47	N	61	23.1	42	0.43
nSP-C	52	N	65	19.4	52	0.43
nSP-C	63	N	64	18.7	78	0.27
nSP-C	71	N	71	18.3	81	0.29
nSP-C	80	N	69	17.4	77	0.37
nSP-C	97	N	71	14.5	87	0.32
nSP-C	47	C	58	21.4	12	0.26
nSP-C	52	C	62	19.2	34	0.29
nSP-C	63	C	59	18.5	43	0.37
nSP-C	71	C	63	18.4	68	0.35
nSP-C	80	C	59	16.4	73	0.31
nSP-C	97	C	64	15.2	79	0.26

Protein	Area per molecule / Å^2	Initial orientation (terminus in subphase)	Average helical content / %	Monolayer Thickness / Å	Helix Tilt with respect to z-axis / degrees	Average helix radius / nm
dpSP-C	47	N	76	24.2	8	0.27
dpSP-C	53	N	83	23.1	7	0.27
dpSP-C	65	N	79	20.1	12	0.32
dpSP-C	73	N	69	18.8	32	0.33
dpSP-C	81	N	65	18	67	0.29
dpSP-C	101	N	67	16.9	73	0.32
dpSP-C	47	C	81	23.5	21	0.25
dpSP-C	53	C	83	20.3	25	0.25
dpSP-C	65	C	76	19.7	37	0.25
dpSP-C	73	C	76	17.8	43	0.27
dpSP-C	81	C	81	17.7	41	0.34
dpSP-C	101	C	71	16.5	54	0.25

Table 5.3 Data showing the properties of the nSP-C helix (top) or dpSP-C helix (bottom) during simulation of the proteins in DPPC monolayers at different initial orientations and different areas per molecule.

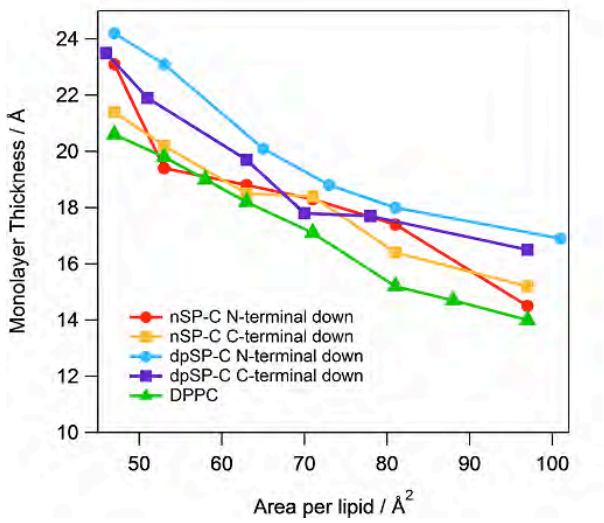

Figure 5.14. Thickness *versus* area per lipid in MD simulations of DPPC monolayers (green), DPPC/nSP-C monolayers (red and orange) and DPPC/dpSP-C monolayers (blue and purple).

Figures 5.15 and 5.16 present the electron density plots of SP-C/DPPC monolayers at the smallest and largest area per molecule for each monolayer. These plots show that the lipid molecules behave as expected when the area per lipid is decreased as the width of the lipid density profiles becomes bigger at higher area per molecule, in agreement with thicknesses increasing. Also, overall density of the lipids decreases with increasing area per lipid, as expected as there is more space between molecules.

The density profile of the protein is different in the different simulations. When there is a bigger area per molecule, the density is lower in all cases, suggesting the protein has a different conformation than at smaller area per molecule. For dpSP-C with an initial orientation of the C-terminus being inserted in the water (Figure 5.16 D) the protein appears to move further into the water layer at higher area per molecule, as the average depth of the protein changes from 14 to 12 Å, therefore it has moved 2 Å further into the aqueous subphase.

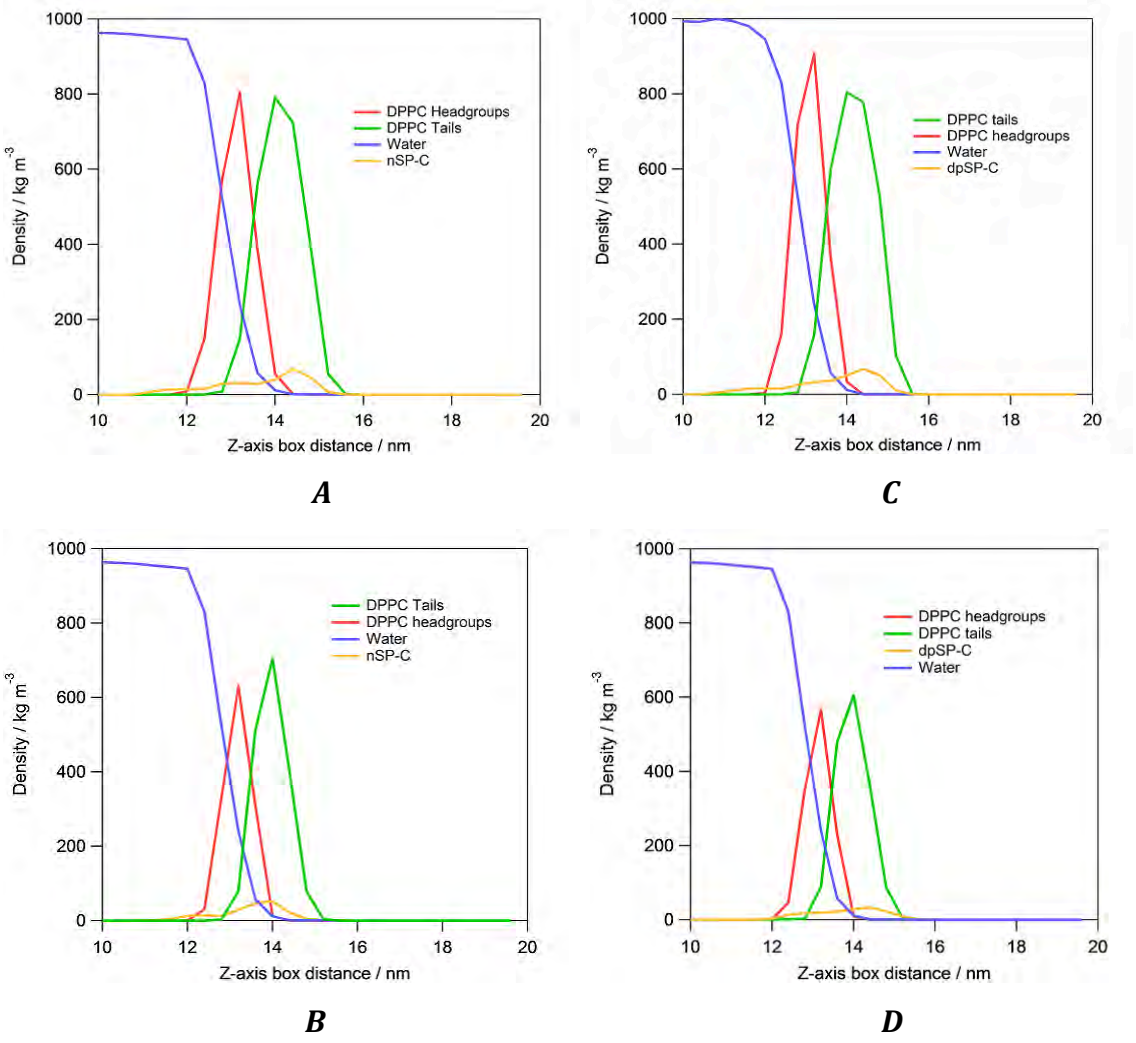

Figure 5.15. Density profiles of DPPC tails (green), DPPC headgroups (red), water (blue) and protein (yellow) during simulation of protein/DPPC monolayers at the air-water interface with N-terminal initially inserted into the subphase.

A is the nSP-C/DPPC monolayer with the N-terminal initially inserted into the subphase at an area per molecule of 47 Å^2 and B is the same monolayer at an area per molecule of 97 Å^2. C is the dpSP-C/DPPC monolayer with the N-terminal initially inserted into the subphase at an area per molecule of 47 Å^2 and D is the same monolayer at an area per molecule of 97 Å^2.

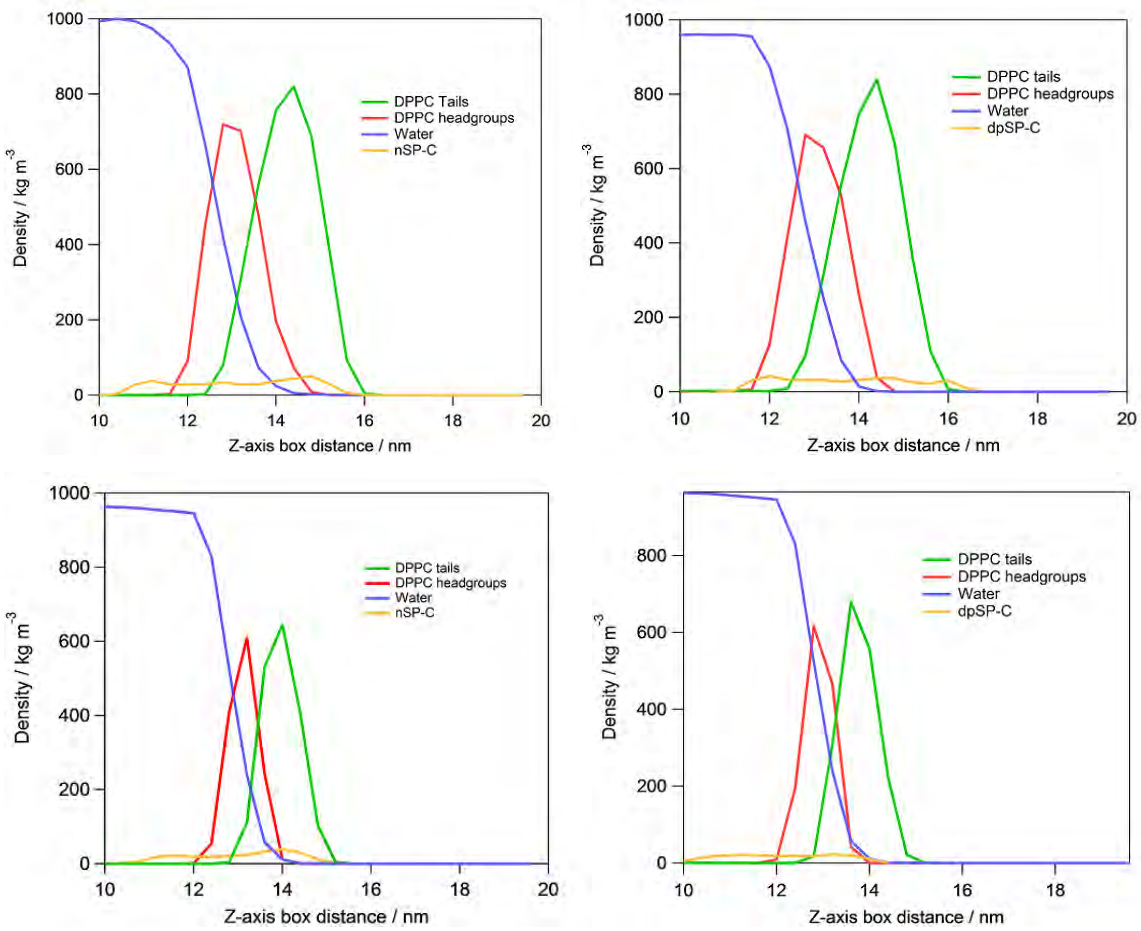

Figure 5.16. Density profiles of DPPC tails (green), DPPC headgroups (red), water (blue) and protein (yellow) during simulation of protein/DPPC monolayers at the air-water interface.

A is the nSP-C/DPPC monolayer with the C-terminal initially inserted into the subphase at an area per molecule of 47 Å^2 and B is the same monolayer at an area per molecule of 97 Å^2. C is the dpSP-C/DPPC monolayer with the C-terminal initially inserted into the subphase at an area per molecule of 47 Å^2 and D is the same monolayer at an area per molecule of 97 Å^2.

The behaviour of the lipid C16 tails was examined using the order parameter, which provides a measure of conformational order of the C-H bonds along the chain. The order parameters are calculated for the CH_2 carbons only. Figure 5.17 shows the order parameters for each monolayer simulated, including those for DPPC alone. It is clear that in all systems the DPPC tails become more ordered with decreasing area per lipid. It appears that the DPPC tails are more ordered at both small and large area per lipid in the presence of dpSP-C than nSP-C. This is highlighted in Figure 5.18, which shows the order parameters of the different monolayers at 47 $Å^2$ and 80 $Å^2$, which shows that at both large and small areas per lipid, the presence of nSP-C, and to greater extent dpSP-C, increases the order of the DPPC chains compared to monolayers of DPPC alone. nSP-C has a small effect on increasing the order of DPPC whilst dpSP-C has a much larger effect. This is observed regardless of the initial geometry used. This indicates that palmitoylation of SP-C could have some lipid ordering purpose in a physical system.

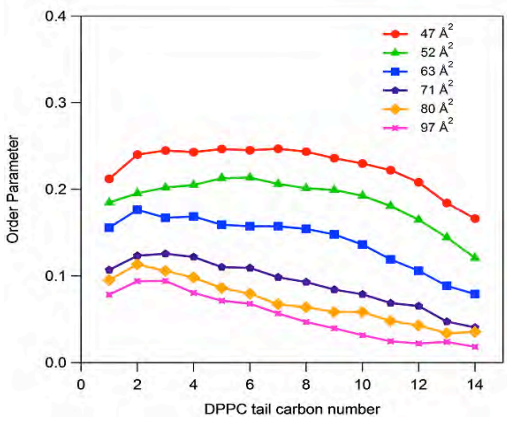

DPPC

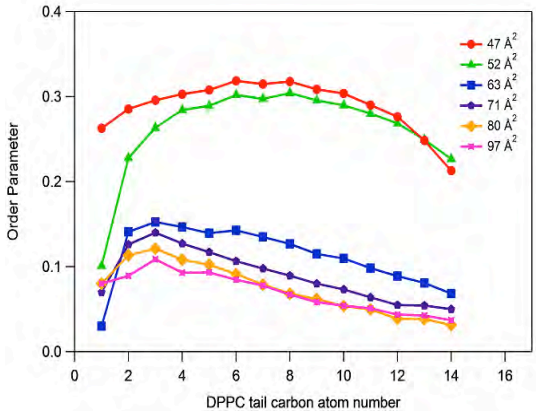

A: nSP-C

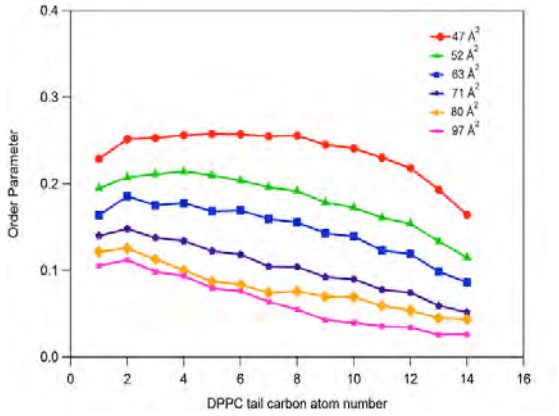

B: nSP-C

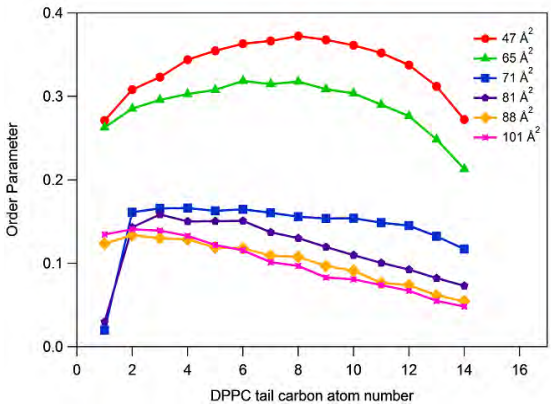

C: dpSP-C

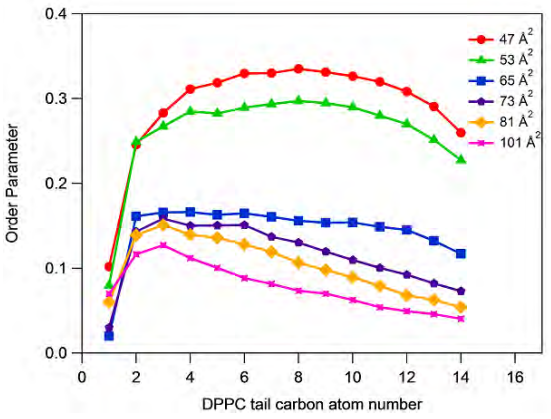

D:dpSP-C

Figure 5.17. DPPC C16 lipid chain order parameter profiles for monolayers in the presence of: DPPC (top); A, nSP-C with N-terminal inserted into the subphase; B, nSP-C with C-terminal inserted into the subphase; C, dpSP-C with N-terminal inserted into the subphase; D, dpSP-C with C-terminal inserted into the subphase.

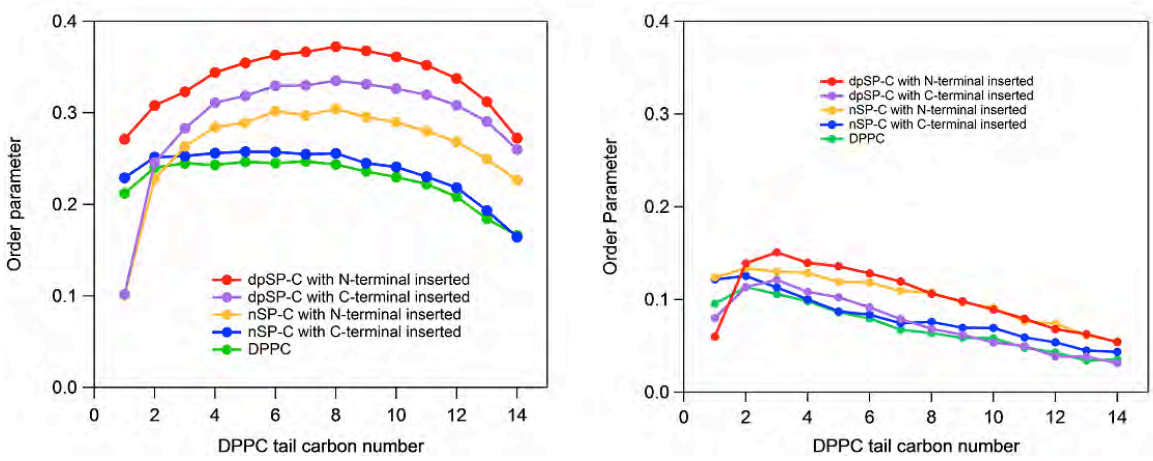

Figure 5.18. DPPC C16 lipid chain order parameter profiles for monolayers at areas per lipid of 47 Å² (left) and 80 Å² (right).

5.5 Discussion

The interaction of dpSP-C with DPPC lipids in a monolayer at the air-water interface was investigated using MD simulations. To probe the role of the palmitoyl chains further, the interaction between nSP-C and the lipid monolayer was also investigated in order to compare to the simulations of dpSP-C.

Initially, simulations of the proteins in water were performed so that changes in the protein structure caused by the presence of the lipid monolayer could be observed. The simulations of the proteins in water were compared to previous studies by Carvalheda *et al.*[194], and the results obtained were similar. Both this work and that of Carvalheda reveal that a ~10 % loss of helical structure in SP-C is related to loss of palmitoyl chains. The percentage helical content observed by Carvalheda *et al.* was 62 % for dpSP-C and 55 % for nSP-C, whereas here the percentage helical content was calculated to be 83 % for dpSP-C and 71 % for nSP-C. The lower values obtained by Carvalheda could be attributed to the longer simulation times (100 ns *versus* 1 ns) used. In both studies it was observed that the nSP-C protein lost its helical structure in the C-terminal region in water. It was shown by Carvalheda *et al.* that with longer simulation times there was some β structure arising from interactions between N and C unfolded regions of nSP-C. This β structure transformation was not observed in these studies, but it is possible that the structural feature could form with longer simulation times.

The simulations of DPPC monolayers at various areas per molecule showed a visible decrease in thickness and order of the lipid tails as area per molecule increases. Where larger numbers of lipid molecules are simulated in the monolayers, e.g. Duncan and Larson[230], the domains of each phase from liquid-condensed (LC) to liquid-expanded (LE) are visible. Here, using 79 DPPC lipids per monolayer, it was possible to see the hexagonal order in the LC phase compared to disorder in the LE phase during simulation of DPPC monolayers as shown in Figure 5.19.

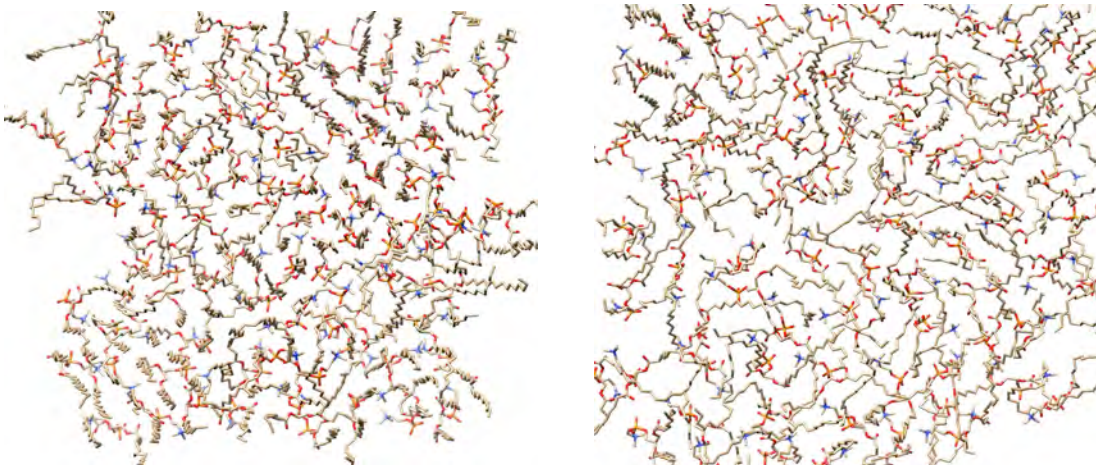

Figure 5.19. DPPC monolayers viewed from above at high and low area per molecule.

Left: DPPC monolayer at 47 Å^2 per molecule (LC part of the surface pressure monolayer) viewed from above showing the hexagonal order. Right: DPPC monolayer at 71 Å^2 per molecule (LE part of the surface pressure monolayer) viewed from above showing no order.

From the density profiles, it was clear that the DPPC monolayers were thinner and less dense (more spread) as area per lipid increased. This agreed with neutron reflectivity experiments performed, where monolayer thicknesses were determined at various areas per molecule. Figure 5.11 shows good correlation between data obtained during simulation and experiment. The discrepancies in the data can be attributed to deuterated d_{62} DPPC being used in the neutron experiment. It has been shown that deuteration can alter the physical states of the DPPC monolayer, meaning that the isotherms are slightly different. In particular, the melting temperature of a d_{62} DPPC monolayer is lower than that of a ^{1}H DPPC monolayer.

Simulation of mixed monolayers of DPPC/nSP-C or DPPC/dpSP-C at the air-water interface showed that addition of the palmitoyl chains changes how the protein resides at the interface. During simulations of monolayers at small areas per lipid, both nSP-C and dpSP-C remained at an almost perpendicular position with respect to the interface. During simulations of the monolayers at areas per molecule of 63 Å^2 or greater, the protein tilted towards parallel to the interface in

varying amounts. In general, dpSP-C tilted less with respect to the interface than nSP-C, therefore remained more perpendicular during the simulations. Consequently, the role of the palmitoyl chains could be to ensure the protein lies in the correct position in the lipid monolayer, particularly at higher areas per lipid, to maximise contact with the lipids.

Kandasamy *et al.* investigated the orientation of the surfactant protein B peptide mimic SP-$B_{1\text{-}25}$ in a DPPC monolayer and found that its helix persistently moved to a parallel position with respect to the interface. The driving force for this orientation was proposed to be to maximise the hydrogen bonding between the polar or charged residues with the water molecules and DPPC headgroups.[231] The same observation was not seen in this research with SP-C because its helix is largely hydrophobic whereas the SP-$B_{1\text{-}25}$ helix is amphiphilic, where one side of the helix consists of more polar residues and one side consists of mainly hydrophobic residues, as shown in Figure 5.20. Therefore, the SP-C helix would prefer to remain associated with the DPPC tails as much as possible.

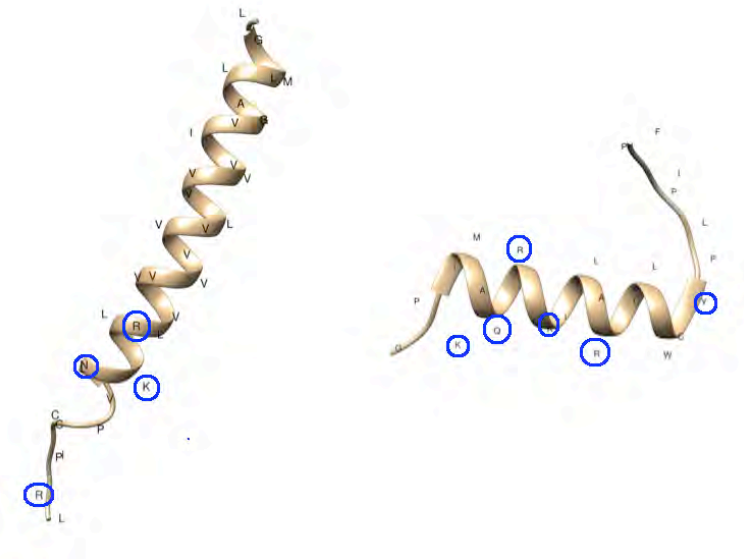

Figure 5.20. The secondary structure of SP-C (left) and SP-$B_{1\text{-}25}$ (right), indicating the hydrophilic amino acid residues.

The amino acids are shown by their one-letter code and the hydrophilic residues are circled in blue.

The helical content of the nSP-C or dpSP-C proteins in DPPC monolayers was generally the same or less than that of the proteins in water. It was previously shown by Vandenbussche *et al.* experimentally that the helical content of the proteins increased by about 5 residues when in phospholipid bilayers.[189] This was not seen in these simulations, which is not unexpected as a protein in a monolayer is much less constrained than in a bilayer.

The presence of the SP-C in a monolayer of DPPC increases the thickness of the monolayer compared to DPPC monolayers alone at the same area per lipid, particularly at higher areas per lipid. Therefore, the addition of the protein changes how the lipids reside in the monolayer. This increase in thickness is even greater when the cysteines are palmitoylated. The increase in thickness upon addition of the palmitoyl chains is not simply because the protein is more bulky, leading to a smaller area per lipid, as the increase in thickness at a particular area per lipid from a monolayer of SP-C/DPPC to dpSP-C/DPPC is much higher than would be expected for the increase in volume of the protein. For example, at an area per lipid of 52 Å^2 the monolayer thickness increases from ~19 Å when nSP-C is present (with the N-terminal down) to 23 Å when dpSP-C is present (with the N-terminal down). From the area per lipid *versus* monolayer graph for DPPC only monolayers shown in Figure 5.11, an increase in monolayer thickness from 19 to 23 Å would require a decrease in area per lipid from ~60 Å^2 to less than 30 Å^2. Since the addition of palmitoyl chains to the protein could not lead to a decrease in area per lipid by such a large amount, the palmitoyl chains must have some role in increasing monolayer thickness, possibly by inducing order in the DPPC monolayer tails. This is evident in Figure 5.17 where the order parameters for dpSP-C, particularly with the N-terminal initially inserted into the subphase, are higher than those of nSP-C, and much higher than those of DPPC only.

The MD simulations were done with either the N-terminal or the C-terminal of dpSP-C initially inserted into the subphase. These simulations have hinted that the N-terminal insertions were more favourable for several reasons. Firstly, the electron density plots of dpSP-C/DPPC monolayers and snapshots of the simulations suggested that at high areas per lipid, the protein would extend further into the aqueous subphase when the C-terminal was inserted, which would be an unlikely property of the protein due to its high hydrophobicity. Furthermore,

the monolayer thicknesses and order parameters were higher for dpSP-C/DPPC monolayers when dpSP-C was initially inserted with its N-terminal down in the subphase than with the C-terminal initially inserted, suggesting that the palmitoyl chains are better able to fulfil their function at this conformation. Additionally, the potential energy of the systems was always lower after energy minimisation of the N-terminal inserted protein than the C-terminal inserted protein, suggesting that this is the more energetically favourable orientation. It is likely that this is due to the hydrophilic residues of SP-C being present towards the N-terminal only, as shown in Figure 5.20; and even though the addition of the hydrophobic palmitoyl chains to this side of the helix would make the protein less amphiphilic, it does not seem to prevent the protein from spanning the monolayer in this orientation.

This study has therefore shown that the presence of the palmitoyl chains bonded to the cysteine residues of SP-C can greatly affect the conformation of the helix, its orientation with respect to the interface and the conformation of the phospholipids in close proximity. The proposed function of the protein is to increase the fluidity of the phospholipid monolayer at the air-water interface of the lung. The results shown here suggest that the ordering capability of the protein could be important for this function.

5.6 Conclusion

This research aimed to perform MD simulations of dpSP-C in a DPPC monolayer at various areas per lipid and to compare these to simulations of DPPC monolayers alone in order to elucidate how the presence of the protein affects the lipid monolayer. Additionally, MD simulations of nSP-C in DPPC monolayer were performed and compared to these results in order to determine how the presence of palmitoyl chains affects both the protein and the lipid monolayer. The results presented here provide insights into the nature of the behaviour of the protein at the interface and its interaction with phospholipids. It was shown that the presence of the palmitoyl chains causes the helix to maintain its high helical content, as shown in both the water simulations and the DPPC monolayer simulations, similarly to previous research of nSP-C and dpSP-C in water.

The presence of the nSP-C or dpSP-C protein in a DPPC monolayer caused increases in thickness and tail carbon order parameters compared to DPPC alone, even at large areas per lipid. This suggests that the protein induces ordering of the phospholipid tails. This effect was significantly greater when the cysteines were palmitoylated on the protein, implying that the role of the palmitic chains is related to ordering the lipid tails even at fairly large areas per lipid. The simulations were performed with either the C-terminal or N-terminal of the protein initially inserted into the subphase and the simulations suggested that the system was more energetically favourable when the N-terminal of the protein was initially inserted, indicating that this orientation might best represent the protein monolayer in a physical system. Furthermore, the lipid ordering capabilities of the protein were greater when the N-terminal was initially inserted.

Further work could include incorporating different lipids within the monolayer, such as anionic POPG or cholesterol, to investigate whether the protein behaves differently in the presence of these lung surfactant components. Additionally, the conformational and positional changes upon oxidation of the protein could be investigated, as well as its interaction with surrounding phospholipids, as it is likely that the structure and function of SP-C would be greatly affected by oxidative damage that leads to changes to its polarity.

Chapter 6 Evaluation of Neutron Scattering and Reflection Techniques for Studying Bilayer Oxidation – Preliminary Data and Future Perspectives

6.1. Introduction

The interaction of reactive oxygen species with biological membranes is known to produce a great variety of different functional modifications, as described in Chapter 1. Considering many studies have examined the pathological conditions resulting from oxidation reactions at lipid membranes, there is little understanding of the early sequences that lead to membrane remodelling. Specifically, little is known about the influence of the oxidation products on the structure of the membrane after oxidation, and how lipid raft formation is affected. This research aims to present the potential uses of neutron scattering and reflectivity techniques for studying the oxidation of lipid bilayers and presents some preliminary results obtained. The neutron is a powerful probe for the study of biological matter, and has significant advantages over other forms of radiation, as discussed in Chapter 2.

Recently, neutron reflectivity has been used to study lipid bilayers as a representation for biological membranes and their behaviour under oxidative conditions from short-wavelength UV light.[232] In initial experiments, DPPC bilayers at a solid/liquid interface were exposed to UV light (forming various ROS) for varying lengths of time. It was found that bilayer thickness remained constant as a function of oxidative stress although membrane surface coverage decreased with exposure time. In addition, FTIR was used to monitor the loss of material, showing the continuous loss of methylene, methyl and carbonyl vibrational modes with increasing exposure time. Mass spectrometry of the exposed samples indicated that nearly all of the DPPC molecules had disappeared after exposure. Therefore, it was evident that the membrane had degraded over time.[232]

It was hypothesised that because the surface coverage after oxidation was significantly lower than required for membrane lysis, the bilayer must have

rearranged in response to the change in molecular forces. Furthermore, it was thought that hydrophilic pores were formed in the membrane.[232] This hypothesis was supported by evidence from fluorescence experiments where bilayers of POPC were labelled with a fluorescent tag and imaged before and after UV exposure. After exposure to UV, black spots appeared in the bilayer, indicating the presence of pores.

Those previous studies focus on the oxidation of membranes from a mixture of various oxidant species, as UV exposure to water allowed the formation of many species. The mechanism and kinetics of oxidation by each individual species is not known. Additionally, not all species may be capable of oxidising the membrane lipids under these conditions. The work presented here builds on this by using chemical knowledge to produce a known amount of a single species of oxidant and to examine the location on the phospholipid membrane of the initial attack and the kinetics of this reaction on the phospholipid membrane. Furthermore, the present research aims to investigate how the oxidation of phospholipids and the presence of oxidised phospholipids changes lipid raft formation. It has been shown by Coban *et al.* using atomic force microscopy (AFM) that oxidation of monolayers of DPPC or sphingomyelin, cholesterol and DOPC in air leads to bigger domains formed at surface pressures of ~ 30 mN m^{-1} than the same monolayers in the absence of air.[233] The same effect was observed by Ayuyen *et al.*, who used fluorescence microscopy to show that larger raft domains formed following photooxidation of lipid vesicles and supported bilayers prepared from sphingomyelin (SM), cholesterol and unsaturated phospholipids compared to the size of non-oxidised domains.[234] More recently it was shown using Brewster angle microscopy (BAM) that the presence of the oxidised lipid, 1-palmitoyl-2-azelaoyl-*sn*-glycerol-3-phosphochline (PAzPC-Figure 4.1) in monolayers of saturated phospholipids and cholesterol leads to an increase in the stability and persistence of the lipid rafts at higher surface pressures.[235]

The L_o phase is thicker than the L_d phase, giving rise to a "height mismatch" (or "hydrophobic mismatch") at the domain edge. The exposure of the hydrophobic tails of the lipids to the aqueous solvent would have a very unfavourable energetic effect, and as a consequence, the membrane distorts at the

boundary to avoid it. This height mismatch has an energetic cost per unit length that is one of the main parameters contributing to the line tension at the phase boundary. It has been suggested that a balance between lipid electrostatic interactions and domain line tension controls the size of the domains. The line tension at the domain boundary reduces the domain boundary length and thus favours large circular domains whereas dipolar or electrostatic interactions between molecules favours small and/or extended or irregular shapes.[236] It has been shown that no detectable changes in average dipole density difference between disordered and L_o phases were seen when PAzPC was present in place of POPC. This suggests that line tension is a major factor in the regulation of domain shape and stability. Domains containing phospholipids with saturated long acyl chains, associated with cholesterol, appear to be thicker than the surrounding unsaturated phospholipid-enriched disordered phase.[236] Therefore, it has been proposed that chemical modification of unsaturated lipids such as POPC to oxidised lipids such as PAzPC would be expected to significantly thin the disordered region of the membrane, increasing the hydrophobic mismatch between the phases, therefore increasing the line tension at phase boundaries, potentially leading to larger lipid raft sizes. [235]

The research presented in this chapter uses small-angle neutron scattering (SANS) in combination with contrast variation to determine the effect of the presence of oxidised lipid (PAzPC) on the formation and persistence of rafts in vesicles comprised of various ratios of DPPC/POPC/cholesterol. It was described in Chapter 1 that some phospholipids have a higher propensity to form micelles rather than vesicles, for example single tailed phospholipids. Therefore these SANS experiments were also able to detect whether the PAzPC would form micelles rather than stay in vesicles. Neutron reflectivity (NR) experiments were also performed on these monolayers to determine whether any off-specular neutron reflectivity could be detected, which would suggest an ordering on the surface that would be indicative of a height mismatch representative of the domains. This was also performed after oxidation of the lipids in order to determine if the off-specular reflectivity changes after, showing changes in the ordering of the lipid rafts.

6.2. Materials and methods

6.2.1 Materials

Chloroform (Chromasolv, ≥99%, with 0.5-1.0% ethanol stabiliser), D_2O (99.9% D), hydrogen peroxide (3% w/w) and sodium hypochlorite (4-4.5% w/w Cl) were purchased from Sigma-Aldrich. H_2O was obtained from a Millipore system with 18 MΩ cm resistivity. All phospholipids, including deuterated phospholipids, were supplied by Avanti Polar Lipids. Cholesterol was obtained from Fluka (European pharmacopoeia reference standard).

6.2.2 Surface Pressure Measurements of DPPC Monolayers Showing Oxidation by Singlet Oxidation

A Langmuir trough was filled with 55 mL hydrogen peroxide solution (10 mM, 6 mg mL^{-1} of 3% solution). 50-100 μL of DPPC (1 mg mL^{-1} in chloroform) was added to the surface using a microliter syringe. The surface pressure was measured using a Wilhelmy plate made from Whatman's chromatography filter paper, coupled to an electrobalance.

For the oxidation experiments, 1.5 mL of sodium hypochlorite (4-4.5% Cl) was injected into the subphase. The surface pressure was measured continuously before, during and after injection. For control experiments, 1.5 mL of water was injected into the subphase. As before, the surface pressure was measured continuously before, during and after injection.

6.2.3 Sample Preparation for Neutron Reflectivity of Phospholipid Bilayers at the Solid-Liquid Interface

The set-up for neutron reflectivity of phospholipid bilayers at the solid-liquid interface in these experiments is shown in Figure 6.1. Phospholipid bilayers were deposited onto a solid quartz substrate. Quartz contrast-matched solutions were used in all oxidation experiments, so that the low scattering length density of

the bilayer would be detectable against the high scattering length density of the quartz, and so reflection should only be off the bilayer. Quartz has a neutron scattering length density of 4.18 x 10^{-6} Å^{-2} and so quartz contrast-match water can be formed by mixing 69% D_2O (scattering length density 6.35 x 10^{-6} Å^{-2}) with 31 vol% H_2O (scattering length density -0.56 x 10^{-6} Å^{-2}).

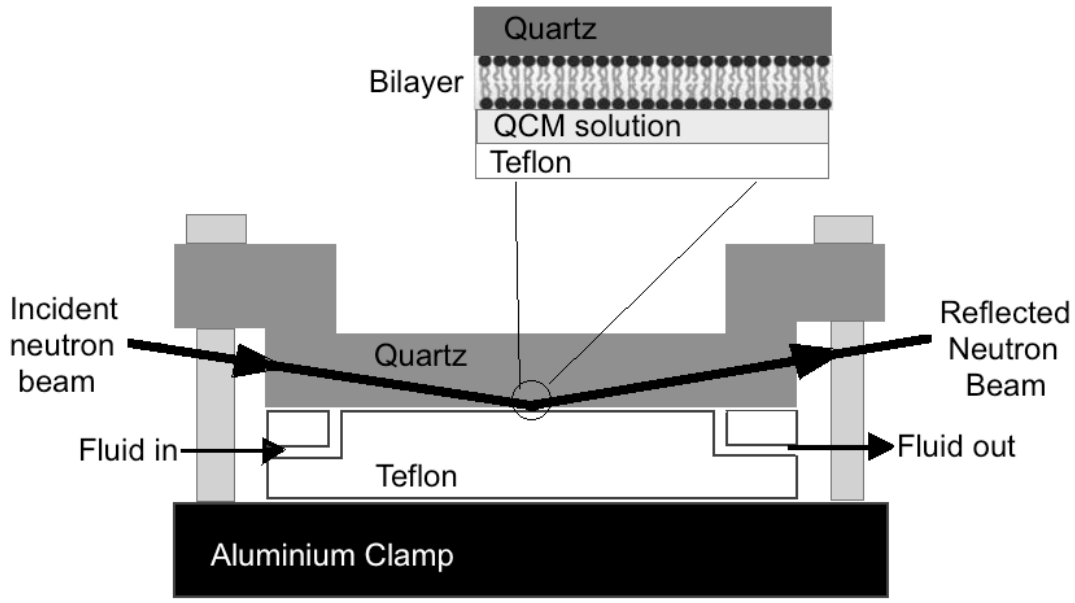

Figure 6.1. Schematic of the solid-liquid interface used in the neutron reflectivity experiments.

The phospholipid bilayer was formed on a hydrophilised quartz slab that was placed into the holder, which was then filled with quartz-contrast matched solution. In the reflectivity experiments, the neutron beam entered through the quartz and was reflected off the solid/bilayer interface.

DPPC and DOPC bilayers were formed using the standard procedures for surface-induced rupture and spreading of small unilamellar vesicles (SUVs).[237] DPPC was purchased in aliquots of 10 mg mL^{-1} in chloroform and the solution was diluted to 0.5 mg mL^{-1}. 10 mL of the diluted solution was dried under a stream of nitrogen gas for 8 hours. The lipid was then hydrated in 10 mL of purified water, heated to 50 ^{o}C and sonicated with a probe-tip sonicator for 1 minute at 100 W

power. This temperature is above the phase transition temperature of DPPC (42°C) and with sonication, lipid vesicles could form.

A monocrystalline quartz slab, used to support the bilayer, was soaked in concentrated sulphuric acid (~50:50 vol/vol with water) for 15 minutes, in order to create a hydrophilic surface, and then rinsed with copious amounts of water. The quartz was fitted into a solid-liquid interface cell as shown in Figure 6.1. This was heated to 50 °C along with the vesicle suspension. The warm vesicle suspension was injected into the warm cell using a clean plastic syringe, with a polypropylene plunger. The vesicles were allowed to fuse onto the surface of the quartz and then cooled to room temperature for one hour. The cell was then rinsed with quartz contrast-match water to remove any unfused vesicles to leave a fused bilayer.

6.2.4 Neutron Reflectivity of Supported Bilayers at the Solid-Liquid Interface

Neutron reflectivity experiments investigating the interaction of DPPC bilayers with 100 mM hydrogen peroxide/sodium hyperchlorite solutions were performed on the INTER reflectometer at ISIS (Oxfordshire, UK). Neutron reflectivity experiments investigating the interaction of DPPC bilayers with 50 mM hydrogen peroxide/sodium hyperchlorite solutions were performed on the SURF reflectometer at ISIS (Oxfordshire, UK). Neutron reflectivity experiments investigating the interaction of DOPC bilayers with sodium hyperchlorite solutions were performed on the OFFSPEC reflectometer at ISIS (Oxfordshire, UK).

The neutron beam was collimated and the incident beam entered through the side of the quartz slab, at a small angle incident to the interface, and reached the interface on which the bilayer resided. On INTER the incident angles were 0.6, 1.2 and 2.3°, whilst on SURF they were 1.2 and 2.3°, and on OFFSPEC they were 0.7 and 2.3°. The liquid phase was entered through the cell inlet to fill the small (0.2 mm) gap between the quartz and the PTFE cell.

The measurements were performed by measuring the ratio of reflected to incident intensity of a collimated neutron beam incident on the sample at a small

angle, θ. The ratio is reflectivity, *R*, and is measured as a function of the momentum transfer vector, *q*.

6.2.5 Reactions of Phospholipid Bilayers with ROS

The solid-liquid cell was set-up to allow a continuous flow of solutions exposed to the lipid bilayer as shown in Figure 6.2. Bilayers of ^{1}H DPPC were exposed to hydrogen peroxide (100 mM, quartz contrast matched) or sodium hypochlorite (100 mM, quartz contrast matched) continuously by pumping the cell with either solution using a HPLC pump flowing at 2 mL min^{-1}. This was to ensure that neither solution alone causes damage to the DPPC bilayer.

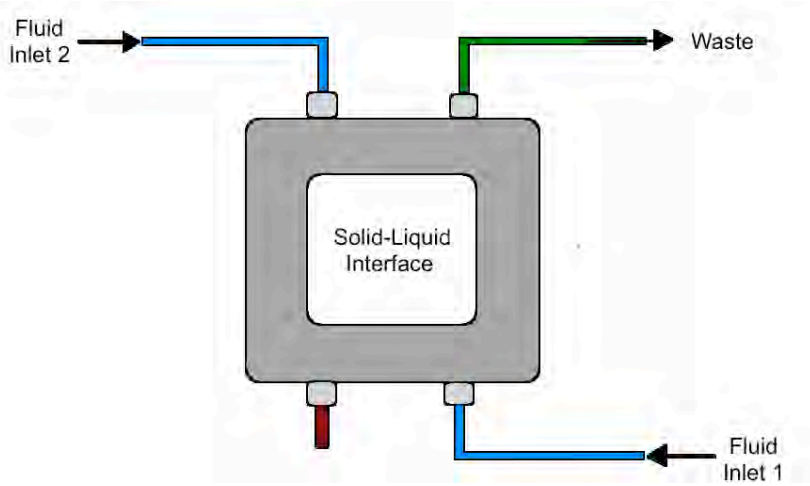

Figure 6.2. The set-up for exposure of reactive oxygen species to phospholipid bilayers on a quartz solid support.

The blue lines indicate the inlets for reacting solutions. The green line represents the waste outlet. Experiments performed on INTER and SURF used a horizontal set-up so the cell was lying flat. Experiments on OFFSPEC used a vertical set-up so that the cell was perpendicular to the horizontal.

For the reaction between DPPC bilayers and singlet oxygen, hydrogen peroxide and sodium hypochlorite solutions were simultaneously pumped through

the solid-liquid cell at a flow rate of 2 mL min^{-1}. Singlet oxygen was produced in the cell by the following reaction scheme:

$$NaOCl + H_2O_2 \rightarrow {}^1O_2 + H_2O + NaCl \quad (6i)$$

Bilayers of ^{1}H DOPC were reacted with hypochlorite ions by initially forming the bilayers in quartz contrast matched water and then flowing a solution of 100 mM sodium hypochlorite in quartz contrast matched water through the cell at a flow of 2 mL min^{-1}.

6.2.6 Fitting Neutron Reflectivity Data of Bilayers Reacting with ROS

The neutron reflectivity as a function of q was modelled, assuming a single bilayer between two semi-infinite media. The neutron reflectivity data was fitted using the fitting procedure *bike*.[21] This fitting program uses a least-squares fitting process to compare modelled reflectivity data as a function of q, calculated according to Abeles optical matrix method [238] with each experimental data set measured in a time sequence. The calculations incorporate a range of features involved in the bilayer. These are summarised in Table 6.1 and the structures of DPPC and DOPC, with the head and tail regions indicated, are shown in Figure 6.3.

The relative amount of material at the interface at each timepoint was calculated by the surface coverage at time = t divided by the surface coverage at time = *0*, where surface coverage is the thickness multiplied by 1/area per lipid. The thickness and area per lipid were obtained by fitting the reflectivity curves.

For DOPC bilayers, some fitting was performed using the simpler model in *drydoc*, as it was evident that a bilayer model was not suitable for modelling the DOPC layer after oxidation.[172] This model assumes a single layer between two semi-infinite media as previously described. This means that the thickness of the whole DOPC layer at the solid-liquid interface was fitted, as well as the scattering length density of the interface.

Bilayer feature	Values used in DPPC fitting	Values used in DOPC fitting
SLD Quartz / 10^{-6} Å^{-2}	4.18	4.18
Roughness at the solid-liquid interface	5	5
Thickness of Lipid Head / Å	Fitted	Fitted
Thickness of Tail Region / Å	Fitted	Fitted
b solvent / fm	13	13
V solvent / Å^3	30	30
b Head Group / fm	60	60
V Head Group / Å^3	325	325
b Tail Group / fm	-32	-21
V Tail Group / Å^3	819	975
Area per headgroup / Å^{-2}	Fitted	Fitted

Table 6.1. Values used for data fitting in neutron reflectivity of DPPC and DOPC bilayers.

SLD = scattering length density, roughness = an error function to describe the variation at the adjoining layers, Lipid head= charged group of DPPC or DOPC, Lipid tail = alkyl/acyl chains of DPPC or DOPC, b = sum of scattering lengths in the molecule (or part) of interest, V = volume of the molecule (or part) of interest.

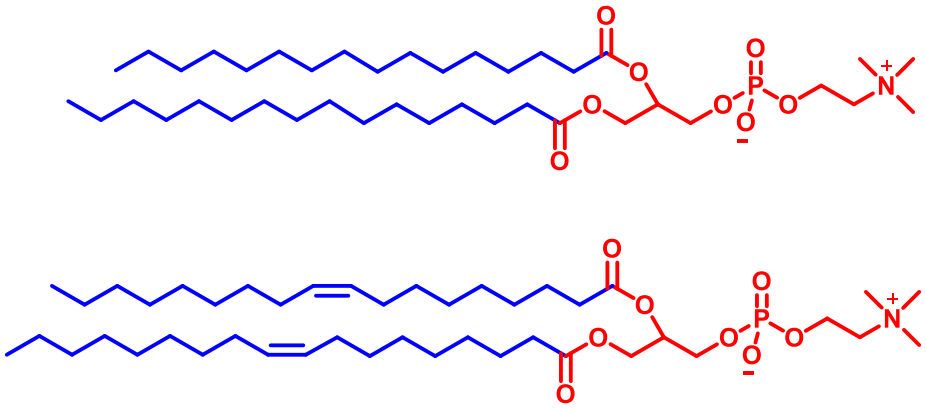

Figure 6.3. The chemical structures of DPPC and DOPC indicating the head and tail regions.

The atoms included in the head group are shown in red and those included in the tail group are shown in blue.

6.2.7 Preparation of Samples for SANS

For investigation of lipid rafts using SANS, various vesicle samples and contrasts were prepared as shown in Table 6.2. Some PAzPC micelles (Table 6.3) were also prepared in order to compare to vesicle samples as it has been shown previously that PAzPC can form micelles in aqueous media.

Solvent Matched Samples

Sample number	Vesicle components	Mol ratio of lipids	SLD of sample / 10^{-6} Å^{-2}	D_2O in solvent / %	SLD of solvent / 10^{-6} Å^{-2}
1	d_{62}DPPC/DOPC/Chol	40:40:20	2.51	44.4	2.51
2	d_{62}DPPC /DOPC/Chol	18:60:22	1.28	26.7	1.28
3	d_{62}DPPC /POPC/Chol	40:40:20	2.53	44.7	2.53
4	d_{62}DPPC /POPC/Chol	18:60:22	1.28	26.7	1.28
5	d_{62}DPPC /PAzPC/POPC/Chol	40:2:38:20	2.56	45.2	2.56
6	d_{62}DPPC /PAzPC/POPC/Chol	18:6:54:22	1.31	27.1	1.31
7	d_{62}DPPC /PAzPC/POPC/Chol	40:5:35:20	2.61	45.8	2.61
8	d_{62}DPPC /PAzPC/POPC/Chol	18:15:45:22	1.36	27.7	1.36
9	d_{62}DPPC /PAzPC/POPC/Chol	40:20:20:20	2.69	47.0	2.69
10	d_{62}DPPC /PAzPC/POPC/Chol	18:30:30:22	1.43	28.8	1.43
11	d_{62}DPPC /PAzPC/Chol	40:40:20	2.85	49.4	2.85
12	d_{62}DPPC /PAzPC/Chol	18:60:22	1.60	31.2	1.60

Sample number	Vesicle components	Mol ratio of lipids	SLD of sample / 10^{-6} Å^{-2}	D_2O in solvent / %	H_2O_2 in solvent / %	SLD of solvent / 10^{-6} Å^{-2}
1	d_{62}DPPC /DOPC/Chol	40:40:20	2.51	44.4	0.8	2.51

Off-contrast Samples

Sample number	Vesicle components	Mol ratio of lipids	SLD of sample / 10^{-6} Å^{-2}	D_2O in solvent / %	SLD of solvent / 10^{-6} Å^{-2}
1	d_{62}DPPC /DOPC/Chol	40:40:20	2.51	75	4.63
2	d_{62}DPPC /DOPC/Chol	18:60:22	1.28	75	4.63
3	d_{62}DPPC /POPC/Chol	40:40:20	2.53	75	4.63
4	d_{62}DPPC /POPC/Chol	18:60:22	1.28	75	4.63
5	d_{62}DPPC /PAzPC/POPC/Chol	40:2:38:20	2.56	75	4.63
6	d_{62}DPPC /PAzPC/POPC/Chol	18:6:54:22	1.31	75	4.63
7	d_{62}DPPC /PAzPC/POPC/Chol	40:5:35:20	2.61	75	4.63
8	d_{62}DPPC /PAzPC/POPC/Chol	18:15:45:22	1.36	75	4.63
9	d_{62}DPPC /PAzPC/POPC/Chol	40:20:20:20	2.69	75	4.63
10	d_{62}DPPC /PAzPC/POPC/Chol	18:30:30:22	1.43	75	4.63
11	d_{62}DPPC /PAzPC/Chol	40:40:20	2.85	75	4.63
12	d_{62}DPPC /PAzPC/Chol	18:60:22	1.60	75	4.63

Table 6.2. Vesicle samples prepared for SANS experiments.

The ftop table shows contrast matched samples, where the solvent (water) was contrast matched to the average SLD of the lipids. The bottom table shows off-contrast samples where the vesicles in table 1 were formed in 75% D_2O.

Sample	Concentration / mg mL^{-1}	D_2O in solvent / %	SLD of solvent / x 10^{-6} $Å^{-2}$
PAzPC	5	100	6.35
PAzPC	2.5	100	6.35
PAzPC	1.25	100	6.35
PAzPC	4	49.4	2.85
PAzPC	6	31.2	1.60

Table 6.3. Details of the PAzPC micelles formed for SANS experiments in this study.

Vesicles were formed using the film method by accurately weighing (using a 6 figure balance) the lipids to yield the ratios described above and drying overnight. The lipid films were then hydrated using the contrast matched solvents shown in table 6.2 and sonicated for 15 minutes. Following this, extrusion of the resultant vesicles through 100 and 50 nm polycarbonate filters, at 60°C under pressure was performed.

Off-contrast vesicles were formed by diluting the contrast-matched vesicles in the required mass of D_2O to form a concentration of 75% (v/v) D_2O.

PAzPC micelles were prepared by suspending PAzPC solid in the required volume of H_2O/D_2O and sonicating for 20 minutes using a probe-tip sonicator.

6.2.8 Small-Angle Neutron Scattering of Vesicle and Micelle Samples

SANS studies were performed on the SANS2D instrument at the ISIS neutron source (ISIS, Rutherford-Appleton Laboratory, Didcot, UK). SANS2D is a time-of-flight instrument, and a wavelength range of 1.75 to 12.5 Å was used, giving a scattering vector q range of 0.004 to 0.76 $Å^{-1}$. SANS2D has a position sensitive two-dimensional detector with ~5.1 mm pixel size. For this experiment, the sample to detector distance was set to 4 m. Comparisons with scattering from a partially deuterated polystyrene standard allowed absolute scattering cross sections to be determined, with an error of ~ ± 2 %.

Samples were placed into clean, disk-shaped fused silica cells of 1 mm path length. SANS measurements were performed at 5°C, 10°C, 25°C and 50°C using a 12 nm diameter neutron beam. Usually 10 μA corresponding to around 15 minutes in the beam were accumulated during a transmission measurement, while 40 μA or more, depending on the scattering intensity of the sample, were accumulated during the scattering measurement. The transmission and scattering runs of all of the solvents used, at each of the temperatures, were measured for the same length of time as the samples and were subtracted from all the corresponding sample runs in order to obtain the scattering from the lipid aggregates.

6.2.9 SANS Data Fitting

SANS data was analysed using solid-body models of the scattering species. This allows for the construction of many kinds of geometrical models (e.g. sphere, hollow shells, core-shell particles, ellipsoid and rod shape structures, etc.), while integrative least-squares fitting procedures enable refinement of the dimensions of the models to fit the data. The program FISH was used for this purpose .[239]

6.2.9.1 Vesicle Fitting

When modelling the off-contrast vesicles dispersed in 75% D_2O as (single) sheets, the fits to the SANS data were obtained by the least-squares refinement of three parameters, namely the bilayer thickness L, $R\sigma$, and the absolute scale factor, where $R\sigma$ is the Lorentz correction factor which provides information about the extent of rigidity/curvature of the lamellar sheets. The polydispersity on the bilayer thickness ($\sigma(L)/L$) was fixed.[24]

6.2.9.2 Micelle Fitting

The structures of the PAzPC micelles and some of the “vesicles” samples (containing large amounts of PAzPC) were analysed using a standard and well-

established model for the structure factor S(Q): the Hayter-Penfold (H-P) structure factor.[156] Each set of experimental data was treated individually with several models for the form factor, including sphere and ellipsoid, coupled with the H-P structure factor in order to obtain the best fit.

For the PAzPC micelles, initial analysis showed that the data fitted best to a prolate ellipsoid model. The scale factor and background were varied until there was an acceptable fit to the experimental data, and then the geometric parameters were varied until the best fit was achieved. The fit values for radii and lengths are considered to have an error of ± 1 due to the high *q* resolution on SANS2D.

6.2.10 Neutron Reflectivity of Lipid Raft Samples

To determine that evidence for raft formation could be detected by looking at the off-specular reflection from lipid monolayers at the air-water interface d_{62} DPPC/DOPC/Cholesterol (2:2:1 by mol), a sample known to form lipid rafts from SANS studies, was prepared to a concentration of 1 mg mL^{-1} in chloroform.

Surface pressure of the lipid raft sample monolayers was measured by forming monolayers on a Langmuir trough (Nima Technology) housed in an environmental chamber as previously described (Chapter 3 Section 3.3.2).

Before and after ozone experiments, an isotherm (plot of surface pressure *versus* trough area performed at constant temperature) of the monolayer was measured by decreasing the trough area until a surface pressure of 40 mN m^{-1} was achieved and then increasing the trough area to maximum area. This was repeated twice. Before experiment, the film was compressed to a surface pressure of 5 mN m^{-1} above the desired surface pressure and then re-expanded to the desired surface pressure. The surface pressure was monitored continuously *versus* time during the experiment, while the trough surface area and temperature were held constant during neutron runs. In between runs, the temperature and trough area (and therefore surface pressure) were controlled manually to achieve the desired values. The Langmuir trough was temperature controlled *via* an external water bath.

Ozonolysis experiments were performed by continuously flowing a dilute (2 ppm) mixture of ozone in oxygen into the Langmuir trough chamber at a constant

flow rate of 2 L min^{-1}. Ozone was generated by passing dry oxygen through a commercial ozone generator (UVP) containing a mercury Pen-Ray lamp, producing ozone through the photolysis of molecular oxygen at 185 nm.

Neutron reflection of monolayers of lipid raft samples was performed on the OFFSPEC reflectometer at ISIS, Rutherford Appleton Laboratory, Didcot, UK. In all experiments the neutrons entered and exited the environmental chamber *via* fused quartz windows. The incident beam contained neutrons with a range of wavelengths, from $1 \leq \lambda \leq 16$ Å. The neutron beam was collimated and inclined to fall at a grazing angle of incidence of 0.7 to the horizontal of the air-liquid interface depending on the instrument. The reflected neutrons were detected and processed to give neutron reflectivity data as a function of momentum transfer normal to the interface, q, as described in Chapter 2.

The reflectivity of the monolayer was acquired for 3 hours at 0.7^{o} to give reflectivity curves. The measured reflectivity of a sample of pure D_2O in the Langmuir trough was used to obtain a scale factor with which to normalise for the intensity spectrum of the incident beam.

The phospholipid neutron reflectivity data was fitted using the fitting procedure *drydoc,*[172] described in Chapter 3. In all cases, the data for the film was fitted by varying the scattering length density and monolayer thickness (*drydoc*) and manually adjusting the interfacial roughness to optimise the fit. The roughness was then held constant at 3 Å for each particular monolayer during an experiment, while thickness and scattering length density were allowed to vary. The relative amount of material at the interface at each timepoint was calculated using Equation 3.2 (Section 3.3.10).

6.3 Preliminary Results presenting the uses of Neutron Techniques for Investigating Oxidative Damage to Lipid Bilayers

Three primary techniques were tested for their use in monitoring oxidative damage to phospholipid membranes. The first is neutron reflectivity at the solid-liquid interface for investigation of ROS damage to lipid bilayers, the second is SANS for the changes in vesicle formation and lipid rafts in the presence of oxidised lipids, and the third is off-specular neutron reflectivity of lipid monolayers at the air-water interface for detection of lipid rafts before and after oxidation. Preliminary results for these techniques are presented in this section.

6.3.1 Production of Singlet Oxygen: Surface Pressure Measurements of DPPC Monolayers

In order to ascertain that singlet oxygen could be produced sufficiently in the reaction between NaOCl and H_2O_2, and that it could react with saturated phospholipids, a DPPC monolayer was formed on a subphase of aqueous hydrogen peroxide in a Langmuir trough. Sodium hypochlorite (4 wt.%) was injected into the subphase to produce the singlet oxygen. The surface pressure was measured using a Wilhelmy plate and balance and was monitored over the course of the reaction. This is presented in Figure 6.4.

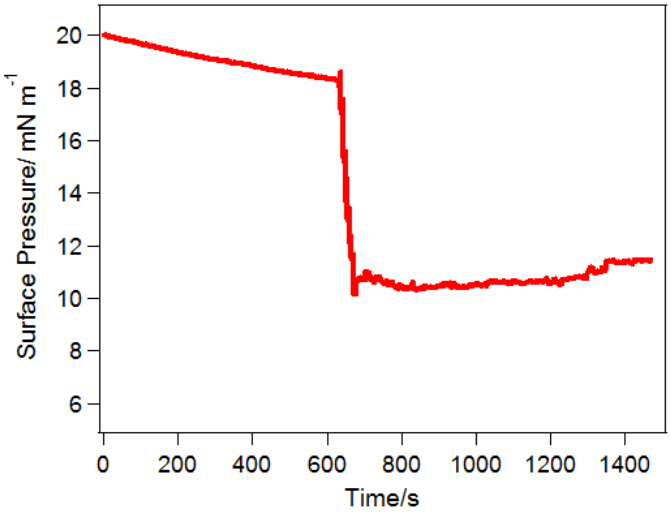

Figure 6.4. The surface pressure of a DPPC monolayer at the air-water interface during reaction with singlet oxygen.

Aqueous hydrogen peroxide was used as a subphase. Sodium hypochlorite was injected into the subphase at 650 s.

There is a large drop in surface pressure at the interface immediately after injection of the sodium hypochlorite. The decrease in surface pressure suggests the DPPC has become less hydrophobic upon production of singlet oxygen, or that the coverage of the monolayer has decreased after oxidation. This can be explained by oxidation of the monolayer, or possible loss of entire DPPC molecules at the interface after oxidation by solubilisation into the subphase.

Two control experiments were also performed. In the first, a DPPC monolayer was formed on a subphase of aqueous hydrogen peroxide, the resulting surface pressure was monitored for 10 minutes and then water was injected into the subphase. In the second experiment, a DPPC monolayer was formed on a subphase of aqueous sodium hypochlorite and the same volume of water was injected, monitoring surface pressure continually. In both cases, there was no change on surface pressure upon the injection of water.

6.3.2 Neutron Reflectivity Studies of DPPC Bilayers Reacting with Singlet Oxygen

A bilayer of DPPC was formed on a monocrystalline quartz slab, fitted into a

solid-liquid interface cell and the cell was filled with quartz contrast-matched water (69% D_2O, 31% H_2O). Neutron reflectivity was recorded at 3 angles and this data was fitted to give an experimental calculated value for the bilayer thickness as 9.5 (± 0.7) Å per head group and 34.9 (± 1.0) Å for both tail groups, and an area per lipid of 50 Å^2. The reported bilayer thickness, by Nagle *et al.*, is 9 Å per lipid head and 34 Å for the tails, giving total bilayer thickness of 52 Å with an area per lipid of 47 Å^2.[25] The calculated values agree within error to those reported.

To ensure that the DPPC bilayer could withstand the reactant H_2O_2 alone for significant lengths of time without reaction, the neutron reflectivity of the bilayer at the solid-liquid interface was monitored for 11 hours whilst flowing 100 mM H_2O_2 through the cell at 2.0 mL min^{-1} at 22^{o}C. The amount of material at the interface *versus* time is shown in Figure 6.5. There is no change over time, therefore the lipid does not react with H_2O_2 in these conditions.

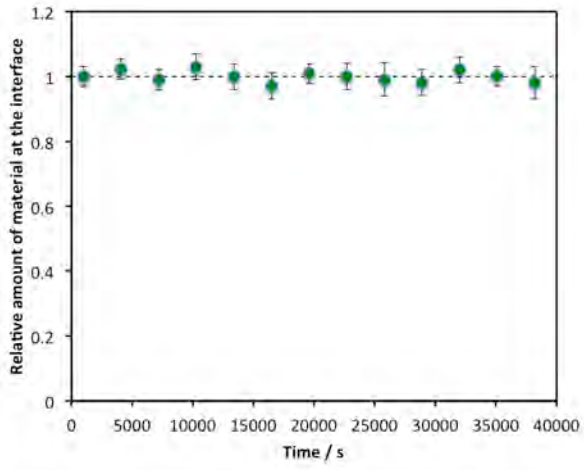

Figure 6.5. The amount of DPPC at the interface *versus* time for the exposure of a bilayer of DPPC to H_2O_2 only for 11 hours.

Green markers represent the relative amount of material, calculated from the surface coverage (1/area per lipid) at time t multiplied by the thickness (δ_t) of the monolayer at time t divided by the surface coverage (1/area per lipid) at time 0 multiplied by the thickness (δ_0) at time 0. These values were calculated by fitting the bilayer area per lipid and thickness to the neutron reflectivity curves at each timepoint, while background and surface roughness were held constant. There is no change in the relative amount, thickness or spread of the monolayer at the air-water interface over this time.

To ensure the bilayer did not react with ROS in the presence of sodium hypochlorite alone the neutron reflectivity of a DPPC bilayer was monitored for 9 hours whilst flowing hypochlorite solution (100 mM) through the cell at 2.0 mL min^{-1} at 22°C. The amount of material at the interface *versus* time is shown in Figure 6.6. There is no change over time, therefore the lipid does not react with hypochlorite in these conditions.

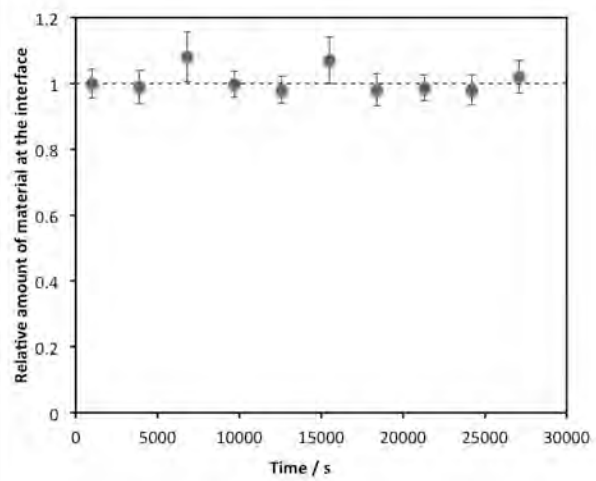

Figure 6.6. The amount of DPPC at the interface *versus* time for the exposure of a bilayer of DPPC to sodium hypochlorite only for 9 hours.

Purple markers represent the relative amount of material, calculated from the surface coverage (1/area per lipid) at time t multiplied by the thickness (δ_t) of the monolayer at time t divided by the surface coverage (1/area per lipid) at time 0 multiplied by the thickness (δ_0) at time 0. These values were calculated by fitting the bilayer area per lipid and thickness to the neutron reflectivity curves at each timepoint, while background and surface roughness were held constant. There is no change in the relative amount, thickness or spread of the monolayer at the air-water interface over this time.

In order to study the kinetics of the reaction between a DPPC bilayer and singlet oxygen, a bilayer of DPPC was formed on monocrystalline quartz in a solid-liquid interface cell. The cell was filled with quartz contrast-match water (69 vol% D_2O, 31 vol% H_2O). Hydrogen peroxide solution (100 mM) and sodium hypochlorite solution (100 mM) were pumped through the cell continuously at 2.0

mL min^{-1} for 12 hours. This was to continuously produce singlet oxygen in the cell at a constant rate. The neutron reflectivity was measured before the flow began, and at regular intervals during the reaction. The reflectivity profile of the bilayer changed as it reacted with singlet oxygen. This is shown in Figure 6.7.

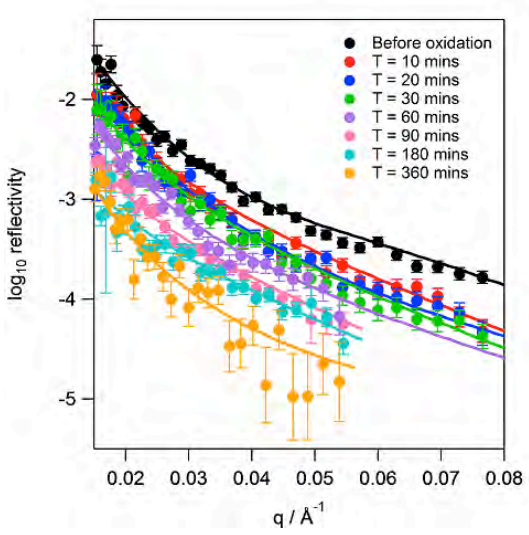

Figure 6.7. The neutron reflectivity profile at low *q* ranges of a bilayer of DPPC at regular time points during reaction with singlet oxygen.

The reflectivity decreases over time, suggesting loss of material from the interface. The markers show the measured neutron data and the lines show the fits to the data described in the text.

The area per molecule at the interface *versus* time was calculated, as well as the thickness of the bilayer, from the reflectivity curves. This is presented in Figure 6.8. The surface coverage decreases immediately upon mixing of hydrogen peroxide and sodium hypochlorite within the cell (hence upon production of singlet oxygen). The initial surface coverage of DPPC bilayer is 1.46 x 10^{18} molecules m^{-2}. This decreases from 100% to 60% within 10 minutes of the reaction, to 53% within 30 minutes, 12.3% within 145 minutes and 3.4% within 705 minutes.

The reaction is initially extremely rapid as the surface coverage decreases at a rate of 4% per minute. This rate decreases throughout the reaction, with an

average rate of surface coverage decrease of 0.3% per minute until no change was observed after 25000 seconds (417 minutes).

The loss of bilayer from the interface can be attributed to oxidation of the lipid, causing significant changes in the structure of the membrane. Some lipids may be lost to the bulk solvent during the reaction as the polarity of the molecules change, leading to a reduction of bilayer bound to the surface.

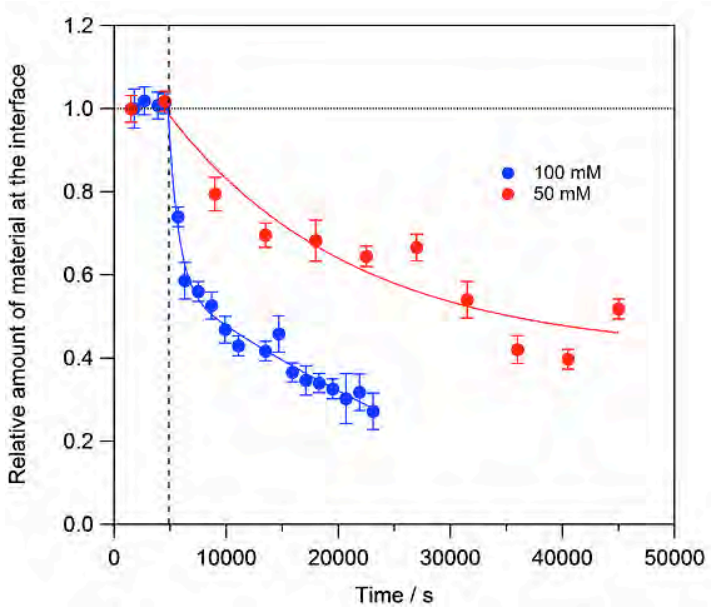

Figure 6.8. The amount of material of a DPPC bilayer at the solid-liquid interface during reaction with singlet oxygen.

The results shown are for the reaction at both 100 mM hydrogen peroxide (blue) and 50 mM hydrogen peroxide (red). The reaction began at 5000 seconds.

The kinetics reaction was also repeated at half the concentration of H_2O_2 (50 mM), whilst the concentration of sodium hypochlorite was kept at 100 mM, and the amount of material at the interface *versus* time is shown in Figure 6.8. It is evident that the rate of reaction increases with the concentration of hydrogen peroxide. Consequently, the rate increases with the increase in formation of singlet oxygen. The loss of material at the interface was fitted to a single exponential (as shown in Equation 3.3) and it was found that the lifetime of the reaction at 100 mM of H_2O_2 was 194 (± 8) minutes with a y-offset of 0.28 (± 0.05) (i.e. 28 % of the material would be left at the interface after reaction) whereas at 50 mM H_2O_2 the

lifetime was 392 (± 9) minutes with a y-offset of 0.34 (± 0.7). Calculating 1/lifetime to obtain the pseudo-first order rate constant gives a value of 5.15 x 10^{-3} min^{-1} for the reaction at 100 mM H_2O_2 and a value of 2.56 x 10^{-3} min^{-1} for the reaction at 50 mM H_2O_2. Therefore, the rate constant is approximately twice as large when the concentration of the reactants is doubled.

Interestingly, data fitting indicated that during the reaction the thickness does not change initially, and it only decreases towards the end of the reaction. This is presented in Figure 6.9 and it suggests that the reaction leads to a rearrangement of the lipid bilayer at the interface. This is examined in more detail in the discussion section.

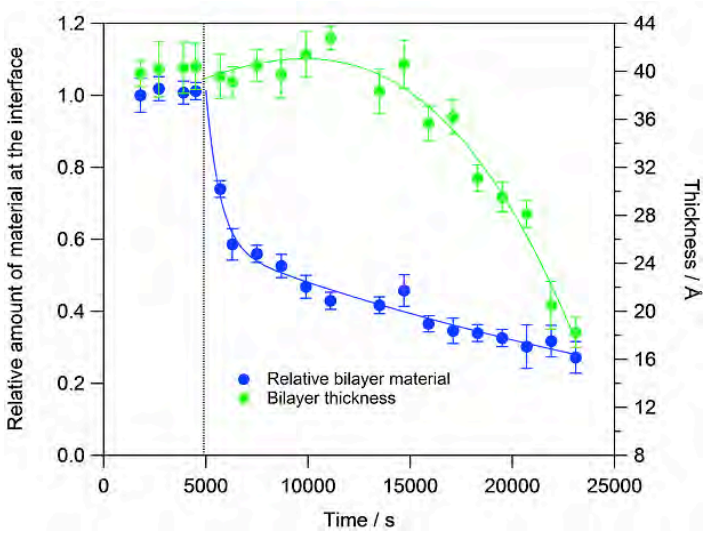

Figure 6.9. The thickness of the DPPC bilayer at the solid-liquid interface during reaction with singlet oxygen.

The results shown are for the reaction at 100 mM hydrogen peroxide (blue) and is presented along with the relative loss of material from the interface from Figure 6.8. The reaction began at 5000 seconds.

6.3.3 Reaction between DOPC Bilayers and Hypochlorite

A bilayer of unsaturated phospholipid DOPC was formed at the solid liquid interface and the cell was filled with quart contrast-matched water. Quartz contrast-matched sodium hypochlorite solution (100 mM) was then pumped

continuously through the cell and the neutron reflectivity at the solid-liquid interface was measured before and during reaction between the bilayer and the hypochlorite. The neutron reflectivity curves of the bilayer before and during the reaction are shown in Figure 6.10, along with the fits to the curves.

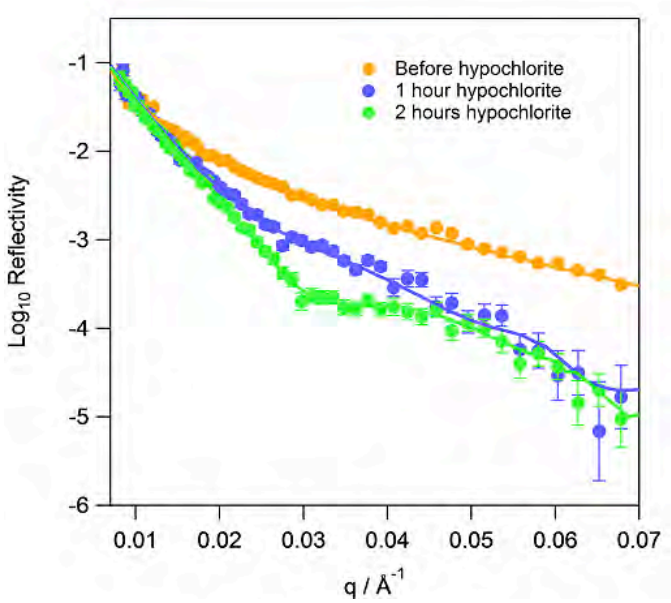

Figure 6.10. Neutron reflectivity curves of supported DOPC bilayers at the solid-liquid interface before exposure to hypochlorite (orange), after 1 hour of reaction with hypochlorite (blue) and after 2 hours reaction (green).

The measured data is represented by the round markers and the best fit of the curves is shown by the solid lines. The fits were calculated by varying the thickness and area per lipid at each timepoint, whilst keeping surface roughness and background constant.

Fitting the data gave values of thickness of lipid heads and tails and area per lipid for the bilayers at each timepoint. Prior to reaction, the thickness of the bilayer was calculated to be 47.9 Å and area per lipid was calculated to be 58.9 Å^2. Following reaction with hypochlorite the reflectivity profile of the bilayer in Figure 6.10 is very different to the reflectivity of the bilayer before reaction. Firstly, the fact that the reflectivity of the bilayer is lower at higher q means that the difference in scattering length density between the bilayer and the quartz has decreased. Secondly, with increasing time the fringe spacing becomes narrower and more pronounced, implying an increase in bilayer thickness.

The bilayer thickness after oxidation was initially estimated using the analysis program *bike* that assumes a single bilayer, which is clearly not the case here. Therefore, in order to fit the scattering length density at the interface and the thickness of the layer, a simpler model (*drydoc*) was used to examine the data, which assumed one layer instead of a head-tails-head model. Fitting to this model showed that the thickness of the DOPC associated with the solid interface doubles to 85.5 (± 2.0) Å after one hour of reaction with HOCl and doubles again after another hour to 192.2 (± 3.7) Å. Additionally, the scattering length density at the interface increased significantly after exposure, from 0.6 to 3.5 x 10^{-6} $Å^{-2}$, therefore much more solvent was incorporated into the thicker layer.

This evidence suggests that as the DOPC lipids are oxidised by hypochlorite, the change in the chemical properties of the molecules leads to a change in the arrangement of the lipids as they are forming higher order structures, such as multilayers. This is a contrast to the reaction between DPPC bilayers and singlet oxygen, where the DPPC bilayer remains as a single layer and whole molecules appear to be lost from the interface to the solvent.

6.3.4 Investigation of the Effects of Oxidation on the Formation of Lipid Rafts

Oxidation of phospholipids in membranes could lead to significant changes in the structure and arrangement of cell membranes, including the formation and viability of lipid rafts or the loss of oxidised lipids to the surrounding aqueous media. In order to determine how oxidation, and the presence of oxidised phospholipids, changes the existence of these lipid rafts, phospholipid vesicles were formed with increasing levels of the oxidised lipid PAzPC (Table 6.2) and the SANS of these samples was measured at various temperatures.

6.3.4.1 Determination of Size and Vesicle Properties of Lipid Raft Samples using SANS

SANS of the mixed phospholipid vesicles, in water containing 75% D_2O, was measured at two temperatures (10 and 25^{o}C) in order to determine the thickness

of the vesicle bilayer, and if the bilayer thickness changed with increasing amounts of oxidised phospholipid and with temperature. The SANS data was initially fitted using a single-layer sheet model. Overlaying the data indicated that for all samples, the SANS was the same at both temperatures. Therefore, the vesicle bilayer did not change with temperature. However, it was observed that the samples containing the oxidised phospholipid PAzPC did not fit well to this model, and it appeared that micelles could also be present in the samples. This possibly suggested that some PAzPC molecules did not form part of the vesicle bilayers and instead formed micelles. Fits of samples 1-4 (containing no PAzPC) using this model are shown in Figure 6.11 and the fitted parameters are presented in Table 6.4.

Sample number	Bilayer Thickness (L) / Å	Vesicle Rσ	Vesicle σ(L)/L	SWSE
1	50.2	251	0.05	543
2	52.2	238	0.05	672
3	52.3	340	0.05	411
4	49.9	351	0.05	403

Table 6.4. The parameters used to fit samples 1-4 in 75% D_2O to a single-sheet bilayer model.

Samples 1 and 2 are formed of DPPC/DOPC/Chol at 2:2:1 and 18:60:22 respectively. Sample 3 and 4 are DPPC/POPC/Chol at 2:2:1 and 18:60:22 respectively. The data shown is for the samples run at 10 ^{o}C. Rσ is the Lorentz factor that describes the flatness of the bilayer sheet and σ(L)/L is the polydispersity of the vesicles. Fitting was performed by a standard iterative least squares method, involving computation of first derivatives of each calculated data point with respect to each parameter in the model, to determine the best structural parameters and also to give a measure of the residuals (sum of weighted squared errors, SWSE) of the fit. The bilayer thickness and Lorentz factors were fitted whilst polydispersity was held constant at a low value.

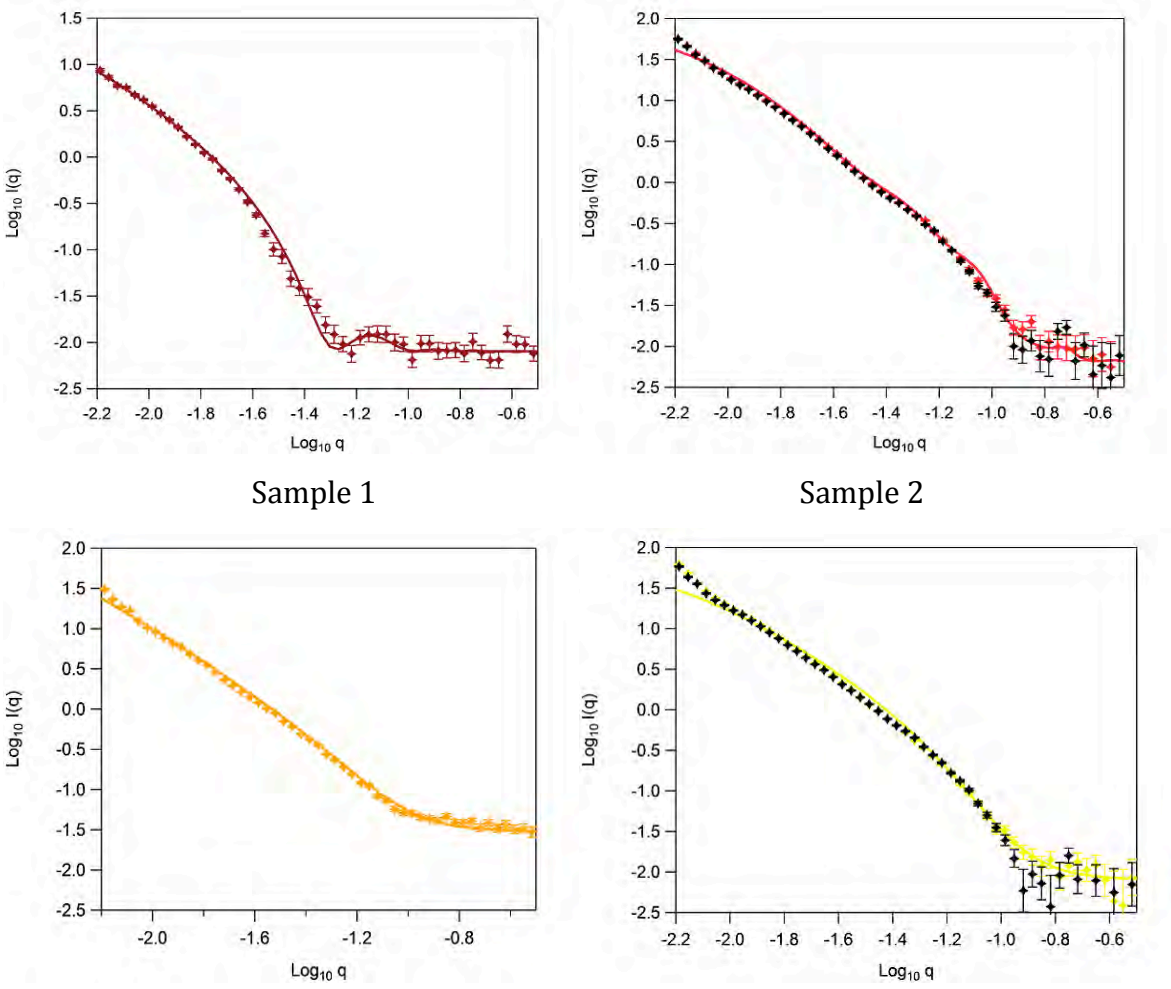

Figure 6.11. SANS data of samples 1-4 in 75% D_2O and fits using a single layer sheet model.

Samples 1 and 2 are formed of DPPC/DOPC/Chol at 2:2:1 and 18:60:22 (by mol) respectively. Sample 3 and 4 are DPPC/POPC/Chol at 2:2:1 and 18:60:22 (by mol) respectively. The data shown is for the samples run at 10 ^{o}C.

In order to fit the vesicle samples containing PAzPC, some knowledge of the PAzPC micelles size and shape was required. Therefore, the SANS of PAzPC micelles was performed and the results are presented below.

6.3.4.2 SANS of PAzPC Micelles

PAzPC micelles were formed in D_2O at 3 different concentrations and the SANS was measured. The scattering profiles of the micelles are presented in Figure 6.12. Initially attempts were made to fit the data to a core-shell model using hard-sphere structure factors, however it was found that a charge on the micelles was required and therefore Hayter-Penfold charge parameters were applied. The parameters for the fits are shown in Table 6.5. With the exception of the scale factor, which is dependent upon concentration, the same parameters were found to fit well to the micelles at each concentration, suggesting therefore that the micelle structure, size and shape did not vary with concentration, over the concentration range tested. When the SANS profile of PAzPC at each concentration were normalised using the scale factor, the curves overlaid each other well.

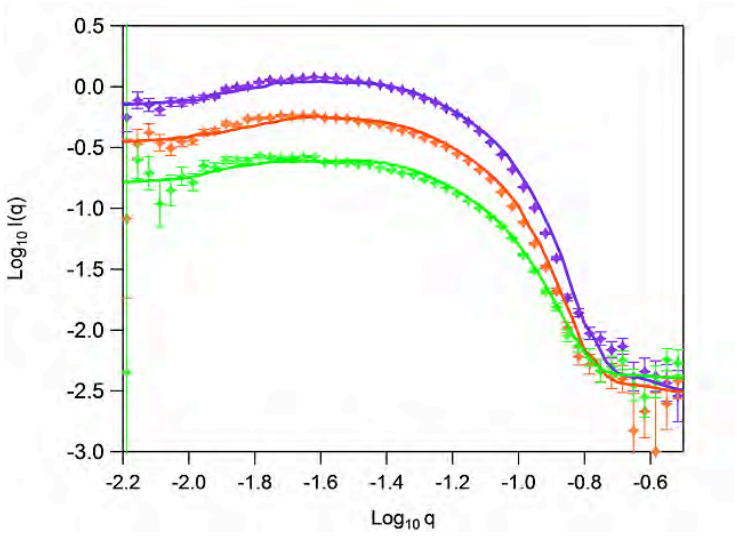

Figure 6.12. The SANS curves of PAzPC micelles at 5 mg mL^{-1}, 2.5 mg mL^{-1} and 1.25 mg mL^{-1}.

The fitted curves to a core-shell model with a hard sphere structure factor are also shown. Purple = 5 mg mL^{-1}, red = 2.5 mg mL^{-1} and green = 1.25 mg mL^{-1}.

Concentration of PAzPC / mg mL^{-1}	Scale	Core Radius / Å	Core axial ratio, x	Core volume / Å^3	Shell thickness / Å	H-P S(Q) radius / Å	Charge / Z	Inv debye / k	SWSE
5.00	0.362	18.8	1.8	50099	9.9	61.9	6.6	0.018	413
2.50	0.178	18.8	1.8	50099	9.9	61.9	6.6	0.018	210
1.25	0.079	18.8	1.8	50099	9.9	61.9	6.6	0.018	114

Table 6.5. The fitting parameters used to fit the SANS of 3 different concentrations of PAzPC micelles in D_2O using a core-shell ellipsoid model and a hard-sphere structure factor with 60 % of solvent in shell.

Core axial ratio shows that the ellipsoid is prolate shaped. For the sample at 5 mg mL^{-1}, all parameters were fitted except for the core volume, which was calculated from the fitted values. For the lower concentration samples, the same parameters were used at 5 mg mL^{-1} and the scale only was fitted. The SWSE is the sum of weighted squared errors of the fit.

6.3.4.3 Fitting SANS Data using a Mixed Bilayer and Micelle Model to Determine Size and Vesicle Properties of Lipid Raft Samples

Following determination of the properties of PAzPC micelles, the samples in 75% D_2O were fitted using a mixed model, which included parameters for both vesicles and micelles. The results from the curve fittings are shown in Figure 6.13 and the data in Table 6.6. The samples contain DPPC/PAzPC/POPC/Chol at molecular ratios of: 40:2:38:20 (sample 5), 18:6:54:22 (sample 6), 40:5:35:20 (sample 7), 18:15:45:22 (sample 8), 40:20:20:20 (sample 9), 18:30:30:22 (sample 10), 40:40:0:20 (sample 11), 18:60:0:22 (sample 12); therefore POPC is being replaced from samples 3 and 4 with 10, 25, 50 and 100 % PAzPC.

It is evident that increasing levels of PAzPC in the sample increases the contribution of the micelles to the SANS profile. In each graph, the data for the SANS performed at both 10^{o}C and 25^{o}C is presented. The curves at each temperature are the same within error, showing that there is no change in the vesicle or micelle structures in the sample with temperature over this range.

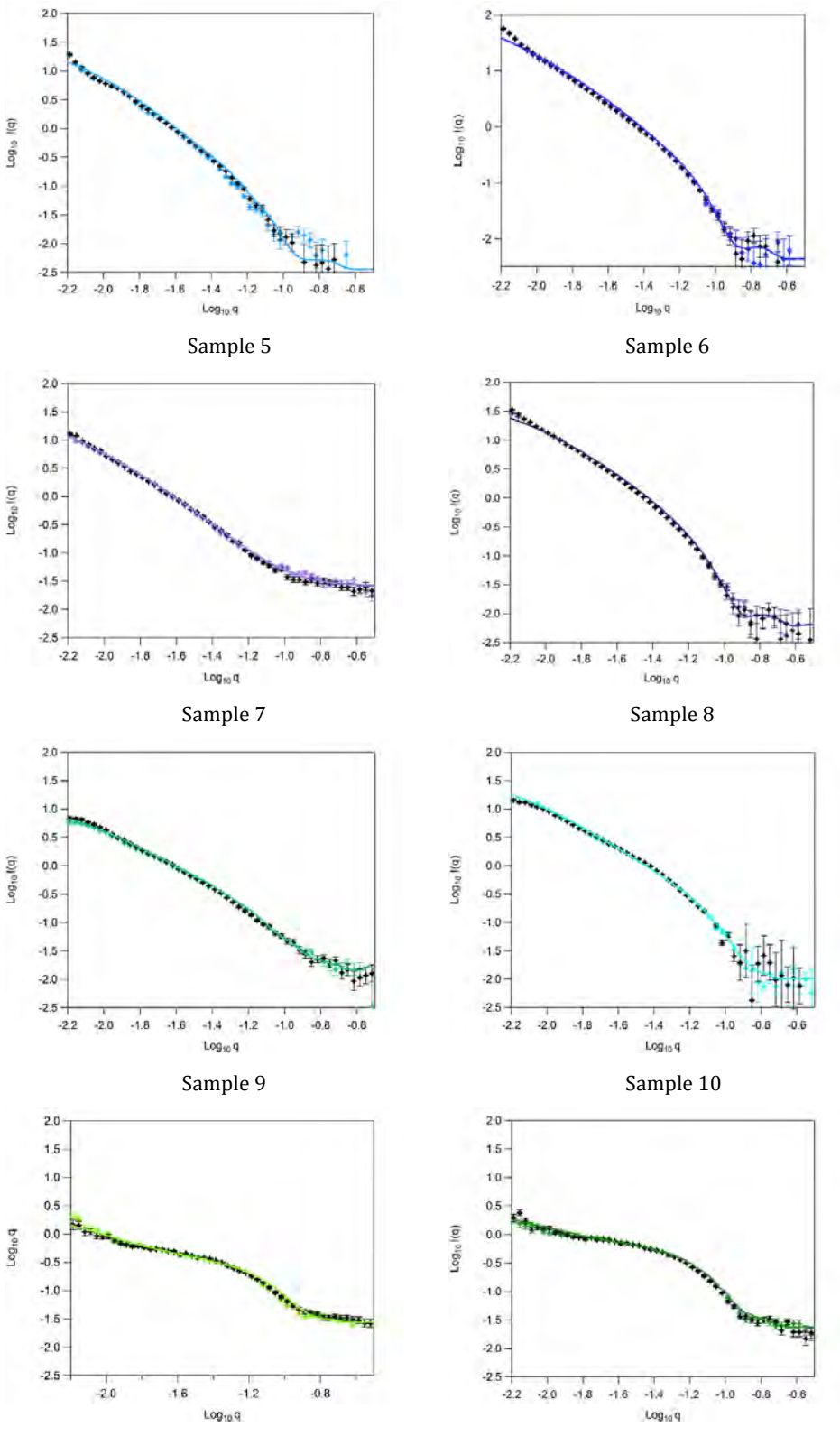

Figure 6.13. SANS data of samples 5-12 in 75% D_2O and fits using a single layer sheet model combined with a micelle model.

Markers represent the experimental data and the solid line shows the fitted curve. Samples 5-12 contain increasing PAzPC levels. See text for sample details.

Sample number	% PAzPC in sample	Bilayer Thickness (L) / Å	Vesicle Rσ	Micelle minimum radius / Å	Micelle maximum radius / Å	Micelle shell radius / Å	Vesicle: micelle scale ratio	SSE
5	2	48.2	274	28.7	43.7	9.9	34.4	231
6	6	48.9	350	28.7	43.7	9.9	26.6	310
7	5	50.6	347	28.7	43.7	9.9	22.6	423
8	15	49.2	236	28.7	43.7	9.9	21.4	348
9	20	50.5	211	28.7	43.7	9.9	2.7	214
10	30	50.9	255	28.7	43.7	9.9	1.6	532
11	40	49.8	250	28.7	43.7	9.9	0.2	135
12	60	50.1	251	28.7	43.7	9.9	0.2	89

Table 6.6. Summary of the individual fitting parameters obtained for samples 5-12 in 75% D_2O fitted by a mixed core-shell ellipsoid model and a hard sphere structure factor for micelles and single-layer sheet model for vesicles.

The samples contain DPPC/PAzPC/POPC/Chol at molar ratios of: 40:2:38:20 (sample 5), 18:6:54:22 (sample 6), 40:5:35:20 (sample 7), 18:15:45:22 (sample 8), 40:20:20:20 (sample 9), 18:30:30:22 (sample 10), 40:40:0:20 (sample 11), 18:60:0:22 (sample 12). The bilayer thickness, Lorentz factor and vesicle/micelle scales were fitted while the polydispersity and micelle parameters were held constant. The micelle radii were calculated from the SANS results in section 6.3.4.2.

6.3.4.4. Contrast-Matched Vesicle and Vesicle/Micelle Samples: Investigation of Lipid Raft Formation

The vesicle samples were formed in H_2O/D_2O solvents that contrast-matched the average scattering length density of the lipids in the samples. If the samples were uniform, e.g. all material in homogeneous vesicles, this would mean that no SANS from the sample would be observed once the solvent was subtracted. However, if lipid raft domains or other structures were present in the sample, which would cause the lipids to be segregated, there would be significant neutron scattering detected. Also, if some lipids did not reside in the vesicles but instead in micelles there would be a scattering length mismatch between the

particles and solvent and neutron scattering would be detected. Samples 1 and 2 contain d_{62}DPPC, cholesterol and DOPC, a mixture that has been shown to readily form domains upon temperature decrease using BAM. The SANS of these samples was measured at temperatures ranging from 5 to 50°C and the resulting curves are presented in Figure 6.14.

It is clear that as the temperature decreases from 50 °C to 5 °C, the intensity of scattering increases significantly in both samples. Since there is no change in overall composition of the samples as the temperature changes, and the off-contrast (75 % D_2O) experiments showed no change in the macro-structure of the vesicles, this shows there is a change in the micro-structure of the vesicles. Therefore, a change in the organisation of the lipids in the bilayer is occurring as the temperature decreases, i.e. domains are forming. As the temperature decreases, the deuterated DPPC and cholesterol could form a liquid ordered (L_o) bilayer raft in a "sea" of liquid-disordered (L_d) lipids enriched in hydrogenated DOPC. This will mean that the scattering length density of the lipids in the L_o phase would no longer equal the scattering length density of the solvent, nor would the scattering length density of the lipids in the L_d.

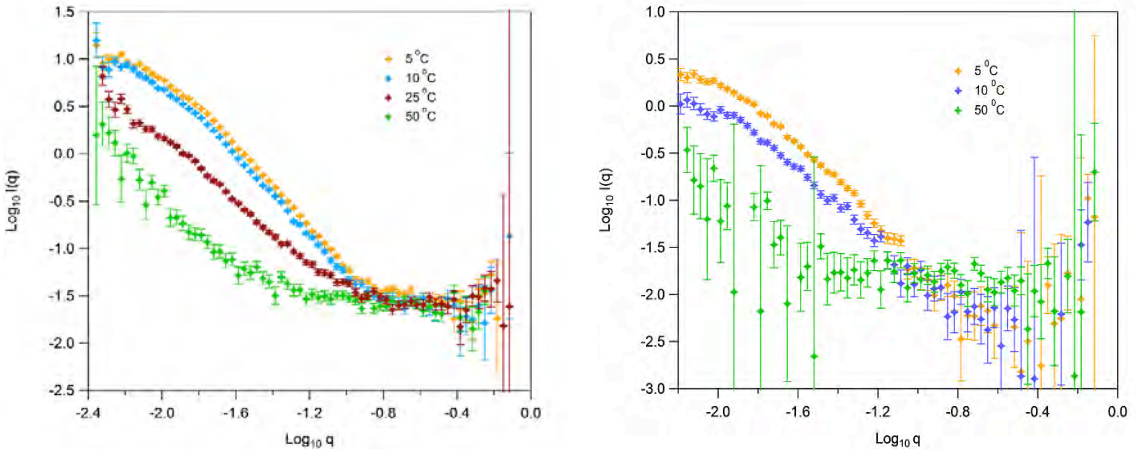

Sample 1 Sample 2

Figure 6.14. The SANS data of i) d_{62}DPPC/DOPC/cholesterol (40:40:20 by mol) at 5, 10, 25 and 50°C and ii) d_{62}DPPC/DOPC/cholesterol (18:60:22 by mol) at 5, 10 and 50°C.

The observed neutron scattering increases dramatically for both samples as the temperature is reduced.

Samples 3 and 4 contain mixtures of d_{62} DPPC, POPC and cholesterol, therefore are the same as samples 1 and 2 except that the unsaturated lipid that could form the L_d region has only one unsaturated tail rather than two. The SANS of these samples was measured at 5 and 25 ^oC and the resulting curves are presented in Figure 6.15. Sample 3 has a clear change in neutron scattering as the temperature decreases, although this increase in scattering is much less than for sample 1. The SANS of sample 4 is the same (within error) at both temperatures. The formation of lipid rafts is much more prominent in the SANS results when DOPC is present rather than POPC. This is probably because POPC has a more extended, ordered conformation than DOPC so there is less of a mismatch between the order and thickness of the L_o and L_d regions compared to when DOPC is present. The DOPC samples would therefore produce bigger lipid rafts to reduce the area at the boundary of the lipid rafts to reduce the line tension. Additionally, it appears that the lipid raft formation is more noticeable when the ratio of d_{62}DPPC to unsaturated lipid is higher. Sample 4 has a much higher ratio of unsaturated lipid to saturated lipids than sample 3, this must mean that the lipid rafts, if any, are too small to detect using SANS at this ratio.

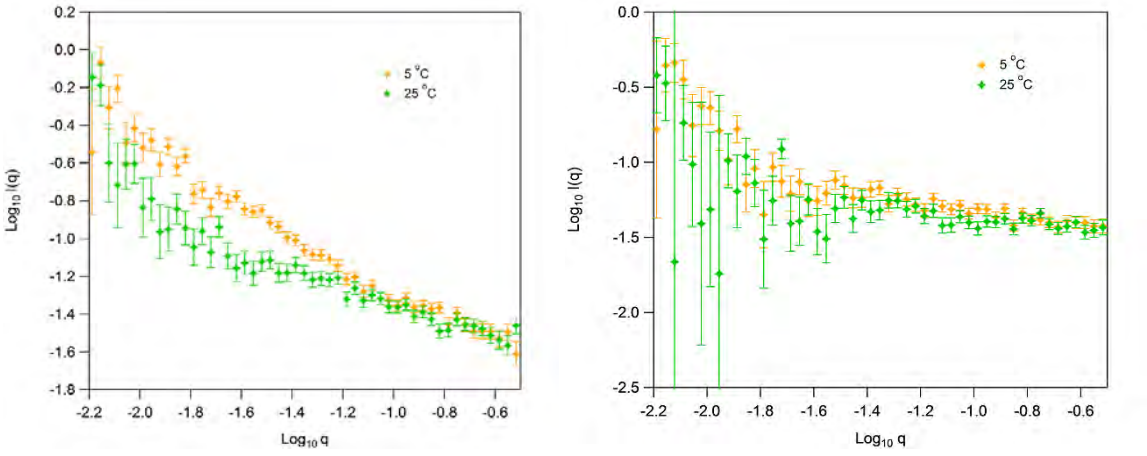

Figure 6.15. The SANS data of i) d_{62}DPPC/POPC/cholesterol (40:40:20 by mol) at 5 and 25 ^oC and ii) d_{62}DPPC/POPC/cholesterol (18:60:22 by mol) at 5 and 25 ^oC.

The results from the "off-contrast" samples revealed that replacing various amounts of POPC with PAzPC changes the macrostructure of the samples as some of the PAzPC tends to form micelles rather than be incorporated into the vesicles, therefore changing the ratio of lipids that would be associated with either the L_o or L_d phase. Samples 5 and 6 are the same as samples 3 and 4 respectively, but have 10 % of the POPC molecules replaced with PAzPC. SANS results of samples 5 and 6 at different temperatures are shown in Figure 6.16. The results are similar to those of samples 3 and 4 as in increase in SANS intensity was observed between 25 to 5 °C for sample 5 and no change was seen for sample 6. This shows that oxidation of 10 % of POPC molecules in sample 3 to PAzPC leads to some micelle formation as PAzPC leaves the vesicles (as shown in Table 6.6), but the lipids remaining in the vesicles still can form lipid rafts upon a decrease in temperature. Oxidation of 10 % of POPC molecules in sample 4 also leads to micelle formation, therefore the ratio of lipids in L_o phase to those in L_d would decrease. However, Figure 6.16 shows that this ratio still is not low enough to detect lipid rafts upon cooling.

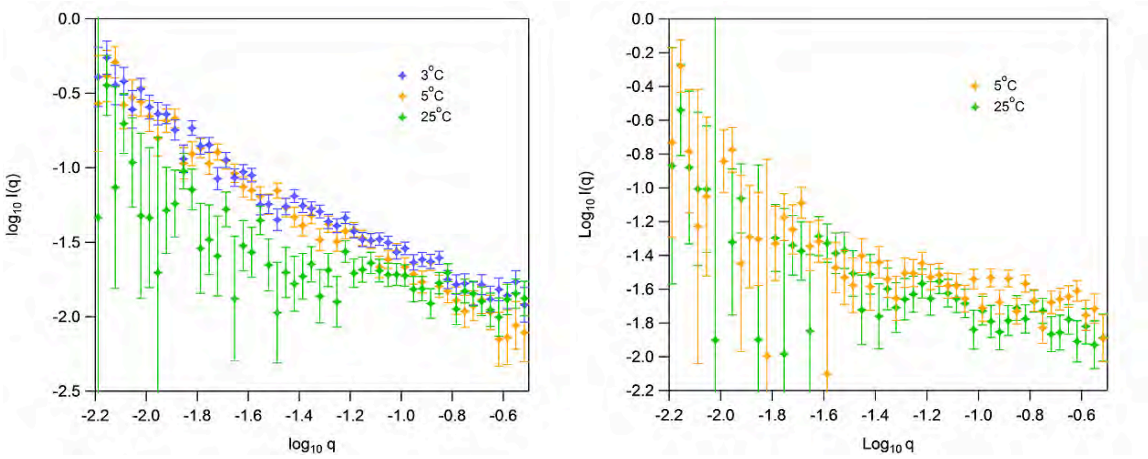

Sample 5 Sample 6

Figure 6.16. The SANS data of i) sample 5: d_{62}DPPC/PAzPC/POPC/cholesterol (40:4:36:20 by mol) at 3, 5 and 25 °C and ii) sample 6: d_{62}DPPC/PAzPC/POPC/cholesterol (18:6:54:22 by mol) at 5 and 25 °C.

The results for samples 7-12, where 25-100% of POPC molecules are replaced with PAzPC, are quite different. If some of the PAzPC forms micelles instead of being in the vesicles, the scattering length density of the vesicles would be higher than the solvent due to the higher ratio of deuterated DPPC whereas the scattering length density of the micelles would be lower than that of the solvent. This means that even at higher temperatures the lipid structures will not be contrast-matched by the samples, therefore it will be more difficult to detect the presence of lipid rafts as temperature is decreased.

Samples 7 and 8 are the same as samples 3 and 4 respectively except that 25 % of the POPC molecules are replaced with the oxidised lipid PAzPC. The SANS results for sample 7 in Figure 6.17 reveal that replacement of 25% of the POPC with PAzPC in sample 3 prevents the formation of detectable lipid rafts as the curves at 5 and 25 ^{o}C. In sample 3 the ratio of DPPC to POPC is 1:1 whereas in sample 7 the ratio is 1:0.75.

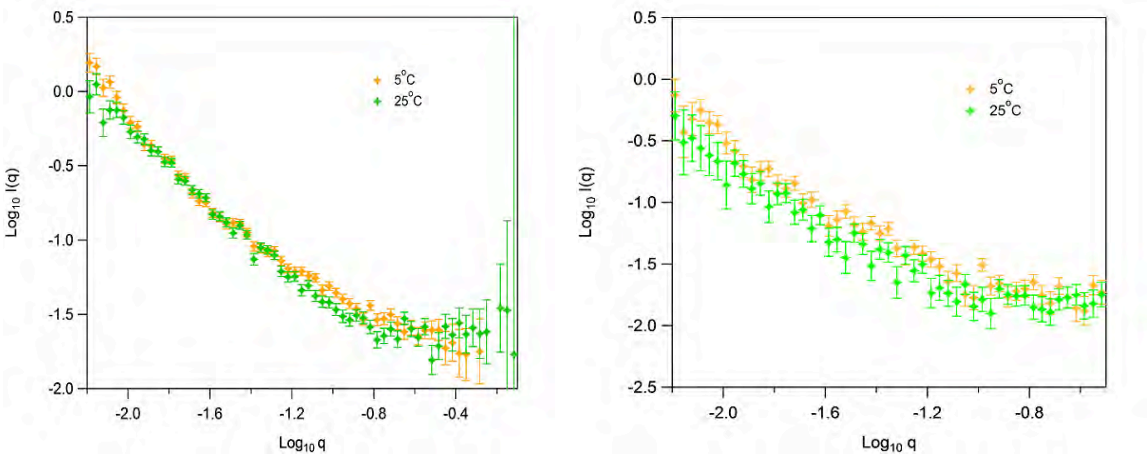

Sample 7 Sample 8

Figure 6.17. The SANS data of i) sample 7; d_{62}DPPC/PAzPC/POPC/cholesterol (40:10:30:20 by mol) at 5 and 25 ^{o}C and ii) sample 8; d_{62}DPPC/PAzPC/POPC/cholesterol (18:15:45:22 by mol) at 5 and 25 ^{o}C.

Samples 9 and 10 are the same as samples 3 and 4 respectively, except that 50 % of the POPC molecules are replaced with PAzPC. The SANS results of these samples is shown in Figure 6.18. Interestingly, in both cases the neutron scattering

of both samples increases as the temperature decreases. This could suggest the formation of rafts due to a larger difference in scattering length densities of the L_o and L_d phases, but could be a result of exchange of lipids between micelles and vesicles, for example if more PAzPC is present in the DPPC/POPC/cholesterol vesicle at 25 °C compared to 5°C it would have a lower scattering length density. However, since there was no detectable change in the ratio of micelles to vesicles at each temperature (Table 6.6), this second scenario is less likely.

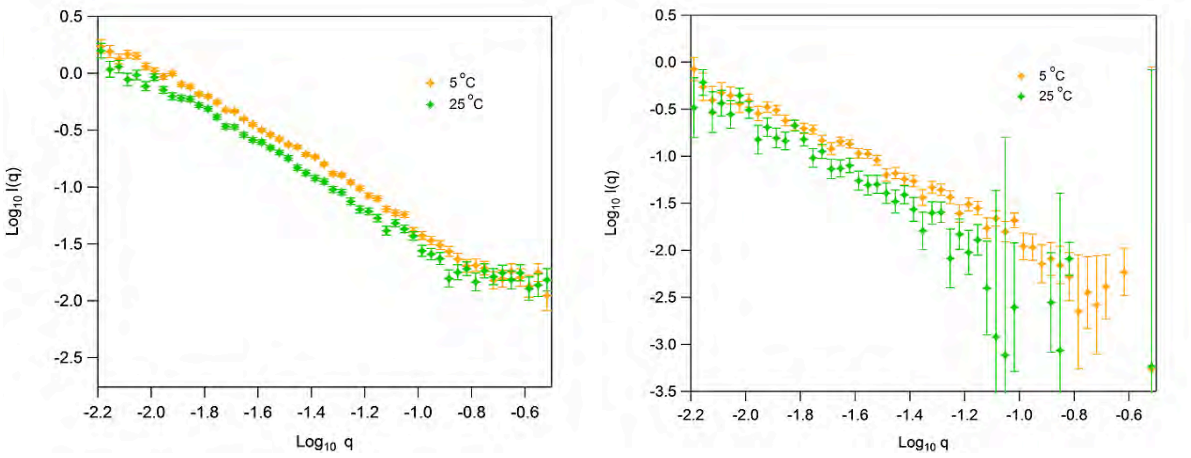

Sample 9 Sample 10

Figure 6.18. The SANS data of i) sample 9; d_{62}DPPC/PAzPC/POPC/cholesterol (40:20:20:20 by mol) at 5 and 25 °C and ii) sample 10; d_{62}DPPC/PAzPC/POPC/cholesterol (18:30:30:22 by mol) at 5 and 25 °C.

In samples 11 and 12, 100 % of the POPC in samples 3 and 4 is replaced with PAzPC. The SANS of these samples at 5 and 25 °C is presented in Figure 6.19 Again, there is an increase in scattering as the temperature decreases. Also shown in Figure 6.19 is the SANS curves of PAzPC micelles alone at the concentration they would be present in samples 11 and 12 and in the same solvent as the vesicle samples. The PAzPC only micelle curve overlays well to the "micelle feature" of the SANS curve of sample 11, however the PAzPC only micelle curve corresponding to the levels in sample 12 is very low as the scattering length density of PAzPC is very similar to that of the solvent, which explains why the SANS of sample 12 does not have a prominent micelle feature like sample 11.

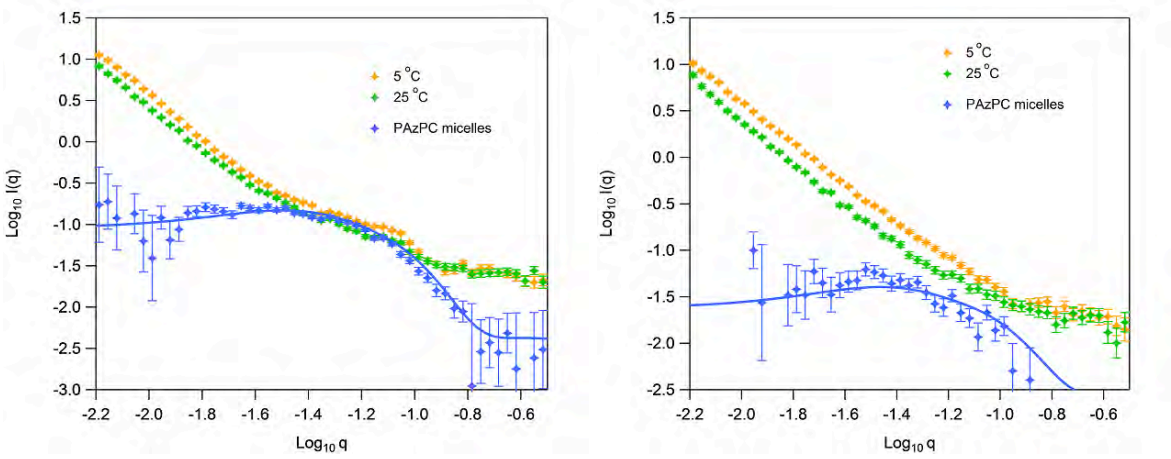

Figure 6.19. The SANS data of i) sample 11; d_{62}DPPC/PAzPC/cholesterol (40:40:20 by mol) at 5 and 25 °C and ii) sample 12; d_{62}DPPC/PAzPC/cholesterol (18:60:22 by mol) at 5 and 25 °C.

Also shown in blue is the SANS of PAzPC micelles at the same concentration as the maximum concentration of the PAzPC in samples 11 and 12.

As shown above, when POPC is replaced with PAzPC prior to formation of vesicles, some PAzPC preferentially forms micelles rather than a vesicle with the other phospholipids and cholesterol. To examine whether the phospholipids remain in vesicles when oxidation occurs *in situ*, sample 1 was formed in dilute H_2O_2 contrast-matched to sample 1 (containing 0.8 % H_2O_2, SLD 2.51). The vesicles were then exposed to UV light (254 nm) for 1 hour to induce oxidation by ·OH. The SANS of the sample measured before and after oxidation is presented in Figure 6.20 at different temperatures. Before oxidation there is a clear increase in SANS I(q) as temperature decreases from 25 to 5°C and the curve shape is typical to that of pure vesicles seen in Figure 6.14. The fit lines shown are using a single sheet model as described in Section 6.2.3, although this cannot be used to accurately describe lipid rafts as it assumes a uniform SLD throughout the vesicles. After oxidation the curves at both 5 and 25°C are very different to before oxidation. Firstly, the difference in intensity between the high and low temperatures is much smaller than prior to oxidation. Secondly the shape of the curve is very different as the I(q)

initially falls much more rapidly with *q* at low *q* and it has a "micelle-like" (smaller particle) feature at mid-*q*. The fit shown uses a mixed vesicle and micelle model, indicating the presence of a smaller particle, which could have formed from oxidation of DOPC if it leaves the vesicles.

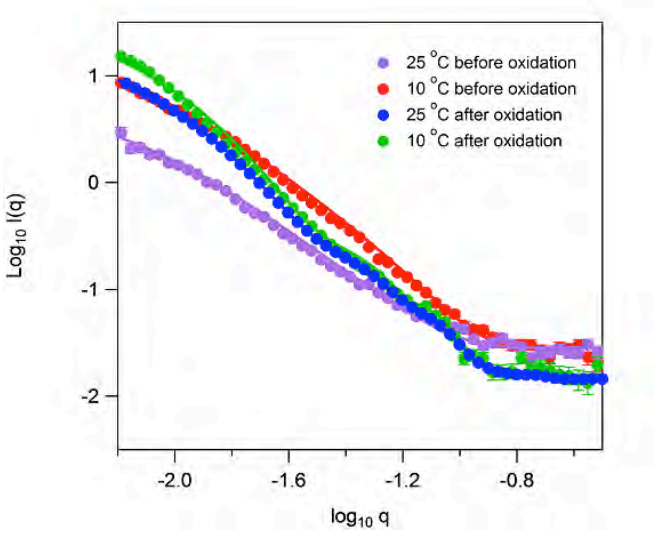

Figure 6.20. The SANS data of sample 1 in H_2O_2 contrast matched solution at 25 °C (dark red) and 5°C (dark blue), as well as the SANS of sample 1 in H_2O_2 after oxidation from exposure to UV for 1 hour at 25 °C (pink) and 5 °C (light blue).

The markers show the experimental data and solid lines show the fits.

6.3.5 Off-Specular Neutron Reflectivity Studies of the Effect of Oxidation on Lipid Raft Formation

SANS results showed that lipid rafts clearly form in sample 1 (d_{62}DPPC/DOPC/cholesterol, 2:2:1 by mol) as the temperature of the vesicles is decreased. The raft formation of these samples was also investigated using off-specular neutron reflectivity at the air-water interface.

A monolayer of sample 1 was formed at the air-NRW interface and compressed to a surface pressure of 30 mN m^{-1}. The neutron reflectivity of the monolayer was measured at various temperatures, whilst holding the barrier positions constant. Since the d_{62} DPPC has the largest scattering length density, this would dominate the neutron reflectivity. The reflectivity curves of sample 1 at 30

and 5 °C are shown in Figure 6.21. There is an apparent increase in reflectivity as the temperature drops from 30 to 5 °C, but since the trough area is constant this cannot be due to a change in the amount of material at the interface. Fitting the curves gave values of a monolayer thickness of 21.0 (± 0.2) Å, scattering length density of 2.10 (± 0.04) x 10^{-6} Å^{-2} and roughness of 3 Å at 30 °C and a monolayer thickness of 22.47 (± 0.7) Å , scattering length density of 2.08 (± 0.07) x 10^{-6} Å^{-2} and roughness of 1 Å at 5 °C. Therefore this increase in reflectivity can be attributed to an increase in the roughness of the monolayer as the temperature increased. More significantly, off-specular neutron reflectivity was measured at 5 °C but not at 30 °C. This is evident in Figure 6.22, which shows all of the neutrons detected during these neutron reflectivity experiments, i.e. both specular and off-specular reflected neutrons. In these graphs the biggest peak represents the specular reflected neutrons and the signal increases from ~70-150 due to the presence of beam-blockers outside of this region. Off-specular reflectivity is detected as an asymmetry in the signal either side of the specular peak, a feature that is evident for the sample at 5°C but not at 30°C. This suggests that lipid rafts are forming at 5 °C as there is an uneven surface due to a height mismatch of the L_o and L_d domains, leading to this off-specular neutron reflectivity.

The monolayer of sample 1 was then exposed to ozone for 1 hour in order to oxidise unsaturated lipids, as previously described in Chapter 4. The neutron reflectivity was then measured at 5 and 30 °C, and is also shown in Figure 6.21. After oxidation the thickness of the monolayer was smaller: 17.1 (± 0.9) Å at 30 °C and 16.4 (± 1.2) Å at 5 °C . This is because the unsaturated DOPC lipid tails would be lost from the interface after ozonolysis, therefore the average thickness would be less. Also, scattering length density increases to 2.43 (± 0.4) x 10^{-6} Å^{-2} at 30 °C and 2.52 (± 0.2) x 10^{-6} Å^{-2} at 5 °C because hydrogenated DOPC material is lost from the interface. The roughness is the same at both temperatures at 3 Å, which explains why the reflectivity no longer changes as temperature is decreased. Following ozonolysis of the samples, no off-specular neutron reflectivity was detected at 30 °C, similarly to before oxidation, and far less off-specular neutron reflectivity was detected at 5 °C compared to before oxidation. This is shown in Figure 6.22 where the off-specular feature after ozone at 5°C is no longer present. This could mean that smaller, or no domains were formed after oxidation of the

lipids as the surface has a more random distribution of lipids (rather than an ordered one) so no off-specular reflectivity would be detected from rafts.

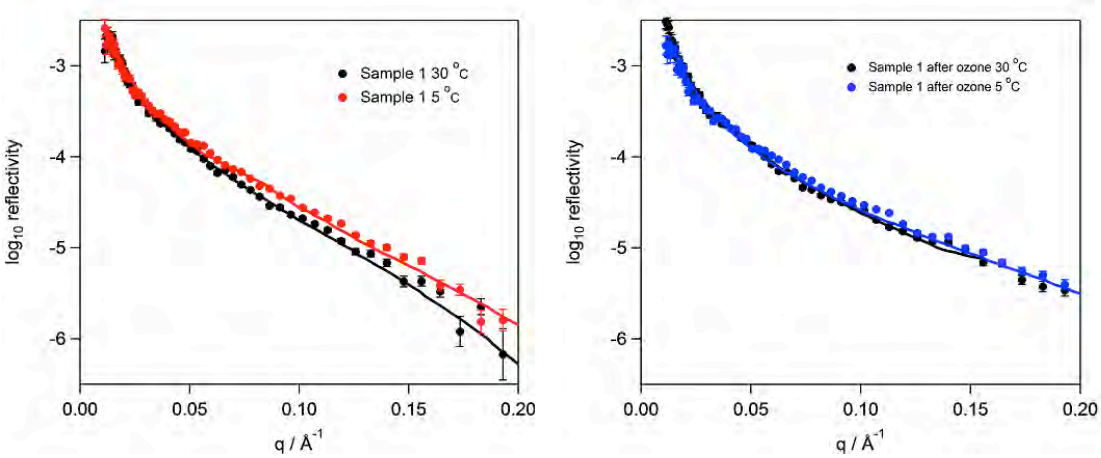

Figure 6.21. The neutron reflectivity curves of a monolayer of d_{62} DPPC / DOPC/ cholesterol (2:2:1 by mol) at the air-NRW interface before (left) and after (right) ozone exposure.

Left panel: The red curve is the reflectivity at 30 °C and the black curve is the reflectivity at 5 °C. The markers show the measured neutron data and the solid lines represent the fits.

Right panel: The blue curve is the reflectivity at 30 °C after ozone and the black curve is the reflectivity at 5 °C after ozone. The markers show the measured neutron data and the solid lines represent the fits.

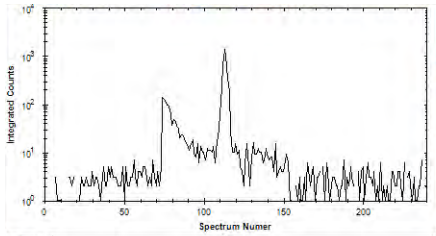

Before ozone 30 °C

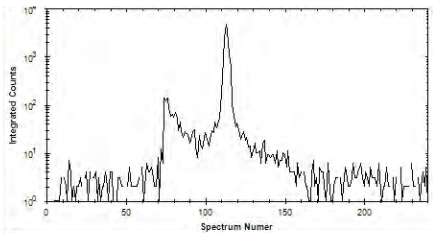

After ozone 30 °C

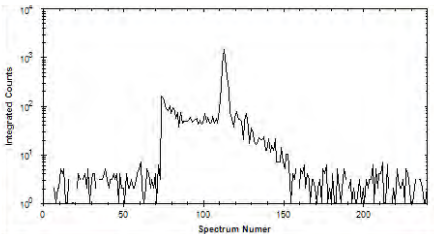

Before ozone 5 °C

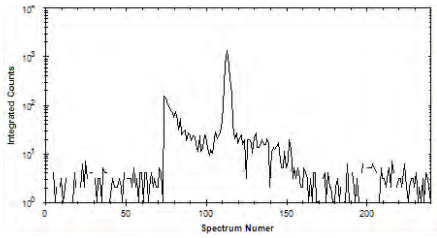

After ozone 5 °C

Figure 6.22. Graphs showing the detection of off-specular neutron reflectivity of a monolayer of d_{62} DPPC/ DOPC/ cholesterol (2:2:1 by mol) at the air-NRW interface.

6.4 Discussion

The damage caused to solid-supported bilayers of the saturated phospholipid DPPC by the ROS singlet oxygen was investigated using neutron reflectivity at the solid-liquid interface. The singlet oxygen was formed using a chemical method in the reaction between aqueous hydrogen peroxide and sodium hypochlorite. Hydrogen peroxide and hypochlorite are known ROS themselves, so prior to reaction with singlet oxygen DPPC bilayers were exposed to each of the reactants alone. By monitoring the thickness and spread of the DPPC bilayer using neutron reflectivity at the solid-liquid interface, it was shown that the bilayer does not react with each individual reactant, as there was no change in the bilayer structure after several hours of exposure.

When a DPPC bilayer was exposed to both reactants at a concentration of 100 mM, producing singlet oxygen, a rapid reaction was observed as the neutron reflectivity of the bilayer decreased significantly during exposure. Fitting the neutron reflectivity curves showed that there was a fast loss of material from the interface, and this loss could be fitted to a single exponential function to give a lifetime of lipids at the interface of 178 minutes. When a DPPC bilayer was exposed to the reactants at the lower concentration of 50 mM, the rate of loss of material was slower. The loss of material from the interface could again be fitted to a single exponential function to give a lifetime of lipids at the interface of 392 minutes. This suggests that the loss of material from the interface is dependent on the concentration of singlet oxygen, therefore the loss of material is a result of the direct reaction between DPPC and singlet oxygen rather than a chain reaction that is initiated by the singlet oxygen reaction.

Interestingly, the thickness of the bilayer does not change initially in the reaction as determined by fitting the thickness. It was proposed by Smith *et al.* that DPPC bilayers would form pores in the membrane during reaction with ROS so that the remaining DPPC would remain in a bilayer configuration. This could explain why no change in the bilayer thickness was observed until a loss of approximately 50 % of the material from the interface. It could suggest that the singlet oxygen is attacking the lipid heads rather than the tails since the bilayer

thickness is not getting shorter and whole molecules are lost from the interface. It has been shown that singlet oxygen can react with nitrogen and phosphorus groups in several studies, such as ATP, butylamine and ammonia,[242] so reactions could be occurring at these positions in the head groups. This is shown in Figure 6.23.

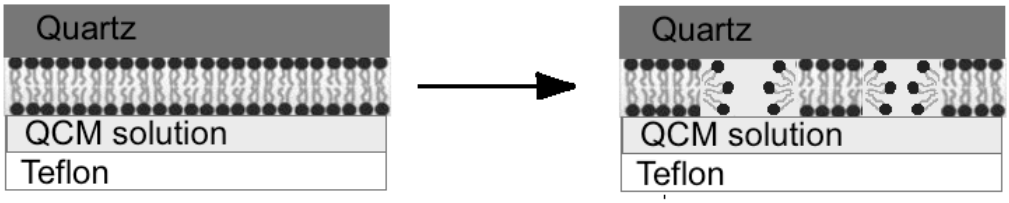

Figure 6.23. A schematic representation of the proposed loss of DPPC bilayer material at the solid-liquid interface during reaction with singlet oxygen.

The exposure of supported DOPC bilayers to the ROS hypochlorite was also investigated using neutron reflectivity at the solid-liquid interface. Measurements of the bilayer in quartz contrast-matched water only showed that it forms a thinner bilayer than DPPC, which would be expected as the DOPC tails contain alkene groups causing "kinks" in the chain that would lead to more disorder in the tail region. This also explains why the bilayer has a greater area per lipid.

Reaction between DOPC bilayers and hypochlorite leads to a change in the neutron reflectivity of the solid liquid interface indicating a rearrangement of the lipids at the surface. Fitting the curves showed that the scattering length density of the bilayer-quartz interface increased during the reaction, suggesting an increase in the contribution of the solvent to the reflectivity at the surface as the scattering length density was becoming closer to that of quartz. Fitting also showed an increase in bilayer thickness upon exposure to hypochlorite. After one hour the thickness had doubled and after a second hour it had doubled again. This increase in thickness can be seen in the reflectivity curves, as the fringes become more pronounced and narrower after reaction, signifying a thicker layer. This suggested that the lipids were not leaving the surface but remaining associated with the

lipids remaining on the quartz surface, possibly forming some sort of multilamellar structure *via* an unknown mechanism.

Therefore, it has been shown that neutron reflectivity at the solid-liquid interface is a useful tool for investigating oxidative damage to supported phospholipid bilayers by reactive oxygen species such as singlet oxygen and hypochlorite. The ability to monitor the reaction *in situ* allows the calculation of reaction kinetics and any changes in the structure, e.g. thickness and spread, of the bilayer at the interface.

It has been proposed that oxidation of unsaturated phospholipids in cell membranes can lead to enlarged lipid rafts. In order to investigate this in lipid bilayers, SANS of vesicles containing various levels of the oxidised phospholipid PAzPC was performed.

SANS of vesicles containing d_{62} DPPC, DOPC and cholesterol (samples 1 and 2) in solvent contrast-matched with the scattering length density of the lipids revealed that very few neutrons were scattering at 50 ^{o}C whereas scattering was much higher when the temperature was decreased to 5 ^{o}C. This indicates the formation of lipid rafts as there are regions of high scattering length density in the L_o regions due to a high concentration of deuterated DPPC and regions of low scattering length density in the L_d regions due to a high concentration of hydrogenated phospholipids. These rafts form as a result of the lipid tails becoming more ordered at the temperature decreases, meaning larger rafts form to reduce the line tension between longer saturated lipids in L_o lipid rafts and unsaturated lipids in L_d regions.

This phenomenon was also observed in sample 3, consisting of d_{62}DPPC, POPC and cholesterol at a molar ratio of 2:2:1 but not in sample 4 at a molar ratio of 18:60:22. The difference in SANS at the different temperatures was also much smaller for sample 3 than sample 1. As discussed above, this can be explained because the height mismatch of DPPC to POPC is much smaller than for DPPC to DOPC since POPC is composed of one saturated and one unsaturated tail whereas DOPC has 2 unsaturated tails. The DOPC samples would therefore produce bigger lipid rafts to reduce the area at the boundary of the lipid rafts to reduce the line tension. Sample 4 has a much higher ratio of unsaturated lipid to saturated lipids than sample 3, this must mean that the lipid rafts, if any, are too small to detect

using SANS at this ratio. Therefore, the experiments do show that SANS can be used to reveal raft formation in mixtures of DPPC:DOPC:Chol and potentially DPPC:POPC:Chol.

SANS of samples 1-4 (d_{62}DPPC/DOPC/Chol at molar ratios of 2:2:1 and 18:60:22 and d_{62}DPPC/POPC/Chol at molar ratios of 2:2:1 and 18:60:22 respectively) in 75 % D_2O was used to determine the bilayer thickness at different temperatures. A single-layer sheet model was used to model the vesicles. The thickness of the bilayers was calculated at approximately 50 Å, which is typical of a bilayer containing DPPC. The SANS curves at high and low temperature overlay with each other and fitted to the same parameters, therefore there was no change in the bilayer thickness with temperature. This confirms that the change in SANS of contrast-matched samples with temperature must be a consequence of the formation of lipid rafts rather than a change in the whole structure of the vesicles.

To investigate formation of lipid rafts after oxidation of bilayers, vesicles were prepared with POPC replaced with the oxidised phospholipid PAzPC. When the SANS of these samples in 75 % D_2O was performed it was immediately evident that smaller structures such as micelles were present in the sample. So in order to determine this, SANS of PAzPC micelles in D_2O was measured at three different concentrations of lipid. Fitting this data indicated that they formed charged particles of a core volume of 50099 $Å^3$. Taking a tail molecular volume of 432.5 $Å^3$ this gives 116 PAzPC molecules per micelle particle, assuming that the oxidised tail forms part of the shell. Calculating the surface area of the core gives 6937 $Å^2$, i.e. an area per lipid of 59 $Å^2$ in the core. This is therefore a good model for representing the micelles. Additionally, from the volume, the surface area of the shell was calculated to be 16165 $Å^2$ giving an area per molecule at the outer edge of the shell (head groups) of 139 $Å^2$, which would be expected considering the heads are large. Wang *et al.* quoted a particle size of 7.7 (± 0.9) nm, determined using dynamic light scattering,[243] which corresponds well to the dimensions determined by SANS, which would give an ellipsoid of 5.7 (smallest diameter) to 10.2 (largest diameter) nm.

Using a mixed model of single sheets for vesicles and the micelle parameters determined above for fitting the SANS data of samples 5-12 containing PAzPC, the size and shape of vesicles and ratio of scales for vesicle/micelle could

be determined. The data fitted well using this model and the ratio of the scales for the vesicle component to the micelle components of the curves decreased with increasing levels of PAzPC in the sample. In samples 11 and 12, where all of the POPC molecules in samples 3 and 4 had been replaced with PAzPC, the scale for micelles was higher than vesicles, demonstrating that the number of micelles was higher than the number of vesicles in the sample. The critical micelle concentration of PAzPC has been reported to be approximately 20 μM, [244,245] which is much lower than the maximum concentration of PAzPC in all samples (>0.8 mM in all samples), therefore it is not unexpected that the lipid would form micelles after leaving the vesicles. This could suggest that oxidation of POPC to PAzPC in real membranes *in vivo* could lead to loss of the lipid from the bilayer, forming micellar structures in surrounding aqueous media.

The off-contrast SANS did confirm that when PAzPC was present in the sample prior to vesicle formation, some molecules did not form vesicles with the DPPC and cholesterol but became micelles. However, this did make it difficult to measure the change in raft formation with the presence of PAzPC. This meant that the vesicles would not be contrast-matched with the solvent at high temperatures as there would by high scattering length density vesicles and low scattering length density micelles present as separate entities.

Lipid raft formation could be seen in the contrast-matched sample 5, where 10% of the POPC in sample 3 is replaced with PAzPC (DPPC/PAzPC/POPC/Chol, 40:4:39:20 by mol). An increase in I(q) was measured as the temperature decreased from 25 to 5 ^{o}C, similarly to that observed for sample 3. Therefore, even though some PAzPC appeared to have formed micelles, the ratio of lipids in L_d and L_o was sufficient to form detectable rafts as temperature was decreased.

No raft formation was observed in these conditions using SANS for samples 6-8. For samples 9-12, which contained 20-60 % PAzPC (by mol), an increase in I(q) was observed in all cases as temperature was decreased. This could be a result of domains forming due to a larger difference in scattering length densities of the L_o and L_d phases, but could be a result of exchange of lipids between micelles and vesicles, for example if more PAzPC is present in the DPPC/POPC/cholesterol vesicle at 25 ^{o}C compared to 5 ^{o}C it would have a lower scattering length density.

However, since there was no detectable change in the ratio of micelles to vesicles at each temperature (Table 6.6), this second scenario is less likely.

To see if oxidation of lipids in sample 1 *in situ* could affect lipid rafts, exposure of sample 1 in H_2O_2 solution to UV, producing ·OH, led to changes in SANS. A change in the shape of the curve after oxidation indicated that smaller particles such as micelles may be present in the sample. This is possible, as oxidation of DOPC would form a more hydrophilic molecule than PAzPC, so it is likely that it would want to leave the lipid bilayer. Again, this makes it difficult to determine the formation of rafts after oxidation.

Therefore, the results have demonstrated that SANS is a powerful tool for studying the formation of lipid rafts in vesicles upon sample cooling. Furthermore, it can be used to determine how a bilayer is affected by oxidation of lipids by ROS, for example whether oxidised lipids remain in the bilayer, and also whether the lipid raft formation is changed. However, the change in scattering length density of the vesicle as the composition changes upon oxidation significantly complicates the data analysis.

The use of off-specular neutron reflectivity was explored for the detection of lipid raft formation in lipid monolayers at the air-water interface. The specular neutron reflectivity curves of a monolayer of sample 1 (d_{62} DPPC/DOPC/Chol at 2:2:1 by mol) showed a decrease in roughness of the monolayer as the temperature decreased from 30 to 5 ^{o}C. This could be because the lipids become more ordered as the temperature decreases (e.g. if segregation into L_o and L_d phases occurs), therefore the overall roughness of the surface would be less. Off-specular reflectivity was also observed at 5 ^{o}C but not at 30 ^{o}C, which could indicate the formation of lipid rafts as temperature decreases. Off-specular neutron reflectivity has not previously been reported from phospholipid monolayers, so this is a new technique of being able to investigate the formation of lipid rafts.

This monolayer of sample 1 was then oxidised for 1 hour by ozone at 2 ppm. As shown in Chapter 4, this would lead to loss of unsaturated lipid tails (the oleoyl strands of DOPC) from the interface, and cholesterol molecules would be oxidised, altering their positions at the interface. Following oxidation, far less off-specular neutron reflectivity was detected from the monolayer when the

temperature was decreased to 5 ^{o}C as was detected before oxidation. This suggests that ozonolysis of the lipids within the monolayer prevents formation of the lipid rafts. Previously it had been shown that the presence of PAzPC in lipid monolayers leads to formation of larger lipid rafts, and this was not observed here using ozone as an oxidant reacting with this monolayer. This could be because both of the lipid tails on the DOPC in sample 1 would react with ozone and the molecule would be significantly more hydrophilic so could solubilise into the aqueous subphase, meaning the ratio of lipids in the L_d to L_o phases is no longer great enough to detect noticeable rafts using this method. Furthermore, the presence of oxidised cholesterol after ozonolysis could change the ordering of the DPPC molecules within the L_o phase, preventing the segregation of the phases. It would be interesting to observe the off-specular neutron reflectivity of samples 3-12 at the air-water interface at different temperatures. These samples contain varying amounts of PAzPC in a DPPC/POPC/cholesterol lipid mixture, therefore it would be a useful way to see if the presence of PAzPC affects the size of the domains at low temperature by comparing to the results for sample 3.

Off-specular neutron reflectivity is a relatively new technique to apply to lipid surfaces, as it is mainly used to explore magnetic rough surfaces; therefore these preliminary results have demonstrated its potential uses to examine changes in lipid raft formation upon oxidation by reactive oxygen species. Further research could lead to the quantification of raft sizes and how this changes with oxidation. These results could then have potential to be applied to other areas of biological research, such as the structure and positioning of proteins associated with lipid rafts.

6.5 Conclusion

Several reactions between phospholipid bilayers and ROS, and the outcomes of these reactions, have been investigated using neutron scattering and reflectivity techniques. It was shown that neutron reflectivity at the solid-liquid interface is useful for examining the structure of supported phospholipid bilayers. The damage caused to these bilayers by reactive oxygen species can also be determined in terms of the kinetics of the loss of the material from the interface as well as the structure of the material that remains. It was also determined that small-angle neutron scattering experiments can be used to investigate the formation of lipid rafts in vesicles of saturated phospholipids, unsaturated phospholipids and cholesterol. The changes in lipid raft formation upon oxidation of phospholipids could also be examined, although the analysis of the changes is complicated by the change in scattering length density of the vesicles due to micelle formation by some of the oxidised lipids. Furthermore, initial experiments have revealed that off-specular neutron reflectivity at the air-water interface can be used to detect the formation of lipid rafts in monolayers of saturated phospholipids, unsaturated phospholipids and cholesterol, and how the formation of rafts changes after oxidation. However, long acquisition times are required to obtain good data and methods for analysis of the data are not yet well developed.

It has therefore been shown that neutron reflectivity and scattering techniques can be used to show how reactive oxygen species can cause drastic rearrangements of lipid bilayers. This work has begun to establish the damage caused to cell membranes by various reactive oxygen species and the reorganisation of biological membrane this could instigate. Future research in oxidation of lipid membranes could employ these techniques to investigate the mechanisms, products and kinetics of these reactions.

Chapter 7 Overall Conclusions and Future Outlook

The work presented in this thesis aimed to investigate oxidative damage to the lung surfactant and lipid membranes, specifically examining the damage caused to the lung surfactant components upon exposure to the atmospheric pollutant ozone and exploration of neutron scattering and reflectivity techniques to determine the damage caused to lipid membranes by reactive oxygen species.

Lung surfactant contains a mixture of proteins and lipids that exists as a monolayer on the fluid lining of the lungs to reduce surface tension in order to maintain normal breathing cycles.[1] The monolayer is composed of mainly the saturated phospholipid DPPC, unsaturated phospholipids, other lipids such as cholesterol and two surfactant proteins: SP-B and SP-C.[8] Exposure of the lungs to the pollutant ozone has been linked to an increase risk of death by respiratory distress, although the causes of this risk are largely unknown.[95] It is thought that ozone exposure to the essential lung surfactant can lead to significant chemical and structural damage to the monolayer that will drastically change its functional capacity.[110-116] In this research, experiments were performed to elucidate the ozone-induced structural damage to monolayers of the lung surfactant components, and the whole lung surfactant, and the changes this causes to the properties of the surface film, as well as the interaction between the components after ozone damage.

In Chapter 3, the structural damage to monolayers of peptide analogues of the lung surfactant protein SP-B by ozone at the air-water interface was researched. Previously, Kim *et al.* observed that methionine and tryptophan residues within SP-B_{1-25} were oxidised by ozone at the air-water interface and proposed that this caused the peptide to leave the interface, presumably due to a change in the hydrophobicity of the peptide.[167] In this thesis, surface pressure measurements showed that both the peptides SP-B_{1-25} and SMB were rapidly oxidised by ozone to form films of lower surface pressure. Two-photon fluorescence microscopy of the tryptophan residue within monolayers of SMB at the air-water interface revealed that all tryptophan residues had reacted after 10

minutes of exposure to ~2 ppm ozone. Reverse-phase HPLC of collected SP-B_{1-25} and SMB monolayers after ozone exposure showed that the peptides did not fragment after reaction but more hydrophobic products were detected in the chromatograms. For SMB, it was proposed that these hydrophobic residues formed as a result of conformational changes in the peptide after oxidation, which led to its hydrophobic core being more exposed. In the case of SP-B_{1-25}, which is a smaller peptide than SMB, it was shown by performing SDS-PAGE that more higher order oligomers of the peptide were present after oxidation, which could explain the presence of more hydrophobic products being eluted in reverse-phase HPLC.

Neutron and X-ray reflectivity experiments of the peptide monolayers at the air-water interface revealed no changes in the thickness or spread of the monolayers during ozone exposure. This means that although the peptides are rapidly oxidised by ozone, the peptides remain at the interface after reaction and even though analyses revealed conformational changes, there was no evident change in monolayer thickness or scattering length density at the interface. Therefore, although it was proposed by Kim *et al.* that SP-B_{1-25} entered the bulk phase after oxidation by ozone,[167] it has been shown unequivocally in this work that this does not occur using these techniques.

The surfactant protein SP-B resides at the air-lung interface in a monolayer of lipids, therefore the oxidation of SMB was investigated in the presence of three different lipids, the Zwitterionic DPPC (the main component of the lung surfactant), and the anionic lipids POPG and DPPG. Neutron reflectivity of mixed monolayers of SMB and DPPC during ozone exposure at the air-water interface revealed that the presence of DPPC did not affect the oxidation of SMB by ozone and the DPPC molecules were not damaged. Additionally, the interaction between SMB and DPPC molecules during compression and expansion cycles was unchanged after oxidation by ozone. In contrast to this, the oxidation of SMB in the presence of anionic lipids did lead to a change in behaviour. Neutron reflectivity experiments showed that after ozonolysis of SMB at the air-water interface, anionic phospholipids were lost to the aqueous subphase upon compression of mixed SMB/anionic phospholipid monolayers. Therefore, it was concluded that the SP-B peptide mimic SMB reacts with ozone at the air-water interface and although it remains at surface, it interacts with anionic phospholipids very differently after

reaction. Since SP-B is thought to function to aid the respreading of phospholipids during breathing cycles by interacting *via* its positively charged residues with anionic phospholipids,[60,61] this finding suggests that ozone exposure could potentially affect the viability of the lungs if its interaction with the anionic lipids is changed.

The reactions between the lipid components of the lung surfactant and ozone at the interface were investigated in Chapter 4, building on previously published work from the Thompson research group.[136,185] Previous work by Pryor *et al.* determined that the aldehydes hexanal, heptanal and nonanal had formed in the lungs following ozone exposure, which was assumed to be due to the Criegee ozonolysis of unsaturated phospholipids.[113] Lai *et al.* and Uhlson *et al.* also showed that POPC reacts with ozone at the air-water interface and the product formed, as detected by MS, showed loss of the unsaturated tail. It has more recently been shown by Thompson *et al.* using neutron reflectivity that in the reaction between POPC monolayers and ozone at the air-water interface, the oleoyl strand is lost rapidly from the interface as the reaction occurs at the carbon-carbon double bond, but loss of the saturated palmitoyl tail was also observed at a much slower rate.[136]

The work presented in this thesis used neutron reflectivity at the air-water interface to show that the unsaturated anionic phospholipid POPG reacts similarly to POPC with ozone, i.e. material from both the oleoyl and the palmitoyl tails was lost from the interface. It was also shown using X-ray reflectivity experiments at the air-water interface that the thickness of both the POPC and POPG monolayers decreases after oxidation. Neutron reflectivity experiments of mixed monolayers of POPC and DPPC revealed that when the number of molecules of DPPC exceeded that of POPC in the monolayer, the rate of reaction at the oleoyl strand was decreased, therefore the oxidation of the lipid is affected by the presence of saturated phospholipids. This decrease in rate with increasing levels of DPPC was also observed by Qiao *et al.* who recently showed that the reaction between low levels of ozone and DOPC monolayers was selective in the presence of DPPC molecules and the rate of reaction between DOPC and ozone lowered with increasing levels of DPPC.[187]

Oxidation of cholesterol monolayers by ozone at the air-water interface has not been studied previously using these techniques. Ozonolysis of monolayers of cholesterol led to an increase in surface pressure upon ozone exposure and X-ray reflectivity experiments showed an increase in the thickness of the monolayer and an increase in the scattering length density at the surface after reaction with ozone. These results suggested that the molecules changed their arrangement at the interface after oxidation, which could significantly change the interfacial properties of the lung surfactant *in vivo*.

The ratio of saturated to unsaturated lipids is important for maintaining the function of the lung surfactant as the presence of unsaturated lipids aids the fluidity of the monolayer during breathing.[19] The presence of cholesterol is also thought to aid lipid respreading during compression and expansion of the monolayer.[27] Therefore, the damage of these lung surfactant components upon exposure to ozone discovered in this current work could be harmful to the function of the lung surfactant if it was to occur in the lungs.

Whole lung surfactant was extracted from pig or sheep lungs and surface pressure measurements showed a distinctive pattern upon ozone exposure, which could be attributed to the reactions between ozone and the individual components occurring at different rates. There was an overall large decrease in surface pressure after ozone exposure, demonstrating that significant oxidation of the lung surfactant had occurred. Neutron and X-ray reflectivity experiments showed that there was a loss of 30-40 % of material from the interface during ozone exposure, and a decrease in the monolayer thickness. These losses are considerably large, considering how sensitive the lung surfactant is to the correct composition in the lungs.

The rapid and significant damage to lipid components of the lung surfactant discovered in this thesis would lead to dramatic changes to the organisation and physical properties of the lung surfactant film, as demonstrated by the remarkable damage seen in exposure to whole lung surfactant presented above. Consequently, this study has provided further insights into the reasons to why ozone air pollution can cause respiratory problems. Future investigations of more complicated model systems, such as protein, phospholipids and cholesterol, could be studied using X-ray and neutron reflectivity techniques in order to further elucidate the changes in

the structure of monolayers and how the interaction between the molecules changes after ozonolysis. Also, chemical changes in the molecules could be investigated by designing analytical methods that can be used to determine how that structure of the components are changed after ozonolysis at the air-water interface.

Very little is known about the second lung surfactant protein, SP-C, a small, extremely hydrophobic protein, which has two palmitoyl chains bonded to two adjacent cysteines.[31] These palmitoyl chains are thought to be important for the function of the protein, although it is not known how they aid the protein in its function.[188] In order to examine the purpose of this structural feature, molecular dynamics simulations of mixed monolayers of palmitoylated SP-C (dpSP-C) and DPPC were performed, as well as monolayers of DPPC alone and DPPC and nonpalmitoylated SP-C (nSP-C) for comparison. In Chapter 5 it was revealed that the presence of the nSP-C or dpSP-C protein in a DPPC monolayer caused increases in thickness and tail carbon order parameters of DPPC compared to monolayers of DPPC alone, even at large areas per lipid. This suggests that the protein induces ordering of the phospholipid tails. This affect was significantly greater when the cysteines were palmitoylated on the protein, implying that the role of the palmitic chains is related to ordering the lipid tails even at fairly large areas per lipid. Now that a method for studying dpSP-C at the air-water interface has been established, the conformational and positional changes upon oxidation of the protein could be investigated, as well as its interaction with surrounding phospholipids, as it is likely that the structure and function of SP-C would be greatly affected by oxidative damage that leads to changes to its polarity.

In the final chapter, neutron scattering and reflectivity techniques were used to investigate reactions between phospholipid bilayers and ROS, and the outcomes of these reactions. The interaction of reactive oxygen species with biological membranes is known to produce a great variety of different functional modifications and has implications in apoptosis, cancer and aging.[129]

Recently, neutron reflectivity has been used to study lipid bilayers as a representation for biological membranes and their behaviour under oxidative conditions from short-wavelength UV light, i.e. a mixture of ROS.[232] It was found that bilayer thickness remained constant as a function of oxidative stress although

membrane surface coverage decreased with exposure time. In this thesis, neutron reflectivity at the solid-liquid interface was used to show that supported bilayers of DPPC reacted rapidly with singlet oxygen causing loss of lipids from the bilayer. This technique was also used to determine that bilayers of DOPC were significantly damaged by the ROS hypochlorite. Therefore, the reaction between lipid bilayers and individual ROS was able to be studied using neutron reflectivity.

Evidence has shown that oxidation of unsaturated lipids within cell membrane can reorganise lipid rafts, thought to be important for cell signalling and membrane trafficking.[123] SANS was used in this thesis to demonstrate the use of the technique for investigating lipid rafts and the change in their arrangement following oxidation. Coban *et al.* and Ayuyen *et al.* used atomic force and fluorescence microscopies to show that oxidation of unsaturated lipids leads to formation of significantly larger lipid rafts.[233,234] This has also been demonstrated using BAM.[235] In this thesis, SANS experiments of vesicles containing DPPC, DOPC and cholesterol and DPPC, POPC and cholesterol showed that they clearly form lipid rafts as temperature decreases. When POPC was replaced with the oxidised form of this lipid, PAzPC, in the vesicles, it was discovered using SANS that some of the oxidised lipid formed micelles rather than vesicles with the other components, meaning that the analysis of the raft formation was complicated by the change in scattering length density of the vesicles. Neutron reflectivity was also used to show that lipid rafts could form in a mixed monolayer of DPPC, DOPC and cholesterol at the air-water interface. Off-specular reflectivity was observed at low temperatures, demonstrating that ordered lipid rafts had formed, but not at high temperatures. Off-specular neutron reflectivity from the monolayer after oxidation by ozone was not detected; therefore lipid oxidation significantly changed the formation of lipid rafts.

Preliminary results have displayed the usefulness of neutron techniques as a tool to investigate the damage caused to cell membranes by various reactive oxygen species and the reorganisation of biological membrane this could instigate. Future research in oxidation of lipid membranes could employ these techniques to determine the mechanisms, products and kinetics of these reactions and reactions between lipid bilayers and other ROS.

References

1) R. King, *J. Appl. Physiol.,* 1982, **53**, 1-8.

2) B. Piknova, V. Schram, S. Hall, *Curr. Opin. Structural Biol.,* 2002, **12**, 487-494.

3) D. Shier, J. Butler, R. Lewis, R., *Hole's Human Anatomy and Physiology*, 11th Ed, McGraw-Hill, 2007, Ch. 19.

4) M. Avery, J. Mead, *Am. J. Dis. Child.,* 1959, **97**, 517-523.

5) J. Clements, R. King, *The Biochemical Basis of Pulmonary Function*, R.G Crystal, NY, Dekker, 1976.

6) C. Rebello, A. Jobe, J. Eisele, M. Ikegami, *Am. J. Respir. Crit. Care. Med*., 1996, **154**, 625–628.

7) J. Goerke, *Biochim. Biophys. Acta.,* 1998, **1408**, 79-89.

8) Y. Zuo, R. Veldhuizen, A. Neumann, N. Petersen, F. Possmayer, *Biochim. Biophys. Acta: Biomembranes,* 2008, **1778**, 1947-1977.

9) V. Im Hof, P. Gehr, V. Gerber, M. Lee, X. Schürch, *Respir. Physiol*., 1997, **109**, 81–93.

10) U. Pison, R. Herold, S. Schurch, *Coll. Surf. A: Physiochem. Eng. Aspects*, 1996, 165-184.

11) K. von Neergaard, *Gesamte. Exp. Med*., 1929, **66**, 373–394.

12) R. Pattle, *Nature*, 1955, **175**, 1125–1126.

13) J. Clements, *Proc. Soc. Exp. Biol. Med*., 1957, **95**, 170–172.

14) M. Williams, *J. Cell. Biol.,* 1977, **72**, 260-277.

15) J. Perez-Gil, T. Weaver, *Physiol.,* 2010, **25**, 132-141.

16) F. Heinz, *Respir. Res.,* 2001, **2**, 33-46.

17) J. Johansson, T. Curstedt, *Eur. J. Biochem,* 1997, **244**, 675-693.

18) V. Kaganer, H. Mohhwald, P. Dutta, *Rev. Mod. Phys.*, 1999**, 71**, 779-819**.**

19) R. Veldhuizen, K. Nag, S. Orgeig, F. Possmayer, *Biochim. Biophys. Acta.,* 1998, **1408**, 90-108.

20) S. Schurch, *Respir. Physiol*. 1982**, 48**, 339-355.

21) E. Weibel, H. Bachofen, *NIPS* 2, 1987, 72-75.

22)http://avantilipids.com/index.php?option=com_content&view=article&id=1700&Itemid=419 (accessed September 2014)

23) C. Daniels, S. Orgeig, A. Smits, *Respir. Physiol.*, 1995, **102**, 121-135.

24) J. Baatz, B. Elledge, J. Whitsett, *Biochem.,* 1990, **29**, 6714-6720.

25) S. Yu, F. Possmayer, *Biochim. Biophys. Acta.,* 1992, **1126**, 26-34.

26) R. Notter, S. Holcomb, R. Mavis, *Chem. Phys. Lipids,* 1980, **27**, 305-319.

27) B. Fleming, K. Keough*, Chem. Phys. Lipids,* 1988, **49**, 81-86.

28) C. Cañadas, *Biochim. Biophys. Acta: Biomembranes*, 2012, **1818**, 2550–2562.

29) J. Head, T. Mealy, F. McCormack, B. Seaton, *J. Biol. Chem*., 2003, **278**, 43254–43260.

30) K. Håkansson, N. Lim, H. Hoppe, K. Reid, *Structure*, 1999, **7**, 255–264.

31) J. Johansson, T. Szyperski, T. Curstedt, K. Wuthrich, *Biochem.*, 1994, **33**, 6015–6023.

32) Y. Kuroki, T. Akino, *J. Biol. Chem.,* 1991**, 266**, 3068–3073.

33) K. Khubchandani, J. Snyder, *FASEB,* 2001, **15**, 59-70.

34) J. Wright, D. Youmans, *Am. J. Physiol*., 1995**, 268**, L772–L780.

35) W. Rice, G. Ross, F. Singleton, S. Dingle, J Whitsett, *J. Appl. Physiol*., 1987, **63**, 692–698.

36) G. Pryhuber, *Mol. Gen. and Met.,* 1998**, 64**, 217-228.

37) M. Ikegami, A. Jobe, D. Berry, *Biol. Neonate*, 1986**, 50**, 121–129.

38) A. Cockshutt, J. Weitz, F. Possmayer, *Biochem.,* 1990**, 29**, 8424–8429.

39) M. Ikegami, T. Korfhagen, J. Whitsett, M. Bruno, S. Wert, K. Wada, A. Jobe, *Am. J. Physiol*., 1998**, 275**, L247–L254.

40) C. Gaynor, F. McCormack, D. Voelker, S. McGowan, L. Schlesinger, *J. Immunol*., 1995, **155**, 5343–5351.

41) C. Benne, B. Benaissa-Trouw, J. van Strijp, C. Kraaijeveld, J. van Iwaarden, *Eur. J. Immunol*., 1997**, 27**, 886–890.

42) J. Ferguson, D. Voelker, F. McCormack, L. Schlesinger, *J. Immunol.,* 1999, **163**, 312-321.

43) M. Allen, R. Harbeck, B. Smith, D. Voelker, R. Mason, *Infect. Immun.,* 1999, **67**,

4563-4569.

44) K. Hartshorn, E. Crouch, M. White, P. Eggleton, A. Tauber, D. Chang, K. Sastry, *J. Clin. Invest.*, 1994, **94**, 311-319.

45) P. Reading, U. Holmskov, E. Anders, *J. Gen. Virol.*, 1998, **79**, 2255-2263.

46) M. Ikegami, A. Jobe, S. West, B. Stripp, R. Morris, S. Glasser, C. Bachurski, H. Iwamoto, J. Whitsett, *Proc. Natl. Acad. Sci*. USA, 1996**, 93**, 9594–9599.

47) L. Gordon, K. Lee, A. Waring, *J. Pept. Res.*, 2000, **55**, 330–347.

48) M. Sarker, A. Waring, V. Booth, *Biochem.*, 2007, **46**, 11047–11056.

49) S. Hawgood, M. Derrick, F. Poulain, *Biochim. Biophys. Acta*, 1998, **1408**, 150–160.

50) J. Johansson, T. Curstedt, H. Joernvall, *Biochem.*, 1991, **30**, 6917–6921.

51) A. Cruz, C. Casals, I. Plasencia, D. Marsh, J. Perez-Gil, *Biochem*, 1998, **37**, 9488–9496.

52) L. Gordon, K. Lee, M. Lipp, J. Zasadzinski, F. Walther, M. Sherman, A. Waring*., J. Peptide Res.,* 2000, **55**, 330-347.

53) R. Bruni, H, Taeusch, A. Waring, *Proc. Natl. Acad. Sci. USA,* 1991, **88**, 7451-7455.

54) L. Gordon, S. Horvath, M. Longo, J. Zasadzinski, W. Taeusch, K. Faull, C. Leung, A. Waring, *Protein Sci*., 1996**, 5**, 1662-1675.

55) S. Kumar, PhD thesis, Conformational analysis of a synthetic fragment of lung surfactant apolipoprotein, University of Minnesota, Minneapolis, 1994.

56) H. Akinbi, *J. Biol. Chem.*, 1997, **272**, 9640-9747.

57) J. Clark, *Am. J. Respir. Cell. Mol. Biol.,* 1997, **16**, 46-52.

58) J. Whitsett, L. Nogee, T. Weaver, A. Horowitz, *Physiol. Rev.*, 1995**, 75**, 749–757.

59) F. Poulain, S. Nir, S. Hawgood, *Biochim. Biophys. Acta*, 1996**, 1278**, 169–175.

60) D. Takamoto, M. Lipp, A. von Nahmen, K. Lee, A. Waring, J. Zasadzinki, *Biophys. J.,* 2001, **81**, 153-169.

61) W. Fullagar, K. Aberdeen, D. Bucknall, P. Kroon, I. Gentle, *Biophys. J.,* 2003, **85**, 2624-2632.

62) J. Johansson, *FEBS Lett.*, 1991, **281**, 119-122.

63) J. Johansson, *Biochem. J.,* 1995, **307**, 525-541.

64) S. Glasser, *PNAS*, 2000, **98**, 6366-6371.

65) S. Yu, F. Passmayer, *J. Lipid. Res.*, 2001, **42**, 1421-1429.

66) M. Oosterlakendijksterhuis, H. Haagsman, L. van Golde, R. Demel, *Biochem.,* 1991, **30**, 10965–71.

67) J. Johansson, G. Nilsson, R. Stromberg, B. Robertson, H. Jornvall, T. Curstedt,

Biochem. J., 1995, **307**, 535–41.

68) A. Gericke, C. Flach, R. Mendelsohn, *Biophys. J.* 1997, **73**, 492–99.

69) P. Nakorn, M. Meyer, C. Flach, R. Mendelsohn, H. Galla, *Eur. Biophys. J.,* 2007**, 36**, 477–489.

70) Z. Wang, *J. Biol. Chem.*, 1996, **271**, 19104-19109.

71) R. Rodriguez, R. Martin, A. Fanaroff*, Respiratory distress syndrome and its management.* Fanaroff and Martin, St. Louis: Mosby, 7th ed., 2002, 1001-1011.

72) R. Schwartz, A. Luby, J. Scanlon, R. Kellogg, *New Eng. J. Med.*, 1994, **330**, 1476-1480.

73) K. Ohashi, A. Sato, T. Takada, *et al., Respir Med*, 2012**, 106**, 284–293.

74) M. Wilder, *J. Perinat. Neonat. Nurs.,* 2004, **18**, 61-67.

75) L. Guillot, R. Epaud, G. Thouvenin, L. Jonard, A. Mohsni, R. Couderc, F. Counil, J. de Blic, R. Taam, M. Le Bourgeois, P. Reix, F. Flamein, A. Clement, D. Feldmann, *J. Med. Genet*., 2009**, 46**, 490-4.

76) S. Yu, F. Possmayer, *J. Lipid Res.,* **39**, 1998, 555-568.

77) S. Hawgood, *The Lung: Scientific Foundations*, 2nd ed., R. Crystal, E. West, P. Barnes (Eds.), Lippincott-Raven, Publishers, Philadelphia, Surfactant: composition, structure, and metabolism, 1997, 557–571.

78) P. Silveyra, J. Florosa, *Swiss Med. Wkly.,* 2012**, 142**, w13579.

79) http://www.lenntech.com/faq-air-pollution.html (accessed September 2014)

80) http://www.cleanerandgreener.org/resources/air-pollution.html (accessed September 2014)

81) http://www.blf.org.uk/Page/Outdoor-Air-Pollution (accessed September

2014)

82) http://www.londonair.org.uk/LondonAir/ (accessed September 2014)

83) http://www.arb.ca.gov/ei/emissiondata.htm (accessed September 2014)

84) http://www.guardian.co.uk/environment/2012/jul/26/olympics-london-smog___(accessed September 2014)

85) http://www.who.int/gho/phe/outdoor_air_pollution/exposure/en/index.html (accessed September 2014)

86) A. van Donkelaar, R. Martin, M. Brauer, R. Kahn, R. Levy, C. Verduzco, P. Villeneuve, *Environ. Health Perspect.,* 2010**, 118**, 847–855.

87) http://www.nasa.gov/topics/earth/features/health-sapping.html (accessed September 2014)

http://www.nasa.gov/centers/goddard/news/topstory/2006/ozone_garden_prt.htm (accessed September 2014)

88) W. McDonnell, H. Kehrl, S. Abdul-Salaam, P. Ives, L. Folinsbee, R. Devlin, R., O'Neil, D. Horstman, *Arch. Environ. Health,* 1991**, 46**, 145-150.

89) M. Arbex, G. de Souza, S. Cendon, F. Arbex, A. Lopes, E. Moyses, S. Santiago, P. Saldiva, L. Pereira, A. Braga, *J. Epidemiol. Community Health,* 2009**, 63**, 777-783.

90) J. Anseth, A. Goffin, G. Fuller, A. Ghio, P. Kao, D. Upadhyay, *Am. J. Respir. Call. Mol. Biol.,* 2005, **33**, 161-168.

91) S. Lagorio, *Environ. Health,* 2006**, 5**, 1-12.

92) R. Johnson, *Circulation,* 2004**, 109**, 5-7.

93) H. Anderson, C. Spix, S. Medina, J. Schouten, J. Castellsague, *et al*., *Eur Respir J.,* 1997, **10**, 1064-1071.

94) M. Bell, A. McDermott, S. Zeger, J. Samet, F. Dominici, *J. Am. Med. Assoc.,* 2004**, 292**, 2372-2378.

95) M. Jerrett, R. Burnett, C. Arden Pope, C. Ito, G. Thurston, D. Krewski, E. Calle, M. Thun, *New Eng. J. Med.*, 2009, **360**, 1085-1095.

96) R. Burnett, R. Dales, M. Raizenne, D. Krewski, *Environ. Res.,* 1994, **65**, 172-94.

97) W. Adams, *Inhal. Toxicol.,* 2006**, 18**, 127-136.

98) J. Browns, T. Bateson, W. McDonnell, *Environ. Health Perspect.,* 2008**, 116**, 1023-1026.

99) A. Podgorski, T. Sosnowski, *J. Aer. Med.,* 2001**, 14**, 455-466.

100) M. Kendall, S. Holgate, *Respirology,* 2012, **17**, 743-758.

101) C. Lorz, J. Lopez, *Anat. Rec.,* 1997**, 249**, 206-212.

102) T. Kanishtha, *Environ. Toxicol. and Pharm.,* 2006, **22**, 325-333.

103) M. Bakshi, *Biophys. J.,* 2008, **94**, 855-859.

104) C. Schleh, *Resp. Res.,* 2009, **10**, 90.

105) C. Lai, B. FinlaysonPitts, *Lipids,* 1991**, 26**, 306-314.

106) R. Cotton, T. Olsson, A. Law, R. Parker, D. Lindshom, A. Silberberg., H. Sundell, K. Sandberg, *Ped. Res.,* 1993, **34**, 495-501.

107) I. Haddad, S. Zhu, J. Crow, E. Barefield, T. Gadilhe, S. Matalon, *Am. J. Phys. – Lung Cell & Mol. Phys.,* 1996, **270**, L898-L906.

108) R. Criegee, *Angew. Chem. In. Ed. Engl.,* 1975, **14**, 745-752.

109) J. Clayden, N. Greeves, S. Warren., *Organic Chemistry,* Oxford UP (2nd edition), 2012.

110) J. Balis, J. Paterson, J. Lundh, E. Haller, S. Shelley, M. Montgomery, *Am. J. Path.,* 1991, **138**, 847-857.

111) W. Su, T. Gordon, *J. Appl. Phys.,* 1996, **80**, 1560-1567.

112) E. Putman, W. Liese, W. Voorhout, L. VanBree, L. VanGolde, H. Haagsman, *Tox. & Appl. Pharm.,* 1997, **142**, 288-296.

113) W. Pryor, E. Bermudez, R. Cueto, G. Squadrito, *Fund. & Appl. Tox.,* 1996, **34**, 148-156.

114) J. Mudd, *Atmos. Environ.,* 1967, **3**, 667-681.

115) S. Enami, M. Hoffman, A. Colussi, *J. Phys. Chem. b,* 2009, **113**, 9356-9358.

116) E. Gilbert, S. Hodenberg, *Ozone:Sci. eng.: J. Int. Ozone Assoc.,* 1997, **19**, 145-156.

117) M. Valko, C. Rhodes, J. Moncol, *Chemico-Biol. Interactions*, 2006, **160**, 1-40.

118) H. Esterbauer, R. Schaur, H. Zollner, *Free Rad. Biol. Med.*, 1991, **11**, 81-128.

119) M. Valko, D. Leibfritz, J. Moncol, M. Cronin, M. Mazur, J. Telser, D. Brown, E.

London, *Int. J. Biochem. Cell Biol*., 2007, **39**, 44-84.

121) K. Simons, E. Ikonen, *Nature*, 1997, **387**, 569-572.

122) K. Simons, R. Ehehalt, *J. Clin. Inv.*, 2002, **110**, 597-603.

123) C. Gómez-Moutón, R. Lacalle, *J. Cell. Biol.,* 2004, **164**, 759-768.

124) E. Cadenas, *Ann. Rev. Biochem.,* 1989, **58**, 79-110.

125) M. Dizdaraglu, P. Jaruga, M. Birincioglu, *Free Rad. Biol. Med.,* 2002**, 32**, 1102-1115.

126) L. Marnett, *Carcinogenesis*, 2000, **21**, 361-370.

127) A. Catala, *Chem. Phys. Lipids,* 2009, **157**, 1-11.

128) J. Kaunig, Y. Xu, K. Wallage, *Free Radical Toxicology,* Taylor & Francis, London, 1997, 375-400.

129) J. Drevs, M. Medinger, C. Scmidt-Gerbasch, *Curr. Drug Target,* 2003, **4**, 113-121.

130) M. Gupta, K. Dobash, E. Greene, *Mol. Cell Biochem.,* 1997, **176**, 337-347.

131) P. Merkel, D. Kearns, *J. Am. Chem. Soc.,* 1972, **94**, 7244-7253.

132) J. Kanofsky, *J. Chem. Biol. Interact*., 1989, **70**, 1-28.

133) A. Krieger-Liszkay, *J. Exp. Bot*., 2004, **56**, 337-346.

134) J. Arnhold, A. Osipov, H. Spalteholz, O. Panasenko, J. Schiller, *Free Radic Biol Med*, 2001, **31**, 1111-1119.

135) O. Panasenko, *Biofactors*, 1997, **6**, 181-190.

136) K. Thompson, A. Rennie, M. King, S. Hardman, C. Lucas, C. Pfang, B. Hughes, A. Hughes, *Langmuir,* 2010, **26**, 17295-17303.

137) P. Atkins, J. de Paula, *Physical Chemistry*, 9th Edition, Oxford University Press.

138) J. Chadwick, *PRSL,* 1932, **A136**, 692, 1-16.

139) E. Fermi, H. Anderson, E. Booth, J. Dunning, F. Slack, *Phys. Rev.,* 1939**, 55**, 511-512.

140) E. Wollan, W. Davidson, C. Shull, *Phys. Rev.,* 1949, **75**, 1348-1352.

141) B. Brockhouse, *Physics Nobel Lecture,* 1994**,** 107-138.

142) W. Marshall, S. Lovesy, *Theory of Neutron Scattering,* Oxford University Press, 1971**.**

143) G. Squires, *Thermal Neutron Scattering,* Cambridge University Press, 1978**.**

144) ISIS Neutron Training Course Handbook, 2012.

145) www.ill.eu/ (accessed September 2014)

146) www.isis.stfc.ac.uk/ (accessed September 2014)

147) J. Penfold, R. Richardson, A Zarbakesh, J. Webster. *J. Am. Chem. Soc. Faraday Trans.,* 1997, **93**, 3899-3917.

148) E. Hecht, *Optics* , Addison Wesley, 2002.

148)http://www.ill.eu/instruments-support/instruments-groups/instruments/figaro/ (accessed September 2014)

149) R. Campbell, M. Wacklin, I. Sutton, R. Cubitt, G. Fragneto, *Eur. Phys. J. Plus,* 2011**, 126**, 107-129.

150) L. Parrat, *Phys. Rev.,* 1954, **95**, 359-369.

151) Ksvnima.com/Langmuir-film (accessed September 2014)

152) KSV Instruments Ltd. Application note #107.

153) S. King, *Small-angle Neutron Scattering*, Wiley, Pethrick, R.A. & Dawkins, J.V. (editors), 1999.

154) M. Kotlarchyk, S. Chen, *J. Chem. Phys. Chem.*, 1983, **92**, 1533-1538.

155) J. Percus, G. Yevick, *Phys. Rev,* 1958**, 110**, 1-13.

156) J. Hayter, J. Penfold, *Colloid Polymer Sc.i,* 1983, **261**, 1022-1030.

157) J. Kattwinkel, *Pediatrics,* 2005, **115**, 1075–76.

158) S. Shanmukh, N. Biswas, A. Waring, F. Walther, Z. Wang, Y. Chang, R. Notter, R. Dluhy, *Biophys. Chem.,* 2005, **113**, 233-244.

159) A. Waring, F. Walther, L. Gordon, J. Hernandez-Juviel, T. Hong, M. Sherman, C. Alonso, T. Alig, A. Braun, D. Bacon, J. Zasadzinski, *J. Pep. Res.*, 2005, **66**, 364–374.

160) E. Veldhuizen, A. Waring, F. Walther, J. Batenburg, L. Van Golde, H. Haagsman, *Biophys. J*., 2000, **79**, 377–384.

161) F. Walther, J. Hernández-Juviel, L. Gordon, A. Waring, P. Stenger, J. Zasadzinski, J., *Exp. Lung Res.*, 2005, **31**, 563-79.

162) F. Walther, J. Hernandez-Juviel, M. Gupta, R. Bruni, A. Waring, *Am. J. Respir. Crit. Care Med.,* 1999, **159**, A895.

163) M. Gupta, J. Hernandez-Juviel, A. Waring, R. Bruni, F. Walther, *Thorax,* 2001,

56, 871-876.

164) M. Gupta, J. Hernandez-Juviel, A. Waring, R. Bruni, F. Walther, *Am. J. Respir. Crit. Care Med.,* 2000, **161**, A656.

165) V. Sarin, S. Gupta, T. Leung, V. Taylor, B. Ohning, J. Whitsett, J. Fox, *Proc. Natl. Acad. Sci. USA*, 1990, **7**, 2633–2637.

166) F. Walther, A. Waring, J. Hernandez-Juviel, L. Gordon, Z. Wang, C. Jung, P. Ruchala, A. Clark, W. Smith, S. Sharma, R. Notter., *PLoS One*., 2010, **5**, e8672.

167) H. Kim, H. Kim, Y. Shin, L. Beegle, W. Goddard, J. Heath, I. Kanik, J. Beauchamp, *J. Am. Chem. Soc*., 2010, **132**, 2254-63.

168) M. Sarker, J. Rose, M. McDonald, M. Morrow, V. Booth, *Biochem.,* 2011**, 50**, 25-36.

169) H. Schagger, *Nature Protocols,* 2006, **1**, 16-22.

170) D. Bucknell, J. Penfold, J. Webster, A. Zarbakhsh, R. Richardson, A. Rennie, J. Higgins, R. Jones, P. Fletcher, R. Thomas, S. Roser, E. Dickinson, *Proc. ICANS XIII, P.S.I. Proceedings*, 1995, **95-02**, 123-129.

171) http://material.fysik.uu.se/Group_members/adrian/mono.htm (accessed September 2014)

172) http://material.fysik.uu.se/Group_members/adrian/drydoc.htm (accessed September 2014)

173) A. Nelson, *J. Appl. Cryst.*, 2006, **39**, 273-276.

174) F. Abeles, *Le Journal de Physique et le Radium*, 1950, **11**, 307–310.

175) H. Fischer, I. Polikarpov, A. Craievich, *Protein Sci.,* 2004, **13**, 2825-2828.

176) R. Armen, O. Uitto, S. Feller, *Biophys. J.,* 1998, **75**, 734-744.

177) L. Nevot, P. Croce, *J. Phys. Appl.* 1980, **15**, T61.

178)http://www.diamond.ac.uk/Beamlines/Surfaces-and-Interfaces/I07/guide.html (accessed September 2014)

179) N. Hardy, T. Richardson, F. Grunfeld, *Colloids Surf*., 2006, **284-285**, 202–206.

180) Y. Fukunaga, Y. Katsuragi, T. Izumi, F. Sakiyama, *J. Biochem.,* 1982, **92**, 129-41.

181) C. Uhlson, K. Harrison, C. Allen, S. Ahmad, C. White, R. Murphy, *Chem. Res.*

Toxicol., 2002**, 15**, 896-906.

182) H. Kim, H. Kim, Y. Shin, L. Beegle, W. Goddard, J. Heath, I. Kanik, J.Beauchamp, *J. Phys. Chem. B,* 2010**, 114**, 9496–9503.

183) E. Bligh, W. Dyer, *Can. J. Biochem. Phys.*, 1959, **37**, 911-917.

184) http://www.gelifesciences.com/webapp/wcs/stores/servlet/productById/en/GELifeSciences/80648470 (accessed September 2014)

185) K. Thompson, S. Jones, A. Rennie, M. King, A. Ward, B. Hughes, C. Lucas, R. Campbell, A. Hughes, *Langmuir*, 2013, **29**, 4594-4602.

186) A. Postle, E. Heeley, D. Wilton, *Comp. Biochem. and Phys. Part A,* 2001, **129**, 65-73.

187) L. Qiao, A. Ge, M. Osawa, S. Ye, *Phys. Chem. Chem. Phys.*, 2013, **15**, 17775-17785.

188) J. Johansson, *Biochim. et Biophys. Acta,* 1998, **1408**, 161-172.

189) G. VandenBussche, A. Clercx, T. Curtedt, J. Johansson, H. Jornvall, J. Ruysschaert, *Eur. J. Biochem*., 1992, **203**, 201-209.

190) W. Wang, O. Gurel, J. Baatz, R. Notter, *J. Biol. Chem*., 1996, **271**, 19104-19109.

191) R. Qanbar, S. Cheng, F. Possmayer, S. Schurch, *Am. J. Physiol*., 1996, **271**, 572-580.

192) R. Dluhy, S. Shanmukh, J. Leapard, P. Kruger, J. Baatzy, *Biophys. J.,* 2003, **85**, 2417–2429.

193) H. Kovacs, A. Mark, J. Johansson, W. Gunsteren, *J. Mol. Biol.*, 1995, **247**, 808-822.

194) C. Carvalheda, S. Campos, M. Machuqueiro, A. Baptista, *J. Chem. Inf. model,* 2013, **53**, 2979-2989.

195) H. Lee, S. Kandasamy, R. Larson, *Biophys. J*., 2005**, 89**, 3807–3821.

196) D. Rose, J. Rendell, D. Lee, K. Nag, V. Booth, *Biophys. Chem.*, 2008, **138**, 67-77.

197) S. Duncan, R. Larson, *Biochim. Biophys. Acta: Biomembranes,* 2010, **1798**, 1632-1650.

198) J. Haile, *Molecular Dynamics Simulation: Elementary Methods,* John Wiley & Sons Inc., USA.

199) H. Berendsen, D. van der Spoel, R. van Drunen, *Comp. Phys. Comm*., 1995, **91**, 43-56.

200) E. Lindahl, B. Hess, D. van der Spoel, *J. Mol. Model,* 2001, **26**, 1701-1718.

201) D. van der Spoel, E. Lindahl, B. Hess, G. Groenhof, A. Mark, H. Berendsen, *J. Comput. Chem.,* 2005, **26**, 1701-1718.

202) W. Van Gunsteren, H. Berendsen, *Mol. Sim.,* 1988, **1**, 173-185.

203) L. Verlet, *Phys. Rev.,* 1967, **159**, 98-103.

204) W. van Gunsteren, H. Berendsen, *Groningen Molecular Simulation (GROMOS) Library Manual,* Biomos, Groningen, The Netherlands, 1987, 1-221.

205) W. van Gunsteren, S. Billeter, A. Eising, P. Hunenberger, P. Kruger, A. Mark, W. Scott, I. Tironi, *Biomolecular Simulation: The GROMOS96 Manual and User Guide,* Vdf Hochschulverlag AG an der ETH Zürich, Zürich, Switzerland, 1996, 1-1042.

206) O. Berger, O. Edholm, F. Jahnig, *Biophys. J.*, 1997, **72**, 2002-2013.

207) W. Jorgensen J. Tirado-Rives, *J. Am. Chem. Soc.* 1988, **110**, 1657–1666.

208) G. Bussi, D. Donadio, M. Parrinello, *J. Chem. Phys*., 2007, **126**, 7.

209) H. Berendsen, J. Postma, W. van Gunsteren, A. DiNola, J. Haak, *J. Chem. Phys.,* 1984, **81**, 3684–3690.

210) S. Baoukina, E. Mendez-Villuendas, P. Tieleman, *J. Am. Chem. Soc*., 2012, **134**, 17543–17553.

211) C. Laing, S. Baoukina, D. Tieleman, *Phys. Chem. Chem. Phys*., 2009, **11**, 1916–1922.

212) J. Jos, G. Casares, L. Camacho, M. Martin-Romero, M. Lopez Cascales, *Chem. Phys. Chem.*, 2008, **9**, 2538–2543.

213) D. Rose, J. Rendell, D. Lee, K. Nag, V. Booth, *Biophys. Chem.*, 2008, **138**, 67-77.

214) B. Hess, C. Kutzner, D. van der Spoel, E. Lindahl, *J. Chem. Theory Comput*., 2008, **4**, 435-447.

215) W. Humphrey, A. Dalke, K. Schulten, *J. Molec. Graphics*, 1996, **14**, 33-38.

216) E. Pettersen, T. Goddard, C. Huang, G. Couch, D. Greenblatt, E. Meng, T. Ferrin, *J. Comput. Chem.,* 2004, **25**, 1605-1512.

217) Avogadro: Version1.08. http://avogadro.openmolecules.net/ (accessed September 2014)

218) M. Frisch, G. Trucks, H. Schlegel, *et al., Gaussian 03, Revision C.02*, Gaussian, Inc., Wallingford CT, 2004.

219) M. Dewar, E. Zoebisch, E. Healy, J. Stewart, *J. Am. Chem. Soc.,* 1985, **107**, 3902.

220) C. Oostenbrink, T. Soares, N. van der Vegt, W. van Gunsteren, *Eur. Biophys. J.*, 2005, **34**, 273-284.

221) B. Olausson, A. Grossfield, M. Pitman, M. Brown, S. Feller, A. Vogel, *J. Am. Chem. Soc*. 2012, **134**, 4324−4331.

222) J. Hermans, H. Berendsen, W. van Guntstren, J. Postma, *Biopolymers*, 1984, **23**, 1513-1518.

223) M. Parrinello, A. Rahman, *J. Appl. Phys.,* 1981, **52**, 7182.

224) T. Darden, D. York, L. Pedersen, *J. Chem. Phys,*, 1993, **98**, 10089-10092.

225) B. Hess, H. Bekker, H. Berendsen, J. Fraaije, *J. Comp. Chem.*, 1997, **18**, 1463–1472.

226) L. Martínez, R. Andrade, E. Birgin, J. Martínez, *J. Comp. Chem.*, 2009, **30**, 2157-2164.

227) C. Kandt, W. Ash, D. Tieleman, *Methods Struct. Biol. Membr. Prot.*, 2007, **41**, 475-488.

228) S. Nose, *J. Chem. Phys.,* 1984, **81**, 511–519.

229) W. Hoover, *Phys. Rev. A*, 1985**, 31**, 1695–1697.

230) S. Duncan, R. Larson, *Biophys. J.*, 2008, **94**, 2965–2986.

231) S. Kandasamy, R. Larson, *Biophys. J.,* 2005, **88**, 1577-1592.

232) H. Smith, M. Howland, A. Szmodis, Q. Li, L. Daemen, A. Parikh, J. Majewski, *J. Am. Chem. Soc.,* 2009, **131**, 3631-3638.

233) O. Coban, J. Popov, M. Burger, D. Vobornik, L. Johnston, *Biophys. J.,* 2007, **92**, 2842-2853.

234) A. Ayuyan, F. Cohen, *Biophys. J.,* 2006, **91**, 2172-2183.

235) R. Volinsky, R. Paananen, P. Kinnunen, *Biophys. J.,* 2012, **103**, 247-254.

236) H. McConnell, *Annu. Rev. Phys. Chem*., 1991, **42**, 171–195.

237) A. Brian, H. Mcconnell, *Proc. Natl. Acad. Sci.,* 1984**, 81**, 6159-6163.

238) http://material.fysik.uu.se/Group_members/adrian/bike.htm (accessed September 2014)

239) R. Heenan, FISH Data Analysis Program, *RAL Report*, *RAL*, 1989, 89-129.

240) J. Percus, G. Yevick, *Phys. Rev.,* 1958, **110**, 1-13.

241) J. Nagle, S. Tristam-Nagle, *Biochim. Biophys. Acta.,* 2000, **1469**, 159-195.

242) F. Wilkinson, W. Helman, A. Ross, *J. Phys. Chem. Ref. Data.,* 1995, **24**, 663-677.

243) Y. Wang, L. Chen, Y. Ding, W. Yan, *Pharm. Nanotech.,* 2012, **422**, 409-417.

244) J. Mattila, K. Sabatini, P. Kinnunen, *Biophys. J.,* 2007, **93**, 3105–3112.

245) A. Pande, S. Kar, R. Tripathy, *Biochim. Biophys. Acta*., 2010, **1798**, 442–452.